.

The German Aerosol Lidar Network: Methodology, Data, Analysis.

J. Bösenberg, M. Alpers, D. Althausen, A. Ansmann, C. Böckmann, R. Eixmann, A. Franke, V. Freudenthaler, H. Giehl, H. Jäger, S. Kreipl, H. Linné, V. Matthias, I. Mattis, D. Müller, J. Sarközi, L. Schneidenbach, J. Schneider, T. Trickl, E. Vorobieva, U. Wandinger, M. Wiegner

February 28, 2001

ISSN 0937–1060

Contents

Abstract

The German Aerosol Lidar Network has attempted, for the first time worldwide, to establish a climatological data set for the aerosol vertical distribution over several stations in a quantitative and coordinated approach. Quantitative results have been obtained by employing advanced lidar methods like Raman or scanning lidar to retrieve profiles of the extinction coefficient directly. To provide for a sufficiently homogeneous data set substantial effort was put into data quality assurance. Intercomparisons were performed at both system and retrieval algorithm levels. A very satisfactory agreement between the different systems was achieved. A rather large data set of aerosol extinction and backscatter profiles was collected using regularly scheduled measurements on predetermined days and times to avoid a bias due to ”preferred” weather conditions for lidar observations. A large number of additional measurements were devoted to studies of special weather conditions. The results of special studies related to the aerosol distribution associated with high pressure systems and cold front passages are reported as well as special studies on the long term development of the stratospheric aerosol distribution, transport processes in an Alpine valley, and long range transport of aerosol. The retrieval of aerosol microphysical properties using lidar measurements at several wavelengths is described mathematically and applied to actual examples, showing very promising results. Several methods for the statistical analysis of the climatological data set are developed making use of the simultaneously collected data set of backtrajectories. Products of these analyses include the seasonal dependence of boundary layer heights, the mean extinction and backscatter profiles, the mean optical depth, separately for PBL and free troposphere, the seasonal dependence of aerosol extinction, the statistical distribution of aerosol extinction and of extinction-to-backscatter ratio values, and the dependence of aerosol optical properties on the airmass history.

Chapter 1

Introduction

by J. Bösenberg

The German Aerosol Lidar Network was established in 1998 as a joint project of six institutes supported by the Federal Ministry of Education and Research in the frame of the funding focus “Atmospheric Aerosol Research (AFS)”. The participating institutions are (from North to South):

- Leibniz-Institut für Atmosphärenphysik, Kühlungsborn (**IAP**)
- Max-Planck-Institut für Meteorologie, Hamburg (**MPI**)
- Institut für Mathematik der Universität Potsdam (**IMP**)
- Institut für Troposphärenforschung, Leipzig (**IfT**)
- Meteorologisches Institut der Ludwig-Maximilians-Universität, München (**MIM**)
- Fraunhofer-Institut für Atmosphärische Umweltforschung, Garmisch-Partenkirchen (**IFU**)

The observational network is established by the institutes in Kühlungsborn, Hamburg, Leipzig, München, and Garmisch-Partenkirchen. The IMP is involved in the development of algorithms to retrieve aerosol microphysical properties from multispectral lidar measurements. Fig. 1.1 shows the geographical distribution of the measurement stations.
The central objective of the German aerosol lidar network is to establish a comprehensive, statistically significant, and unbiased climatological data base of the vertical aerosol distribution over Germany. This is considered necessary, because

- Aerosols play an important role in the climate system, and affect mens life in many ways.
- The retrieval of the vertical distribution of aerosol is important to assess the role of transport processes for the observed aerosol load.
- Reliable data on the vertical distribution of aerosols are too sparse to be representative, even over regions that are usually well covered by environmental observations.
- Germany is a suitable area to characterize the natural and man-made variability of tropospheric aerosol.
- An investigation of correlations between aerosol and meteorological parameters requires long-term measurements at selected sites.

- Lidar methods are particularly suited for establishing a statistically representative data set of the aerosol vertical distribution.

In order to reach this objective the goals of the joint project were:

- to install a small number of stations where suitable lidar systems and groups with sufficient experience in their operation for aerosol retrievals were available
- to establish a common observation scheme,
- to assess data quality,
- to build a common data set of quantitative aerosol parameter profiles,
- to develop methods for analysis of aerosol spatial and temporal distributions,
- to form the core of a future larger network.

Great emphasis was put on the requirement to provide quantitative aerosol properties, in this case the aerosol extinction and/or backscatter coefficients as a function of height. Special care was taken to retrieve these quantities unambigously, from the selection of instruments as well as from retrieval schemes.

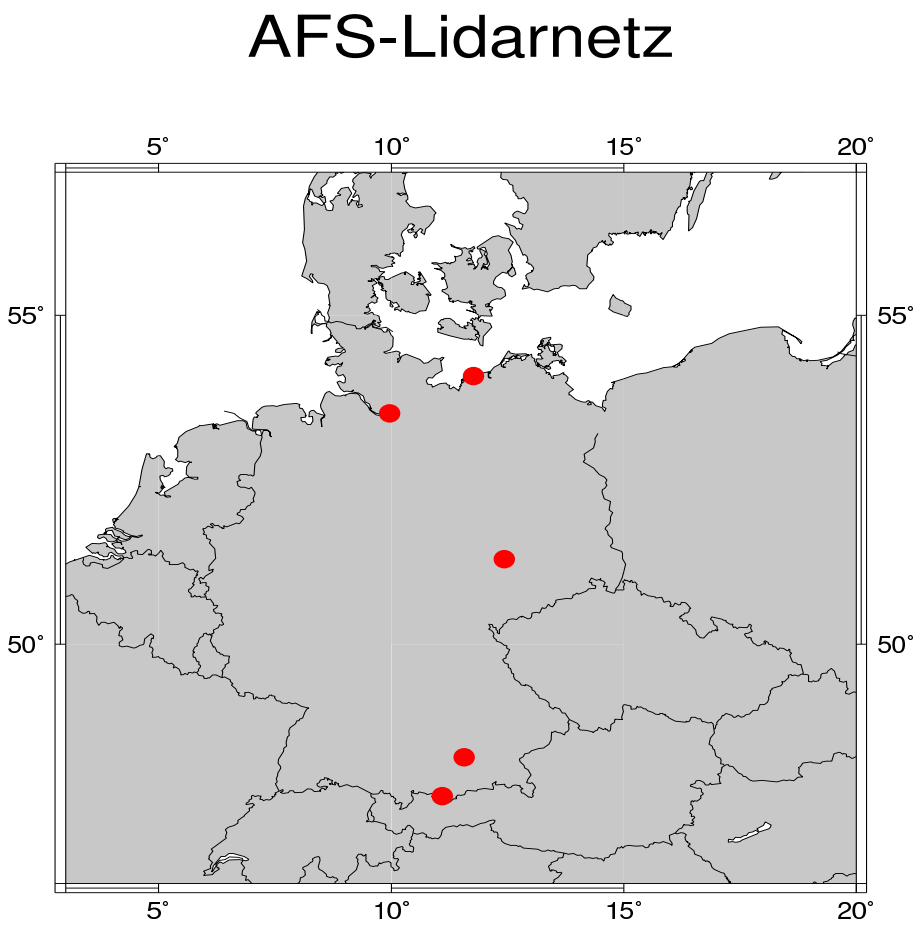

Figure 1.1: The stations of the German Aerosol Lidar Network.

It was clear from the beginning that five stations would not be sufficient to provide full coverage of the troposphere over Germany in a statistically representative way. However, the selection of stations provided for the possibility to characterize quite different airmasses and aerosol types: more or less pristine maritime (Hamburg and Kühlungsborn), rural (Kühlungsborn, Garmisch), urban (Munich, Leipzig, Hamburg), anthropogenic industrial (Leipzig), and of course many different mixtures between the basic types. Coordinated measurements also provided for the possibility, at least in principle, to study the tranformation of airmasses while they were tranported over Germany.
This report is organized as follows: a description of the basic methodology of the aerosol retrievals and the sampling strategy is followed by a brief description of the instruments. A larger part is devoted to the quality assurance, both at the algorithm and the instrument level. The retrieval of microphysical parameters from lidar measurements is discussed both from a mathematical standpoint and from practical applications. In the main part different approaches for statistical data analysis for the five stations are presented. This also includes a special chapter on the use of trajectories and associated cluster analysis. In addition to the climatological measurements a fairly large number of additional observations have been performed, in particular for high pressure conditions, cold front passages, related to long range transport, and concerning the vertical transport mechanisms in the Alps. The German lidar network also provided a frame for the continuation of a long time series of stratospheric aerosol measurements at Garmisch-Partenkirchen, the results of these studies are also included.

Chapter 2

Methodology

2.1 Lidar methods

by J. Bösenberg

For the analysis of measurements taken at different times and different locations it is very important that the measurements are quantitative. Lidar methods are sufficiently mature now to provide reliable and quantitative aerosol measurements, but in order to come up with well defined physical parameters it is necessary to use a combination of several methods.
The basis of any lidar signal analysis is the lidar equation which describes the receiver signal as a function of atmospheric and system parameters. The standard form of the lidar equation for the case of quasimonochromatic emission, instantaneous elastic scattering, negligible multiple scattering processes, and neglible coherence of the backscattered signal is

$$P(\nu, R) = 0.5 \cdot E_L \cdot c \cdot A \cdot R^{-2} \cdot \eta(\nu, R) \cdot \beta(\nu, R) \cdot e^{-2\int_0^R \alpha(\nu,r)dr} \tag{2.1}$$

where $P(\nu, R)$ is the received signal power from distance R, ν the wavenumber of the transmitted light, R the distance of the scattering volume from the transmitter/receiver, E_L the transmitted pulse energy, c the velocity of light, A the active area of the receiving telescope, $\eta(\nu, R)$ the total system efficiency, $\beta(\nu, R)$ the total backscatter coefficient at distance R, and $\alpha(\nu, R)$ the total atmospheric extinction coefficient.

2.1.1 Backscatter lidar

For the purpose of inversion of eq. 2.1 it is useful to write it in differential form

$$\frac{d}{dR} ln(P \cdot R^2) = \frac{d}{dR} ln\, \beta - 2\alpha\,. \tag{2.2}$$

In this equation the measured quantity is P, the distance R is known, and β and α are unknowns. It is obvious that there is no unique solution to this equation. This problem of the standard backscatter lidar retrieval is usually "solved" by assuming a constant ratio between backscatter and extinction,

$$S_L = \frac{\alpha}{\beta}\,, \tag{2.3}$$

where S_L is called "lidar ratio". There are numerous publications on retrieval algorithms based on these equations, the most commonly used ones are described in (Fernald, 1984; Klett, 1981; Klett,

1985; Sasano and Nakane, 1984). In principle these publications describe the same algorithm, which will be treated in detail in section 4.1.2. It is worth mentioning that this algorithm does account for different lidar ratios for molecular and aerosol scattering, and at least in principle accepts a height-dependend lidar ratio. The clear disadvantages of this retrieval are: it requires a calibration value, i.e. an absolute value of the backscatter coefficient at a selected range (calibration range); it is numerically unstable for integration beyond the calibration range; it is sensitive to noise in the signal; it requires the input of the lidar ratio, which is a usually not well known aerosol property. There are numerous publications on the properties of these solutions, in particular on the sensitivity to the choice of input parameters and error propagation. For an overview see, e.g., (Bösenberg et al., 1997). It has to be emphasized that this inversion method is not quantitative because of the dependence on the input of unknown aerosol parameters. However, although the original application for which this method had been developed was the retrieval of the extinction coefficient in turbid media, it can yield useful results for backscatter profiles in clean areas of the atmosphere. This is mainly true for the upper troposphere and the stratosphere, and there also the aerosol microphysical parameters are often rather well known, e.g. for some types of stratospheric aerosols. Since the backscatter lidar is rather easy to operate and the signal is at least a byproduct of any lidar measurement this method is used to a large extent. It should, however, be stated explicitly that in contrast to the backscatter coefficients the extinction coefficients obtained through this method are accurate only to that extent to that the lidar ratio has been guessed. For tropospheric aerosol this guess is usually rather poor.
So far three methods have been demonstrated to overcome the limitations of the backscatter lidar for quantitative retrievals of aerosol optical parameters: high spectral resolution lidar, Raman lidar, and scanning lidar.
The high spectral resolution lidar uses extremely narrow filters to separate the aerosol from the molecular return (Grund and Eloranta, 1991). Because of the rather demanding technology it is implemented at very few experimental sites only. It is not considered here because it was not used within the network.

2.1.2 Raman lidar

The use of Raman scattering from nitrogen or oxygen in addition to measuring the elastic backscatter is a well established tool for determining the extinction profile separately from the backscatter profile (Ansmann et al., 1992b). While the Raman and HSRL techniques are equivalent in performance, at least in principle, the preferred method within the network is the combination of Raman and elastic scattering at one UV wavelength around 355 nm. Three of the five stations have applied this technique.
The lidar equation in differential form for the case of the Raman lidar reads

$$\frac{d}{dR} ln(P \cdot R^2) = \frac{d}{dR} ln\, \beta_R - 2\alpha\,. \tag{2.4}$$

Again P is the measured quantity, R is known, the Raman backscatter coefficient β_R is generally known with sufficient accuracy as a function of height, and the extinction coefficient α is the only unknown in this equation. Hence it can be solved uniquely, and the known α provides for a unique solution for β as well. This also permits the determination of the lidar ratio, S_L, and measured profiles demonstrate that the assumption of a constant lidar ratio is generally not justified.

2.1.3 Scanning lidar

The third possibility to retrieve the extinction profile independently is to perform measurements at two or more different zenith angles simultaneously or at least alternating (Gutkowicz-Krusin, 1993).

When sufficient temporal averaging is applied it may be assumed under many conditions that the aerosol properties are the same for both directions. Then the set of two lidar equations can be solved directly to yield extinction and backscatter profiles. The corresponding differential lidar equation reads

$$\frac{d}{dR} ln \left(\frac{P_{\varphi_1}}{P_{\varphi_2}} \right) = -2 \frac{cos\varphi_2 - cos\varphi_1}{cos\varphi_2 \cdot cos\varphi_1} . \alpha \tag{2.5}$$

This method has its main advantage at longer wavelengths where Raman scattering is too weak. The disadvantage of course is that horizontal homogeneity is required, which may be difficult to prove for specific applications. The systems at Munich and Leipzig are capable of operating in this mode.

2.2 Aerosol characterisation

The characterisation of the aerosol type was intended in a phenomenological way. The plan was to use the wavelength dependence of the backscatter coefficient, obtained from measurements at approximately 1.06, 0.53, and 0.35 μm, to characterise the aerosol type. In the course of the project this turned out to be more difficult as expected because in more complex situations the inversion of the 1.06 μm lidar measurements is not reliable. On the other hand it turned out that many successful measurements of the extinction-to-backscatter ratio could be performed and that this value, the so-called lidar ratio, is quite characteristic for the type of aerosol. Hence for statistical investigations this quantity seems to be preferable over the wavelength dependece of the backscatter coefficient. Both quantities have actually been used. The best characterisation of aerosol of course is presented by its microphysical parameters, e.g. number concentration, mass density, surface density, mode radius, refractive index, etc. Because the methods to derive these quantities from lidar measurements have not been available in the beginning but rather been developed within the frame of this project, such evaluations were limited to a few examples only. No sufficient data set to perform a solid statistical analysis could be collected. This was also due to the fact that most lidar systems were not capable of providing the necessary input profiles, at least not during routine operation. However, the results of the microphysical retrieval studies indicate that in principle a microphysical rather than a phenomenological characterisation is possible.

2.3 Sampling strategy

The German aerosol lidar network was made up by 5 stations that have not been chosen from first principles in view of optimum location with respect to areal coverage, but rather because of the existence of suitable lidar systems and groups that have sufficient experience in tropospheric aerosol research. While the density of the network is certainly not sufficient to claim that the region of Germany is well covered, the locations are representative for different important types of aerosols that are likely to occur over Germany. Hamburg and Kühlungsborn are located well in the north with clear maritime influence, Leipzig is located in East Germanys industrialised region, Munich is an urban area in the south, and Garmisch-Partenkirchen is an alpine station with strong orographically induced flow patterns. The aerosol types that occur over these stations may be considered quite representative for the most common aerosol types that occur over Germany as a whole.

It is also important to note that measurements are performed under a broad range of atmospheric conditions. One of the important advantages of lidar over passive remote sensing methods is that it can yield reliable results even in case of the presence of complex cloud fields that are variable in height and horizontal extension. In order to avoid any bias in the results due to selection of specific

conditions for the measurements, the climatological data set has been collected on a regular schedule on preselected dates, regardless of weather conditions. If weather conditions did not permit lidar operation during the scheduled period, e.g. due to rain or fog, this fact is noted in the data record, thus providing also a statistics of occasions when aerosols do not play a major role for most atmospheric processes.

With respect to the frequency of measurements a compromise between requirements for good coverage and limitations of resources had to be found. Initially it was decided to make 2 measurements per week, Monday and Thursday, around 13 UT, when the boundary layer usually is well developed, plus one measurement each Monday at or after sunset to permit the use of Raman lidar for best extinction measurements. The exact time for the sunset measurement was not considered very important, since previous observations had shown that no fast changes in the boundary layer structure occur at this time of the day. It is more or less the period when convective mixing has died out and the residual layer has formed with relatively small dynamic changes.

In the course of the project it became very clear that the Raman measurements would become the backbone of the data set. Hence it was decided to add another sunset measurements to the regular schedule, namely Thursday evening, and eventually drop the measurement at Thursday noon.

Although this schedule may look not very intense it turned out that the performance of these regular measurements was a rather heavy burden for the groups. It also turned out that even this rather modest schedule was sufficient to increase the statistical data base dramatically. In fact this collection of measurements provide for the first time a suitable data base for statistical studies of the vertical distribution of aerosol on a regional scale.

Chapter 3

System descriptions

3.1 Max-Planck-Institut für Meteorologie, Hamburg

The aerosol lidar system of the MPI für Meteorologie is based on a XeF excimer laser emitting at 351 nm. The laser beam is expanded three times and emitted vertically into the atmosphere.
Equipped with two receiving telescopes, the height range covered with aerosol backscatter measurements is from ca. 300 m to 10000 m. Measurements of the Raman backscatter on atmospheric nitrogen at 382 nm are used to determine an aerosol extinction profile. These measurements are limited to darkness because too high counting rates from the solar background saturate the detectors at daytime. The Raman measurements allow the independent determination of aerosol extinction and backscatter profiles in altitudes between ca. 500 m and 5000 m.
For both detection wavelengths, photomultiplier tubes (PMT) from Thorn EMI are used as detectors. The Raman channel is equipped with a specially for photon counting purposes designed PMT with a small cathode to reduce dark counts. Elastic backscattered signals are detected in analog mode with 12 bit analog-digital-converters (ADC) with a typical resolution of 15 m and 10 s. The photon counting system used for the Raman channel has a height resolution of 30 m and a typical time resolution of 30 s. The measured dead time of the receiving detector and the following electronics is in the order of 8-11 ns, leading to maximum used counting rates of ca. 20 MHz.
The whole system is built in a standard 20 feet container and can be transported by truck. It has been used for routine measurements at Hamburg within the German Lidar Network and for the LACE 98 field campaign at Lindenberg. Detailed information can be found in table 3.1.
During LACE 98 the system has also been used for daytime aerosol lidar measurements in the solar blind region at 268 nm. This is possible because the system can easily be changed to a combined ozone DIAL/UV Raman lidar. For this purpose, the emitted wavelength of the excimer laser is changed to 248 nm, which can be done in a few hours. Additional wavelengths at 268 nm, 292 nm and 320 nm are generated by stimulated Raman scattering in deuterium at 40 bar. Raman scattering from atmospheric nitrogen can be detected at 286 nm (emitted wavelength 268 nm) and 306 nm (emitted wavelength 292 nm). Both measurements have to be corrected for ozone which can be done with the simultaneously measured ozone profile. Therefore range and accuracy of these measurements is limited in comparison to the nighttime measurements at 382 nm. These measurements have only been performed during the LACE campaign. For more details about the MPI aerosol lidar see (Matthias, 2000).
Since July 2000 the MPI operates a new aerosol lidar based on a three wavelengths flash lamp pumped Nd:YAG laser. Regular measurements with this system started in November 2000 within the frame of the EARLINET project.

Station		
Contractor	MPI für Meteorologie	
Location	Hamburg	
Coordinates	53.568 N, 9.973 E	
Emitter		
Laser type	XeF Excimer, Lambda Physik EMG 201	
Emitted wavelength	351 nm	
Typ. energy	50 mJ	
Repetition rate (typ.)	10 Hz	
Beam expansion	$3\times$	
Beam divergence	$< 0.2\mathrm{mrad}$	
Receiving Optics		
	Telescope 1	Telescope 2
Diameter	400 mm	150 mm
Focal length	1400 mm	450 mm
Field stop	1.25 mm quartz fibre	
Manufacturer	MPI	MPI
Scanning capability	no	
Zenith angle	0	
Beam/Telescope Configuration	biaxial	
Wavelength separation	beam splitter	
Detectors		
Elastic channels		
Wavelength	351 nm	
Detector	PMT, EMI 9883 QB	
Preamplifier	FEMTO HCA-S	
Filter bandwidth	10 nm interference filter	
Raman channels		
Wavelength	382 nm	
Detector	PMT, EMI 9893 QB 350	
Discrminator	Phillips Scientific 6904	
Data acquisition mode	700 MHz photon counting, Optech FDC700M	
Filter bandwidth	1.5 nm	
Data acquisition		
	Elastic	Raman
Acquisition system	12 bit analog	700 MHz photon counting
Manufacturer	PENTEK/MPI	Optech
Range resolution (raw)	15 m	30 m
Time resolution anal. (raw)	10 s	30 s
Continuous acquisition	yes	yes
Surrounding		
Transportable system	yes	
Size	ca. $2.5\mathrm{m} \times 2.5\mathrm{m} \times 6.0\mathrm{m}$ (Container)	
Weight	ca. 8 tons	

Table 3.1: The MPI aerosol lidar system: detailed technical information on the configuration used for routine measurements within the German Lidar Network.

3.2 Leibniz-Institute of Atmospheric Physics, Kühlungsborn

The Leibniz-Institute of Atmospheric Physics (IAP) uses a Nd:YAG laser system (Spectra Physics GCR 290) emitting at the fundamental (1064 nm) and the first and second harmonic (532 and 355 nm). Detected signals include the three emitted wavelength plus the nitrogen Raman shifted return signals at 607 and 387 nm. Additionally, the vertical depolarized return signal at 532 nm is detected. All signals are detected with 50 m vertical resolution. The receiver site consists of two telescopes (50 cm diameter each) of which the first is mounted coaxially to laser beam and is used for detection of the 355 nm, 532 nm, 1064 nm, and the 607 nm Raman signal. Full geometric overlap is reached at 1000 m, approximately. The second is mounted off-axis and is used for the 387 nm and the depolarized signal. Here, full geometric overlap is reached only at 2000 m. The system is located at Kühlungsborn, Germany (54°07' N, 11°46' E), in a rural environment near the shore of the Baltic Sea, and is in operation since June 1997 (Alpers et al., 1999). In the detection branch the wavelengths are seperated by dichroic beam splitters, filtered using interference filters (Barr Associates, Inc.), and detected by photomultiplier tubes. The technical data of the system are summarized in the following table.

Station		
Contractor	Leibniz-Institut für Atmosphärenphysik	
Location	Kühlungsborn	
Coordinates	54°07'N, 11°46'E	
Emitter		
Laser type	Nd:YAG, Spectra Physics GCR 290	
Emitted wavelength	1064, 532, 355 nm	
Typ. energy	500, 400, 200 mJ	
Repetition rate (typ.)	30 Hz	
Beam expansion	$10\times$	
Beam divergence	$< 0.2\mathrm{mrad}$	
Receiving Optics		
	Telescope 1	Telescope 2
Diameter	500 mm	500 mm
Focal length	1200 mm	1200 mm
Field stop	1 mm quartz fibre	
Manufacturer	LFM (Laboratory for Precision Machining), University of Bremen	
Scanning capability	no	
Zenith angle	0	
Beam/Telescope Configuration	coaxial	biaxial
Polarization filter	optional	optional
Wavelength separation	beam splitter	

Detectors	
Elastic channels	
Wavelength	354.7 nm
Detector	PMT, Hamamatsu 4220P (selected)
Preamplifier	SMT MEA15-30SF-V5D
Filter bandwidth	0.92 nm interference filter
Wavelength	532.1 nm (Telescope 1)
Detector	PMT, Hamamatsu 4632P (selected)
Preamplifier	SMT MEA15-30SF-V5D
Filter bandwidth	0.35 nm interference filter
Wavelength	532.1 nm (Telescope 2)
Detector	PMT, Hamamatsu 4632P (selected)
Preamplifier	SMT MEA15-30SF-V5D
Filter bandwidth	0.36 nm interference filter
Wavelength	1064.1 nm
Detector	PMT, Hamamatsu R3236 (selected), cooled
Preamplifier	EG&G VT120
Filter bandwidth	1.0 nm interference filter
Raman channels	
Wavelength	386.7 nm
Detector	PMT, Hamamatsu 4220P (selected)
Preamplifier	SMT MEA15-30SF-V5D
Filter bandwidth	1.0 nm interference filter
Wavelength	607.4 nm
Detector	PMT, Hamamatsu 4632P (selected)
Preamplifier	SMT MEA15-30SF-V5D
Filter bandwidth	0.36 nm interference filter
Data acquisition	
Acquisition system	100 MHz photon counting
Manufacturer	Joerger Enterprises, Inc., Model S3
Range resolution (raw)	50 m
Time resolution anal. (raw)	8 s, 33 s, 133 s (typical)
Continuous acquisition	yes
Surrounding	
Transportable system	no

Table 3.2: The IAP aerosol lidar system: detailed technical information

3.3 Institut für Troposphärenforschung, Leipzig

The transportable IfT multiwavelength lidar was used for the intercomparison measurements during LACE 98. The general setup of the system is shown in Fig. 3.1. The system is described in detail in (Althausen et al., 2000). Two Nd:YAG and two dye lasers emit laser pulses simultaneously at 355, 400, 532, 710, 800, and 1064 nm with a repetition rate of 30 Hz. All six laser beams are co-aligned onto one optical axis with polarizing and dichroic mirrors. A lens telescope expands the laser beam tenfold, before it is emitted into the atmosphere. A scanning unit allows measurements under zenith angles from -90^o to $+90^o$.

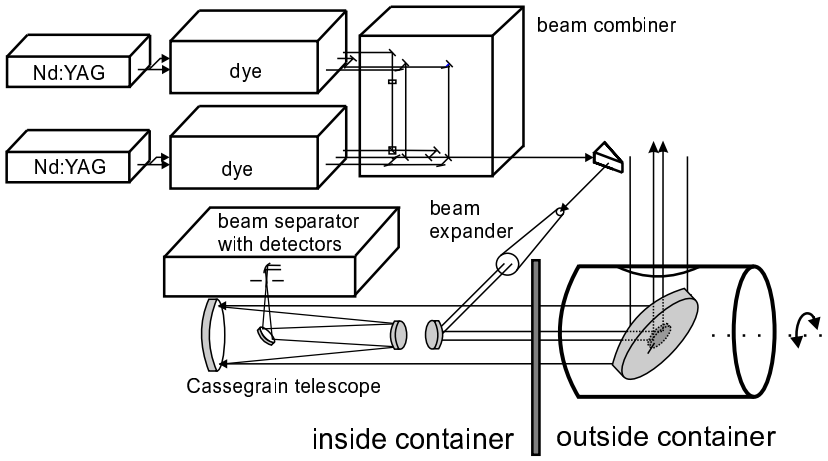

Figure 3.1: Schematic view of the IfT multiwavelength lidar (from (Althausen et al., 2000)).

The backscatter signals are collected with a 0.53-m Cassegrain telescope, separated according to their wavelength, and detected by photomultipliers. In eleven channels the elastic backscatter signals at the six emitted wavelengths, the cross-polarized signal at 710 nm, and the Raman signals of nitrogen at 387 and 607 nm and of water vapor at 660 nm are detected. Signals are selected with dichroic and polarizing beamsplitters and narrow-band interference filters. Photomultiplier tubes (PMT) are used as detectors at all wavelengths. Whereas for the elastic backscatter signals (except at 355 nm) the analog PMT output is digitized (12 bit, 10 MHz) and stored, the Raman signals, the elastic backscatter signal at 355 nm, and part of the elastic backscatter signal at 532 nm are detected in the photon-counting mode. PMTs, discriminators, and photon counters operate at 300 MHz. Raman signals can be measured at nighttime only. Table 3.3 summarizes the parameters determined from the eleven backscatter signals of the IfT multiwavelength lidar.

Table 3.3: Data determined with the IfT multiwavelength lidar.

Parameter	Wavelength, nm	Day	Night	Parameter	Wavelength, nm	Day	Night
Backscatter Coefficient	1064	x	x	Extinction Coefficient	532	x	x
	800	x	x		355		x
	710	x	x	Depolarization Ratio	710		x
	532	x	x				
	400	x	x	Water-Vapor Mixing Ratio			x
	355	x	x				

Station						
System	multi-wavelength aerosol Raman lidar					
Contractor	Institute for Tropospheric Research					
Location	Leipzig (51.35 N, 12.43 E); Lindenberg (52.22 N; 14.12 E)					
Emitter						
Laser types	2 Nd:YAG, Spectra Physics GCR 5-30 2 Dye, Lambda Physik LPD 3002					
Emitted wavelengths	1064 nm	532 nm	355 nm	800 nm	710 nm	400 nm
Typ. energy	500 mJ	250 mJ	80 mJ	3 mJ	10 mJ	1.5 mJ
Repetition rate	30 Hz					
Beam expansion	10-fold					
Beam divergence	< 0.1mrad					
Receiving Optics						
Telescope	Cassegrain					
Diameter	0.53 m					
Effective focal length	2.973 m					
Field stop	1-17.5 mm					
Manufacturer	Carl Zeiss Jena GmbH					
Scanning capability	yes					
Zenith angle	-90^{o} to $+90^{o}$					
Beam/telescope config.	coaxial					
Wavelength separation	beam splitters, interference filters					
Detectors						
Elastic channels, analog						
Wavelengths	1064 nm	800 nm	710 nm $\parallel$	710 nm $\perp$	532 nm	400 nm
Detectors (PMT)	Hamamatsu R632	Hamamatsu R2228			EMI 9817QB	EMI 9214QB
Filter bandwidth	5.0 nm	0.42 nm	0.40 nm	0.37 nm	1.1 nm	0.33 nm
Elastic channels, photon counting						
Wavelengths	532 nm			355 nm		
Detectors (PMT)	EMI 9893A/350			Hamamatsu R5600P-03		
Filter bandwidth	5.0 nm			0.35 nm		
Raman channels						
Wavelengths	660 nm (water vapor)		607 nm (nitrogen)		387 nm (nitrogen)	
Detectors (PMT)	EMI 9893A/350				Hamamatsu R5600P	
Filter bandwidth	3.0 nm		3.0 nm		2.8 nm	
Data acquisition						
	analog			photon counting		
Discriminator				Phillips Scientific, Octal 300 MHz, NIM model 708		
Acquisition system	12 bit analog-digital converter			300 MHz multichannel scaler		
Manufacturer	Intelligent Instrumentation			MEDAV GmbH		
Range resolution (raw)	15 m			60 m (typical)		
Time resolution (raw)	30 s (typical)			30 s (typical)		
Continuous acquisition	yes			yes		
Surrounding						
Transportable system	yes (2 standard containers, ca. 12 tons)					
Additional instruments	sun photometer, Vaisala radiosonde					

Table 3.4: The IfT multiwavelength lidar.

The aerosol Raman lidar (ARL) is used for the regular measurements of the lidar network project. The Raman lidar was primarily designed for performing long-term studies of optical aerosol properties in the boundary layer, the free troposphere and, the stratosphere (Mattis et al., 2001). The non-transportable system is installed in a laboratory under the roof of the institute building, which is located near the center of Leipzig. This lidar site is situated in a highly industrialized region, where brown-coal mining and large power plants are strong aerosol sources.

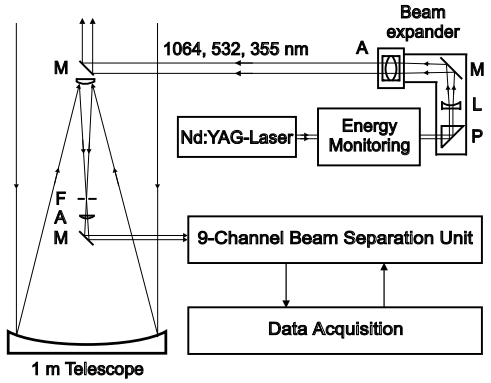

Figure 3.2: Schematic view of the dual-wavelength aerosol Raman lidar. P, L, M, F, and A indicate a prism, a lens, mirrors, the field stop, which determines the receiver field of view, and achromatic lenses, respectively.

Figure 3.2 illustrates the general setup of the Raman lidar. A seeded Nd:YAG laser emits pulses with an overall power of about 1.2 J. An eight-fold lense beam expander reduces the divergence to less than 0.1 mrad. The backscattered light is collected with a 1-m Cassegrain telescope. Within a 9-channel receiver the elastically backscattered signals and the Raman signals of nitrogen and of water vapor are separated by the use of dichroic beam-splitters and interference filters. A polarizer discriminates the parallel- and cross-polarized components of the 532-nm backscatter signal. Two pure rotational Raman signals are separated with a double-grating monochromator. These signals are used to determine temperature profiles by means of the pure rotational Raman technique (Arshinov et al., 1983,). The optical aerosol properties and meteorological data listed in Table 3.5 can be derived from the 9 measured signals.

In a co-operation with the Institute for Atmospheric Optics of the Siberian Branch of the Russian Academy of Sciences at Tomsk, Russia, the transmission properties and the background suppression of the double-grating monochromator were steadily improved (Arshinov and Bobrovnikov, 1999; Arshinov et al., 2001,).

Aerosol Properties				Meteorological Data		
Parameter	Wavelength, nm	Day	Night	Parameter	Day	Night
Backscatter Coefficient	1064	x	x	Water-Vapor Mixing Ratio		x
	532	x	x			
	355	x	x			
Extinction Coefficient	532	(x)	x	Temperature		x
	355	(x)	x			
Depolarization Ratio	532	x	x	Relative Humidity		x

Table 3.5: Data provided by the Raman lidar. Data in parentheses are determined in the lower troposphere only.

Station			
System	multi-wavelengths aerosol Raman lidar		
Contractor	Institute for Tropospheric Research		
Location	Leipzig		
Coordinates	51.35 N, 12.43 E		
Emitter			
Laser type	Nd:YAG, Spectra Physics GCR-290-30		
Seeder	Spectra Physics CE GCR/PRD		
Emitted wavelengths	1064 nm	532 nm	355 nm
Typ. energy	450 mJ	450 mJ	450 mJ
Repetition rate	30 Hz		
Beam expansion	8×		
Beam divergence	$< 0.1\mathrm{mrad}$		
Receiving Optics			
Telescope	Cassegrain		
Diameter	1 m		
Effective focal length	10 m		
Field stop	1-1.8 mm		
Manufacturer	Carl Zeiss Jena GmbH		
Scanning capability	no		
Zenith angle	0		
Beam/Telescope Configuration	coaxial		
Wavelength separation	beam splitters, interference filters		
Detectors			
Elastic channels			
Wavelengths	355 nm	532 nm (parallel) 532 nm (cross)	1064 nm
Detectors (PMT)	EMI 9893Q/350B	EMI 9893Q/350A	Hamamatsu R3236
Filter bandwidth	5-nm interference filter		
Vibrational Raman channels			
Wavelengths	387 nm (nitrogen)	408 nm (water vapor)	607 nm (nitrogen)
Detectors (PMT)	EMI 9893Q/350A		
Filter bandwidth	3-nm interference filter		
Pure rotational Raman channels			
Wavelengths	530.3 + 533.7 nm		529.0 + 535.0 nm
Detectors (PMT)	EMI 9893Q/350B		
Filter bandwidth	0.63-nm double-grating monochromator		
Data acquisition			
Discrminator	Phillips Scientific, Octal 300 MHz, NIM model 708		
Acquisition system	300 MHz photon counting (Purana)		
Manufacturer	MEDAV Digitale Signalverarbeitung GmbH		
Range resolution (raw)	60 m		
Time resolution (raw)	30 s		
Continuous acquisition	yes		
Surrounding			
Transportable system	no		
Additional instruments	sun photometer (routine measurements)		
	Vaisala radio sonde		

Table 3.6: The IfT aerosol Raman lidar.

3.4 Ludwig-Maximilians-Universität, Meteorologisches Institut, München

The lidar system, which has been constructed by Sensorlab GmbH in 1993/94, passed through several changes since then.
At the beginning of AFS, the system (see Table) agreed with the original specifications (Wiegner et al., 1995) with some minor modifications, e.g. the implementation of dithering in front of the AD-converters to improve the signal dynamic range in absence of sufficient detector and preamplifier noise. The special feature of the original setup was the digital optical fiber connection between the data acquisition front-end (AD-converters) and control electronics, which was assembled as a part of the scanning system, to the controlling and data storing computer. Thus, electromagnetic interference from external sources into the signal path were minimal.
The first major change was the movement of the lidar site from the laboratory in the Barbarastraße in Munich (altitude 510 m) to the laboratory on the roof of Meteorological Institute in the Theresienstraße (altitude 539 m) in January 1998. Now it was possible to perform scanning measurements over a wide range.
Unfortunately, the microprocessor unit of the data acquisition and system control was damaged during LACE98 in August 98 due to overheating caused by excess ambient temperatures. This defect was not repairable, and an immediate temporary solution to finish the campaign was the basis for a subsequent complete renovation of the data acquisition and the scanning electronic system.
A Tektronix TDS510a oscilloscope was used for data acquisition (8 bit, 50 MS/s). The manual control of the data acquisition and storage was replaced in Janaury 1999 by automatic computer control via GPIB, and simultaneously the manual scanning was replaced by computer controlled scanning via the original optical fiber link, which still worked with some bypasses. The control software was written in QuickBasic and Borland C; the PC was repalced by a 133 MHz Pentium.
The major drawback of this system was an increased sensitivity to external electromagnetic radiation due to the long electric cables for the analog signals and some unavoidable ground loops partly caused by the necessary modifications of the system, partly inherent in the original system. Our investigations in 1999 therefore focused on a new concept for an improved grounding scheme of the system. At the same time we extensively tested several transient recorders and various concepts for the control and scanning electronics. As a result, a 12 Bit transient recorder PC-card PCI.412 by Spectrum GmbH (`http://www.spec.de/index_e.htm`) with a sampling rate of 40 MS/s has been integrated in January 2000 and the modular scanning and control electronic system made by Jetter AG (PROCESS PLC NANO-B, `http://www.jetter.de/gb/main/index2.htm`) has been assembled shortly after. The controlling and analysis software has been redeveloped in Visual Basic. The final system specs are also summarized in the Table.

Parameter	Status 01/1998	Status 08/2000
Location:	Munich, 510 m asl	539 m asl
Coordinates:	48.14 N, 11.58 E	48.15 N, 11.57 E
Laser type:	Nd:YAG, Continuum Surelite II	
Emitted wavelengths:	355 nm, 532 nm, 1064 nm	
Typ. pulse energy:	175 mJ, 50 mJ, 175 mJ	
Repetition rate:	10 Hz	
beam divergence:	0.6 mrad fwhm	
Telescope:	Cassegrain	
focal length:	940 mm	
diameter:	301 mm	
field of view:	1 to 8 mrad full width	
1. Channel Wavelength:	355 nm	
1. Channel Detector:	PMT, Hamamatsu R5600	
1. Channel Filter bandwidth:	1.0 nm interference filter	
2. Channel Wavelength:	532 nm	
2. Channel Detector:	PMT, Hamamatsu R5600	
2. Channel Filter bandwidth:	1.1 nm interference filter	
3. Channel Wavelength:	1064 nm	
3. Channel Detector:	PIN	
3. Channel Filter bandwidth:	2.7 nm interference filter	
Data acquisition system:	Sensorlab custom made	Spectrum PCI.412
Number of analog channels:	4	
Data acquisition mode:	8 bit analog	12 bit analog
Sampling rate:	30 MS/s	40 MS/s
Range resolution (raw):	5 m	3.75 m
Scanning capability:	yes, automatic	
azimuth range:	-175° to +175 deg	
elevation range:	-5° to +95°	
Altitude range (typ.):	250 m - 5000 m	
Time resolution (raw):	0.1 s	
continuous acquisition:	yes, up to RAM size, single shot	yes, single shot
PC:	486 / 66 MHz	Pentium / 250 MHz
Programming language:	Borland C	Visual Basic, Fortran90

Table 3.7: MIM Lidar Specifications

3.5 Fraunhofer-Institut für Atmosphärische Umweltforschung, Garmisch-Partenkirchen

Four of the IFU lidar systems have been operated within the aerosol lidar network:

1. The NDSC lidar (532 nm) for the stratospheric routine measurements and routine measurements in the upper troposphere (see Table 3.8)

2. The mobile three-wavelength lidar for tropospheric routine measurements (355 nm, 532 nm, 1064 nm; see Table 3.9)

3. The stationary tropospheric ozone lidar (277 nm, 292 nm, 313 nm) for special transport studies

4. The mobile eyesafe aerosol lidar (1560 nm); system upgrading and testing only

The stratospheric lidar was originally built by Impulsphysik (Hamburg) in 1973 and was initially based on a ruby laser as the light source. The system was completely rebuilt in 1990 and the following years for high-resolution studies of contrails (Freudenthaler et al., 1994). High-precision angular scanning was implemented for this purpose. A Nd:YAG laser replaced the ruby laser. The stratospheric measurements are carried out exclusively during nighttime to eliminate background radiation. The three-wavelength lidar was built by Impulsphysik in 1978 and upgraded in the late 1980s. Since this time a small single-stage Nd:YAG laser is used in the transmitter section. This system has been applied in numerous field campaigns (e. g., (Bissonnette and Hutt, 1994; Kunz and Trickl, 1996; Carnuth and Trickl, 2000)). Within this project the plastics cover of the rear section of the lidar trailer was replaced by a stable cover made of aluminium which can be opened by simple shifting. In addition, the receiver optics, detection electronics have been replaced step by step by proven components developed for the IFU ozone lidar systems.
The ozone lidar (Eisele and Trickl, 1997) was used for routine measurements within the VOTALP project till February 1998. After this, mostly due to major damages, the soundings had to be reduced to about 100 per year. The results obtained may serve as an extension of the measurements with the aerosol lidars for some episodes of interest.
The eyesafe lidar (Carnuth and Trickl, 1994) was optimized in 1999. The Raman-shifted Nd:YAG laser source was further improved to yield about 270 mJ at 1560 nm which corresponds to a unprecedented conversion efficiency in deuterium of 33%. A residual magnetic interference observed during the 1997 Sylt field campaign could be eliminated. However, the planned simultaneous measurements with the three-wavelength lidar were cancelled due to staff limitations.

Station		
Contractor	Fraunhofer-Institut für Atmosphärische Umweltforschung	
Location	Garmisch-Partenkirchen	
Coordinates	47.476 N, 11.063 E, 730 m a. s. l.	
Emitter		
Laser type	QuantaRay GCR-4, Nd:YAG	
Emitted wavelength	1064 nm	
Additional wavelengths (by H/G)	355 nm, 532 nm	
Typ. energy	550 mJ (532 nm), 280 mJ (355 nm)	
Repetition rate	10 Hz	
Beam expansion	no	
Beam divergence	≤ 0.5 mrad	
Receiving Optics		
Diameter	520 mm	
Focal length	4076 mm	
Divergence	2.5 mrad	
Manufacturer	Impulsphysik GmbH (and self)	
Scanning capability	yes (high precision, computer controlled)	
Zenith angle	$0 \ldots 90$ deg.	
Azimuth angle	-90 deg $\ldots +90$ deg.	
Beam/Telescope Configuration	biaxial	
Wavelength separation	beam splitter	
Detectors		
Analog		
Wavelengths	355 nm, 532 nm (2 depolarization channels)	
Detectors	EMI 9128A photomultiplier tubes	
Preamplifier	Analog Modules	
Filter bandwidth	1 nm interference filters	
Photon counting		
Wavelength	532 nm	
Detector	EMI D341/350	
Discriminator	2-channel FAST 200 MHz	
Filter bandwidth	1 nm ... 3 nm interference filter	
Data acquisition		
	Analog	Photon counting
Acquisition system	TR40 12 bit/40 MHz	200 MHz
Manufacturer	FAST ComTec	FAST ComTec
Range resolution (raw)	15 m	75 m typical
Continuous acquisition	no	no
Surrounding		
Transportable system	yes	
Size	2.5 m $\times$ 2.9 m $\times$ 6.0 m (container)	
Weight	about 7 tons	

Table 3.8: The NDSC lidar at IFU

Station	
Contractor	Fraunhofer-Institut für Atmosphärische Umweltforschung
Location	Garmisch-Partenkirchen
Coordinates	47.476 N, 11.063 E, 730 m a. s. l.
Emitter	
Laser type	QuantaRay DCR-11, Nd:YAG
Emitted wavelength	1064 nm
Additional wavelengths (by H/G)	355 nm, 532 nm
Typ. energy (total)	400 mJ
Repetition rate	10 Hz
Beam expansion	no
Beam divergence	≈ 1 mrad
Receiving Optics	
Diameter	300 mm
Focal length	2300 mm
Field stop	3 mm iris diaphragm
Manufacturer	Impulsphysik GmbH
Scanning capability	yes
Zenith angle	$0 \ldots 90$ deg.
Azimuth angle	-90 deg $\ldots +90$ deg.
Beam/Telescope Configuration	biaxial
Wavelength separation	beam splitter
Detectors	
355 nm, 532 nm	
Detector	EMI 5816 photomultiplier tube
Preamplifier	DSP 1020 differential amplifier
Filter bandwidth	1 nm interference filters
1064 nm	
Detector	photo diode
Preamplifier	DSP 1020 differential amplifier
Filter bandwidth	1 nm interference filter
Data acquisition	
Acquisition system	DSP 2012S 12 bit/10 MHz analog
Manufacturer	DSP Technology, Inc.
Range resolution (raw)	15 m
Continuous acquisition	no
Surrounding	
Transportable system	yes
Size	about 2.0 m $\times$ 2.0 m $\times$ 7.0 m (trailer)
Weight	about 2.5 tons

Table 3.9: The mobile IFU three-wavelength lidar

Chapter 4

Quality assurance

For the purpose of using data from different stations in joint studies, and for the reliability of the data base as a whole it is important that the data quality is checked independently from the efforts of the individual groups. Data quality depends on system hardware as well as evaluation software. Tests have been performed for both areas separately and for overall performance. These will be described in detail in the following two sections.

4.1 Algorithm intercomparison

by C. Böckmann and U. Wandinger

Besides the system intercomparison (see Sec. 4.2), a basic exercise to assure the quality of network measurements is the comparison of the algorithms used to calculate the optical parameters from the lidar signals. Especially, the determination of the particle backscatter coefficient from a single elastic backscatter signal has to be proven. The general problem of the method to determine a quantity from a signal, which is influenced by two unknowns, may lead to differences between solutions obtained from different algorithms. Therefore, an intercomparison of algorithms applied by different lidar groups for retrieving the particle backscatter-coefficient profile was organized as part of the German Lidar Network. Using their individual algorithms all participating groups processed four sets of synthetic lidar data. The goal and the procedure of the simulation study is briefly described in the next section. After a short description of the Klett-Fernald-Sasano method (Klett, 1981; Klett, 1985; Fernald, 1984; Sasano et al., 1985), details of the individual algorithms of each group are presented in Sec. 4.1.2. Finally the results of the intercomparison study are discussed.

4.1.1 Data simulation and evaluation procedure

Synthetic lidar signals were used for the algorithm intercomparison. In this way, the numerical correctness and accuracy of the algorithms as well as the experience of the groups and the limits of the method itself could be tested for examples with different degree of difficulty. The synthetic lidar signals were calculated with the IfT lidar simulation model.[1] This software permits one to simulate and to evaluate elastically and inelastically backscattered lidar signals of arbitrary wavelengths in dependence on a variety of system parameters for a variable model atmosphere with arbitrary aerosol

[1]The simulations were performed by a person who was not involved in the evaluation of these data for the intercomparison study and the input data were not known to other persons.

and cloud layers. Sky background, background noise, and signal noise are considered as well. Atmospheric input parameters are profiles of temperature and pressure to calculate Rayleigh scattering and profiles of extinction coefficients and lidar ratios for the simulation of aerosol and cloud layers.
For the algorithm intercomparison four different data sets of elastic backscatter signals at wavelengths of 355, 532, and 1064 nm were simulated. A US standard atmosphere (United States Committee on Extension to the Standard Atmosphere, 1976) with a ground pressure of 1013 hPa and a ground temperature of 0 °C, a tropopause height of 12.0 km, and isothermal conditions above were assumed. The signal profiles were simulated without signal noise in cases 1 and 2 and with signal noise in cases 3 and 4. An incomplete overlap of laser beam and receiver field of view below 250 m was introduced. Typical system parameters (laser power, telescope diameter, etc.) were used for the calculations. However, they are not of importance for the algorithm intercomparison.
The input profiles of extinction and lidar ratio for the four simulation cases are shown in Fig. 4.1. They represent different atmospheric conditions with increasing degree of difficulty in data evaluation:

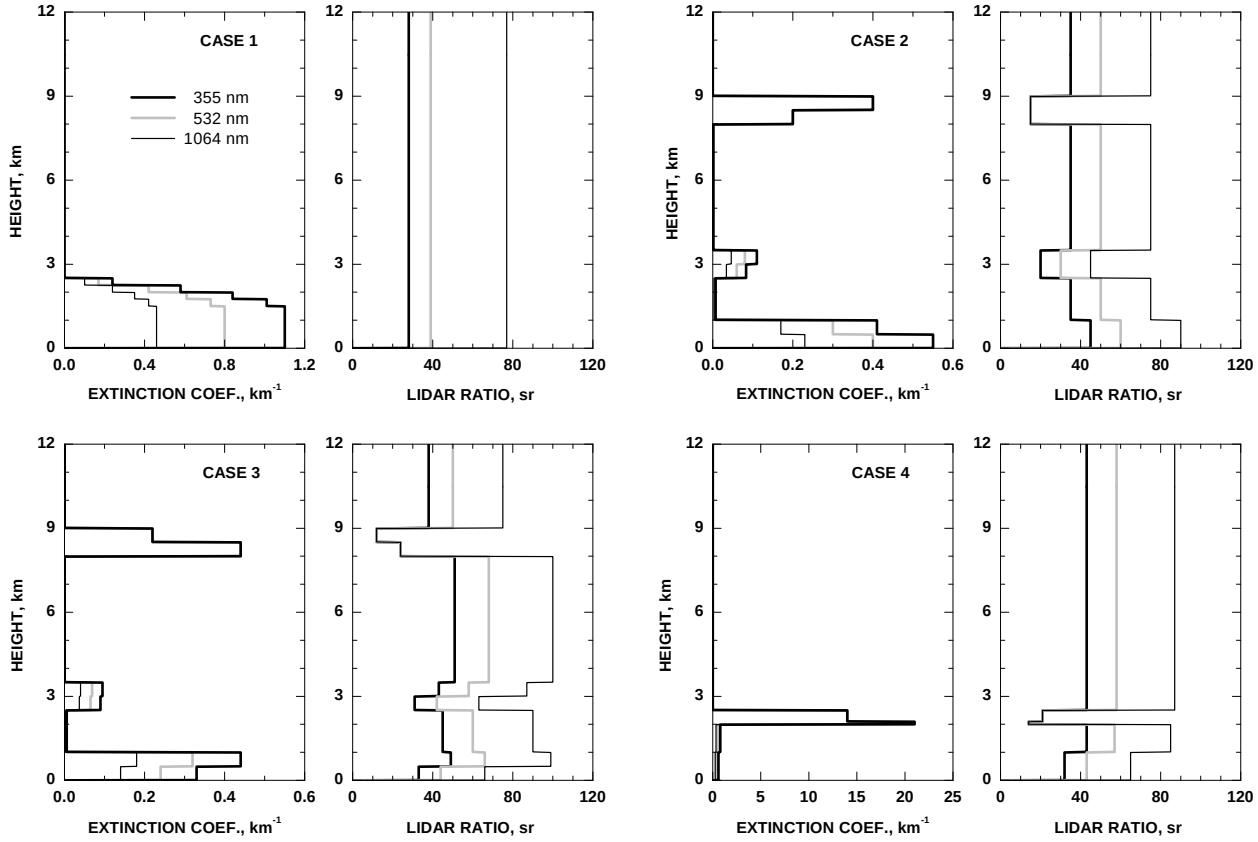

Figure 4.1: Input profiles of extinction and lidar ratio at 355, 532, and 1064 nm for the four simulation cases.

Case 1: The first case considers an atmospheric dust layer from ground to 2.5 km height. The extinction coefficient decreases with wavelength and with height. The lidar ratio also depends on wavelength but is height-independent.

Case 2: In the second case, a dust layer of 1 km height and a second aerosol layer at 3 km height were assumed. The lidar ratios are different in the two layers and depend on wavelength. Between 8 and 9 km height, a cirrus cloud with wavelength-independent scattering properties was introduced.

Case 3: Case 3 is similar to case 2 with the difference that the lidar ratio changes with height in both aerosol layers and also in the cirrus cloud.

Case 4: In case 4, a water cloud at the top of the atmospheric dust layer was simulated with wavelength-independent but height-dependent scattering properties. Extinction coefficient and lidar ratio in the dust layer vary with wavelength and with height.

The procedure of the algorithm intercomparison was as follows. First, the simulated signals were distributed to all groups without any information on the input parameters, except the used standard atmosphere. The groups calculated particle backscatter-coefficient profiles with their individual algorithms and sent the solution to IMP (the IMP group is not involved in experimental lidar work and acted as the referee). This first stage was the most difficult and most realistic one, because lidar-ratio profiles and reference values were unknown. Therefore, not only the correctness and accuracy of the algorithms was proven but also the experience in estimating the lidar ratio and choosing the reference value. In the second stage, the input lidar-ratio profiles were distributed and the groups had to evaluate the signals again. In the third and final stage, both lidar-ratio profiles and reference values were given to the participants. Thus, the final stage proves definitively the numerical correctness, i.e., the accuracy and stability of the algorithms depending on the noise level and other circumstances as explained below. The results of each group from each step were compared with the input data in order to determine the systematic errors. They are discussed at the end of the next Section.

4.1.2 Klett-Fernald-Sasano method and intercomparison results

Assuming a monochromatic laser pulse $P_0(\lambda)$ at wavelength λ, the lidar signal $P(\lambda, z)$ received during the integrating time Δt from the scattering of the laser light in the atmospheric layer located at altitude z is given by

$$P(\lambda, z) = C(\lambda) P_0(\lambda) \beta(\lambda, z) \frac{1}{z^2} \exp\{-2 \int_0^z \alpha(\lambda, u) du\}, \tag{4.1}$$

with the backscatter coefficient

$$\beta(\lambda, z) = \beta^{Ray}(\lambda, z) + \beta^{Aer}(\lambda, z) \tag{4.2}$$

and the extinction coefficient

$$\alpha(\lambda, z) = \alpha^{Mol}(\lambda, z) + \alpha^{Aer}(\lambda, z) = \alpha^{Mol}_{abs}(\lambda, z) + \alpha^{Ray}_{sca}(\lambda, z) + \alpha^{Aer}_{abs}(\lambda, z) + \alpha^{Aer}_{sca}(\lambda, z) \; . \tag{4.3}$$

The signal depends on the backscatter coefficients of molecules and aerosol particles β^{Ray} and β^{Aer}, respectively, and on attenuation due to molecular scattering α^{Ray}_{sca} and absorption α^{Mol}_{abs} and particle scattering α^{Aer}_{sca} and absorption α^{Aer}_{abs}. C is the system constant.
The determination of the aerosol backscatter coefficient $\beta^{Aer}(\lambda, z)$ from the elastic backscatter signal of Eq. (4.1) requires the solution of a Bernoulli differential equation. As the result one obtains

$$\begin{aligned} \beta^{Aer}(z) &= \frac{P(z) z^2 \exp\left\{ 2 \int_z^{z_0} \left[S^{Aer}(u) - S^{Ray} \right] \beta^{Ray}(u) \, du \right\}}{\frac{P(z_0) z_0^2}{\beta^{Aer}(z_0) + \beta^{Ray}(z_0)} + 2 \int_z^{z_0} S^{Aer}(u) P(u) u^2 \exp\left\{ 2 \int_u^{z_0} \left[S^{Aer}(v) - S^{Ray} \right] \beta^{Ray}(v) \, dv \right\} du} \\ &- \beta^{Ray}(z) \; , \end{aligned} \tag{4.4}$$

with the lidar ratios of molecular and particle scattering

$$S^{Ray} = \frac{\alpha^{Ray}}{\beta^{Ray}} = \frac{8\pi}{3} \text{ and } S^{Aer}(\lambda, z) = \frac{\alpha^{Aer}(\lambda, z)}{\beta^{Aer}(\lambda, z)}, \tag{4.5}$$

respectively. Molecular absorption is neglected here. Molecular scattering can be calculated from

$$\alpha_{sca}^{Ray}(z, \lambda; P, T) = \frac{8\pi^3(m_{air}^2 - 1)^2}{3\lambda^4 N_S^2} \frac{6 + 3\gamma}{6 - 7\gamma} N_S \frac{T_0}{p_0} \frac{p(z)}{T(z)} \tag{4.6}$$

with the refractive index of the air m_{air}, the depolarization factor γ (γ is 0.0301, 0.0284 and 0.0273 for 350, 550 and 1000 nm, respectively), and the molecular number density $N_s = 2.547 * 10^{19}\text{cm}^{-3}$ for standard atmospheric conditions at ground level (p_0=1013.25 hPa, T_0=15°C, 0.03% CO_2). Profiles of temperature $T(z)$ and pressure $p(z)$ are taken from actual radiosonde measurements or from a standard atmosphere with actual ground values of temperature and pressure (Edlen, 1953; Elterman, 1968; Bodhaine et al., 1999).

Two unknown quantities, the particle lidar ratio and the particle backscatter coefficient $\beta^{Aer}(z_0)$ at a suitable reference height z_0, have to be estimated in the determination of the particle backscatter-coefficient profile after Eq. (4.4). The numerical application of Eq. (4.4) has been discussed in the literature for more than 20 years. Contributions to the problem given by Klett (Klett, 1981; Klett, 1985), Fernald (Fernald, 1984), and Sasano et al. (Sasano et al., 1985) are usually considered in the algorithms. Thus, the numerical schemes differ from each other only in minor details. Before Eq. (4.4) can be applied to measured lidar signals, the signals are averaged over the time interval of interest, corrected for background, and, if necessary, spatially averaged (smoothed). For the synthetic data used here, this procedure was not necessary. In the following, details of the individual algorithms with respect to the estimate of the input parameters are briefly given.

Algorithm of IAP (A1)

The reference value is set to a height with obviously low aerosol load. The backscatter-coefficient profile is calculated stepwise in forward and backward direction from that point. If possible, the reference value is set into a height region above aerosol layers of interest, so that the numerically stable backward integration can be applied. A height-dependent or a constant lidar ratio can be chosen.

Algorithm of IfT (A2)

The same method as at IAP is chosen. Usually, the lidar ratio is set to 50±25 and 10±5 sr in aerosol layers and cirrus clouds (if present), respectively. Appropriate setting of the reference value is tested by inspection of the backscatter profile in the stratosphere, where values around 0 should be measured in the absence of volcanic aerosols.

Algorithm of MPI (A3)

The lidar ratio is usually set to a constant value of 50 sr, but if more information on the lidar ratio is available, it can be set to stepwise constant values with step sizes down to 15 m (which is the resolution of the raw data) and as many steps as desired. The calibration value can be defined in an altitude window of typically a few hundred meters. The calibration is then applied to an average of all data points in that window. The calibration height is usually chosen in high altitudes (5–10 km) with very low aerosol backscatter. Downward and upward integration are then calculated from that height down to the lowest and up to highest desired altitude, respectively.

Algorithm of MIM (A4)
A lidar ratio, which is variable in height, can be chosen. To find an appropriate reference height, a Rayleigh signal is calculated from temperature and pressure values of a suitable radiosonde ascent and compared to the range-corrected lidar signal. If the slope of both, the calculated and the measured signal, agree over a sufficient range in the upper free troposphere, it is assumed that no aerosols are present in this range, and the reference value is set to 0 there. For the algorithm comparison, temperature and pressure values from the US standard atmosphere have been used as proposed.

Algorithm of IFU (A5)
The evaluation of experimental data is based on sequential measurements for two wavelength pairs, 532/1064 nm and 355/1064 nm, and elevation angles of (typically) 15, 45 and 90 degrees. The Bernoulli integral equation is solved under the assumption of a constant lidar ratio. For routine work, an a-priori lidar ratio of 33 sr is chosen based on earlier experience at this site. Both the lidar ratio and the reference value are modified if the results look unrealistic. The reference value is refined by applying criteria such as the congruence of the profiles of the extinction or backscatter coefficients at different wavelengths in individual layers, for which constant optical properties of the aerosol may be assumed and a reasonable magnitude of the Angström coefficients describing the wavelength dependence of aerosol scattering. The IFU algorithm was modified after the intercomparison to handle a height-dependent lidar ratio. In this new approach, in particular, the lidar ratio inside clouds is treated separately and mostly chosen around 10 sr. Stage 3 of the intercomparison was repeated with the new algorithm and the new results are presented.

Tables 4.1 to 4.4 and Figs. 4.2 to 4.4 summarize the results of the algorithm intercomparison. For case 1, which was simulated without statistical noise, without clouds, and with a height-independent lidar ratio, the results are shown in detail in the six parts of Fig. 4.2 and in Tab. 4.1. In general, the errors stayed well below 15% in the first stage. With increasing knowledge on the input parameters (stages 2 and 3), the errors decreased to a few percent in all cases, which indicates that all algorithms work well and can in general reproduce the simulated profiles if all input parameters are known.
The results for case 2, which is a more realistic one with a height-dependent lidar ratio but still without statistical noise and without clouds, are shown in Fig. 4.3(a)-(d), Fig. 4.4(c),(d), and Tab. 4.2 for 532 nm in dependence on the stage and in Fig. 4.4(a)-(f) and Tab. 4.3 in dependence on the wavelength. The errors are somewhat larger in this case, which is mainly caused by the height-dependent lidar ratio. Even with known input parameters, the simulated profiles cannot be reproduced if the algorithm works with a constant value for the lidar ratio, or if the altitude grid of the simulated data is not matched exactly (e.g. A3).

group	Stage 1		Stage 2		Stage 3			
	532 nm	mean error	532 nm	mean error	355 nm	532 nm	1064 nm	mean error
A1	6	6	3	3	0.5	0.8	0.2	0.5
A2	3	3	1	1	1.5	1.5	1.8	1.6
A3	13	13	10	10	3	8	8	6.3
A4	2	2	1	1	0.5	0.8	0.2	0.5
A5	deliv.		deliv.		5.5	9	1	5.2
mean error	6	6	3.8	3.8	2.2	4.0	2.2	2.8

Table 4.1: Mean errors for simulation case 1 in dependence on the stage and for the third stage in dependence on the wavelength.

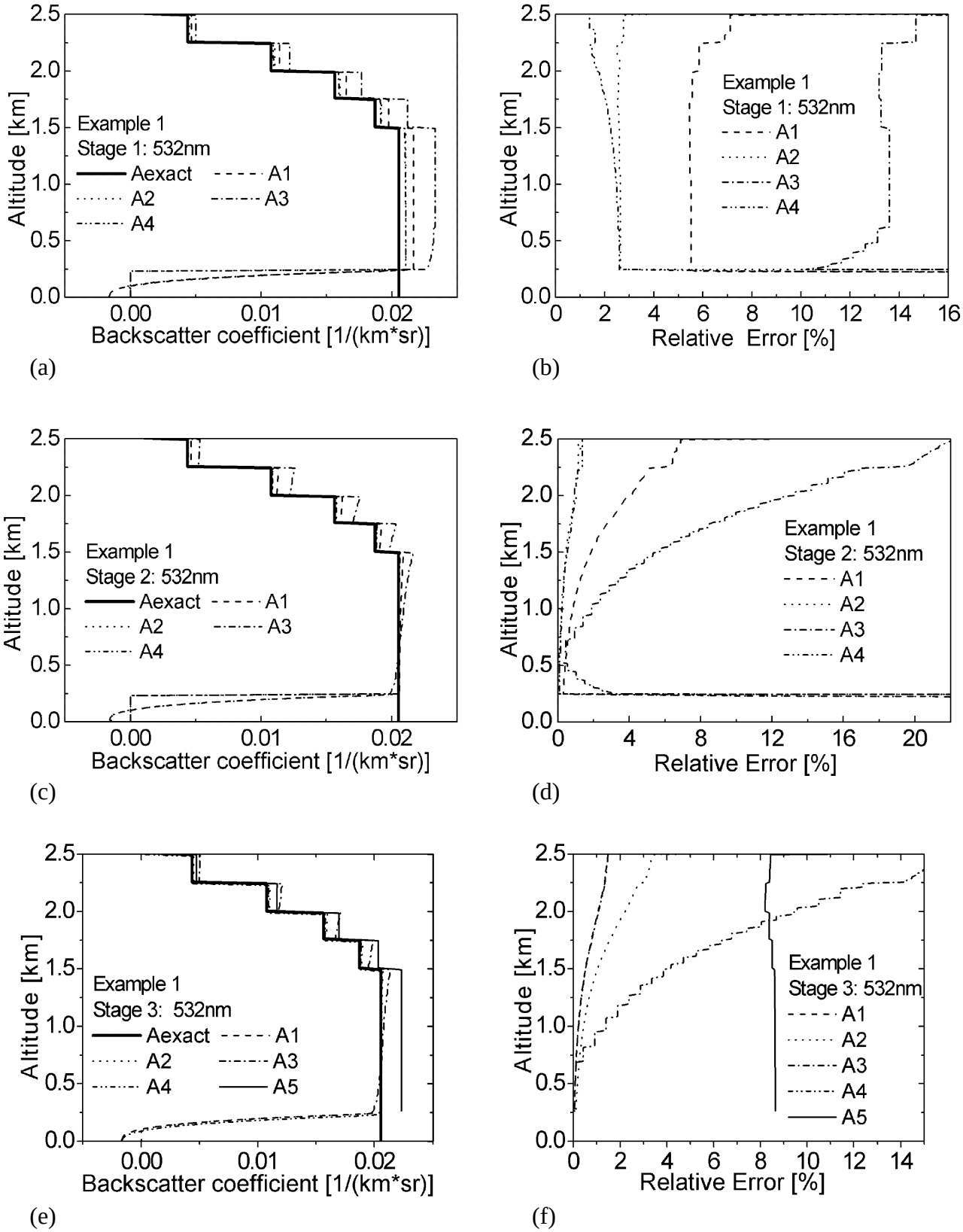

Figure 4.2: Retrieved particle backscatter coefficients at 532 nm in comparison to the simulation input profile and respective relative errors for stages 1 to 3 of simulation case 1.

group	Stage 1				Stage 2			
	532 nm				532 nm			
	1000 m	3000 m	9000 m	mean error	1000 m	3000 m	9000 m	mean error
A1	19	17	7.5	14.5	2	4	5	3.7
A2	1	1	1	1	1	1	1.5	1.2
A3	17	22.5	22.5	20.7	3	11	19	11
A4					1	1	1.5	1.2
A5					delivery			
mean error	12.3	13.5	10.3	12.1	1.8	4.2	6.8	4.3

Table 4.2: Mean errors for simulation case 2 in dependence on the stage and on the height.

group	Stage 3							
	355 nm				532 nm			
	1000 m	3000 m	9000 m	mean error	1000 m	3000 m	9000 m	mean error
A1	0.6	2.8	1.2	1.5	0.5	2	1.2	1.2
A2	0.8	1.7	4	2.2	4	8.5	14	8.8
A3	0.7	6	13	6.8	2.5	9	13	8.2
A4	0.7	0.8	1.1	0.9	0.5	0.8	1.2	0.8
A5	3	4	5	4	5.5	5	7.5	6
mean error	1.2	3.1	4.9	3.1	2.6	5.1	7.4	5.0

group	Stage 3				
	1064 nm				total
	1000 m	3000 m	9000 m	mean error	mean error
A1	0.2	0.4	0.2	0.3	1.0
A2	0.4	0.5	0.8	0.6	3.9
A3	4	8.5	13.5	8.7	7.9
A4	0.1	0.1	0.2	0.2	0.6
A5	2	2	3	2.3	4.1
mean error	1.3	2.3	3.5	2.4	3.5

Table 4.3: Mean errors for simulation case 2 in dependence on wavelength and height.

group	Stage 3							
	355 nm				532 nm			
	1000 m	3000 m	9000 m	mean error	1000 m	3000 m	9000 m	mean error
A1	0.5	8	16	8.2	3	12	17	10.7
A2	1.3	8	28	12.4	7	20	37	21.3
A3	2	10	22	11.3	10	20	40	23.3
A4	1.4	6	17	8.1	4	12	20	12
A5	3	10	28	13.7	8	18	35	20.3
mean error	1.6	8.4	22.2	10.7	6.4	16.4	29.8	17.5

group	Stage 3				
	1064 nm				total
	1000 m	3000 m	9000 m	mean error	mean error
A1	18	22	30	23.3	14.1
A2	4	6	8	6	13.3
A3	25	30	40	31.7	22.1
A4	2	2	2	2	7.4
A5	7	10	14	10.3	14.8
mean error	11.2	14.0	18.8	14.7	14.3

Table 4.4: Mean errors for simulation case 3 in dependence on wavelength and height.

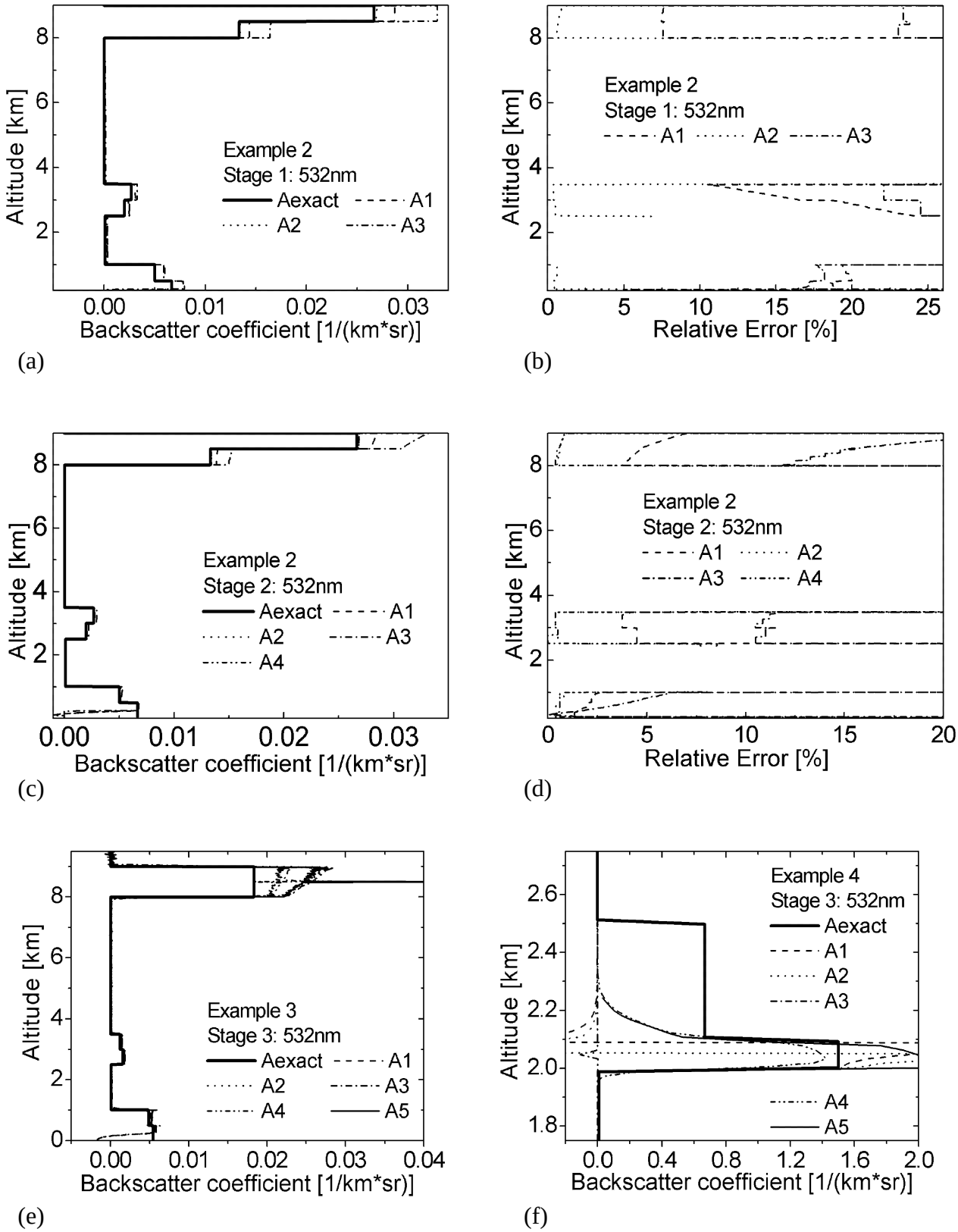

Figure 4.3: Retrieved particle backscatter coefficients at 532 nm in comparison to the simulation input profile and respective relative errors for stages 1 and 2 of simulation case 2 and retrieved particle backscatter coefficients at 532 nm in comparison to the simulation input profile for stage 3 of simulation cases 3 and 4.

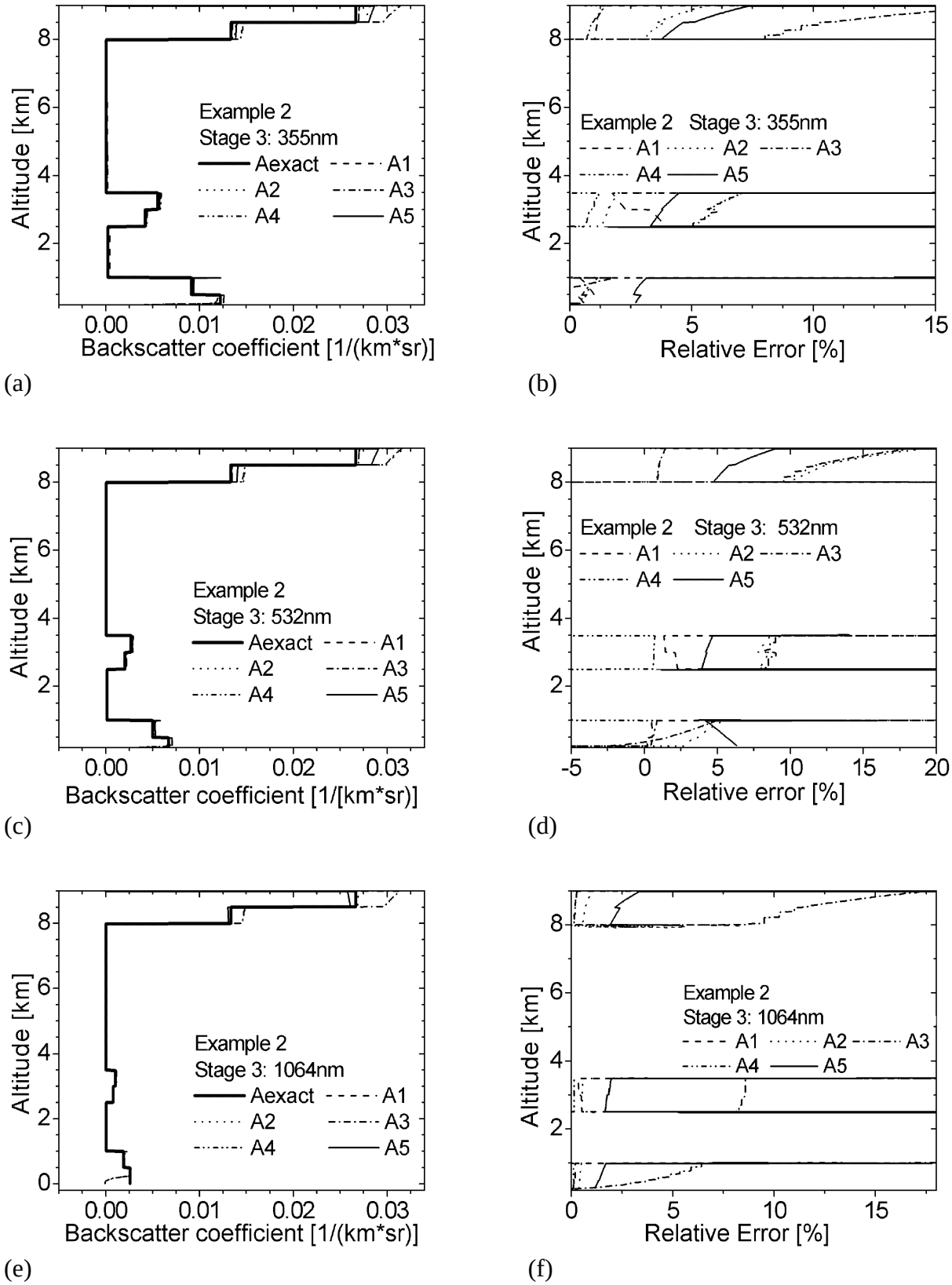

Figure 4.4: Retrieved particle backscatter coefficients at all three wavelengths in comparison to the simulation input profiles and respective relative errors for stages 3 of simulation case 2.

Case 3 was even more difficult, because the lidar ratio varied not only from layer to layer but also within each layer. In addition, a small statistical noise was added to the signals. The results for this case are shown in Fig. 4.3(e) and in Tab. 4.4. The mean errors grow well above 20% in the first stage (not shown here) and remain of the order of 15% in the third stage.
Case 4 with a water cloud at the top of the atmospheric dust layer is in principle not solveable as shown in Fig. 4.3(f). Even if a reference value in the free troposphere is given, it does not help in the evaluation, because the signal is fully attenuated above the cloud. The results have errors of more than 50%.
The algorithm intercomparison showed that in general the data evaluation schemes of the different groups work well. Even errors that are marginal compared to the errors caused by incorrect input parameters have been detected. E.g., the MPI-algorithm has been improved with respect to the results shown here by incorporating a better atmospheric density model. Differences in the solutions can mainly be attributed to differences in the estimate of the input parameters. If the input parameters are known, remaining errors are of the order of a few percent. The unknown height-dependent lidar ratio had the largest influence on the solutions, which again demonstrates the need for independent measurements of the particle extinction coefficient, e.g., with the Raman method. The unknown reference value was of minor importance for the examples presented here, because height regions with dominating Rayleigh scattering were present in all cases. It should be mentioned, however, that this is not necessarily the case under atmospheric conditions. Especially at 1064 nm, particle scattering often dominates the signals in the entire measurement range, which may cause additional errors that were not discussed here.

4.2 System intercomparison

by V. Matthias and V. Freudenthaler

4.2.1 Intercomparison between lidar systems

The intercomparison at system level was complicated by the fact that not all systems were transportable, and that no special funds were made available for dedicated intercomparison campaigns. Five of the systems involved in network measurements, namely the MIM aerosol lidar, the IfT multiwavelength lidar, the IFU aerosol lidar, the MPI UV lidar and the MPI water vapour DIAL are mobile. The systems in Kühlungsborn and the IfT Raman Lidar are fixed. The core of the intercomparison exercise was performed during the Lindenberg Aerosol Charcterization Experiment LACE 98 in July and August 1998, where the IfT, MIM, and both MPI systems were participating in a joint experiment. Further intercomparisons were made in Kühlungsborn against MIM, in Leipzig with the two systems operated by IfT, and, after the end of the project, IFU against MIM in Garmisch. So each system has been compared to at least one other system, which itself has been compared to at least one different system.
Three episodes at the end of LACE 98 (August 9^{th} to 11^{th}) have been chosen as intercomparison times (see table 4.5). Two of them are during nighttime, when additional Raman measurements have been performed, one is at daytime. During the three selected episodes, different meteorological conditions with high and low aerosol load in different height regimes were present. On the 9^{th} of

Main lidar intercomparison episodes				
Date [UT]	IfT	MIM	MPI	IAP
5.8.98 23:08 - 23:47	355 ext.		268 ext.	
9.8.98 22:30 - 23:00	355 bsc.	355 bsc.	320 bsc.	
	532 bsc.	532 bsc.		
	800 bsc.		728 bsc.	
11.8.98 12:07 - 12:12			268 ext.	
	355 bsc.	355 bsc.	320 bsc.	
	532 bsc.	532 bsc.		
11.8.98 21:15 - 21:45	355 ext.	355 ext.	351 ext.	
	355 bsc.	355 bsc.	351 bsc.	
	532 bsc.	532 bsc.		
	1064 bsc.[1)]	1064 bsc.[1)]		
16.8.98 18:41 - 19:01		355 bsc.		355 bsc.
		532 bsc.		532 bsc.
16.8.98 20:51 - 21:22		355 bsc.		355 bsc.
		532 bsc.		532 bsc.
		1064 bsc.		1064 bsc.

Table 4.5: Main intercomparison episodes used for the quality assurance of the lidar data taken within the German aerosol lidar network. [1)]: 20:20 - 22:20 UT.

August, a pronounced aerosol layer originating from Canadian forest fires (Wandinger et al., 2000) was observed in altitude levels between 3500 m and 5500 m. At low altitudes the aerosol extinction was low. On the 11^{th} of August, two aerosol layers with different aerosol types and high aerosol backscatter up to 3000 m could be seen. In the evening, these layers were lying directly one above the other, forming an inhomogeneous aerosol layer up to 2200 m.
Intercomparisons between the lidar derived aerosol backscatter profiles were performed at several wavelengths between 351 nm and 1064 nm. For the night time measurements, aerosol extinction profiles in the ultraviolet spectral region have also been compared. UV extinction measurements at 268 nm (MPI) and 355 nm (IfT) have been compared at nighttime on August 5^{th}.
The intercomparisons between the MI Munich and the IAP Kühlungsborn took place directly after the LACE experiment on August 16^{th} 1998. The IFU lidar was not available for intercomparisons during the project.

The compared quantities and the times when the measurements have been taken are listed in table 4.5. All profiles were similarly averaged in time and space, but anyhow the signal statistics can be quite different between the systems due to different emitted laser power and different sizes of the receiving telescopes. Only proven algorithms (see chapter 4.1) have been taken for the evaluation and the groups agreed on common boundary values and lidar ratios before processing the aerosol backscatter data.
Figure 4.5 - 4.9 show several examples of the intercomparisons at different wavelengths and times. The profiles generally show very good agreement for the same or nearly the same wavelength. Some differences occur for the IfT system in the near range, since the applied overlap correction yields some additional error. On the other hand, with the applied correction scheme measurements can be taken also in the near range although a large receiving telescope with a narrow field of view is used.

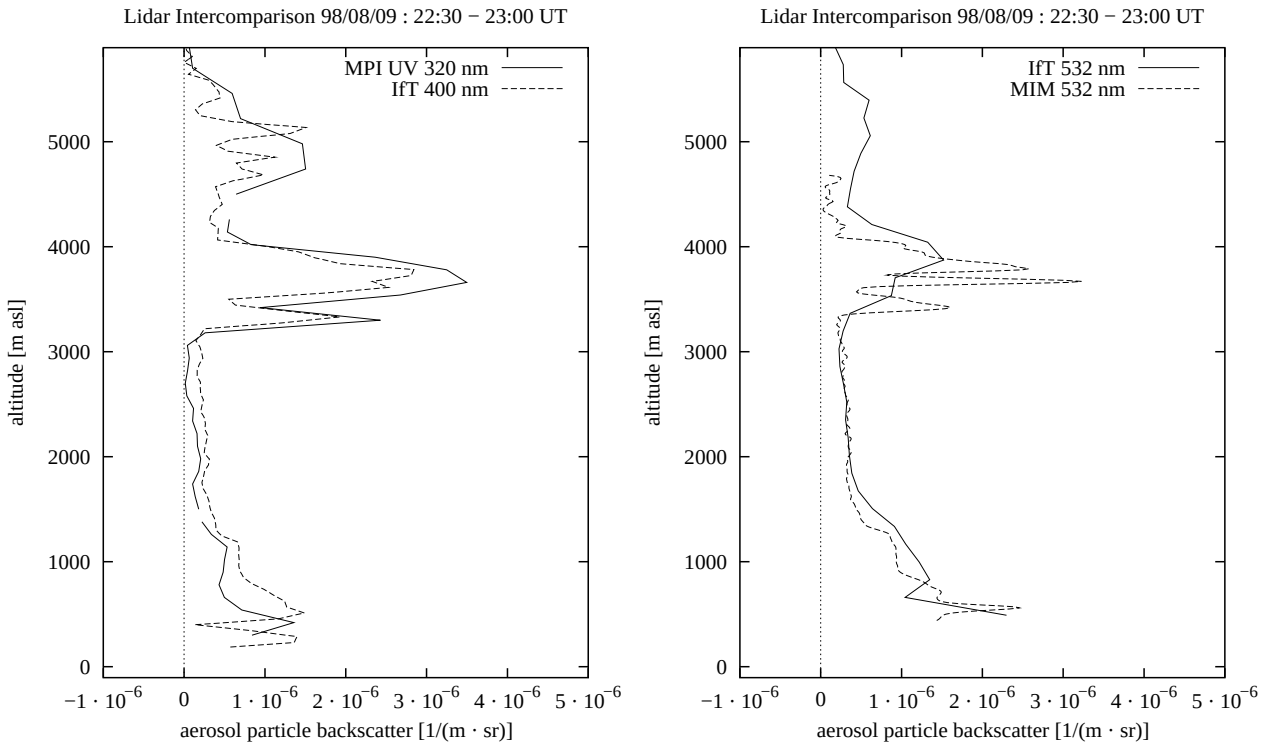

Figure 4.5: Intercomparison of aerosol backscatter in the UV at 355 nm (IfT and MIM at 355 nm, MPI at351 nm) and in the green (IfT and MIM at 532 nm) during LACE 98.

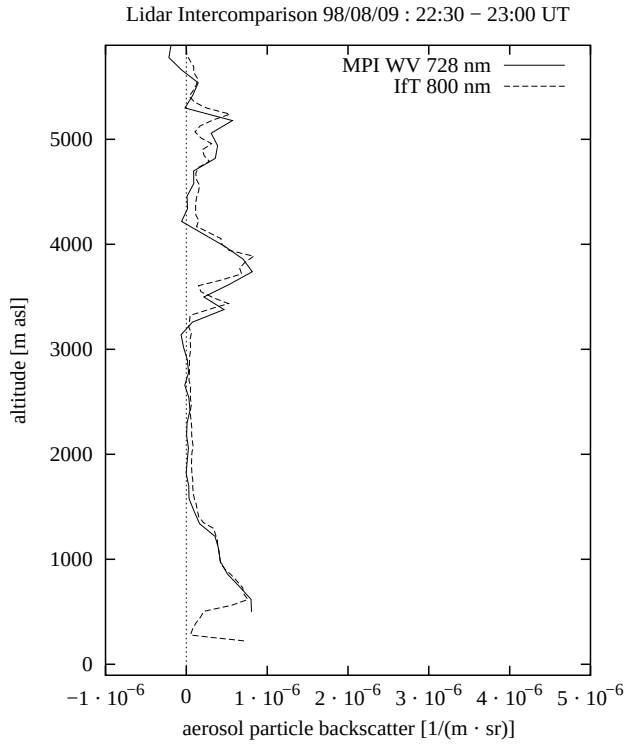

Figure 4.6: Intercomparison of aerosol backscatter profiles at 800 nm (IfT) and 728 nm (MPI) during LACE 98.

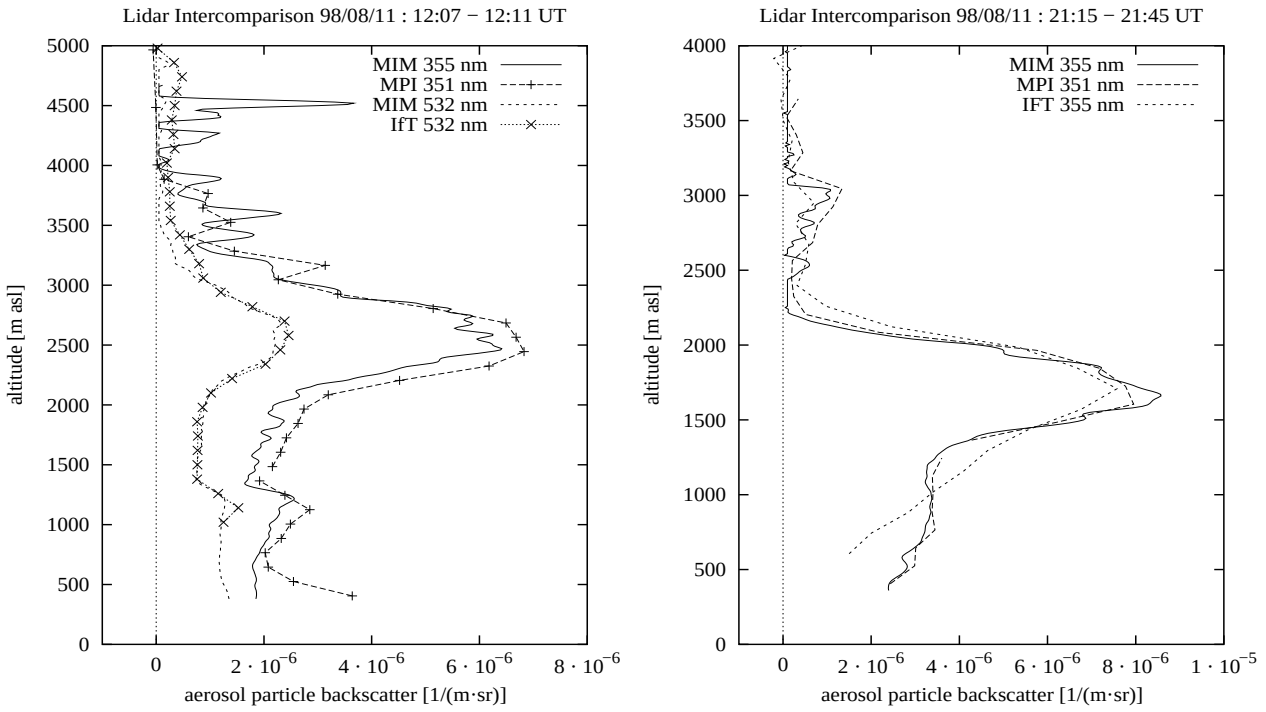

Figure 4.7: Left side: intercomparison of aerosol backscatter profiles in the UV (MIM 355 nm and MPI 351 nm) and in the green (IfT and MIM at 532 nm) on August 11th 1998, 12:07 -12:12 UT. Right side: intercomparison of aerosol backscatter profiles in the UV (MIM 355 nm and MPI 351 nm) on August 11th 1998, 21:15 - 21:45 UT.

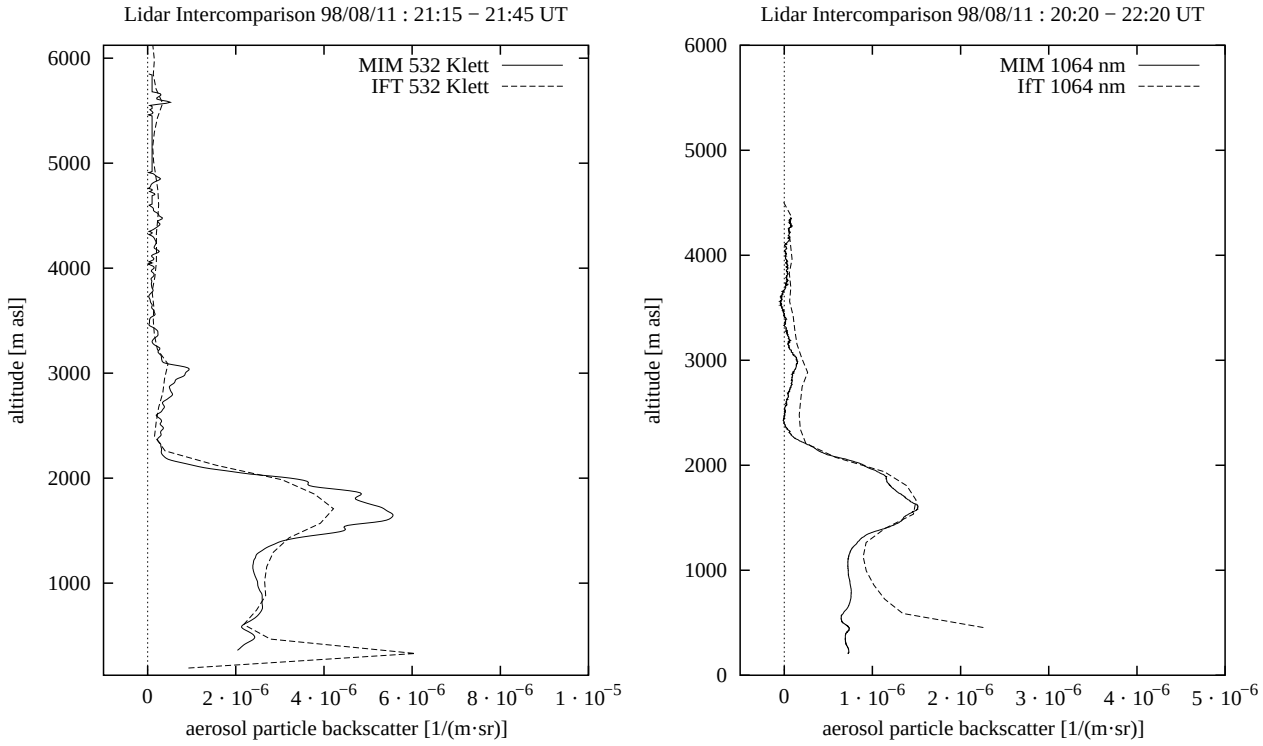

Figure 4.8: Intercomparison of aerosol backscatter in the green (532 nm) and infrared (1064 nm) between IfT and MIM during LACE 98.

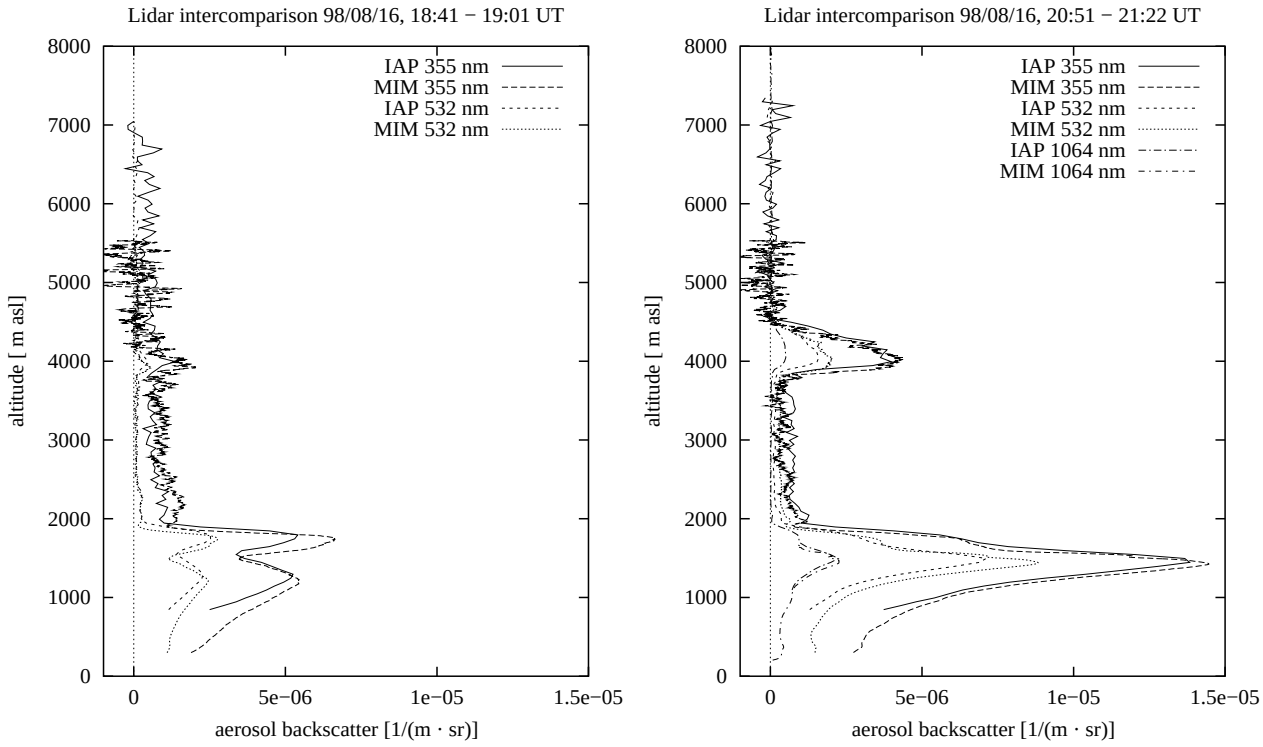

Figure 4.9: Intercomparison of aerosol backscatter at 355 nm and 532 nm (IAP and MIM) on August 16^{th} 1998, 18:41 - 19:01 UT (left side) and 20:51 - 21:22 UT (right side).

The measured aerosol backscatter profiles were compared in different height ranges and the absolut and relative deviations and their standard deviation have been calculated for all intercomparison episodes and compared wavelengths (see table 4.6). For high aerosol load, which is usually found in the planetary boundary layer, the deviations between the systems are typically not larger than 20 %. In regions with low aerosol load, which is usually called the free troposphere, typical deviations are in the order of $1 \cdot 10^{-7}(m \cdot sr)^{-1}$ at 355 nm and of $5 \cdot 10^{-8}(m \cdot sr)^{-1}$ at 532 nm.
Higher deviations occur in the UV between MPI and IfT on August 9^{th}. They can at least partly be explained by the different used wavelengths. For the calculation of the backscatter profiles, different lidar ratios had to be used to get reliable results in the aerosol free part of the atmosphere between 1500 m and 3000 m. The lower lidar ratio of the MPI evaluation leads to higher backscatter values in the upper part of the atmosphere, which can usually be expected at lower wavelengths. For higher accuracy of the results, the wavelengths dependence of the lidar ratio has to be known.
The comparisons at 1064 nm turned out to be difficult. Because of the long wavelength, almost the whole backscattered signal comes from aerosol particles, Rayleigh scattering is already very small at this wavelength. Therefore, from aerosol free parts of the atmosphere, where usually the necessary system calibration is done, only very low signals can be detected. This leads to high errors in the calibration and since on the other hand the calculated backscatter profile depends strongly on the calibration, accurate aerosol backscatter profiles at 1064 nm are quite hard to achieve. Only in presence of cirrus clouds accurate calibration can be done in the cirrus assuming no wavelength dependence of the aerosol backscatter and using the values from 355 nm and 532 nm.
Additionally the used detectors frequently show nonlinearities or instabilities which makes it also rather difficult to derive “hard numbers“ for the aerosol backscatter coefficient at 1064 nm. However at this wavelength also very small aerosol layers can be detected which are sometimes negligible against the Rayleigh background signal at 355 nm and 532 nm. So the main purpose of measurements at that wavelength is to get the structure of the aerosol distribution in the whole troposphere.
For these reasons, the intercomparisons at 1064 nm were restricted to only one case during LACE and one case for the MIM/IAP intercomparison (figures 4.8 and 4.9). On August 11^{th} 1998, 20:20 - 22:20 UT good agreement could be achieved between the MIM and the IfT lidars in a height range from 1200 m - 4300 m. Below that altitude the IfT-profile shows obvious deviations from the correct aerosol distribution. These errors can be assigned to the overlap correction which is applied below 1200 m and which yields to too high values in lower altitudes in this case. The profiles at 532 nm and 355 nm (figures 4.8 and 4.7) indicate that the profile derived with the Munich lidar is much more reliable.
The measurements at 1064 nm from August 16^{th} 1998 show good agreement between the MIM and the IAP only in a relativly small height range between 1100 and 1700 m. The measured signals showed deviations above that altitude which are most likely due to detector nonlinearities. Further investigations on reliable detectors for 1064 nm are necessary but were not subject of this project.

Gradients in the aerosol distribution can be seen in the lidar data with very high accuracy in height, although the systems were located at a distance of several hundred meters and different elevation angles have been used for the measurements. Deviations are in the order of the height resolution of the data acquisitions.
A problem in height determination occured during the IAP/MIM intercomparisons (see figures 4.9). The plots reveal an altitude difference between the data of IAP and MIM of about 60 m. The data have been corrected for the altitude difference between the laser systems (10 m) during the comparison. The error is most likely due to the IAP system. The difference corresponds to the altitude resolution of the IAP system (50 m), suggesting that in the data aquisition of the IAP system, an offset of one altitude channel may occur. Up to now, the error in the aquisition system could not be found and for this reason, no data correction has been performed. In the Klett algorithm, a bias of 50 m leads to a

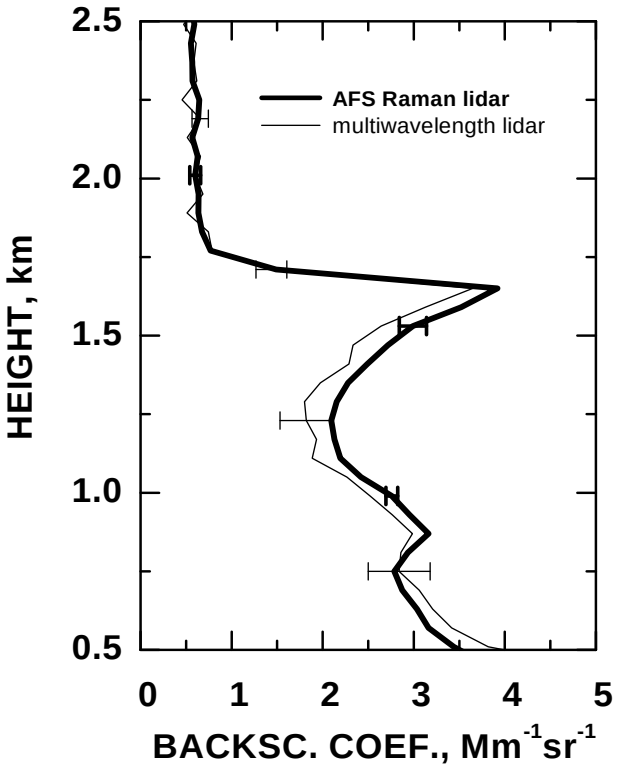

Figure 4.10: Particle backscatter coefficient at 532 nm determined with the IfT Raman lidar and the IfT multiwavelength lidar at Leipzig on 17 March 1997, 2047-2147 UTC. The error bars indicate statistical and systematic uncertainties.

deviation in the Klett backscatter profiles of 3-4 % at the lower altitude range of the IAP system (1000 m), decreasing with altitude. Raman backscatter calculations are not affected, since this technique relies on signal ratios, and range cancels.

The IfT in Leipzig has two different aerosol lidar systems. The mobile multiwavelength lidar performed the measurements during LACE which have been taken for the intercomparisons with the MPI and the MIM. Since the routine measurements have been taken with the stationary aerosol Raman lidar, a separate intercomparison of these systems has been done. Figure 4.10 shows a comparison of particle backscatter coefficients at 532 nm determined with the two IfT lidar systems at Leipzig on 17 March 1997. Analog signals measured with 60 m resolution were used from the multiwavelength lidar. The Klett method was applied under the assumption of a lidar ratio of 50 sr. The photon-counting signals of the Raman lidar measured with 15 m resolution were smoothed with a gliding average of 60 m and evaluated with the Raman method.

Differences may be caused by different detection schemes and resolution (analog and photon counting), reference-value estimate (for both solutions) and lidar-ratio estimate (for Klett solution), overlap-correction effect (for Klett solution), atmospheric inhomogeneities. Anyhow the overall differences remain small and the agreement can be regarded as excellent.

The determination of extinction profiles following Ansmanns formula (Ansmann et al., 1992b) doesn't require additional assumptions except for the wavelength dependence of the aerosol extinction. This value is usually chosen to be $k = 1$. The agreement between the nighttime aerosol extinction profiles at 351 nm (MPI) and 355 nm (IfT) (fig. 4.11) can be regarded as excellent. The mean

Lidar intercomparisons: results in regions with high aerosol					
Date [UT]	Quantity	height range	IfT/MIM	MIM/MPI	MPI/IfT
9.8.98 22:30 - 23:00	355 nm bsc.[1)]	600 -1300	–	–	-39.0 ± 53.0
	532 nm bsc.	600 -1300	-7.7 ± 27.1	–	–
	800 nm bsc.[2)]	600 -1300	–	–	12.7 ± 16.1
9.8.98 22:30 - 23:00	355 nm bsc.[1)]	3300 -4200	–	–	-37.7 ± 52.9
	532 nm bsc.	3300 -4200	4.1 ± 44.7	–	–
	800 nm bsc.[2)]	3300 -4200	–	–	10.3 ± 32.9
11.8.98 12:07 - 12:12	355 nm bsc.[1)]	500 - 3200	–	-16.1 ± 19.7	–
	532 nm bsc.	500 - 3200	8.6 ± 12.6	–	–
11.8.98 21:15 - 21:45	355 nm bsc.[3)]	600 -2000	11.3 ± 18.5	1.5 ± 7.5	-12.9 ± 16.2
	532 nm bsc.	600 -2000	2.9 ± 17.2	–	–
	1064 nm bsc.[4)]	1200 -2200	5.6 ± 9.3	–	–
	355 nm ext.[3)]	600 -2000	–	–	4.7 ± 11.9
Lidar intercomparisons: results in regions with low aerosol					
Date [UT]	Quantity	height range	IfT/MIM	MIM/MPI	MPI/IfT
9.8.98 22:30 - 23:00	355 nm bsc.[1)]	1500 -3000	–	–	$-1.3 \pm 1.4 \cdot 10^{-7}$
	532 nm bsc.	1500 -3000	$-0.25 \pm 0.87 \cdot 10^{-7}$	–	–
	800 nm bsc.[2)]	1500 -3000	–	–	$-0.40 \pm 0.46 \cdot 10^{-7}$
11.8.98 21:15 - 21:45	355 nm bsc.[3)]	2400 - 3800	$-0.6 \pm 2.2 \cdot 10^{-7}$	$-0.4 \pm 2.0 \cdot 10^{-7}$	$1.5 \pm 3.2 \cdot 10^{-7}$
	532 nm bsc.	2400 - 3800	$-0.6 \pm 1.2 \cdot 10^{-7}$	–	–
	1064 nm bsc.[4)]	2400 - 4300	$0.9 \pm 1.0 \cdot 10^{-7}$	–	–
	355 nm ext.[3)]	2400 -3800	–	–	$1.7 \pm 2.5 \cdot 10^{-5}$

Table 4.6: Mean deviations (in $(m \cdot sr)^{-1}$ for backscatter values and m^{-1} for extinction values in regions with low aerosol, in % in regions with high aerosol) for different measured quantities during the LACE experiment. [1)] MPI 320 nm, [2)] MPI 728 nm, [3)] MPI 351 nm, [4)] 20:20 - 22:20 UT.

Lidar intercomparisons: MIM/IAP					
Date [UT]	Quantity	height range	high aerosol	height range	low aerosol
16.8.98 18:41 - 19:01	355 nm bsc.	850 -1800	11.8 ± 18.2	2200 - 3600	$2.9 \pm 3.7 \cdot 10^{-7}$
	532 nm bsc.	850 -1800	5.0 ± 17.7	2200 - 3600	$0.04 \pm 0.4 \cdot 10^{-7}$
16.8.98 20:51 - 21:22	355 nm bsc.	850 -1800	1.6 ± 10.6	2200 - 3600	$2.8 \pm 3.6 \cdot 10^{-7}$
	532 nm bsc.	850 -1800	16.8 ± 22.8	2200 - 3600	$1.8 \pm 1.9 \cdot 10^{-7}$
	1064 nm bsc.	1100 -1700	2.6 ± 16.2	–	–

Table 4.7: Mean deviations (in $(m \cdot sr)^{-1}$ for backscatter values in regions with low aerosol, in % in regions with high aerosol) between the IAP and the MIM lidar for three different wavelengths.

deviation is lower than 5 % in the main aerosol layer up to 2200 m, with a standard deviation of 12 %. Above that height the mean difference is $1.7 \cdot 10^{-5} \pm 2.5 \cdot 10^{-5} m^{-1}$ which is well in the order of the statistical error (see table 4.6). With the Munich lidar system, measurements under several elevation angles between 0° and 70° have been performed. Out of these measurements, three extinction values for different height regimes could be evaluated at 355 nm. These values have obviously some deviations to the Raman profiles, but not higher than ca. 25 %. This is a good result, having in mind that the Munich system measured for some minutes around 21:50 UT and the Raman profiles are averaged over 80 minutes between 21:00 and 22:20 UT. The low ground value from a horizontal measurement

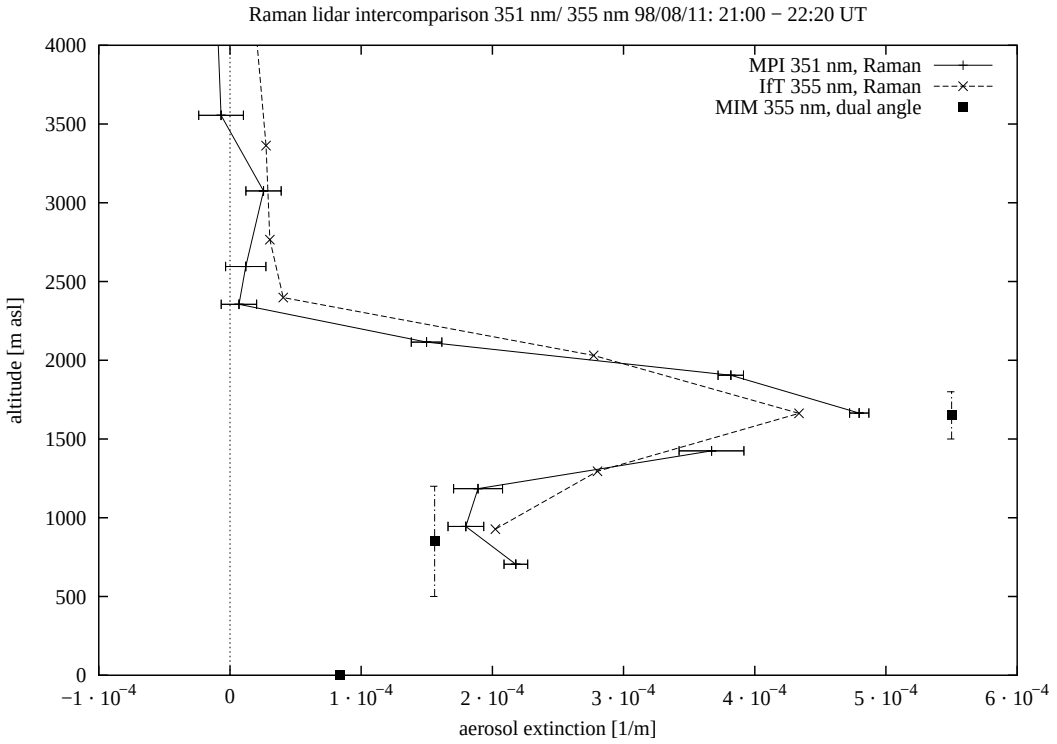

Figure 4.11: Intercomparison of aerosol extinction profiles at 355 nm (IfT) and 351 nm (MPI) during LACE 98

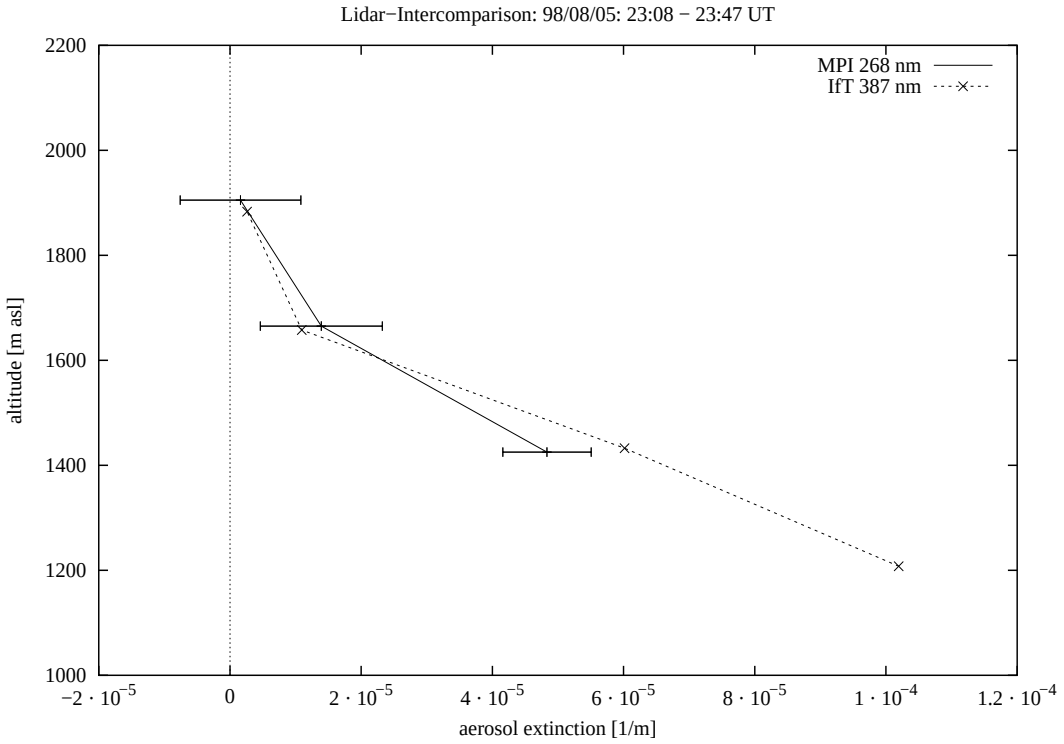

Figure 4.12: Intercomparison of aerosol extinction profiles at 355 nm (IfT) and 268 nm (MPI) during LACE 98

fits good with the backscatter profiles, which show a remarkable decrease of the aerosol backscatter below 600 m.
The MPI lidar has also the capability of measuring daytime aerosol extinction profiles at 268 nm. The measurements require an ozone correction which is done via simultaneous ozone DIAL measurements with the same lidar system. Numerous profiles have been taken during the LACE experiment, one intercomparison with the 355 nm extinction measurement of the IfT system is shown in figure 4.12. Although the height range for the intercomparison is quite small, one can see the good agreement between the measurements. The wavelength dependence of the aerosol extinction does not have a major influence on Raman retrievals at wavelengths below 350 nm. This fact is also shown by intercomparison of optical depth measurements with sun photometer and lidar in the next section. Anyhow, a quantification of the deviations between the measurements taken at different wavelengths is not really useful since the deviations between the profiles are strongly influenced by the aerosol type and its wavelength dependence.

4.2.2 Comparison between lidar and photometer

In Lindenberg, the aerosol backscatter and extinction profiles could also be compared to other instruments as sun- and starphotometers. These intercomparisons were not necessarily done simultaneously with the comparisons between the lidar systems themselves. Additionally, the measurements have been compared to *in situ* airborne measurements aboard the Falcon and Partenavia research aircrafts (Wandinger et al., 2000).

The aerosol optical depth can be derived from lidar profiles of the aerosol extinction by linearly extrapolating the lowest value in the aerosol profile down to ground and then integrating the whole

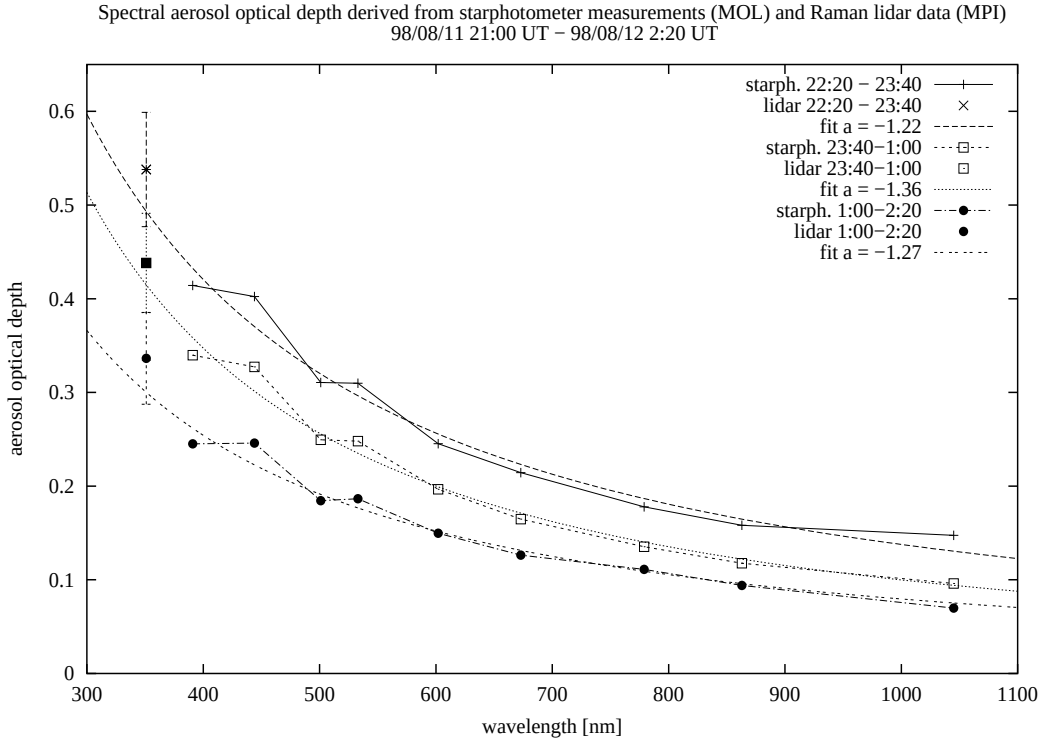

Figure 4.13: Intercomparison of aerosol optical depth at 351 nm (MPI) and starphotometer measurements from the Meteorologisches Observatorium Lindenberg (MOL) during LACE 98. The photometer data has been extrapolated in the UV using a fit with $OD \propto \lambda^a$.

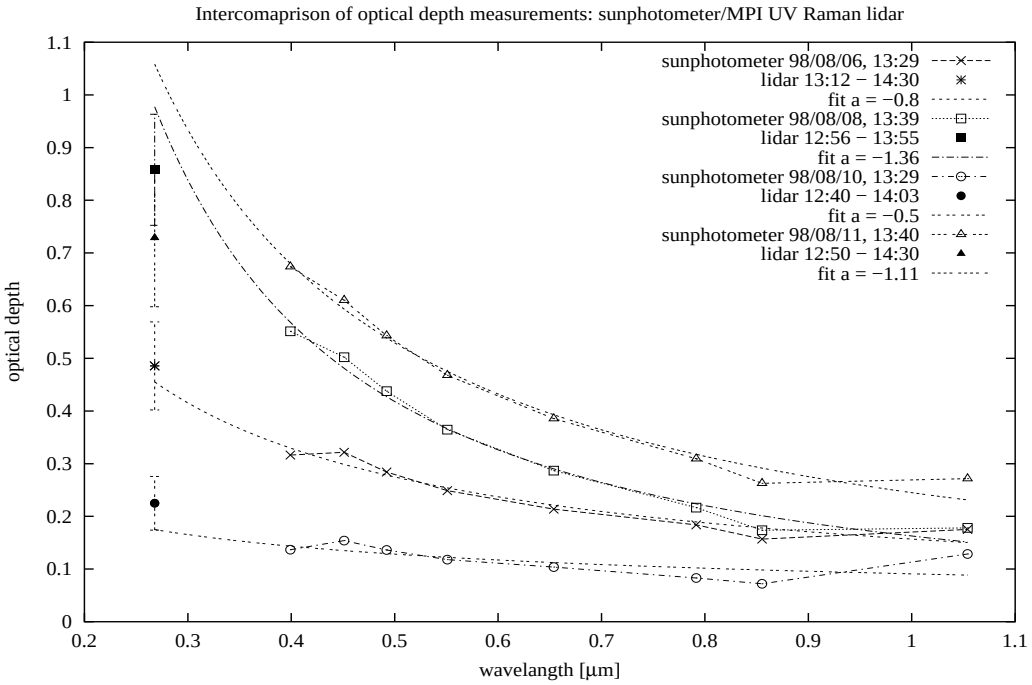

Figure 4.14: Intercomparison of aerosol optical depth at 268 nm (MPI) and sunphotometer measurements from the Meteorologisches Observatorium Lindenberg (MOL) during LACE 98 at selected cloudfree times. The photometer data has been extrapolated in the UV using a fit with $OD \propto \lambda^a$

.

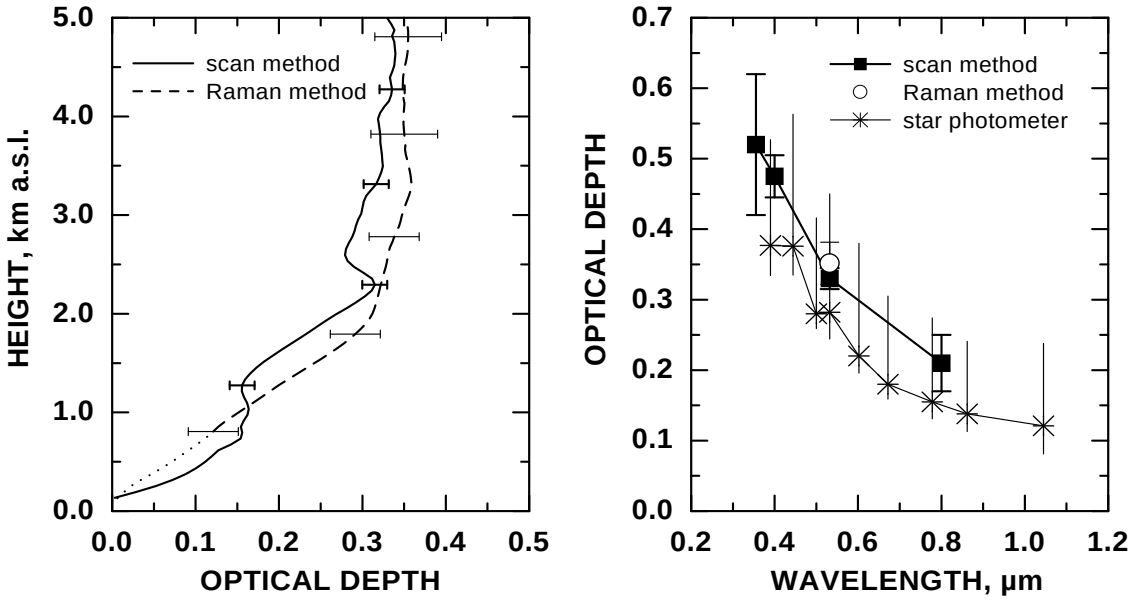

Figure 4.15: Particle optical-depth profiles at 532 nm (left) and spectral particle optical depth (right) determined with the IfT lidar by applying the Raman and the scan methods and with the MOL star photometer at Lindenberg on 11/12 August 1998, 2330–0030 UTC. Error bars indicate statistical and systematic uncertainties of the lidar measurements. For the star photometer, mean values and the range of measured values are given.

profile. At nighttime this value can be compared to starphotometer measurements which have been performed during LACE 98 by the Meteorologisches Observatorium Lindenberg (MOL). Although the lowest measured wavelength of the starphotometer is around 390 nm, one can clearly see the good agreement between the measurements in fig. 4.13.
The agreement is not that clear looking at the 268 nm extinction profiles. They have been compared to sunphotometer measurements at selected cloud free afternoons, when the aerosol in the boundary layer was generally well mixed. The lidar values are in most cases lower than the sunphotometer values which have been extrapolated in the UV. This is on the other hand not really surprising, it shows that the spectral behaviour of the extinction is changing in the spectral region below 400 nm, as it is predicted by aerosol models (Völger et al., 1996; Hess et al., 1998; Matthias, 2000), see also fig. 4.15.
The whole set of lidar measurements taken during LACE in Lindenberg allows also comparisons of the spectral behaviour of the aerosol optical depth from the lidar measurements with star photometer results. In the first case (fig. 4.15) the aerosol optical depth determined with the IfT lidar from the scan method and from the Raman method and with star photometer is shown. The measurements were taken on August $11^{th}/12^{th}$ 1998 between 23:30 and 0:30 UT. The scan method is described, e.g., in (Gutkowicz-Krusin, 1993) and (Althausen et al., 2000).
In the case of the Raman method, the integrated extinction coefficient profile is used for heights above 800 m. Below, where extinction coefficients cannot be determined because of the overlap effect, the backscatter coefficient profile from the Raman method multiplied by an estimated lidar ratio of 50 sr was used. One can see the fairly good agreement between the scan method and the Raman method (left side of figure 4.15) as well as similar spectral dependence of the optical depth measurements of the two systems. The lidar derived optical depth remains slightly higher than the starphotometer value but the difference stays in the given uncertainty limits.

4.2.3 Comparison between lidar and in situ measurements

Measured aerosol optical depth at three wavelengths and aerosol backscatter coefficients at six wavelengths have been compared to calculated values based on *in situ* aircraft measurements taken at Lindenberg on 9 August 1998, 2200-2400 UTC.. Figure 4.16 shows spectral backscatter and extinction coefficients measured with four different lidar systems (IfT multiwavelength lidar, MPI water vapour DIAL, MPI UV lidar and DLR HSRL) in a biomass-burning aerosol layer that originated from forest fires in northwestern Canada (Wandinger et al., 2000; Forster et al., 2000) (see also Sec. 8.5).
In situ measurements of particle size distributions and of particle absorption coefficients were performed aboard the research aircraft Falcon. The Falcon flew about 5 km to the east of the lidar site. The airborne instrumentation is described in (Fiebig et al., 2000). The absorption measurements indicated a soot content of about 35%. For the calculation of spectral backscatter and extinction coefficients, the particle size distribution measured between 3500 and 4000 m was taken and an external mixture of 65% ammonium-sulfate-like and 35% soot-like particles was assumed. Details of the measurements are discussed in (Wandinger et al., 2000) and (Fiebig et al., 2000).
The data shown in this figure are used for the inversion of microphysical particle properties (see Sec. 5).
Humidity corrected airborne *in situ* measurements taken aboard the Partenavia have also been compared to lidar backscatter measurements at 532 nm, taken with the IfT lidar. Figure 4.17 shows the backscatter profile measured in a pollution layer at Lindenberg on 11 August 1998 around 1230 UTC in comparison to profiles obtained from airborne *in situ* measurements of the particle size distribution aboard the research aircraft Partenavia. The aircraft descended in the vicinity of the lidar beam from 3.7 to 0.2 km height between 1220 and 1240 UTC. A description of the Partenavia instrumentation is

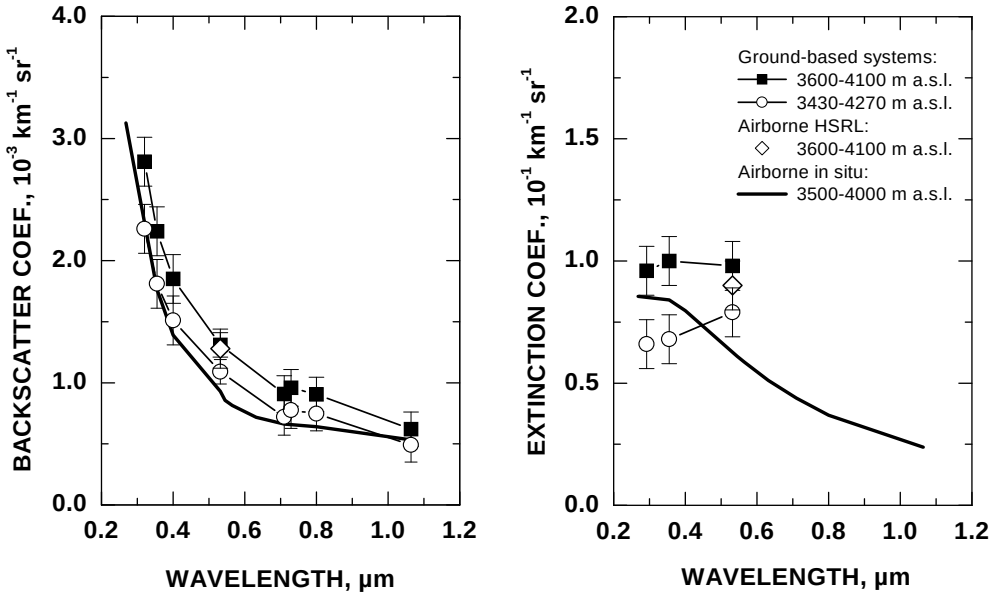

Figure 4.16: Spectral backscatter coefficients (left) and spectral extinction coefficients (right) measured with lidar and calculated from airborne *in situ* measurements of particle size distributions and absorption coefficients in a biomass-burning aerosol layer at Lindenberg on 9 August 1998, 2200–2400 UTC. Lidar measurements were taken with the IfT multiwavelength lidar (355, 400, 532, 710, 800, 1064 nm), the MPI UV lidar (320 nm), the MPI water-vapor DIAL (729 nm), and the DLR airborne high-spectral-resolution lidar (532 nm). Mean values for the height regions 3600–4100 and 3430–4270 m are shown. The error bars indicate statistical and svstematic uncertainties.

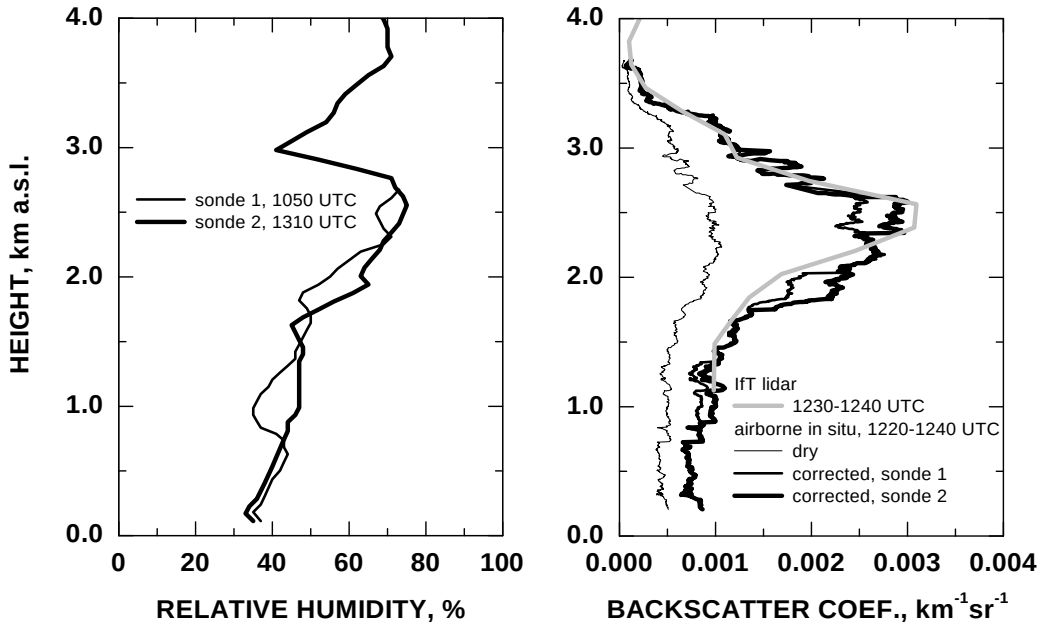

Figure 4.17: Relative humidity measured with radiosondes launched at Lindenberg at 1050 and 1310 UTC on 11 August 1998 (left) and backscatter coefficients at 532 nm (right) determined with the IfT lidar after the Klett method with a height resolution of 180 m and calculated from airborne *in situ* measurements of the particle size distribution with a height resolution of ≈40 m.

given in (Wendisch, M. et al., 2000).
The humidity growth of the particles, which were measured in the dry state, was estimated by using relative humidities measured with two radiosondes (launched at 1050 and 1310 UTC) and by applying humidity growth factors for ammonium sulfate (Tang and Munkelwitz, 1993).
Details of the measurement are discussed in (Wandinger et al., 2000). The agreement between these totally different measurement methods is remarkable and shows again the high quality lidar measurements performed within this project.

Chapter 5

Retrieval of microphysical aerosol parameters

by C. Böckmann and D. Müller

Several instruments of the lidar network deliver information on particle extinction and backscatter coefficients at multiple wavelengths. This information can be used to invert physical particle properties such as particle size, number, surface-area, and volume concentration, as well as complex refractive index. However, the inversion problem in a mathematical sense is non-linear and ill-posed and its solution requires the application of appropriate mathematical methods. Therefore, one part of the project was to develop and investigate inversion algorithms for optical data sets, which are obtained with different lidar systems of the network.

In this chapter, we first describe the inversion problem from the mathematical point of view investigated at the Institute of Mathematics of the University of Potsdam (IMP). After that, we introduce two inversion methods that were developed at the IMP and at the Institute for Tropospheric Research (IfT). In contrast to the IfT algorithm, which was especially developed for the inversion of the six backscatter and two extinction coefficients measured with the IfT multiwavelength lidar, the IMP algorithm permits one to process variable data sets with different numbers and combinations of optical data.

The performance of the algorithms was extensively studied and the results of these studies have already been published (Böckmann and Sarközi, 1999; Böckmann, 2001; Müller et al., 1999b; Müller et al., 1999a; Müller et al., 2000). We, therefore, concentrate our discussion in this chapter on one measurement example. During the Lindenberg Aerosol Characterization Experiment LACE 98 intercomparison measurements with the transportable systems of MPI, IfT, and MIM were performed (see Section 4.2). The combined information of these instruments consists of up to 11 vertically-resolved optical data (eight backscatter and three extinction coefficients). These data were used to invert physical particle properties with the two inversion schemes. Furthermore, LACE 98 offered the unique opportunity to validate the inversion results through the comparison with airborne *in situ* measurements. In Sec. 5.3.1 we present our findings for a biomass-burning aerosol layer in the free troposphere, which was observed on 9 and 10 August 1998.

Finally, we discuss the possibility to use a minimum data set of three backscatter and two extinction coefficients in the inversion. The set of backscatter coefficients at 355, 532, and 1064 nm and of extinction coefficients at 355 and 532 nm is the standard output of an advanced aerosol Raman lidar based on a single Nd:YAG laser. The stationary systems at Kühlungsborn and Leipzig make use of this configuration and more lidars of this kind are part of EARLINET.

5.1 Mathematical description

The mathematical model, which relates the optical and the physical particle parameters, consists of a Fredholm system of two integral equations of the first kind for the backscatter and extinction coefficients β^{Aer} and α^{Aer}:

$$\beta^{Aer}(\lambda, z) = \int_{r_0}^{r_1} K_\pi(r, \lambda, m, s)\, n(r, z)\, dr = \int_{r_0}^{r_1} \pi\, r^2\, Q_\pi(r, \lambda, m)\, n(r, z)\, dr, \tag{5.1}$$

$$\alpha^{Aer}(\lambda, z) = \int_{r_0}^{r_1} K_{ext}(r, \lambda, m, s)\, n(r, z)\, dr = \int_{r_0}^{r_1} \pi\, r^2\, Q_{ext}(r, \lambda, m)\, n(r, z)\, dr, \tag{5.2}$$

where r denotes the particle radius, m is the complex refractive index, s is the shape of the particles, r_0 and r_1 represent suitable lower and upper limits, respectively, of realistic radii, λ is the wavelength, z is the height, n is the particle size distribution we are looking for, K_π is the backscatter and K_{ext} is the extinction kernel. The kernel functions reflect shape, size, and material composition of the particles. In the framework of this chapter, homogeneous spherical particles, i.e., Mie scattering theory (Mie, 1908), are used under the assumption that small particles in a first approximation behave like spherical scatterers (Bohren and Huffman, 1983). First examinations of the influence of inhomogeneous non-spherical particles on the inversion process are shown by (Böckmann and Wauer, 2000; Böckmann and Wauer, 2001) and (Sarközi, 2000). The following formulas hold for extinction and backscatter efficiencies of homogeneous spheres (Bohren and Huffman, 1983):

$$Q_\pi = \frac{1}{k^2 r^2} \left| \sum_{n=1}^{\infty} (2n+1)(-1)^n (a_n - b_n) \right|^2,\; Q_{ext} = \frac{2}{k^2 r^2} \sum_{n=1}^{\infty} (2n+1) \mathrm{Re}(a_n + b_n), \tag{5.3}$$

where k is the wave number defined by $k = 2\pi/\lambda$ and a_n and b_n are the coefficients which one can get from the boundary conditions for the tangential components of the waves (Bohren and Huffman, 1983). Now Eqs. (5.1) and (5.2) are formulated into a more specific and more solid form:

$$\Gamma^{Aer}(\lambda, z) = \int_{r_0}^{r_1} K^v_{\pi/ext}(r, \lambda, m)\, v(r, z)\, dr = \int_{r_0}^{r_1} \frac{3}{4r}\, Q_{\pi/ext}(r, \lambda, m)\, v(r, z)\, dr, \tag{5.4}$$

where the $v(r, z)$ term is the volume concentration distribution we are finally looking for. Γ^{Aer} stands for β^{Aer} and/or α^{Aer}, respectively, depending on the measurement data. The determination of the particle volume distribution v from a small number of backscatter and extinction measurements is an inverse ill-posed problem and because the refractive index m in the kernels $K^v_{\pi/ext}$ is an unknown, too, the problem is a highly nonlinear one, i.e., solutions are non-unique and highly oscillating without the introduction of appropriate mathematical tools such as discretization and regularization.

5.1.1 Ill-posed problem and regularization

The Eqs. (5.1), (5.2), and (5.4) are ill-posed on all three counts (existence, uniqueness, and stability). Stability means a solution that changes only slightly with a slight change in the input data (Groetsch, 1993). We consider an operator of the form $Tx = y$ where $T : H_1 \to H_2$ is a compact, linear (but not necessarily self-adjoint) operator from a Hilbert space H_1 into a Hilbert space H_2. For a bounded linear operator T a solution $x \in H_1$ of the equation $Tx = y$ exists if and only if y belongs to $R(T)$, the range of T. As T is linear, $R(T)$ is a subspace of H_2, which in generally does not exhaust H_2. We may enlarge the class of functions y for which a type of generalized solution exists

to a dense subspace of function in H_2. This enlargement is accomplished by introducing the idea of a least-squares solution. A function $x \in H_1$ is called a least-squares solution if

$$||Tx - y|| = \inf\{||Tu - y|| : u \in H_1\} \tag{5.5}$$

holds. The set of all least-squares solutions is closed and convex. Therefore, there is a unique least-squares solution with smallest norm which we call generalized solution. The mapping $T^\dagger$ that associates a given $y \in D(T^\dagger) = R(T) + R(T)^\perp$ with the unique least-squares solution, $T^\dagger y$, is called the Moore-Penrose generalized inverse of T. In our scheme $T^\dagger$ is then the mechanism which provides a unique solution for any $y \in D(T^\dagger)$. In this sense, $T^\dagger$ settles the issues of existence and uniqueness for generalized solutions. The generalized pseudoinverse operator $T^\dagger : D(T^\dagger) \to H_1$ is a closed densely defined linear operator which is bounded if and only if $R(T)$ is closed. Because both lidar integral operators are compact, each of them can have closed range if and only if $R(T)$ is a finite dimensional subspace of H_2. But the range $R(T)$ of the lidar operators is infinite dimensional. Therefore, $R(T)$ is not closed and thus $T^\dagger$ is unbounded, i.e., $T^\dagger$ is discontinuous. Very small changes in the right hand side $y(\lambda)$ can be accounted for by large changes in the solution $x(r)$. That the instability is fundamental, and not just a consequence of some special form of the kernels, follows from the Riemann-Lebesgue lemma.
If we wish to obtain a well-posed problem, we need a so-called regularization. In general, regularizations are families of operators

$$T_\gamma : H_2 \to H_1 \quad \text{with} \quad \lim_{\gamma \to 0} T_\gamma y = T^\dagger y \quad \text{for all} \quad y \in D(T^\dagger) \ , \tag{5.6}$$

i.e., the convergence is pointwise on $D(T^\dagger)$ (Louis, 1989). The parameter γ is the so-called regularization parameter. In the case of noisy data y^δ with $||y - y^\delta|| \leq \delta$ we determine a solution

$$x_\gamma^\delta = T_\gamma \, y^\delta \ . \tag{5.7}$$

However, the total error consists of two parts , i.e., two summands,

$$x_\gamma^\delta - x = T_\gamma(y^\delta - y) + (T_\gamma - T^\dagger)y \ . \tag{5.8}$$

The first part is the data error and the second part the approximation error or regularization error. Generally, if $\gamma \to 0$, the approximation error tends to zero (with respect to the H_1-norm), whereas the data error tends to infinity. Therefore, the total error can never be zero and we are in a dilemma. We have to look for an "optimal" regularization parameter γ which minimizes the total error.

5.1.2 Degree of ill-posedness

The operators $T^*T : H_1 \to H_1$ and $TT^* : H_2 \to H_2$ are compact self-adjoint linear operators where T^* is the adjoint operator of T. The nonzero eigenvalues of T^*T or of TT^* (they have the same eigenvalues) can be enumerated as $\lambda_1 \geq \lambda_2 \geq \ldots$. If we designate by $v_1, v_2, \ldots$, an associated sequence of orthonormal eigenfunctions of T^*T, then $\{v_1, v_2, ...\}$ is complete in the range $\overline{R(T^*T)} = N(T)^\perp$ (orthogonal compliment of the null space of T). Let $\mu_j = \sqrt{\lambda_j}$ then $Tv_j = \mu_j u_j$ and $T^*u_j = \mu_j v_j$. Moreover, $TT^*u_j = \mu_j T v_j = \mu_j^2 u_j = \lambda_j u_j$ and it is easy to see that the orthonormal eigenfunctions $\{u_j\}$ of TT^* form a complete orthogonal set for $\overline{R(TT^*)} = N(T^*)^\perp$. The system $\{v_j, u_j; \mu_j\}$ is called the singular system of T and the numbers μ_j are called singular values of T.

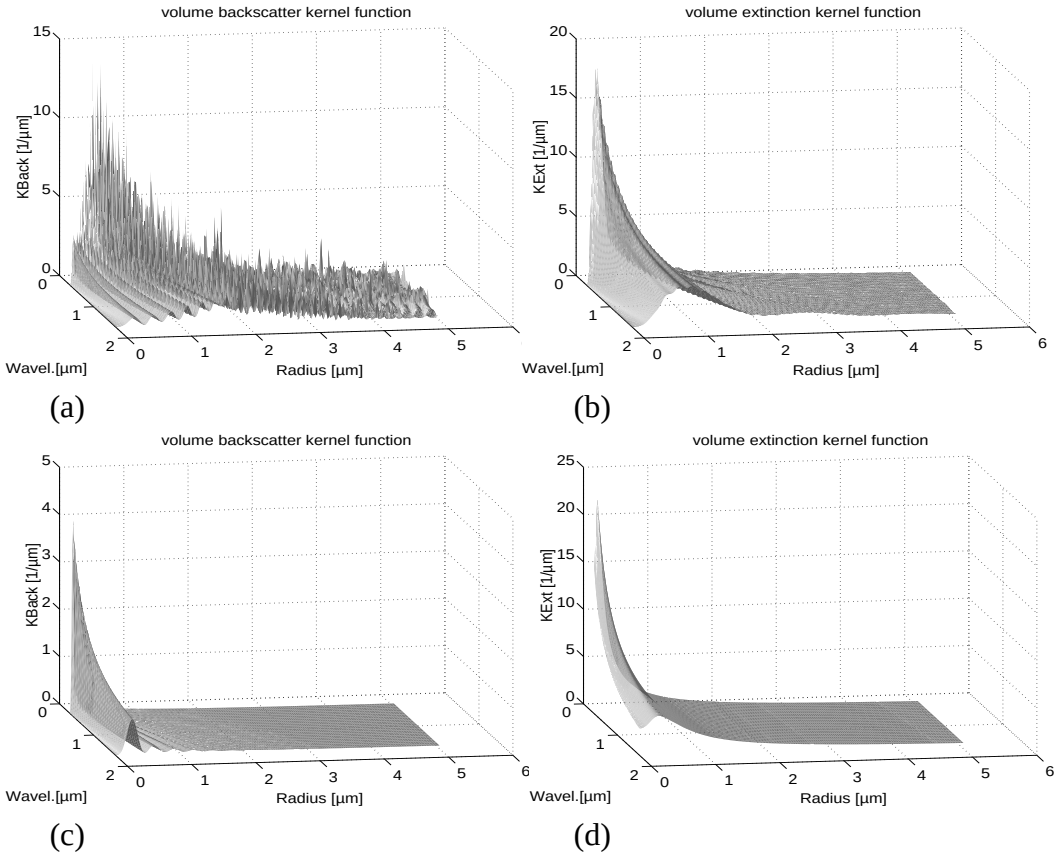

Figure 5.1: Volume backscatter and extinction kernel function $K^v_{\pi/ext}$ for different refractive indices: (a), (b) without absorption ($m_1 = 1.5 + 0.0i$) and (c), (d) with strong absorption ($m_2 = 1.5 + 0.5i$).

Every square-integrable kernel of a linear integral operator has a singular value expansion (SVE) which is a mean convergent expansion of the form

$$K(r,\lambda) \;=\; \sum_{1=1}^{\infty} \mu_i u_i(r)\overline{v_i(\lambda)},\; r \in I_r = [r_0, r_1],\; \lambda \in I_\lambda = [\lambda_0, \lambda_1], \tag{5.9}$$

where $\{u_i, v_i\}$ are the left and right singular functions of the kernel (Hansen, 1998). The behaviour of the singular values and functions is strongly connected with the properties of the kernel. Roughly speeking, the smoother the kernel the faster the singular values μ_i decay to zero, where smoothness is measured by the number of continuous partial derivatives of the kernel (Chang, 1952; de Hoog, 1980). It holds under some assumptions $\mu_i = o(i^{-p-3/2}),\; i \to \infty$, where $p-1$ is the number of continuous partial derivatives with respect to the second variable (the wavelength). This number p of the given lidar kernels, if one exists, is hardly to derive. We decide to deal with a numerical approximation. The smaller the μ_i the more oscillations in the singular functions u_i and v_i (see below).
The inversion of the Mie backscatter kernel is potentially interesting because the kernel itself possesses a high degree of oscillation if the absorption is weak, i.e., the imaginary part of the refractive index is small (see Fig. 5.1(a)), which suggests that the classic instability due to the smoothing out of fast oscillatory components in the solution space may not occur. However, in practice the oscillation of the kernel is so fine that the particle distribution would need to be computed on an extremly fine quadrature grid. This fact itself produces attendant problems with noise in the data. On the other side, if the absorption is strong, i.e., the imaginary part of the refractive index is large (see Fig. 5.1(c)), the

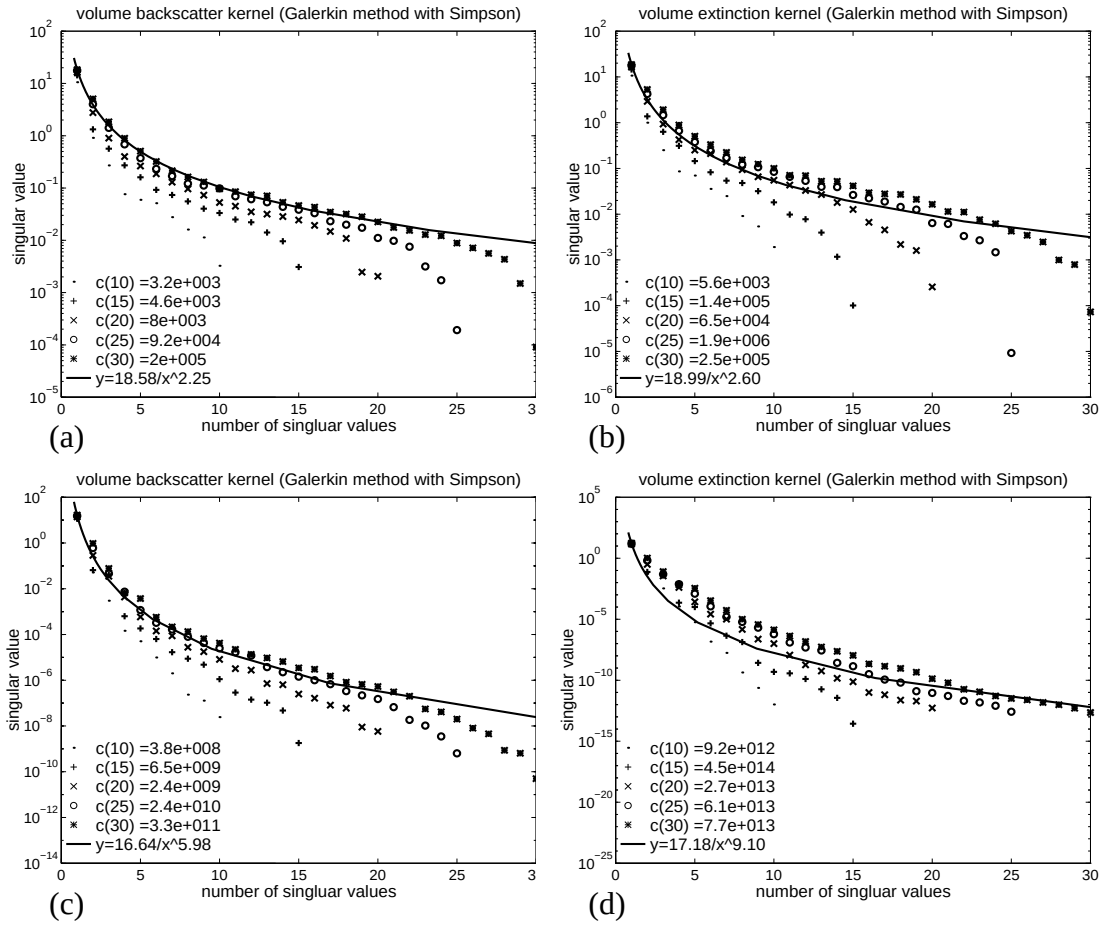

Figure 5.2: Approximation to the singular values and to the degree of ill-posedness of the volume backscatter and extinction lidar operators $K^v_{\pi/ext}$, (a), (b) without absorption ($m_1 = 1.5 + 0.0i$) and (c), (d) with strong absorption ($m_2 = 1.5 + 0.5i$). The $c(n),\ n = 10, 15, 20, 25, 30$ are the condition numbers of the resulting coefficient matrices after Galerkin discretization (Hansen, 1988) in dependence on the discretization dimension n.

kernel is smooth. In contrast to the backscatter kernel the Mie extinction kernel is very smooth in both absorption cases (see Fig. 5.1(b),(d)).

The SVE is a powerful analysis tool, but unfortunately it is only known analytically in a limited number of cases. Hence, approximations to the SVE can always be computed numerically when Eqs. (5.1) and (5.2) or (5.4), respectively, are discretized by means of the Galerkin method followed by computation of the singular-value decomposition (SVD) of the matrix obtained in this way. Choose orthonormal basis $\phi_1, ..., \phi_n$ and $\psi_1, ..., \psi_n$ in the spaces $L_2(I_r)$ and $L_2(I_\lambda)$, respectively, and define a matrix $A = \left(a_{i,j}\right)$ as follows

$$a_{ij} \ = \ (\psi_i, T\phi_j) \ \ i, j = 1, ..., n, \tag{5.10}$$

where $(\cdot, \cdot)$ denotes the scalar product in the space $L_2(I_\lambda)$. Then the SVD of A immediately gives approximations to the SVE of the kernel. Let $A \in R^{n,n}$ be a square matrix. Then the SVD of A is a decomposition of the form

$$A = UDV^T = \sum_{i=1}^{n} u_i \sigma_i v_i^T, \tag{5.11}$$

where $U = (u_1, ..., u_n)$, $V = (v_1, ..., v_n) \in R^{n^2}$ are matrices with orthonormal columns and where the diagonal matrix $D = \text{diag}(\sigma_1, ..., \sigma_n)$ has nonnegativ diagonal elements appearing in non-increasing order such that $\sigma_1 \geq \sigma_2 \geq ... \geq \sigma_n \geq 0$. The numbers $\sigma_i > 0$ are the singular values of A, while the vectors u_i and v_i are the left and right singular vectors of A, respectively. In connection with discrete ill-posed problems, two characteristic features of the SVD are very often found. First, the singular values decay gradually to zero with no particular gap in the spectra. An increase of the dimensions of A will increase the number of small singular values as in our lidar application (see Fig. 5.2). Second, the left and right singular vectors tend to have more sign changes in their elements as the index i increases, i.e., σ_i decreases. Both features are consequences of the fact that the SVD of A is closely related to the SVE of the underlying kernel (Allen et al., 1985; Hansen, 1998; Wing, 1985).
The singular values μ_j of T are then approximated by the algebraic singular values σ_j of A. In detail, the n singular values $\sigma_i^{(n)}$ of A are approximations to the n singular values of the kernel. Moreover, if we introduce the functions

$$\overline{u}_j(\lambda) = \sum_{i=1}^{n} u_{ij}\psi(\lambda),\ j = 1, ..., n, \tag{5.12}$$

$$\overline{v}_j(r) = \sum_{i=1}^{n} v_{ij}\phi(r),\ j = 1, ..., n, \tag{5.13}$$

where u_{ij} and v_{ij} are the elements of U and V, then these functions are approximations to n left and right singular functions of the kernel. We compute the double integrals in (5.10) by Simpsons numerical quadratur scheme, so that we can expect that the quadratur errors do not exceed the approximation errors caused by the basis functions. Due to (Hansen, 1988) and (Hansen, 1992) the singular values $\sigma_i^{(n)}$ (where n is the number of basis functions) are increasingly better approximations to the true singular values μ_i, in other words it holds

$$\sum_{i=1}^{n}(\mu_i - \sigma_i^{(n)})^2 \leq \Delta_n^2 \tag{5.14}$$

and

$$\sigma_i^{(n)} \leq \sigma_i^{(n+1)} \leq \mu_i, 0 \leq \mu_i - \sigma_i^{(n)} \leq \sqrt{||T||^2 - ||A||_F^2} =: \Delta_n,\ i = 1, ..., n. \tag{5.15}$$

The true singular values μ_i of T are bounded by the computed singular values $\sigma_i^{(n)}$ as follows: $\sigma_i^{(n)} \leq \mu_i \leq ((\sigma_i^{(n)})^2 + \Delta_n^2)^{1/2}$. If $\Delta_n \to 0$ for $n \to \infty$, then the approximate singular values $\sigma_i^{(n)}$ converge uniformly in n to the true singular values μ_i (see Fig. 5.2(a)-(d)).
Moreover, for the singular functions hold

$$\max\{||u_i - \overline{u}_i||_2, ||v_i - \overline{v}_i||_2\} \leq (\frac{2\Delta_n}{\mu_i - \mu_{i+1}})^{1/2}. \tag{5.16}$$

That means, the corresponding approximate singular functions converge in the mean to the true singular functions. Notice the square root in (5.16), which means that the singular value estimates $\sigma_i^{(n)}$ are usually much more accurate than the approximate singular functions.
The intervalls I_r and I_λ are each divided into n subintervalls $\{I_r^{(i)}\}$ and $\{I_\lambda^{(i)}\}$ of the same lengths h_r and h_λ, respectively, and the basis functions are then given by

$$\phi_i(r) = \begin{cases} h_r^{-1/2} & : \quad r \in I_r^{(i)} \\ 0 & : \quad \text{else} \end{cases},\ \psi_i(\lambda) = \begin{cases} h_\lambda^{-1/2} & : \quad \lambda \in I_\lambda^{(i)},\ i = 1, ..., n. \\ 0 & : \quad \text{else} \end{cases} \tag{5.17}$$

Let the lower and upper limits of particle radius and laser wavelength $r_0 = 0.001$ μm, $r_1 = 5$ μm, $\lambda_0 = 300$ nm, and $\lambda_1 = 1100$ nm, which are real-life domains in the lidar field, then the formulas give second-order approximations to the singular values μ_i (see Fig. 5.2).

All singular values of A, which arise in such a discrete ill-posed problem from the sampling of a

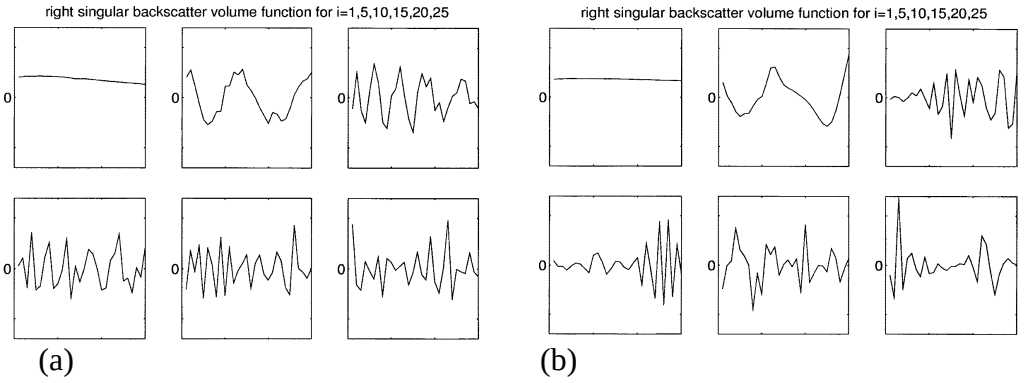

Figure 5.3: Qualitative approximation to six right singular functions v_i for $i = 1, 5, 10, 15, 20, 25$ of the volume backscatter lidar operator, (a) $m_1 = 1.5 + 0.0i$ and (b) $m_2 = 1.5 + 0.5i$. We see that the higher the index, the more high-frequency components are present in v_i.

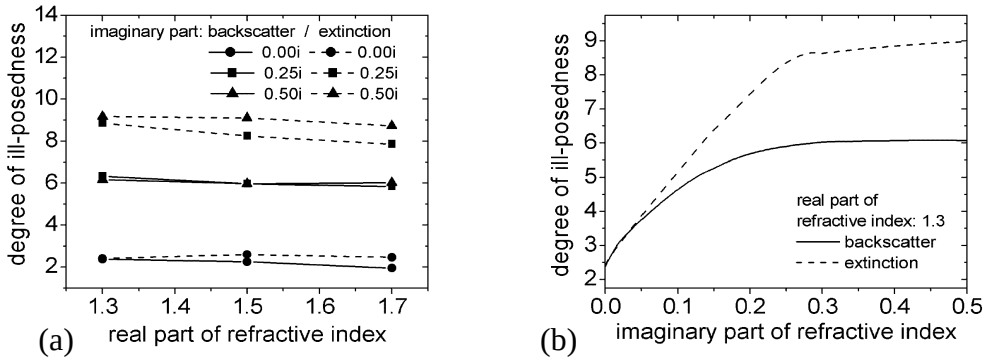

Figure 5.4: Degree of ill-posedness of the volume lidar operators in dependence on the real and imaginary part of the refractive index. We see on the one hand no remarkable influence of the real part (a) and on the other hand the important influence of the imaginary part, i.e., the absorption influence (b).

Fredholm integral equation of the first kind, decay on the average to zero. There is no practical gap in the singular value spectrum, typically, the singular values follow a harmonic progression $\sigma_i \simeq i^{-\alpha}$ or a geometric progression $\sigma_i \simeq e^{-\alpha i}$, where α is a positive real constant. The decay rate of the singular values μ_i is so fundamental for the behaviour of ill-posed problems that it makes sense to use this decay rate to characterize the degree of ill-posedness of the problem. Hofmann (Hofmann, 1999; Hofmann, 1994) gives the following definition: if there exists a positive real number α such that the singular values satisfy $\mu_i = O(i^{-\alpha})$, then α is called the degree of ill-posedness. The problem is characterized as *mildly* or *moderately ill-posed* if $\alpha \leq 1$ or $\alpha > 1$, respectively. On the other hand, if $\mu_i = O(e^{-\alpha i})$, i.e., the singular values decay very rapidly, then the problem is termed *severely ill-posed*.

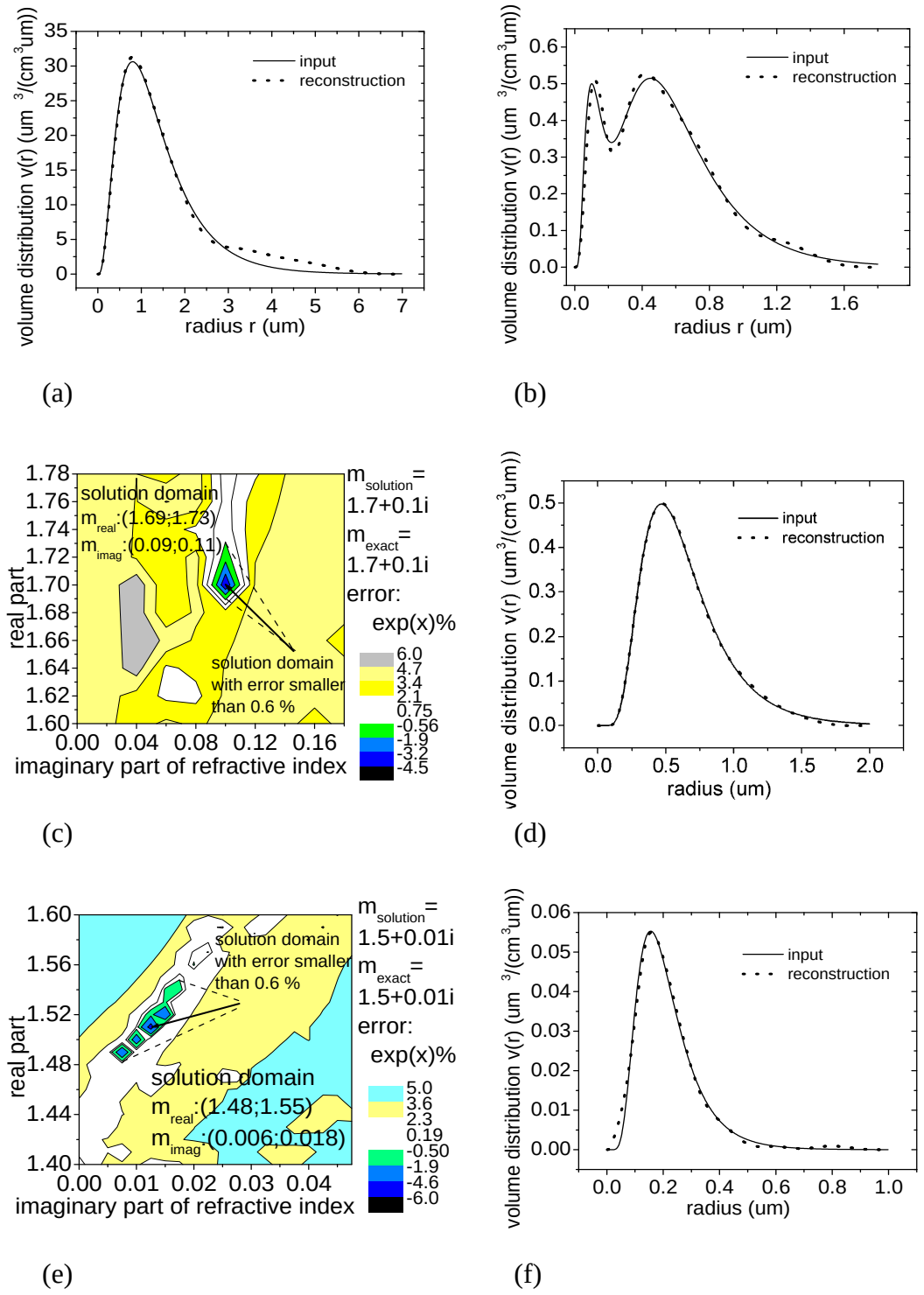

Figure 5.5: Regularized inversion results of noiseless data, i.e. the determination of the particle distributions of different types from six simulated backscatter $\beta^{Aer}(\lambda_i)$ and two simulated extinction $\alpha^{Aer}(\lambda_j)$ coefficients: (a) modified Gamma distribution with $r_{\text{eff}} = 0.89$ μm, (b) bimodal logarithmic-normal distribution with $r_{\text{eff}} = 0.3$ μm, (d) monomodal logarithmic-normal distribution with $r_{\text{eff}} = 0.52$ μm and (c) additional determination of the unknown refractive index m (strong absorption case) in the kernel functions $K^{v}_{\pi/ext}(r, \lambda, m)$ for the distribution (d), (f) monomodal logarithmic-normal distribution with $r_{\text{eff}} = 0.13$ μm and (e) additional determination of the unknown refractive index m (weak absorption case); for more details see (Böckmann, 2001).

For our lidar operators of Eq. (5.4) we determined the condition numbers and, by a numerically weighted nonlinear least-squares method fit, an approximation to the degree of ill-posedness (see Fig. 5.2(a)-(d)). In general, one observes that the lidar operators are moderately ill-posed, since α is between 2.25 and 9.10. In detail, one can see that the degree of the extinction operator is higher than the degree of the backscatter operator (see Fig. 5.2). Moreover, if the absorption of the particles is strong, then the degree grows rapidly (see Fig. 5.2(c),(d)). Realizing the logarithmic scale in Fig. 5.2(d), one can see that the singular values are almost located on a straight line. Therefore, this extinction operator with strong absorption is nearly severely ill-posed. As one expects, the condition numbers grow with n and they show the same behaviour as the degree. The matrices are always highly ill-conditioned, and its numerical null space is spanned by vectors with many sign changes. Fig. 5.3(a),(b) shows qualitatively six approximations of the right singular functions $v_i,\ i = 1, 5, 10, 15, 20, 25$, and the typical behaviour that the higher the index i the higher the spectral components in v_i. Due to the higher degree of ill-posedness, it seems that the behaviour of the oscillations is more unstructured in the strong absorption case (see Fig. 5.3(b)).
With respect to the evaluation of lidar measurements it is necessary to know, how the degree of ill-posedness depends on the real and imaginary part of the refractive index of the particles. This dependence is shown in Fig. 5.4. On the one hand, there is no influence of the real part in the real-life domain between 1.3 and 1.7. On the other hand, the imaginary part in the domain between 0 and 0.5 has a very important influence on the degree. The degree grows rapidly between 0 and 0.25, which is a very realistic domain in our atmosphere. The growth rate can be compared with a root function in the underlying domain.

5.2 Inversion methods

5.2.1 IMP algorithm

Based on the theoretical knowledge, a special hybrid regularization technique in the sense of Eqs. (5.6) and (5.8) was developed, which is described in detail in (Böckmann, 2001; Böckmann and Sarközi, 1999). The hybrid regularization technique developed at IMP is designed to work with different kind and number of optical data, i.e., experimental data obtained with different systems at various wavelengths can be evaluated. The algorithm does neither require any *a priori* information on the analytical shape of the investigated distribution function nor an initial guess of it. Even bimodal and multimodal distributions can be retrieved without any knowledge of the number of modes in advance (see Fig. 5.5(b)). The first regularization step in this method is performed via discretization, in which the investigated distribution function is approximated with variable B-spline functions. The projection dimension (number of basis functions) and the order of the used B splines serve as regularization parameters. In the second step, regularization is controlled by the level of truncated singular-value decomposition performed during the solution process of the resulting linear equation system. In order to reduce the computer time, a collocation projection is used. The highly nonlinear problem of the complex refractive index as a second unknown is handled by introducing a grid of a wavelength- and size-independent mean complex refractive index and by enclosing the area of possible real/imaginary-part combinations through inversion and back-calculation of optical data. Inversion results are given in terms of volume distributions, effective particle radius, volume, surface-area, and number concentrations.
Figure 5.5 shows a few simulation results. The hybrid regularization technique that amalgamates three regularization parameters works excellent for different distributions with different modes and with different effective radii (see Fig. 5.5(a),(b),(d),(f)). In addition, the unknown refractive index can

be captured (see Fig. 5.5(c),(e)). In contrast to the described fact that the degree of ill-posedness is higher with respect to the inverse problem with known refractive index if the absorption is strong, here we observe the opposite. If $m_{\mathrm{imag}} = 0.1i$, (see Fig. 5.5(c)) the solution domain can easily be defined and is small. This is plausible. If a slightly incorrect refractive index is used, the inverse problem responds with a large output error that is due to the high ill-posedness degree. In the case of weak absorption the solution is not so well determined (see Fig. 5.5(e)). We observe a more elongated and often disconnected solution domain of possible refractive indices, a fact that was observed for the IfT algorithm, too.

5.2.2 IfT algorithm

The IfT scheme, which is described in detail in Müller et al. (Müller et al., 1999b), uses a Tikhonov regularization with constraints to invert the eight optical data measured with the IfT multiwavelength lidar. The strength of regularization, which determines the degree of smoothness of the solution, is found from generalized cross-validation (Golub et al., 1979). The investigated volume concentration distribution is approximated with a discrete set of eight basis functions, which have the shape of B splines of the second order, i.e., linear polynomials. Fifty inversion windows of variable width are defined through variation of the lower and upper limits of the basis-function range from 0.01 to 0.2 and from 1 to 10 μm, respectively. The basis functions are distributed logarithmically equidistant within the windows. The inversion is performed for every window and for refractive indices that vary from 1.33 to 1.8 in real and from 0 to 0.7 in imaginary part.
From the inversion solutions only those are selected, for which the back-calculated optical data agree with the original data within the limits of the measurement error. Mean and integral particle parameters, i.e., effective radius, volume, surface-area, and number concentrations, are calculated from the selected solutions, and their mean values and standard deviations are presented as final inversion results. Furthermore, the single-scattering albedo is calculated from the volume concentration distribution and the complex refractive index as in the IMP algorithm, too.
From extended simulation studies, it was shown that an appropriate reconstruction of the volume distribution together with a mean complex refractive index is found from the eight optical data derived with the IfT multiwavelength lidar (Müller et al., 1999a). It was demonstrated that information on particle extinction is necessary at two wavelengths at least and that the optical data must be determined with errors of $\leq$10%–20%.

5.3 Inversion results

5.3.1 Biomass-burning aerosol measured during LACE 98

In the following, we present an example of the inversion of experimental data with both algorithms and the comparison of the results with airborne *in situ* measurements onboard the research aircraft Falcon. The measurements were taken during LACE 98, when a distinct aerosol layer, which originated from forest fires in northwestern Canada, was present in the free troposphere (see also Sec. 4.2 , Sec. 8.5, and (Wandinger et al., 2000)). The optical data shown in Fig. 4.16 were used as input in the two inversion algorithms described above.
For the IfT algorithm the six backscatter and two extinction coefficients of the IfT multiwavelength lidar were used only. With the IMP algorithm all 11 data were processed and several tests were performed to check the influence of certain wavelengths on the inversion results. Table 5.3.1 shows the inversion results of both algorithms in comparison to the Falcon *in situ* measurements. In general,

Parameter	Lidar, inversion		Falcon, *in situ*	
	IfT algorithm	IMP algorithm	particles with $r \geq 1.5$ nm	particles with $r \geq 50$ nm
r_{eff}, μm	0.27±0.04	0.24±0.01	0.24±0.06	0.25±0.07
v_t, $\mu\text{m}^3\text{cm}^{-3}$	13±2	11±1	9±5	8±5
a_t, $\mu\text{m}^2\text{cm}^{-3}$	139±7	134±2	110±50	95±55
n_t, cm^{-3}	291±70	361±57	640±174	271±74
m_{real}	1.64±0.09	1.61±0.04	(1.56)	
m_{imag}	0.05±0.02	0.088±0.011	(0.07)	
SSA (532 nm)	0.83±0.06	0.73±0.03	0.78±0.02	0.79±0.02

r_{eff}–effective radius, v_t–total volume concentration, a_t–total surface-area concentration, n_t–total number concentration, m_{real}–real part of refractive index, m_{imag}–imaginary part of refractive index, SSA–single-scattering albedo.

Table 5.1: Physical particle parameters from inversion of lidar data measured in the height region from 3600–4100 m a.s.l. on 9 August 1998, 2200–2400 UTC, and from *in situ* measurements of particle size distributions aboard the Falcon from 3500–4000 m a.s.l.

the data agree well within their error limits. An effective radius of 0.25±0.03 μm was found. Surface-area and volume concentrations derived from the inversion are about 30% higher than those measured *in situ* in the lower layer. The spectral backscatter coefficients calculated from the measured size distributions differ in the same way from those measured with lidar. This finding indicates that the deviation is caused by the spatial inhomogeneity of the aerosol layer rather than by uncertainties in either the measurement or the inversion. The airborne measurements were taken on a 80-km flight leg about 5 km to the east of the lidar site around 2300 UTC. The lidar profiles were averaged over two hours from 2200–2400 UTC.

In general, number concentrations are difficult to determine from the inversion of optical data (Böckmann, 2001; Müller et al., 1999a), because usually the majority of particles is too small to be optically active and thus does not contribute to the optical coefficients measured with lidar. The inversion algorithms indicate this uncertainty by the large error limits, which are obtained from the scattering of the investigated parameters within their solution space. If one separates the *in situ* measurements into the different modes of the size distribution (Aitken mode with particle radii r<0.05 μm, accumulation mode with 0.05<r<0.5 μm, and coarse mode with r>0.5 μm) and compares the respective number concentrations with the inversion results, it becomes evident that the inversion of the multiwavelength lidar data gives mainly information on particles in the accumulation and coarse modes (see Table 5.3.1). However, because the Aitken mode does not significantly contribute to total particle surface area and volume, these concentrations, and thus also the effective radius, are reconstructed very well with the inversion.

As mentioned above, a variable, but wavelength- and size-independent mean complex refractive index is used in both inversion schemes. As has been shown previously (Böckmann, 2001; Müller et al., 1999a), solutions are obtained for certain combinations of real and imaginary parts of the complex refractive index only. If the real and imaginary parts are ordered in a matrix-like scheme, the solutions for the refractive index are arranged along a diagonal in this matrix if the absorption ist weak (smaller than approximately $m_{\text{imag}} = 0.08i$ in the IMP algorithm, see Fig. 5.5(e) and Ref. (Böckmann, 2001)). That is, smaller real parts are connected with smaller imaginary parts and larger real parts with larger imaginary parts. This fact should be taken into account in the interpretation of the error limits given for the refractive index.

The refractive index for the airborne *in situ* measurements was calculated from a volume-weighted, internal mixture of absorbing, soot-like and non-absorbing, ammonium-sulfate-like material under

consideration of the absorption coefficient measured with the particle soot absorption photometer (PSAP). One should have in mind that closure of the backscatter coefficients calculated from the size distribution with the lidar backscatter coefficients was obtained for an external mixture of the two aerosol components only, i.e., by introducing a separate refractive index for ammonium sulfate of $1.53-0.0i$ and for soot of $1.75-0.45i$ (Fiebig et al., 2000). Calculations for an internal mixture could not reproduce the lidar measurements. For that reason, the values of the refractive index in Table 5.3.1 are given in parentheses. The inversion results gave similar values, which are thus assumed to indicate a mean complex refractive index, that well characterizes the scattering and absorption properties of the entire particle ensemble.

The latter fact is confirmed by the comparison of the single-scattering albedo, which is derived from the particle size distribution (either inverted or measured) and the complex refractive index (either inverted or derived from appropriate mixing of soot and ammonium sulfate) with Mie-scattering calculations. In the case of the airborne measurements, an external mixture of ammonium sulfate and soot was assumed. Again, a good agreement between inversion results and *in situ* measurements is found, though the IfT results are slightly larger and the IMP results are slightly smaller than the *in situ* values. Values of the order of 0.8 indicate a rather high influence of absorption on the radiative properties of the particles.

The sensitivity studies with the IMP algorithm concerning the different number of data used in the inversion showed that, e.g., the use of six backscatter and two extinction coefficients determined with the IfT multiwavelength lidar instead of all 11 available optical data (eight backscatter and three extinction coefficients) does not change the results for particle size and concentration significantly. However, a remarkable sensitivity of the complex refractive index was noted. Especially, the introduction of the extinction values at the shortest wavelength (292 nm) lead to a very large solution space, which included unrealistically high real and imaginary parts of the refractive index. One possible reason for that is the large uncertainty of the values in the UV because of the necessary ozone correction. On the other hand, there seems to occur a systematic difference in the solutions for the refractive index from the two inversion algorithms. Larger imaginary parts are found in most cases with the IMP algorithm in comparison to the IfT algorithm independently of the number of optical data used. As a consequence, the single-scattering albedo determined with the IMP algorithm is smaller than the values derived from the IfT algorithm.

5.3.2 Minimum data set

Both inversion algorithms were tested with respect to a minimum data set, which may be delivered from aerosol Raman lidars based on a single Nd:YAG laser. Backscatter coefficients at 355, 532, and 1064 nm and extinction coefficients at 355 and 532 nm are available in this case (3+2). Table 5.3.2 shows the results that were obtained from the same optical data set as those in Tab. 5.3.1. The IfT algorithm was modified for this study. A finer resolution of the refractive-index grid with 320 instead of 140 complex values was used. A re-calculation on this finer grid was performed also for the case of six backscatter and two extinction coefficients (6+2), which lead to slightly different values in Tab. 5.3.2 compared to Tab. 5.3.1. Excellent agreement of the results from the reduced data set (3+2) with those from 6+2 data and thus also with the airborne *in situ* measurements was obtained, which indicates that the 3+2 information is sufficient for a successful inversion in this case. Further investigations are necessary concerning the determination of the imaginary part of the refractive index which is very sensitive.

In general, it was found that inversion errors increase with the reduction of measurement data and that a higher accuracy of the reduced data set is required for a successful inversion. Simulations with the IMP algorithm showed that for noiseless data the mean and integral parameters of the particle size

Parameter	Ift algorithm		IMP algorithm	
	3+2	6+2	3+2	6+2
r_{eff}, μm	0.27±0.04	0.27±0.04	0.26 ±0.03	0.24±0.01
v_t, μm^{3}cm^{-3}	13±2	13±3	12±2	11±1
a_t, μm^{2}cm^{-3}	145±8	142±7	141±5	134±2
m_{real}	1.63±0.09	1.62±0.09	1.62±0.06	1.61±0.04

Table 5.2: Comparison of inversion results from 3 backscatter and 2 extinction coefficients (3+2) with the results from 6 backscatter and 2 extinction coefficients (6+2). The same set of parameters as in Tab. 5.3.1 was used. In the IfT algorithm a finer grid of the complex refractive index with 320 instead of 140 values was used.

distribution, except the number concentration, can be limited to 3% error in the 6+2 case. For the reduced data set this error increases to 7%. Errors in the input data of the order of 10% lead to errors in the physical particle parameters of 7% for the 6+2 case and of 15% in the 3+2 case.

Chapter 6

Statistical analysis of the atmospheric trajectories for the lidar network

by I. Mattis

The lidar network was established to derive a general characterization of the vertical aerosol distribution and its dependence on season, weather regime, diurnal cycle, and local effects and to investigate the temporal and spatial development of the aerosol properties. In this section a method is described, which permits one to classify profiles of optical aerosol properties derived by the routine observations in dependence on the large-scale weather regime (Mattis et al., 2001). The atmospheric trajectories are calculated by the German Weather Service for all lidar-network stations for two arrival times each day, which correspond approximately to the times of the routine lidar observations at noon and at sunset.

Because the quantity of available trajectory data sets (two per day) is much larger than the number of measured aerosol profiles (usually not more than four per week) we suggest to apply any method of statistical analysis primarily to the trajectories and not directly to the lidar profiles. The analytical trajectories provide information about the origin of the observed aerosols and about the synoptic patterns corresponding to the measurements. They were divided into distinct clusters by means of cluster analysis. Then each lidar profile was assigned to the cluster of its corresponding trajectory. Because a trajectory cluster represents one large-scale atmospheric transport pattern, each of the profiles within the corresponding class of optical aerosol properties was obtained from a lidar observation under similar large-scale synoptic conditions. Investigations of the properties of these aerosol classes will show the dependence of optical aerosol properties on the corresponding weather regime.

6.1 Trajectories for the lidar network project

The atmospheric 4-day backward trajectories used in this study were calculated by the German Weather Service from the wind fields of its European numerical weather prediction model (Kottmeier and Fay, 1998). They are available since December 1997. The trajectories are calculated on a 3-dimensional grid. This calculation method leads to lower uncertainties in comparison to those of other methods, e.g. isentropic calculation. The accuracy of the calculated trajectories depends on the synoptic conditions. The higher the wind speed the lower the uncertainty of the trajectories. Usually the deviation between the calculated and the actual track of an air parcel is about 10% to 20% of the trajectory length for the trajectories used in this study (Stohl, 1998). In Table 6.1 the characteristic

properties of the trajectories are summarized.

trajectory model	
data base	European numerical weather prediction model of the German Weather Service
spatial resolution	$0.5\,^{\circ}$
time resolution	6 hr
available trajectory data set	
trajectory length	4 days
2 arrival times	13 UTC, 19 UTC each day
6 arrival pressure levels	975, 850, 700, 500, 300, 200 hPa
5 lidar sites	Hamburg Kühlungsborn Leipzig Munich Garmisch-Partenkirchen

Table 6.1: Characteristical properties of the backtrajectories used in this study.

6.2 Statistical analysis of the atmospheric trajectories for the lidar network

Cluster analysis provides algorithms to separate a large number of data sets (in our case sets of trajectories) into groups, the so-called clusters. The separation of the data sets has to be done in such a way that similar trajectories are merged within one cluster and dissimilar ones belong to different clusters. In this study a clustering algorithm for atmospheric trajectories recommended by (Dorling et al., 1992) was used. Modifications concerning the starting conditions provide additional information on the uncertainty of the derived results. As an advantage of the used clustering algorithm the optimum number of clusters follows from the algorithm itself and has not to be assumed.
The following steps shortly describe the clustering algorithm:

1. A set of seed trajectories is generated. Modifying Dorlings algorithm synthetical rather than real trajectories were used. As an example Figure 6.1 shows 30 seed trajectories arriving at Leipzig.

2. Each trajectory is assigned to that seed, which is closest in terms of the used measure of distance. In this study, we simply used the 2-dimensional Euclidian distance concerning only the longitude and latitude data of the trajectories. Then the average trajectory of each group is calculated from all group members. These mean trajectories are the so-called centroids.

3. It is checked, whether each real trajectory is in the right cluster in terms of its distance to the clusters centroid. After reassigning the trajectories, the centroids have to be recalculated.

   This step has to be reiterated until all trajectories are correctly assigned.

4. The Root Mean Square Deviation ($RMSD$) of each trajectory from its centroid is calculated. The sum of these $RMSDs$ gives the total $RMSD$.

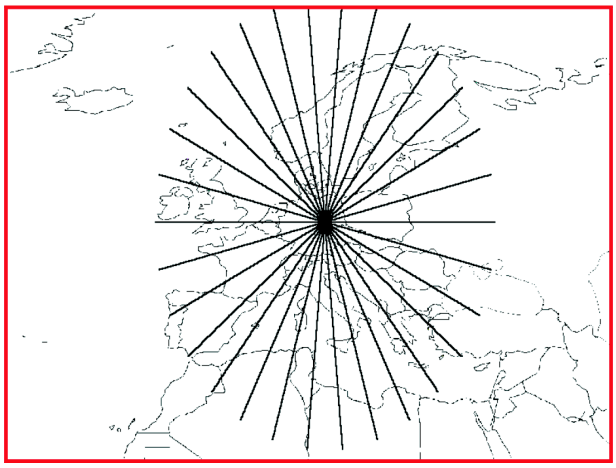

Figure 6.1: Thirty synthetic seed trajectories arriving at Leipzig.

5. Those two clusters are merged, for which the centroids are closest. The centroid of the merged cluster is calculated and the steps 3 and 4 have to be repeated.

6. Step 5 is repeated consecutevely until the number of clusters N is 1. The derived total $RMSDs$ are plotted versus N. The reduction of cluster numbers leads in general to a weak increase in $RMSD(N)$. A steep increase in $RMSD(N)$ is observed when significantly different trajectories formerly located in distinct clusters are merged into one cluster. So the the optimum number of clusters is the N before the steep increase in $RMSD(N)$.

7. In this study, Dorlings algorithm was extended toward a repetition of steps 2 to 6 with slightly varied seed trajectories. For that purpose, the clustering was first calculated for all seeds, then every sixth seed trajectory was left out, starting with the first one. In the next iteration step every sixth seed, starting with the second one was left out, etc.

Figure 6.2 shows as an example the resulting curves of the total $RMSDs$ versus N for all trajectories arriving at Leipzig at 850 hPa in 1998, 1999, and 2000 corresponding to the seven different initial conditions. All seven curves converge when the number of clusters is reduced from six to five. That means, if the number of clusters is smaller or equal to six, the different initial conditions lead to the same result. But if N is larger than six, no stable clusters can be found and any peaks in the percentage change of $RMSD$ for more than six clusters should be neglected in the search for the optimum number of clusters. Thus only the steep increase in the total RMSD when N is reduced from five to four is significant, and the optimum number of clusters for this example was found to be five.

6.3 Results

The cluster analysis described above was used in combination with lidar profiles only for trajectories, which end at 850 hPa (see Section 6.1). These trajectories are believed to be most representative for the main air transport in the upper part of the atmospheric boundary layer. The trajectories arriving at

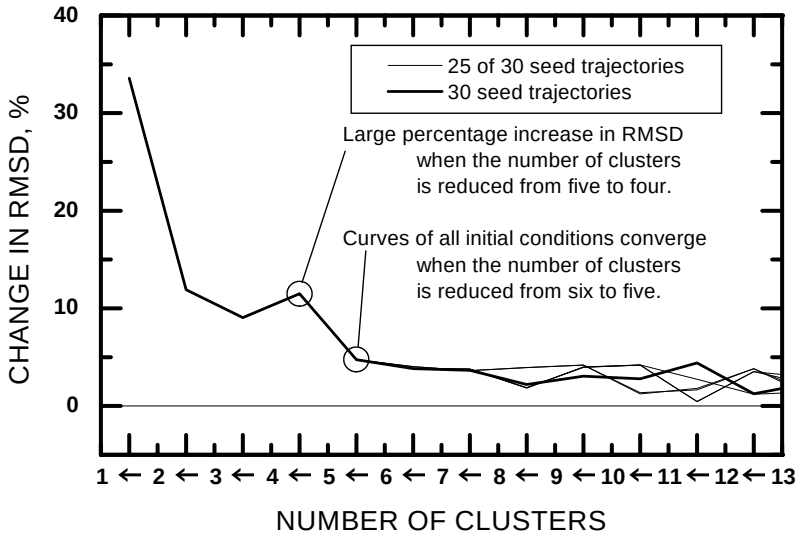

Figure 6.2: Change of the total RMSD for all trajectories arriving at Leipzig at 850 hPa in 1998, 1999, and 2000. Each thin curve represents the result of the clustering algorithm for one of the initial conditions.

975 hPa are more influenced by the earth surface and therefore their uncertainty is larger. Nevertheless, the cluster analysis was also applied to trajectories arriving at Leipzig at 975 hPa simply to give an example and an idea about the conditions in the lower boundary layer.

Figure 6.3 shows the total $RMSD$ versus the number of clusters for all lidar sites. The optimum number of clusters was found to be five for almost all of the cases. The curves of different initial conditions merge at higher Ns for the southerly stations Munich and Garmisch-Partenkirchen and for the 975-hPa trajectories. For Kühlungsborn no single solution could be found. The curves of the seven initial conditions do not merge into one but into two final curves. For the trajectories arriving at Kühlungsborn this means, the clustering algorithm finds two stable clustering states, which are marked with I and II in the plot. The optimum N for state I seems to be six. The Total $RMSDs$ plotted in Figure 6.4 show the same pattern. The $RMSD$ of 5 clusters as well as the total $RMSD$ of all trajectories is larger for the northerly stations Leipzig, Hamburg, and Kühlungsborn than for the southerly stations. Also the $RMSD$ is larger for the 850 than for the 975-hPa trajectories ending at Leipzig. For the Kühlungsborn trajectories the total $RMSD$ of 5 clusters is lower for the clustering state II than for state I. This fact may indicate that state II is the 'correct' solution. Nevertheless, further investigations have to be carried out to find a more stable solution for the Kühlungsborn trajectories.

Figure 6.5 illustrates, how the trajectories of 1998, 1999, and 2000 are assigned to the five clusters identified by the clustering algorithm for all six cases. For Kühlungsborn solution II is shown. The pattern are very similar for the five locations and also for the two different pressure levels. The five clusters represent weather regimes with different wind directions and speeds. Cluster a) contains all trajectories coming to Germany from easterly directions with low speeds. Air parcels which were transported to central Europe from northwest with higher wind speeds are merged within cluster b). Cluster c) combines trajectories from the Mediterranian Sea and very slow ones from western Europe. Those trajectories, which have their origin over the Atlantic ocean are combined in clusters d) and e) with the latter one characterized by very high wind speeds.

Figure 6.6 shows that most of the trajectories are associated with cluster c). For the southern stations Munich and Garmisch-Partenkirchen this statement held for the summer months (April to September)

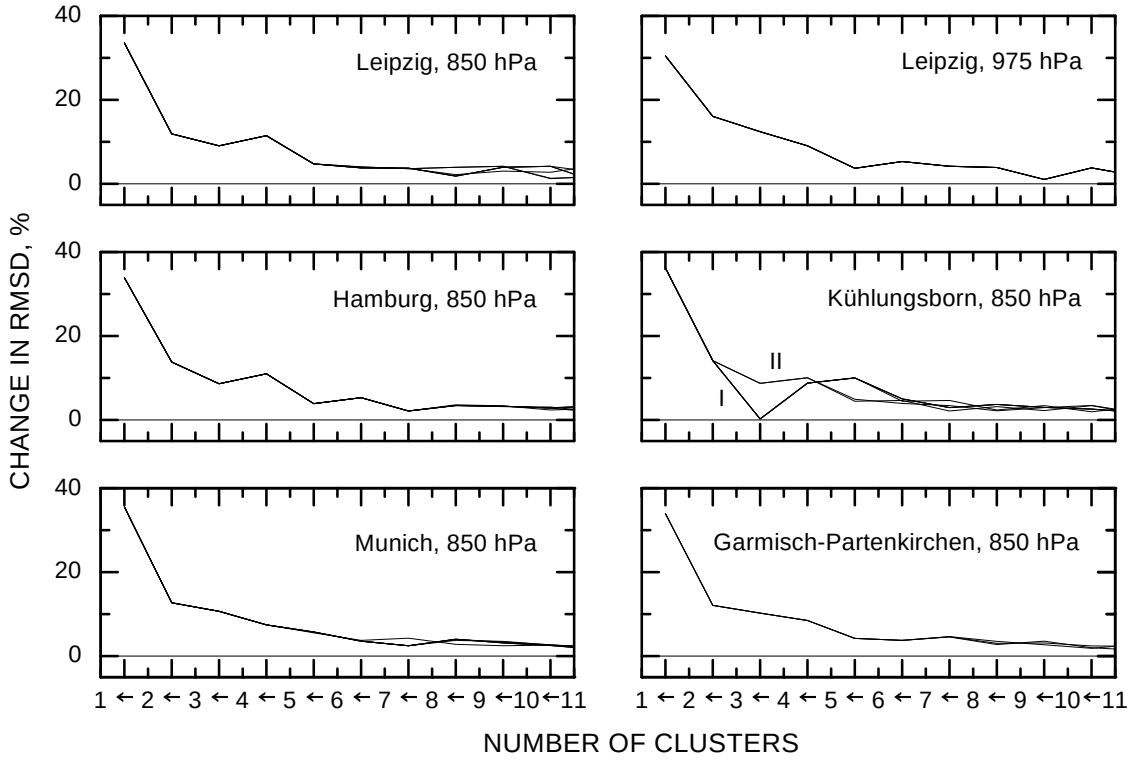

Figure 6.3: Change in the total $RMSD$ for all trajectories arriving at 850 hPa at all 5 lidar sites and at 975 hPa at Leipzig in 1998, 1999, and 2000. Every curve represents a result of the clustering algorithm for one of the initial conditions. For Kühlungsborn no significant solution could be found. The resulting two stable clustering states are marked with I and II.

as well as for the winter period (October to March). In all cases the quantity of trajectories inside this cluster is clearly higher in summer than in winter except for the 975-hPa level. The occurence of the trajectories in the clusters c and d, which are associated with moderate westerly winds, is nearly the same for the two northern stations. It is not surprising that the members of cluster e), which corresponds to weather regimes with very fast westerly winds, are almost only winter trajectories for all lidar sites as well as for the two pressure levels.

The $RMSD$ of the cluster members in general is higher for the winter trajectories than for the summer trajectories. The absolute values of the $RMSD$ decrease from north to south and from 850 to 975 hPa. This fact is in agreement with the finding of Figure 6.3 that the N, for which the curves of different initial conditions merge, shows the same behaviour with latitude and pressure level. However, this result should not be extrapolated to other European stations, because the properties of the $RMSD$ of a trajectory set should less be affected by the latitude but more by orography. The stations in northern Germany are located at the coast, the southern ones at the rim of the Alps, and Leipzig lies in between (in a geographical sense as well as in the results of the cluster analysis).

As outlined at the beginning of this section, the results of the previously described clustering algorithm should be used to classify optical aerosol properties in dependence on the large-scale weather regime. Each lidar observation has to be assigned to the cluster of its corresponding trajectory to derive groups of optical aerosol properties obtained from lidar observations under similar large-scale synoptic conditions. In section 7.3, the results of this procedure will be presented for the example of the routine observations at Leipzig.

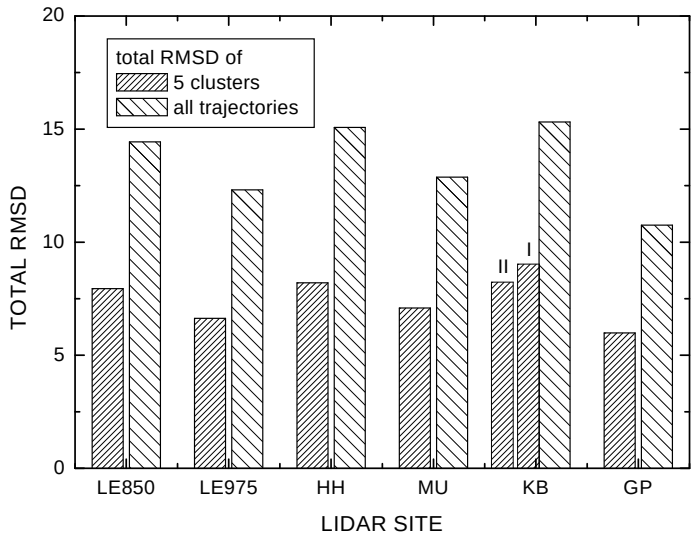

Figure 6.4: Total $RMSD$ for all trajectories arriving at 850 hPa at Leipzig (LE850), Hamburg (HH), Munich (MU), Kühlungsborn (KB), Garmisch-Partenkirchen (GP), and at 975 hPa at Leipzig (LE975) in 1998, 1999, and 2000. The left columns stand for the total $RMSD$ of all trajectories grouped within 5 clusters and the right ones show the total $RMSD$ of all trajectories. The two results for Kühlungsborn are marked with I and II.

6.4 Conclusions

In the preceding section a method was suggested, which allows to classify profiles of optical aerosol properties derived by the routine observations in dependence on the large-scale weather regime. This method can be applied not only the Leipzig data set but also to the trajectories and aerosol data of the other members of this German lidar-network project as well as to the data of the participiants of the EARLINET project which is funded by the EC and started in February 2000.
The described clustering algorithm was modified to get an estimation on its uncertainties. This examination will be continued to find possibilitis to derive significant solutions in cases like the Kühlungsborn trajectories, too.
Changing the used measure of distance in the clustering algorithm will allows to examine other questions than only the dependence on large-scale weather regime. Increasing the weight of the distance between two trajectories with decreasing distance to their arrival site will cause the algorithm to combine those trajectories into one cluster, which have crossed the same aerosol sources near the arrival site even if they originated from different regions. This tendency may be amplified by inserting any information about the surface below the trajectories (for instance emission maps) into the measure of distance.

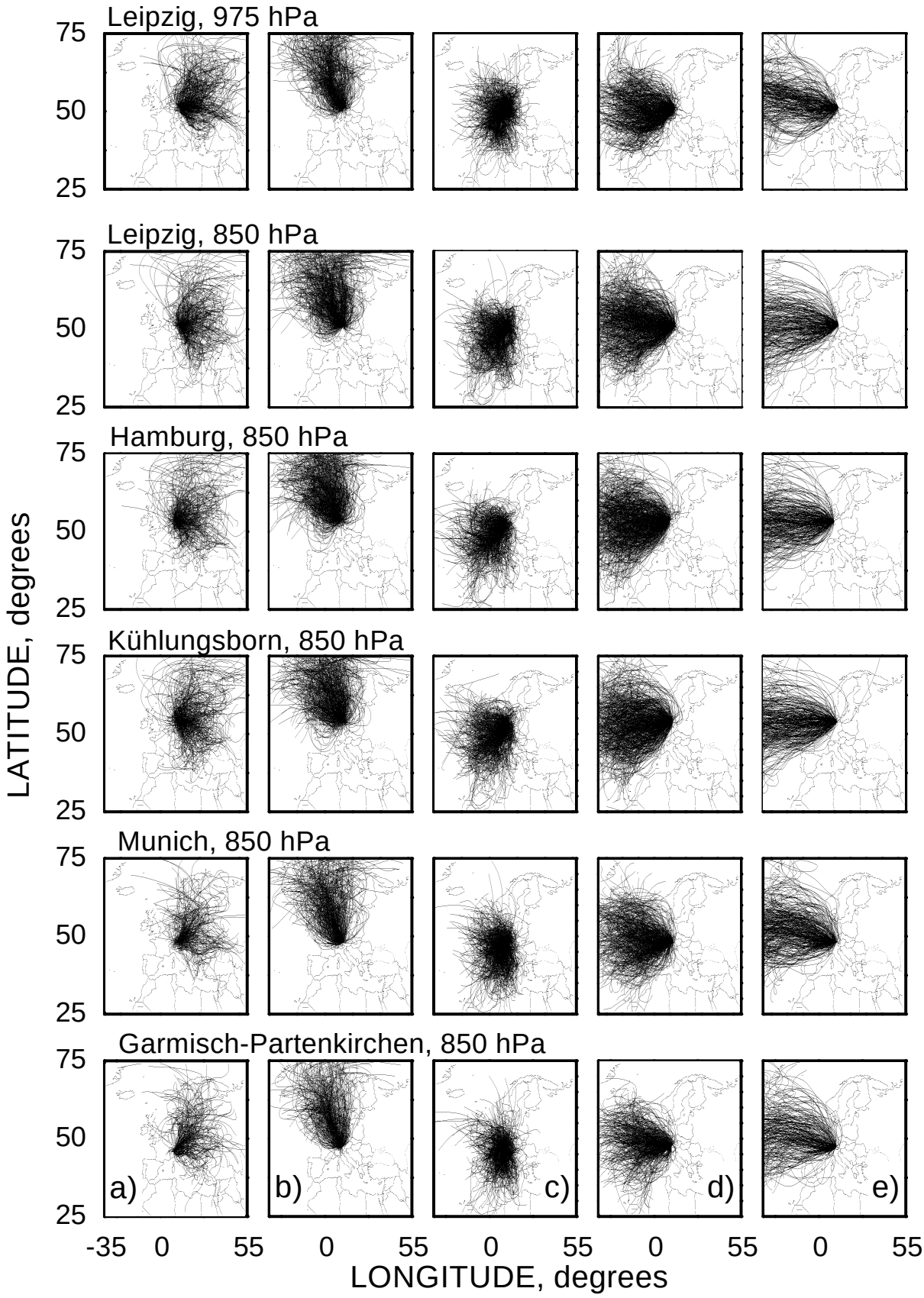

Figure 6.5: All trajectories of 1998, 1999, and 2000 in the five clusters identified by the clustering algorithm for the lidar sites and pressure levels listed in the upper left corner of each row. For Kühlungsborn solution II is shown. The characters in the lowest row identify the clusters.

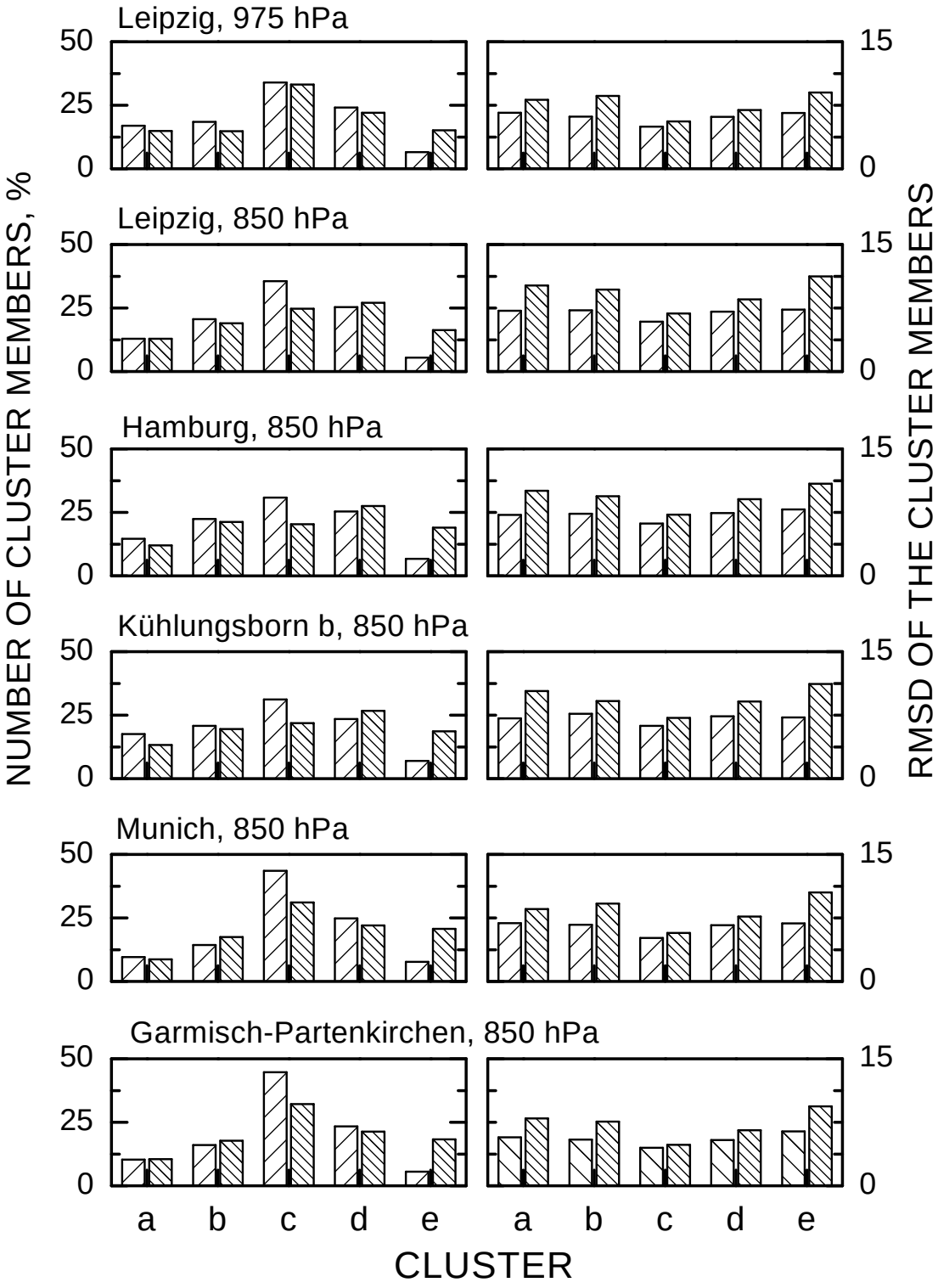

Figure 6.6: Left: Number of members of the five clusters for the different lidar sites and pressure levels. Right: $RMSD$ of every cluster calculated separately. The left columns are associated with the summer trajectories only (April to September). The right ones belong to the winter trajectories (October to March). For Kühlungsborn the cluster members for solution II are shown.

Chapter 7

Climatology of the vertical aerosol distribution

7.1 Kühlungsborn

by J. Schneider

At IAP Kühlungsborn, the measurement time of the German Lidar Network began on 1997-12-01 and ended on 2000-03-16, since a major reconstruction of the institute made lidar measurements impossible until the start of the follow-up project, EARLINET, on 2000-05-01. During the above time frame, the climatological measurements have been performed each Monday at noon and after sunset, and each Thursday at noon. From January 1^{st}, 2000, it was decided in the network to shift the Thursday measurements to after sunset. A statistical overview of all climatological measurements can be found in table 7.3.
In this analysis, only the after-sunset Raman measurements obtained in this time frame are included, since the Raman measurements allow the calculation of the backscatter coefficients down to the lowest lidar return signal. For the climatological analysis, we selected the cloud-free days out of the fixed measurement schedule mentioned above. We investigated planetary boundary layer heights and

Measurements 1997/12/01 – 2000/03/31						
months	possible measurem.	performed measurem.	perf./poss. measurem. [%]	class 1	class 2	class 1/ perf. meas. [%]
12/97 - 3/98	53	33	62.3	21	12	63.6
4/98 - 9/98	78	48	61.5	21	27	43.8
10/98 - 3/99	79	35	44.3	14	21	40.0
4/99 - 9/99	79	55	69.6	21	34	38.2
10/99 - 3/00	78	48	61.5	29	19	60.4
all	367	219	59.7	106	113	48.4
class 1 : measurement without low clouds possible class 2 : measurement with clouds below 2000 m						

Table 7.1: Overview of all climatological measurements performed at IAP Kühlungsborn during the time frame of the German Lidar Network.

monthly mean backscatter and extinction coefficients, the latter restricted only to altitudes above the boundary layer.

7.1.1 Measurements

7.1.1.1 Determination of the aerosol optical parameters

Calculation of the extinction coefficient $\alpha^{aer}(\lambda, z)$ from the Raman signals follows the method described in (Ansmann et al., 1990; Ansmann et al., 1992a). This method allows to determine the extinction coefficient independently, with the only necessary assumption of the wavelength dependence of the aerosol extinction coefficient $\alpha^{aer}(\lambda) \sim \lambda^{-k}$. Since the ratio between emitted and Raman shifted wavelengths is close to unity, deviations of this assumption do not contribute to significant errors. Observations indicate that *k* varies between 0 and 2 (Ferrare et al., 1998). For cirrus clouds, *k* equals zero (Ansmann et al., 1992a). Generally, $k = 1$ is assumed for all measurements except for cirrus clouds, where $k = 0$ is chosen. To obtain the nitrogen molecule number density and the Rayleigh scattering coefficient $\alpha^{mol}(\lambda, z)$, air temperature, density, and relative humidity are available from local radiosonde measurements, performed by the German Weather Service (DWD) on a regular basis. Radiosonde data are available at noon and midnight from two stations, one located 120 km east (Greifswald), the other located 150 north-west (Schleswig). Additionally, on certain occasions radiosondes can be launched at IAP Kühlungsborn. For days where no radiosonde data were available, the US Standard Atmosphere was used. In order to calculate the derivative $d/dz(\ln(PR^2))$, the received Raman signal has to be averaged in time and altitude. To reduce the influence of small scale variability, a minimum time interval of 30 minutes (approximately 54000 laser shots) was chosen in the German Lidar Network. Typical height intervals are: 200 m (4 channels) between 1 and 5 km, 500 m between 5 and 10 km, and 1000 m above 10 km. These values are subject to change dependent on the actual shape of the lidar return signal, the averaged time interval and thereby the total count rate. Since this technique is based on the absolute lidar return signal, it can only be applied above the height at which the laser beam and the telescope field-of-view fully overlap. This reduces our data to altitudes above 1 km, thereby excluding most of the boundary layer. Examples for extinction measurements are shown in Figure 7.1.
Once the aerosol extinction coefficient is known, the aerosol backscatter coefficient $\beta^{aer}(\lambda, z)$ can be determined from the ratio of the Rayleigh/Mie return signal and the Raman return signal, corrected for aerosol extinction and normalized at the reference altitude z_0 (Ansmann et al., 1992a). The reference height z_0 is usually chosen in a way that $\beta^{aer}(z_0) \ll \beta^{mol}(z_0)$. These conditions are found frequently in the upper troposphere around 6 to 8 km. Then $\beta^{aer}(z_0)$ is assumed to be zero for all wavelengths. As above, the molecular scattering coefficient $\beta^{mol}(\lambda, z)$ is calculated from the radiosonde data. The aerosol extinction coefficient at 355 and 1064 nm is extrapolated from the measurement at 607 nm with the chosen *k* value. Below the lowest measured value, the extinction coefficient is assumed to be constant. Since this method is based on the ratio of two signals, it can be applied also at altitudes where the laser beam and the telescope field-of-view do not fully overlap, i. e. below 1 km. Examples of aerosol backscatter measurements are given in Figure 7.1.

7.1.1.2 Error discussion

The error of the extinction coefficient is mainly determined by the statistical error of the Raman return signal. This error is assumed to be the square root of the absolute count rate and is calculated via the law of error propagation to the error in the extinction coefficient. As (Ansmann et al., 1992a) pointed out, a rapid change in the aerosol extinction coefficient during the averaged period induces a significant error in the mean extinction coefficient. To avoid such errors, only periods with approximately

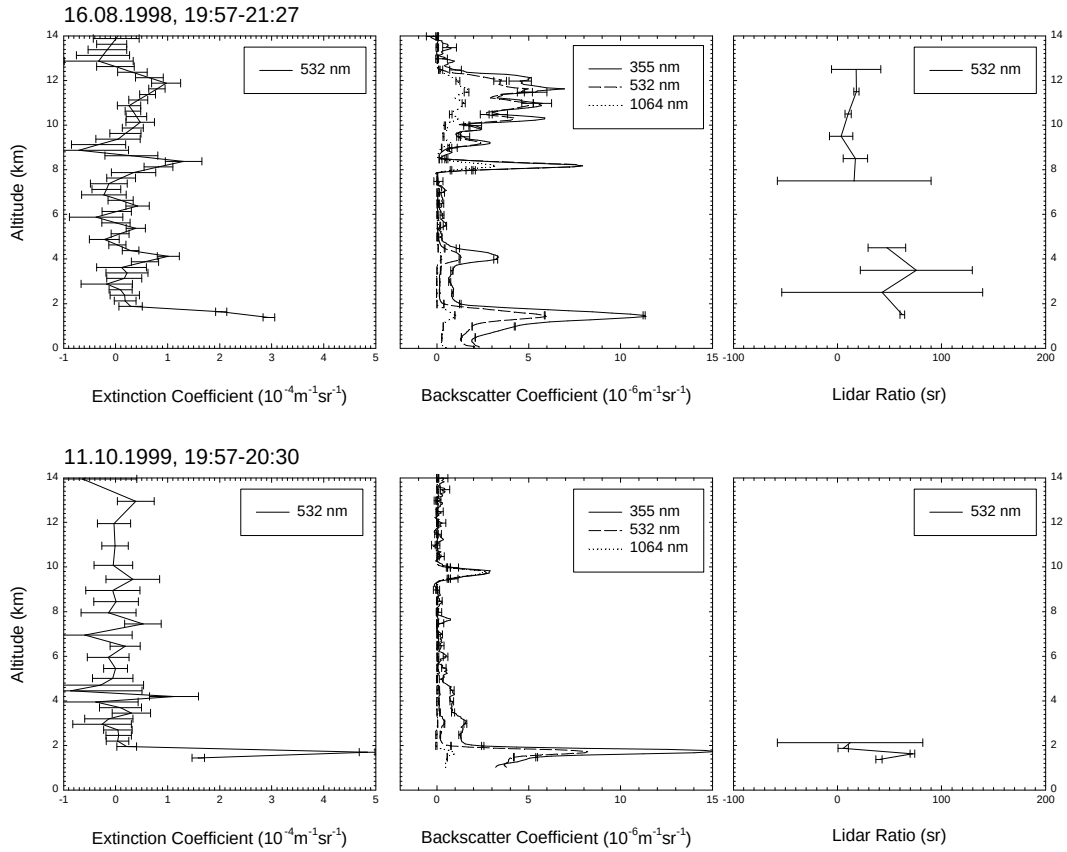

Figure 7.1: Examples for vertical profiles of extinction and backscatter coefficients. Upper panel: 98-08-16, 19:57-21:27 UT, lower panel: 99-10-11, 19:57-20:30. The extinction coefficient has been determined at 532 nm, while the backscatter coefficient can be calculated for 355, 532, and 1064 nm. On 98-10-11, the lidar ratio could only be determined below 2 km, due to the fact that the extinction coefficient is close to zero above.

constant aerosol backscatter signals have been averaged. The error of the backscatter coefficient is mainly determined by the chosen reference height and the chosen aerosol backscatter coefficient at this altitude (we chose zero at all measurements). The calculation of the backscatter coefficient needs the extinction coefficient as an input. Since no Raman signals are available for 355 and 1064 nm, the extinction coefficient measured at 532 is extrapolated with the chosen *k* value, which introduces an additional uncertainty. As mentioned above, the extinction coefficient is assumed to be constant below the lowest measured value (around 1 km), which causes an additional error, especially if the boundary layer height is very low. Although adjustable neutral density filters are placed in front of the photomultiplier tubes, it could not always been avoided that the photomultiplier used in the 1064 nm channel is overloaded by the strong backscatter signal from the boundary layer. This results in a too low signal in the boundary layer and also in the altitude range above, and the calculated backscatter coefficient can then turn out to be too low. This problem has first been observed during the instrument intercomparison (see chapter 4.2 for more details). Also the low Rayleigh scattering at 1064 nm, making it difficult to find a reference height with negligible aerosol content, can cause negative values at altitude regions with a very low aerosol content. In these cases the backscatter coefficient is regarded to be below the detection limit.

7.1.2 Results

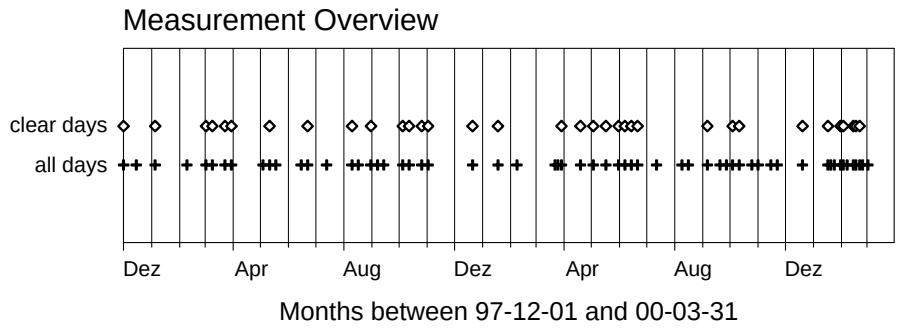

Figure 7.2: Overview of the climatological Raman measurements performed between 97-12-01 and 00-03-31 at IAP Kühlungsborn. Raman measurements were taken after sunset each Monday and, from 00-01-01 on, also each Thursday. "all days" denotes all performed measurements, "clear days" denotes all measurements without clouds below 5 km.

Figure 7.2 shows the annual distribution of Raman lidar measurements on the preselected days at IAP for the time period between December 1^{st}, 1997 and March 31^{st}, 2000. In total, of 137 possible measurement days (public holidays excluded), on 60 days Raman measurements have been performed. This corresponds to a percentage of 43.8%. On the other days, it was either raining or the possibility for rain was too high. On 34 days (24.8%), no clouds were present below 5 km. These days are attributed as "clear" days and will be used for the further aerosol analysis, in order to separate cloud top height and boundary layer height, and to assure that only aerosol properties are discussed.

7.1.2.1 Backscatter coefficients

Figure 7.3 shows the annual cycle of the aerosol backscatter coefficient at 532 nm for the "clear days" (no clouds below 5 km). The shown time period is 01.12.1997 - 31.03.2000. A running mean over 3 months was applied. The figure reveals an annual variability of the planetary boundary layer (PBL) height between 800 and 2000 m, with a minimum in winter and a maximum in summer. The maximum PBL height in 1998 is reached during months March through June, while in 1999, the maximum is between June and October. However, no "clear" measurements have been possible in July and August 1999. White areas indicate that the backscatter coefficient was below the detection limit of $10^{-9}m^{-1}sr^{-1}$, which may be caused by overload of the photomultiplier or by a incorrectly chosen reference point. For the following analysis, the PBL height was defined as that altitude where the aerosol backscatter coefficient (532 nm) decreased to 50% of the mean value below, as shown in Figure 7.4.
Figure 7.5 shows the annual cycle of the PBL height for the "clear days", The data points represent monthly means between 97-12-01 and 00-03-31. A curve fit to the data points is also shown, indicating the maximum of the PBL height to be around the beginning of August (around the 1^{st}) while the minimum is in the mid of February (17^{th}), corresponding to a mean phase shift of about 50 days with respect to the summer/winter solstices. The calculated period *b* of the oscillation is 10.8 ± 1.7 months, which means that the annual cycle can be reproduced, but that the statistic up to now is still rather sparse. Here, it has to be reminded that these data can not be assumed to be representative for the maximum PBL height during the day since these measurements were taken after sunset. In general, the PBL height reaches its maximum around 14:00 local solar time and decreases later through the

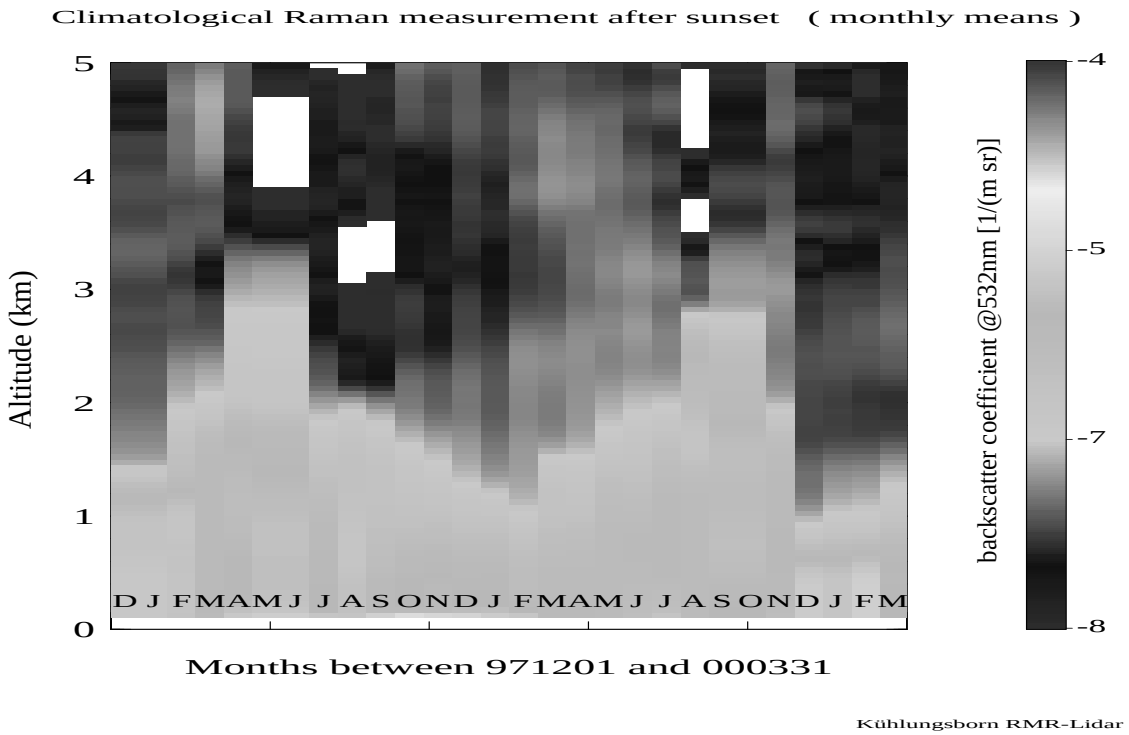

Figure 7.3: Annual cycle of aerosol backscatter coefficient at 532 nm, cloudless days only. Shown are monthly mean values. White areas indicate values below the detection limit.

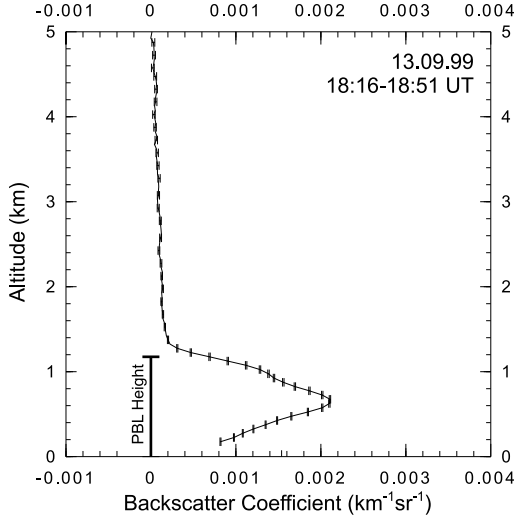

Figure 7.4: Example for the definition of the PBL height as defined in this work: The altitude z where the mean backscatter coefficient decreases to half on the mean value between the lowest measurement level and z. To determine the PBL height, the data measured at 532 nm have been used.

day, but there are also occasions on which the PBL continues growing throughout the day, as is shown in Figure 7.6, where a diurnal cycle of backscatter coefficients is shown.
During daytime, when no Raman signals are available, we can not calculate the backscatter coefficients below the altitude of full overlap between laser beam and field-of-view of the glass fibre (> 1000 m). That means, we can determine the height of the boundary layer, but not the true values for the backscatter coefficients. For figure 7.6 the backscatter coefficient was assumed to be constant

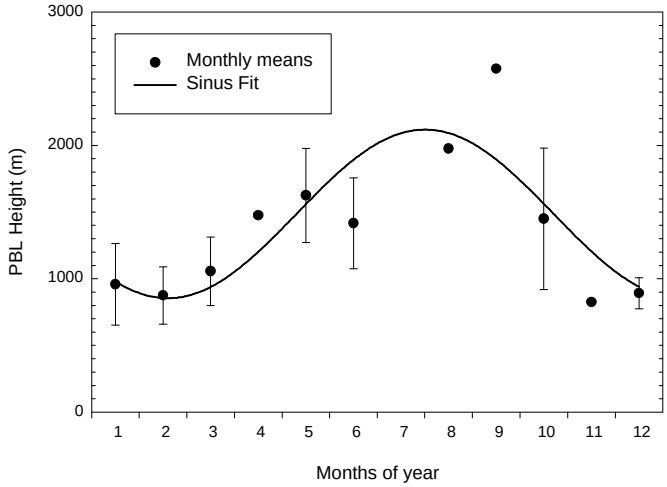

Figure 7.5: Annual cycle of the monthly mean planetary boundary layer height, inferred from the backscatter coefficient at 532 nm for the "clear days". Monthly means between 97-12-01 and 00-03-31 are shown. The bars denote standard deviations, data points without bars represent one single measurement during this month. The fit curve represents a least-squares fit of the function $y = y_0 + a\sin((2\pi/b)x + c)$.

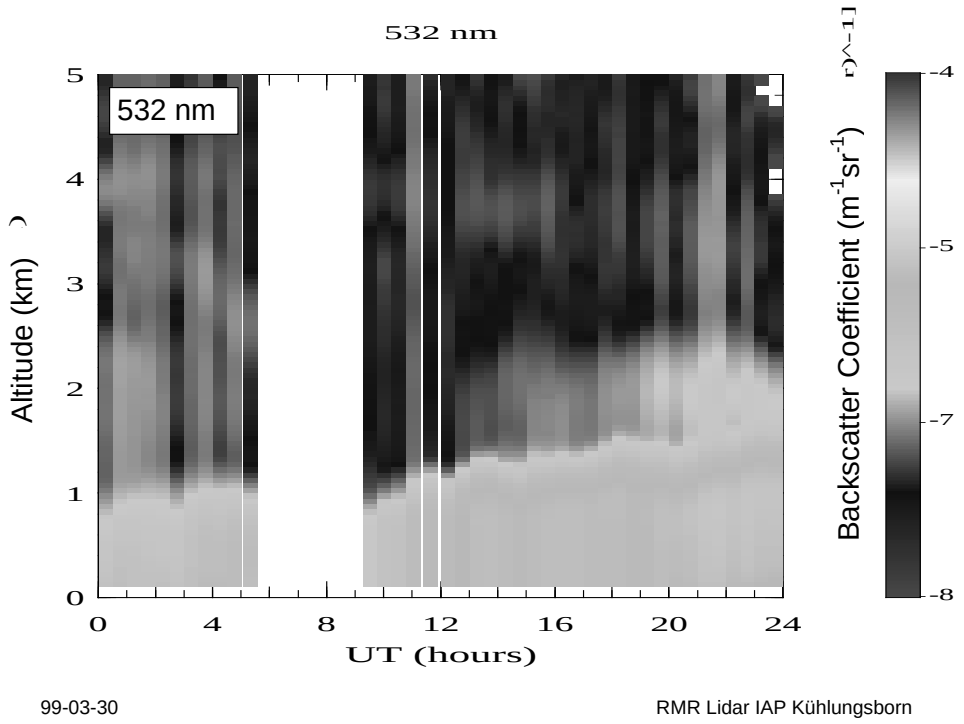

Figure 7.6: Diurnal cycle of the aerosol backscatter coefficient at 532 nm measured on March 30, 1999. This day is an example for a steadily increasing boundary layer during a stable high pressure period.

below the lowest measured value.
The backscatter coefficients in and above the PBL do not show a signifcant annual cycle. Mean values

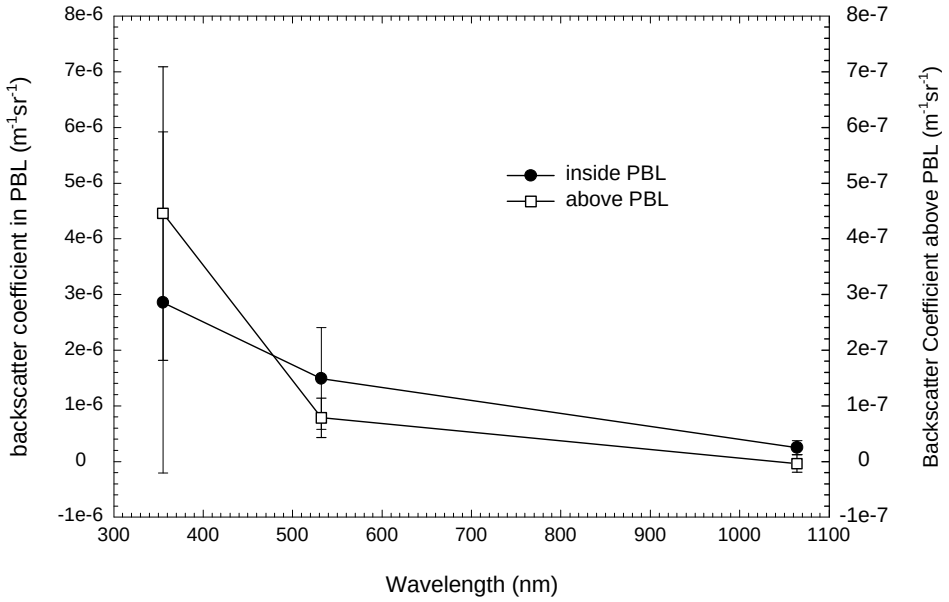

Figure 7.7: Spectral dependence of mean backscatter coefficients inside and above the PBL. The right scale is expanded by a factor of 10 compared to the left scale.

	$\overline{\beta}_{355}(m^{-1}sr^{-1})$	$\overline{\beta}_{532}(m^{-1}sr^{-1})$	$\overline{\beta}_{1064}(m^{-1}sr^{-1})$	$\overline{\alpha}_{532}(m^{-1})$	$\overline{AOD}_{532}$	$\overline{LR}_{532}(sr)$
In PBL	$(2.9 \pm 3.1) \times 10^{-6}$	$(1.5 \pm 0.9) \times 10^{-6}$	$(2.5 \pm 1.2) \times 10^{-7}$	–	–	–
Above PBL	$(4.5 \pm 2.6) \times 10^{-7}$	$(7.8 \pm 3.5) \times 10^{-8}$	$(-0.4 \pm 1.6) \times 10^{-8}$	$(3.5 \pm 7.2) \times 10^{-6}$	$(1.2 \pm 0.3) \times 10^{-2}$	44 ± 94

Table 7.2: Mean Values of Backscatter and Extinction Coefficients and Lidar Ratio in and above the PBL for the 2-year period 97-12-01 and 99-11-30.

were calculated using only the period from 97-12-01 to 99-11-30, in order to have two complete years. The values are summarized in table 7.1.2.1 and plotted vs. wavelength in Figure 7.7. The vertical axis for the values above the PBL is stretched by a factor of 10 compared to the axis for the values in the PBL, indicating that, inside the error limits for both data sets, the backscatter coefficients in the PBL are at higher by approximately a factor of 10 than above. Comparing our data with those given by (Müller et al., 1998), who report aerosol backscatter coefficient measured at Leipzig, Germany, in and above the PBL, the values obtained inside the PBL agree quite well, while our values above the PBL are lower by at about a factor of two than those reported by (Müller et al., 1998). However, since (Müller et al., 1998) are showing only one single measurement, and our data are mean values over two years, this discrepancy is not severe.

7.1.2.2 Extinction coefficients

Figure 7.8 shows the mean extinction coefficient measured between the PBL and 5 km along with the optical depth in this altitude region. Again, only the time period between 97-12-01 and 99-11-30 was considered. The negative values are most likely due to a wrong estimation of the Rayleigh scattering coefficients, which can be explained by the fact that the radiosondes from which the temperature and pressure data have been used have been launched about 100 km off our measurement site, or, if no radiosonde data were available, the US Standard Atmosphere has been used. For the mean value of

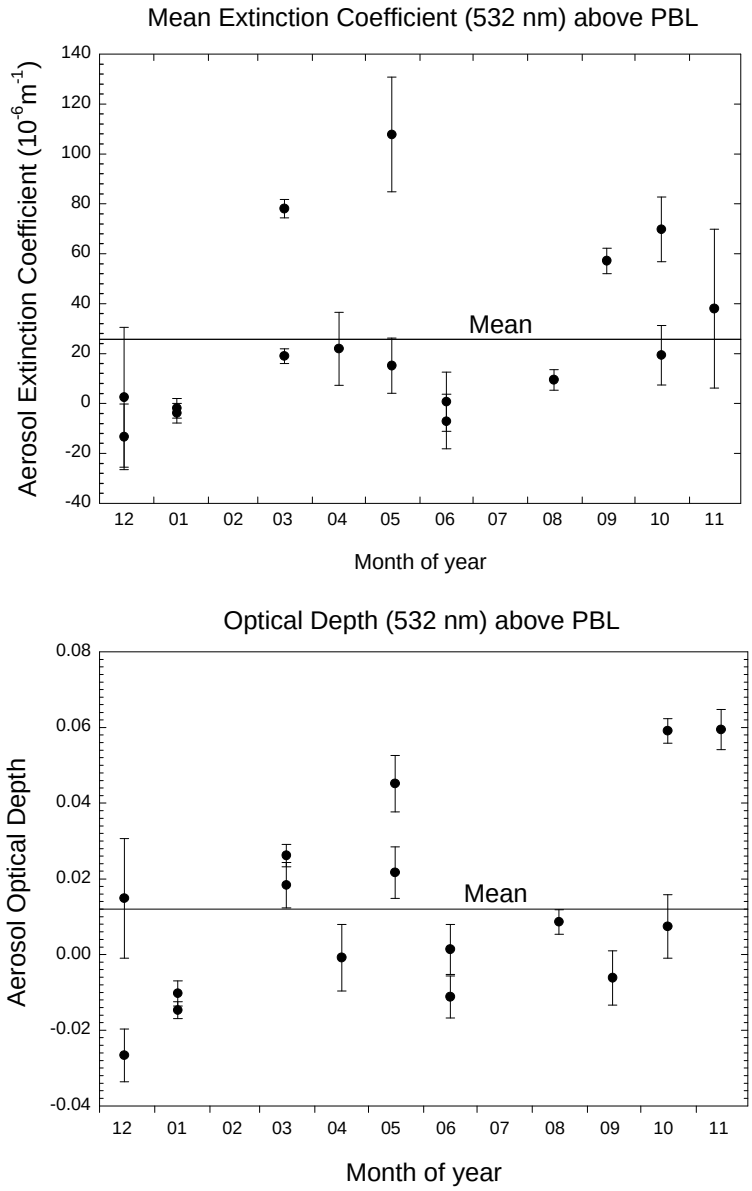

Figure 7.8: Mean extinction coefficient and optical depth at 532 nm between boundary layer and 5 km. Only the time period between 97-12-01 and 99-11-30 was considered.

the extinction coefficient see table 7.1.2.1. The mean aerosol optical depth (AOD) obtained above the PBL, as shown in the lower panel of Figure 7.8, yields a mean value of $(1.2 \pm 0.33) \times 10^{-2}$. This value, which is comparable to the value of 0.012, which is obtained from the Global Aerosol Data Set (GADS) (Hess et al., 1998), implies that the contribution of the middle free troposphere (well below the tropopause but above the boundary layer) on cloudless days can almost be neglected when discussing total AOD. AOD values over Central Europe at 555 nm, obtained from satellite data, range between 0.1 and 0.6 (Gonzales et al., 2000). AOD values obtained for the planetary boundary layer at the Atlanctic coast of the U.S. at 450 nm are in the same order of magnitude (Hartley et al., 2000).

7.1.2.3 Implication for lidar ratios

Due to the large variations especially in the extinction coefficient, the standard deviation of the mean lidar ratio above the PBL (table 7.1.2.1) is more than 100% of the mean value itself. Although the mean value of 44 sr is a very reasonable value for continental and maritime aerosol (Ackermann, 1998), and also for the "free tropospheric" aerosol component in the Global Aerosol Date Set (Hess et al., 1998), the variability of our data is too high to draw any conclusions. The values inside the PBL (see Figure 7.1) are much better, but since the PBL height has been frequently below our lower measurement altitude, extinction could not be determined inside the PBL except for a few cases. This problem has been solved in the meantime by installing an additional telescope with short focal length to detect also the Raman signal from inside the boundary layer.

7.1.2.4 Trajectory analysis

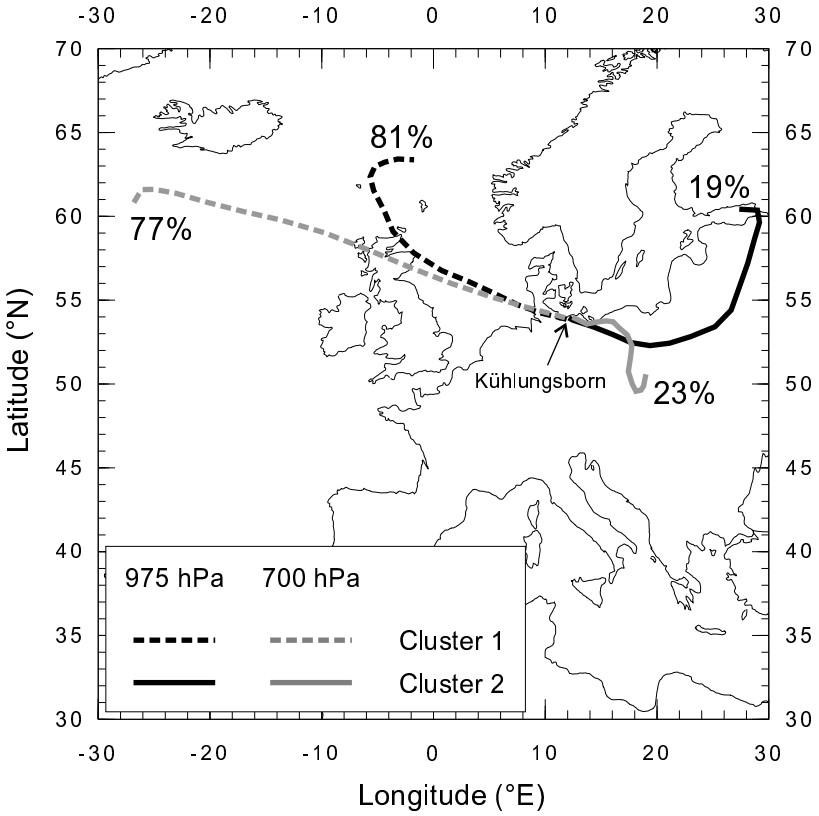

Figure 7.9: Map of central Europe, showing the results of the cluster analysis of the backward trajectories arriving above Kühlungsborn (54N, 12 E) at 19:00 UT on the measurement days. 2 arrival heights are shown. Gray lines: 975 hPa (inside PBL), black lines: 700 hPa (above PBL). The numbers give the percentage of trajectories contained in the individual clusters.

The lidar station Kühlungsborn is located at the southern shore of the Baltic Sea, west (30 km) of the city of Rostock, and east (150 km) of the city of Hamburg. Thus, we would expect the aerosol properties to be dependent on the wind direction. To obtain information about the origin of the air masses, the 3-dimensional backward trajectories provided by the German Weather Service (DWD)

were analysed by means of cluster analysis. The cluster algorithm used here is similar to that described in chapter 6 and will be discussed in detail in (Eixmann, 2001). In contrast to the analysis has been performed for the “clear” days within the 2-year period between 97-12-01 and 99-11-30. For 26 out of 28 “clear” measurement days during this time frame, trajectories were available. Two trajectory arrival heights above Kühlungsborn of 975 hPa (corresponding to 300 m, certainly in the PBL) and 700 hPa (corresponding to 3000 m, always above the PBL), and the last four days prior to the arrival of the air mass above Kühlungsborn were considered. At both altitude levels, it was possible to represent all trajectories with 2 clusters. Figure 7.9 shows the two dominating trajectory directions for both altitudes. At both levels cluster 1, containing the trajectories coming from the north-west, is dominating with 77% and 81%, respectively, of all trajectories contained in this cluster. At 975 hPa, the northern direction predominates, while at 700 hPa, more trajectories arrive from further west. Cluster 2 contains the eastern components, at 700 hPa originating from south-east, and at 975 hPa coming from north-east. The length of the clusters displayed are 4 days, indicating that the air masses were travelling at higher wind speeds when coming from the west, especially at 700 hPa. In order to find out if a difference in the aerosol properties dependent on the origin of the air masses exists, the backscatter coefficients measured on the days contained in the 2 clusters for both arrival heights were averaged. Figure 7.10 shows the result for 532 nm: no difference can be found in the absolute values of the backscatter coefficient, which implies that the total aerosol load is almost the same, regardless of the origin of the air masses.

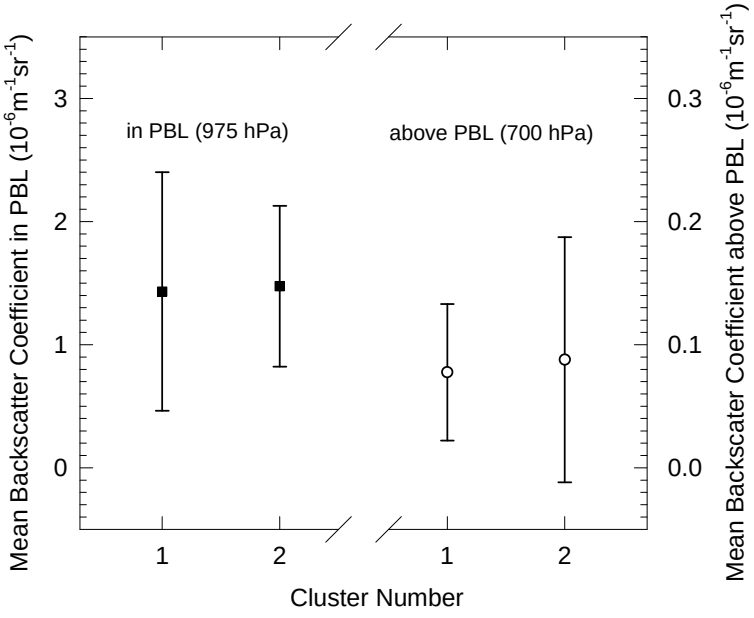

Figure 7.10: Mean aerosol backscatter coefficients at 532 nm measured in the individual clusters given in Figure 7.9. No significant differences in the aerosol load can be found between air masses originating from the east and the west.

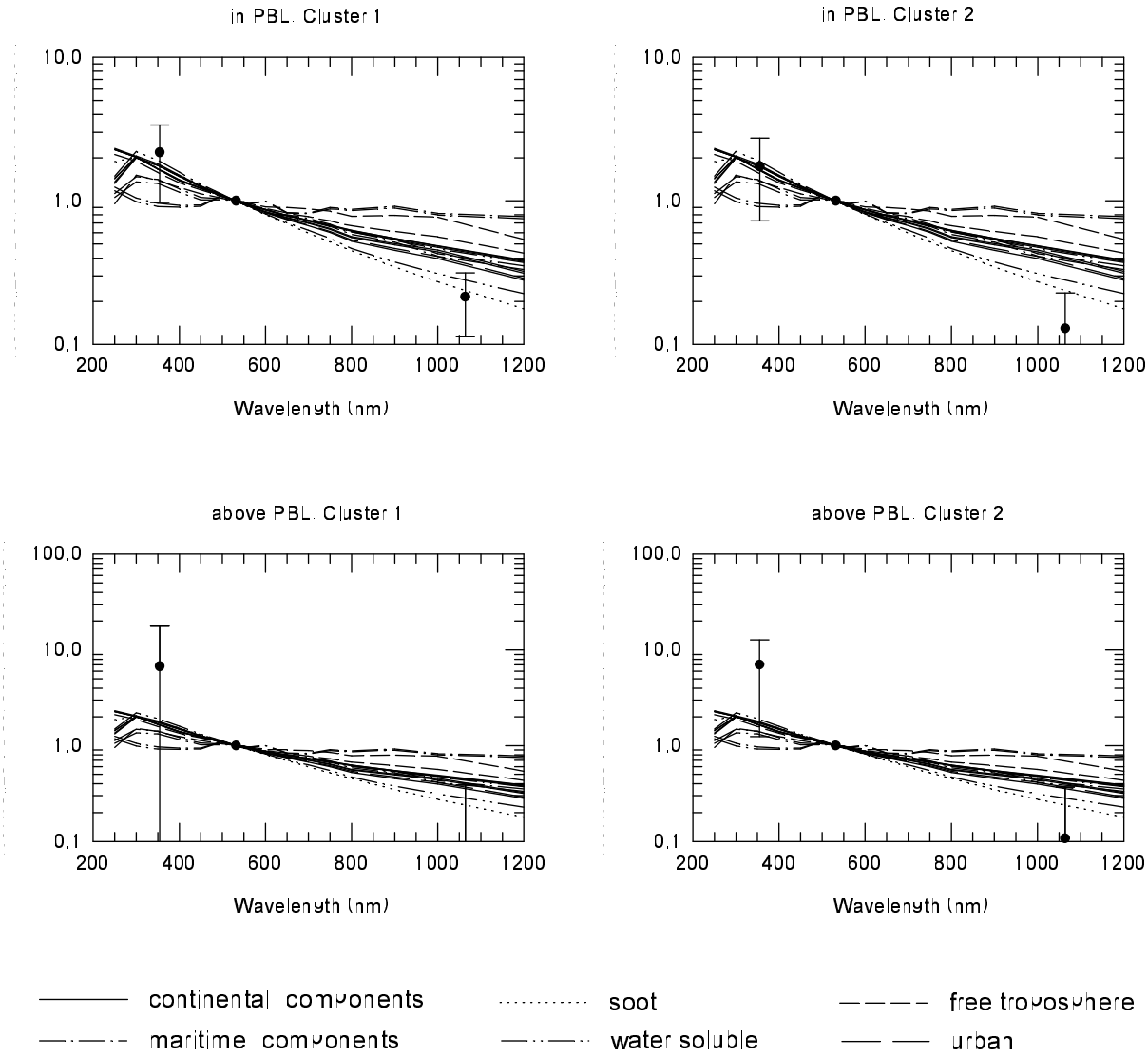

Figure 7.11: Backscatter coefficient measured in the individual clusters given in Figure 7.9 normalized at 532 nm, along with selected aerosol types and components from the Global Aerosol Data Set (GADS). For details see text.

7.1.2.5 Comparison with the Global Aerosol Data Set

In order to analyse the wavelength dependence, the data from the individual clusters have been normalized to the value at 532 nm. The result is given in Figure 7.11. The error bars indicate the standard deviation, which is zero at 532 nm due to the normalization. Also shown in Figure 7.11 are calculated backscatter coefficients for different aerosol types taken from the software package OPAC (Optical Properties of Aerosols and Clouds), which based on the Global Aerosol Data Set (GADS). Both are freely available on the World Wide Web (Hess et al., 1998). In this data set, the large variability of natural aerosols is reduced by the use of a dataset of typical aerosol components. The size of the individual particles in the OPAC software package is controlled by the relative humidity. We selected from this dataset those aerosol types and components which are likely to be observed at our station, for example “continental”, “maritime”, “free tropospheric”, at their minimum and maximum relative humidities, and compared their calculated backscatter coefficients with our measurements. These backscatter coefficients were also normalized to the measured value at 532 nm. The values measured

inside the PBL in the air masses originating from the west (cluster 1) match only with the smallest aerosol components, “soot” and “water soluble” at the lowest relative humidity (0%). The mode radii of the particle size distributions of these components are 11.8 nm and 21.2 nm, respectively. The values of cluster 2 do not even fit to these two aerosol components. Between 355 and 532, all selected aerosol components are in agreement with our data. The aerosol components “continental”, divided into the subgroups “clean”, ”average” and ”polluted”, represented by the straight lines, would fit to both clusters if the measured value at 1064 nm would be somewhat higher. This finding may suggest that the measured backscatter coefficient at 1064 nm is too low, which, as discussed above, can be caused by overload of the photomultiplier tube. The difference between the aerosol contained in cluster 1 and cluster 2, however, is very small and can not regarded to be significant. The “maritime” aerosol, represented by the dash-dotted lines, shows a weak wavelength dependence that fits slightly better to the 355 and 532 nm data of cluster 2, but then the 1064 nm value would have to be underestimated by at least a factor of 4, which we consider to be rather unlikely. For the values obtained above the PBL the standard deviation at 355 nm is very large in cluster 1, so that all aerosol types fit to the data. Also here the 1064 nm coefficient is very low, although more aerosol types fit through the range of the given standard deviation. A significant difference between the 2 clusters can not be found. The “free tropospheric” aerosol components from the GADS (dashed lines) would fit the data only with a higher experimental value at 1064 nm.

7.1.3 Summary and conclusions

We have presented two complete annual cycles of vertical aerosol profiles between 0 and 5 km, and thereby also the annual cycle of the planetary boundary layer height. Mean values for the aerosol backscatter coefficients in and above the PBL are given for 355, 532, and 1064 nm. Values at 1064 have to be taken with care, as they can suffer from photomultiplier overload. The backscatter coefficients above the PBL are significantly lower (by about a factor of 10) than the values inside the PBL. Since the planetary boundary layer has also a diurnal cycle, and our data represent night-time data (taken between sunset and midnight) they will not represent the maximum boundary layer height at our lidar site. The annual cycle, however, is reproduced very well by these after-sunset measurements. The extinction coefficient could only be determined above the PBL for 532 nm. The inferred optical depth agrees with the value expected from the Global Aerosol Data Set. A trajectory cluster analysis performed on 4-day backward trajectories did not reveal a significant difference in the aerosol load with respect to the dominating wind directions (north-west and east). The comparison with the Global Aerosol Data Set (GADS) showed that our measured aerosol backscatter coefficient at 1064 nm does not agree with most of the expected aerosol types. Our measured value is much lower than calculated for the assumed size distributions in the GADS. This may have two reasons: firstly, our measurement at 1064 may be systematically too low, or secondly, the GADS overestimates the backscatter coefficients in the near infrared. The latter may be due to the use of lognormal size distributions, thereby overestimating the amount of larger particles which increases the backscatter values in the infrared. A systematic error in our measurements may occur by overload of the photomultiplier, as discussed above. Above the PBL, where values are close to the detection limit, this may induce a large error, but from Figure 11 it reveals, that the greatest discrepancy was found for data obtained inside the PBL. Future measurements and analyses will have to include the extinction coefficient at at least a second wavelength, in as well as above the PBL, and also the daytime data to fully record the PBL development. For this purpose, better input data for the lidar ratio are required.

7.2 Hamburg

by V. Matthias

7.2.1 Boundary layer aerosol

Regular aerosol lidar measurements started in Hamburg on December 1st 1997. Three times a week, measurements have been performed, two of them were afternoon measurements of elastic backscatter at 351 nm, once a week around sunset also aerosol extinction profiles have been determined using the Raman technique.
In table 7.3 the measurement statistics can be seen. For this statistics, only measurements from days for routine measurements with lowest clouds in about 800 m were taken. These measurements were divided into two classes. Class 1 means that an aerosol backscatter measurement without clouds or only with clouds in altitudes above 2 km could be taken. Sometimes, even very small gaps in between clouds are sufficient for a backscatter profile. So all cases without clouds and those with at least small cloud gaps are named "cloudfree". In class 2, cloud coverage was present during the whole measurement period with clouds were at altitudes below 2000 m. During the almost three years from December 1st 1997 to October 31st 2000, 276 routine measurements could be made which is ca. 63 % of all possible measurements. On the other days, no measurements were possible due to rain or low clouds, due to technical problems or because the lidar system was located in Lindenberg for the intercomparisons. The intercomparison time has not been included in the number of possible measurements between April and September 1998. In July and October 1999, the used excimer laser was broken for about three weeks each time, which is one of the reasons for the relatively small number of measurements during winter 1999/2000. In the other cases mainly bad weather prevented lidar measurements.
From all performed measurements, in only 16 % of the cases complete cloud coverage below 2000

Measurements 1997/12/01 – 2000/10/31						
months	possible measurem.	performed measurem.	perf./poss. measurem. [%]	class 1	class 2	class 1/ perf. meas. [%]
12/97 - 3/98	53	31	58.5	20	11	64.5
4/98 - 9/98	55	43	78.2	35	8	81.4
10/98 - 3/99	79	48	60.8	35	13	72.9
4/99 - 9/99	79	58	73.4	54	4	93.1
10/99 - 3/00	78	42	53.8	38	4	90.5
4/00 - 9/00	78	48	61.5	45	3	93.8
10/00	14	6	42.9	6	0	100.0
all	436	276	63.3	233	43	84.4

Table 7.3: Measurement statistics for the MPI Hamburg on the basis of calculated backscatter profiles on routine measurement days (Monday afternoon and evening, Thursday afternoon). Class 1 summarizes all cases where measurement without low clouds were possible, class 2 all measurements with complete cloud coverage below 2000 m.

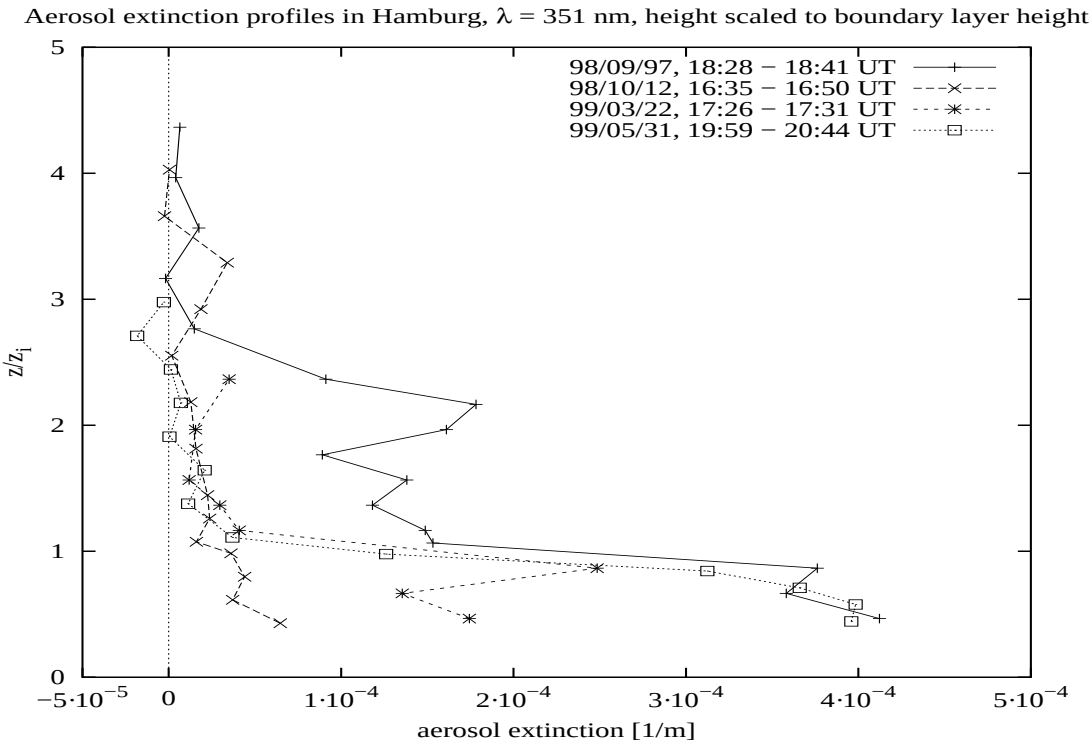

Figure 7.12: Examples of aerosol extinction profiles measured in Hamburg in 1998 and 1999. The height z is scaled to the boundary layer height z_i.

m was present. These measurements have to be handled carefully, since a correct calibration of the backscatter profile is very difficult, if a region of the atmosphere with very low aerosol content cannot be reached. This is on the other hand not true for the aerosol extinction measurements with the Raman method, which are not dependent on calibration and can also be taken during complete cloud coverage.

In almost all cases, the aerosol backscatter or extinction could be measured within the planetary boundary layer. Within this layer, highest aerosol concentrations can be found since this layer has per definition contact to the ground and almost all aerosol sources are at ground level. In only two cases, the top of the boundary layer was below the lowest measurement height, which is ca. 600 m for extinction profiles and 400 m for backscatter profiles. These cases have not been used for the statistics.

Separate statistics have been made for aerosol backscatter and aerosol extinction measurements. During the first two years, extinction profiles have been taken once a week on Monday evening. Starting in January 2000, measurements have been made also on Thursday evening to get a better statistics. 92 extinction profiles are forming the basis for the statistics. Since these measurements do not need to be calibrated in an aerosol free region, the statistics includes measurements out of both defined classes, also those with low clouds.

For the 92 extinction profiles, the average aerosol extinction in the boundary layer has been calculated by integrating the aerosol extinction up to the top of the boundary layer (which gives the aerosol optical depth) and then dividing the optical depth by the boundary layer height. The lowest extinction value was assumed to be representative down to the ground. This is the best possible assumption, since the boundary layer is still fully developed at sunset. Only turbulence has decreased and no further mixing can be observed.

Out of the backscatter measurements performed on routine observation days, only the afternoon

measurement has been taken for the statistics. If on some days, only evening measurements were possible due to bad weather in the afternoon, these measurements have additionally been taken. On the other hand, all measurements under low cloud conditions have been sorted out due the high errors that are connected with the calibration under those conditions. In summary, 164 measurement days could be used for the statistics, which is 54 % of all possible days within the almost three years. This is the same value as the quotient of all class 1 measurements to all possible measurements.
Average aerosol backscatter values have been determined in a similar manner taking the integrated aerosol backscatter up to the top of the PBL and then dividing by the PBL-height. Looking at these measurements, one has to have in mind, that the calculated aerosol backscatter profile depends on the chosen lidar ratio, which is not known without additional extinction measurement. Most of the used afternoon backscatter profiles have therefore been calculated with a lidar ratio of 50 sr, a quite typical value in northern Germany (see section 7.2.3).

Fig. 7.12 gives examples of aerosol extinction profiles derived with the Raman method. The profiles

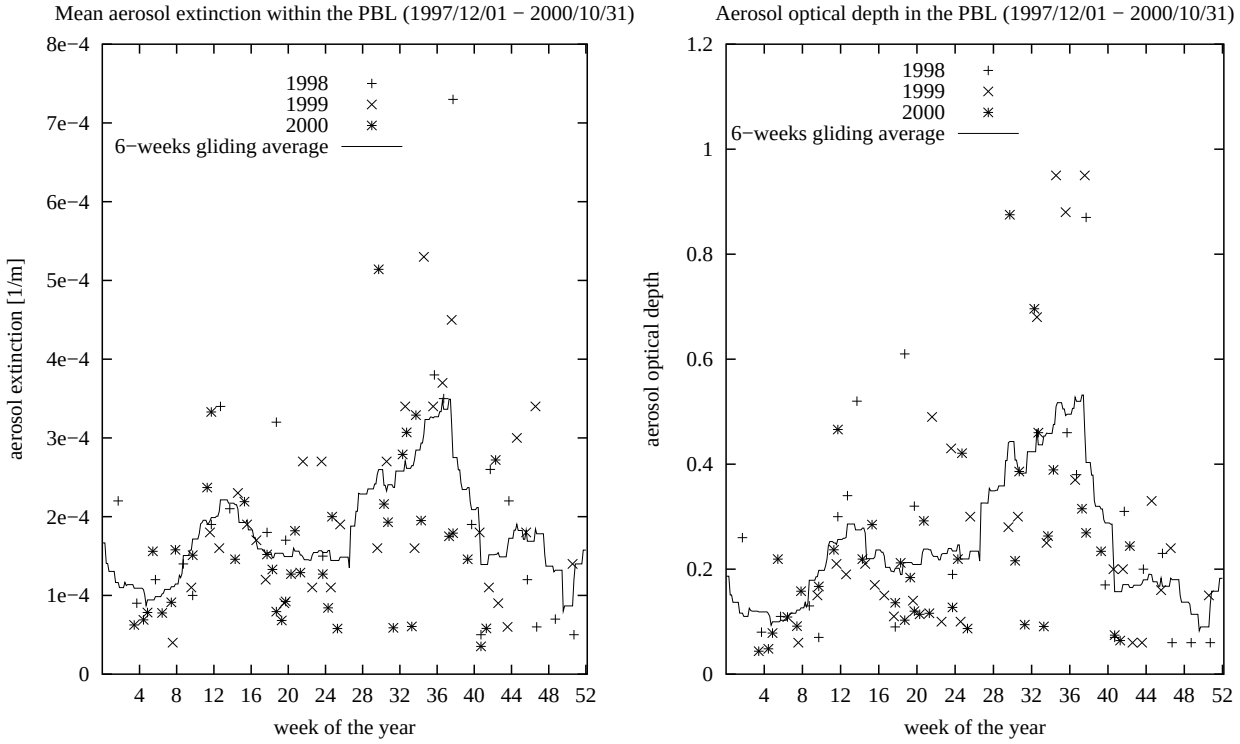

Figure 7.13: Annual cycle of the average aerosol extinction and the optical depth in the boundary layer in Hamburg taking data from 1997/12/01 to 2000/10/31.

are scaled in height to the top of the boundary layer z_i which can be clearly seen in the lidar signal and in the aerosol profiles. In most cases, the aerosol extinction in the boundary layer is much higher than above it. However in 14 cases within the three years of measurements, a second aerosol layer above the boundary layer could be seen, e.g., on September 7th, 1998, in Fig. 7.12.
The annual cycle of the mean aerosol extinction in the boundary layer in Hamburg on the basis of 92 measurements from December 1st 1997 to October 31st 2000 can be seen in fig. 7.13. A six-week gliding average was also plotted, showing only small variations in the gliding average between October and June with a not very pronounced “spring maximum” in April. In the late summer, between July and September, the avearge aerosol extinction in the PBL is remarkably higher than during the rest of the year, with a maximum in September with values roughly twice the average of the other months. However these high values refer mostly to very high values in September 1999,

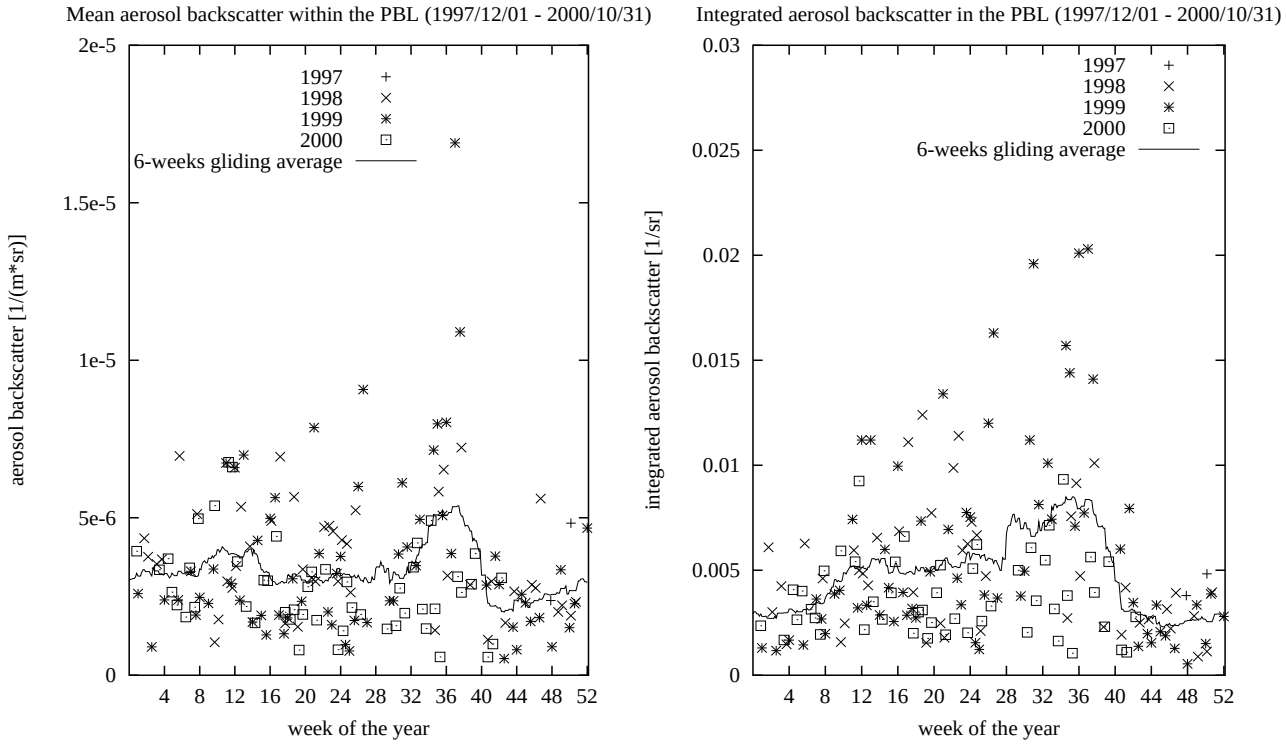

Figure 7.14: Annual cycle of the average aerosol backscatter and the integrated aerosol backscatter in the boundary layer in Hamburg taking data from 1997/12/01 to 2000/10/31.

which was exceptionally hot and dry in Hamburg. So since only three years of measurements could be taken for this figure, this feature is still of high uncertainty. Further measurements will be taken at least up to the end of 2002 within the project “A European aerosol research lidar network to establish an aerosol climatology - EARLINET”. That will give a much better data basis.
In fig. 7.13 one additionally recognizes slightly lower values in winter than in summer and a wide spread of measured values during the whole year. Very low extinction values can appear in summer months as well as in winter months. On the other hand, very high values are mostly limited to April - September.

The annual cycle of the optical depth (fig. 7.13, right side) is more pronounced than that of the average extinction. This is due the inclusion of the boundary layer height which is in winter generally much lower than in summer. The other features remain the same.
Looking at the annual cycle of the aerosol backscatter, the picture is very similar. The average aerosol backscatter in the boundary layer shows only small seasonal variations with a maximum in late summer and a less pronounced maximum in early spring. Again remarkable is the wide spread of values with maximum values occuring in summer. The integrated aerosol backscatter, which is defined analog to the optical depth, shows a clearer annual cycle since PBL heights are much smaller in winter than in summer.
Fig. 7.15 displays the PBL-height determined from the afternoon backscatter measurements. The gliding average shows a maximum of ca. 2000 m in mid summer and a minimum of ca. 900 m in mid winter. The sinus fit shows almost no phase shift, highest PBL can be expected around July 1st, lowest around January 1st. The real PBL-height can of course be very different from those statistical values. The standard deviation of the average value of 1510 m is 599 m (40%).
These aerosol extinction and backscatter values have been analyzed statistically. The cumulative frequency distribution (fig. 7.16) shows that the distribution is not Gaussian. It has positive skewness

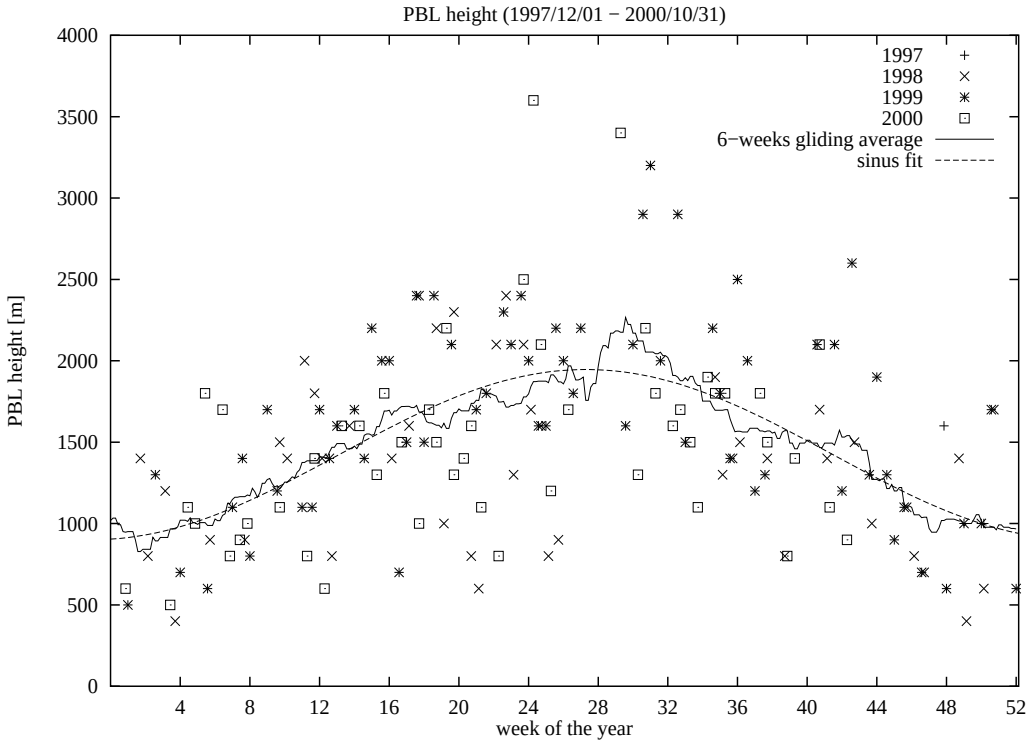

Figure 7.15: Planetary boundary layer heights derived from 164 aerosol backscatter measurements between 1997/12/01 to 2000/10/31. Also shown is a 6 weeks gliding average and a sinus fit which shows a phase shift of -7 days.

with high values being more frequent than low ones, as is typical for many meteorological quantities with only positive values. The characteristic quantities of the distribution are displayed in table 7.4

aerosol extinction				
category	μ $[10^{-4}\mathrm{m}^{-1}]$	σ $[10^{-4}\mathrm{m}^{-1}]$	γ	median $[10^{-4}\mathrm{m}^{-1}]$
97/12/01 - 00/10/31	1.87	1.21	1.59	1.65
1998	2.05	1.50	1.87	1.95
1999	2.09	1.18	0.91	1.85
2000 (1-10)	1.60	1.00	1.34	1.50
summer	2.21	1.35	1.49	1.85
winter	1.47	0.86	0.78	1.25
optical depth				
category	μ	σ	γ	median
97/12/01 - 00/10/31	0.28	0.23	1.57	0.205
1998	0.26	0.21	1.30	0.195
1999	0.30	0.25	1.58	0.205
2000 (1-10)	0.23	0.18	1.78	0.185
summer	0.34	0.25	1.18	0.27
winter	0.16	0.10	0.83	0.155

Table 7.4: Characteristic quantities of the frequency distribution of the aerosol extinction (in $10^{-4}\mathrm{m}^{-1}$) and the optical depth in the boundary layer in Hamburg. It has been distinguished between the years and between summer and winter. μ: average, σ: standard deviation, γ: skewness.

aerosol backscatter				
category	μ $[10^{-6}(\mathrm{m}\cdot\mathrm{sr})^{-1}]$	σ $[10^{-6}(\mathrm{m}\cdot\mathrm{sr})^{-1}]$	γ	median $[10^{-6}(\mathrm{m}\cdot\mathrm{sr})^{-1}]$
97/12/01 - 00/10/31	3.37	2.15	2.20	2.90
1998	3.64	1.63	0.47	3.20
1999	3.64	2.79	2.14	2.60
2000 (1-10)	2.79	1.39	0.85	2.70
summer	3.62	2.47	2.19	3.10
winter	3.04	1.56	0.81	2.80
integrated backscatter				
category	μ $[10^{-3}\mathrm{sr}^{-1}]$	σ $[10^{-3}\mathrm{sr}^{-1}]$	γ	median $[10^{-3}\mathrm{sr}^{-1}]$
97/12/01 - 00/10/31	5.00	3.79	1.80	3.90
1998	4.88	2.95	0.82	4.30
1999	6.04	4.99	1.31	3.90
2000 (1-10)	3.79	1.91	0.92	3.30
summer	6.18	4.34	1.38	5.00
winter	3.41	2.03	1.35	3.10

Table 7.5: Characteristic quantities of the frequency distribution of the aerosol backscatter (in $10^{-6}(\mathrm{m}\cdot\mathrm{sr})^{-1}$) and the integrated backscatter (in $10^{-3}(\mathrm{sr})^{-1}$) in the boundary layer in Hamburg. It has been distinguished between the years and between summer and winter. μ: average, σ: standard deviation, γ: skewness.

(for extinction) and table 7.5 (for backscatter). One recognizes very similar averages in the years 1998 and 1999 and lower values in 2000. This holds also for the optical depth and the integrated backscatter.
The standard deviation of the individual measurements is quite high. This represents the fluctuations in aerosol extinction and backscatter which can occur in quite short time intervals of a few hours. As the cumulative frequency distributions (fig. 7.16 and 7.17) show, the distribution is not Gaussian and the skewness is always positive with values up to 2.20. Therefore, the median represents much more the values one can expect than the mean does. It is between 10 and 20 % lower than the mean.
Part of the variability can already be explained by distinguishing between two seasons only, October to March and April to September. The lower values of the aerosol extinction and backscatter in winter can be seen in the mean and the median. Since very high aerosol extinction is measured mainly in summer, the skewness and the standard deviation of both semi-annual distributions are reduced compared to the overall distribution. This is especially significant for the integrated values and in winter, the standard deviation of the summer backscatter values is even little higher than the overall standard deviation.

7.2.2 Analysis of source regions

Of course the separation into two seasons only is rather coarse, but as the individual values in the annual cycle already showed, the aerosol load can change totally from day to day. This depends mainly on the origin of the air mass. Therefore, an analysis of the origin of the probed air mass has been made using back-trajectories calculated by the German Weather Service for all partners within the German Lidar Network. This analysis has been restricted to aerosol extinction measurements. These values are much more reliable than the backscatter values because no calibration has to be

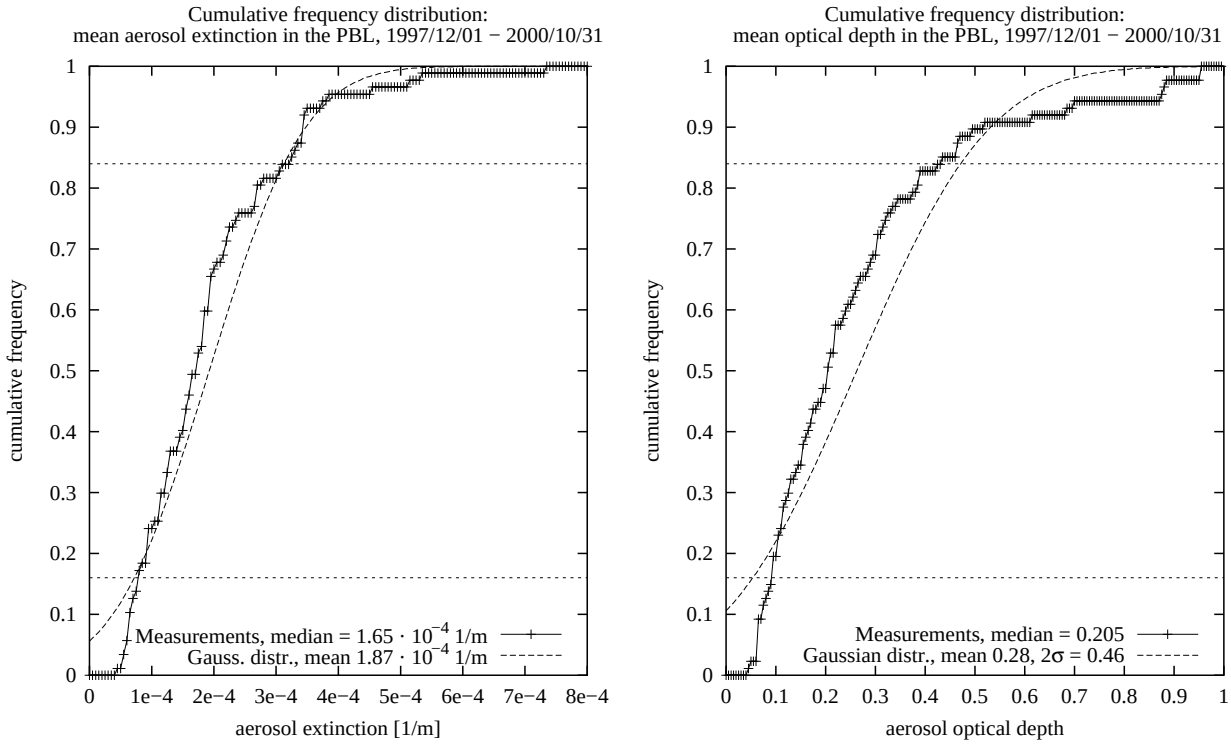

Figure 7.16: Cumulative frequency distribution of the mean aerosol extinction (left side) and the optical depth (right side) in the boundary layer in Hamburg including data from 1997/12/01 to 2000/10/31. For extinction the medain is $1.65 \cdot 10^{-4}\mathrm{m}^{-1}$ with a 69%-interval width of $2.4 \cdot 10^{-4}1/\mathrm{m}$. The optical depth has a medain of 0.205 with a 69%-interval width of 0.34. In both pictures also Gaussian distribution using the μ- and σ-values from table 7.4 are plotted.

made and the lidar ratio has not to be guessed. From the back-trajectories, only data 36 hours before the arrival of the air mass at 13 UT on the measurement day has been taken.

Seven classes have been defined, representing the origin of the air mass, namely northwest (NW), west (W), southwest (SW), southeast (SE), east (E), northeast (NE) and “local”. The class “local” represents very short trajectories with an air parcel staying for a long time close to Hamburg. Each of the seven classes contains only between 7 (SE) and 21 (NW) measurements. Therefore a further separation into summer and winter (which would certainly be useful) has not been made in order to maintain statistical significance. The result can be seen in Fig. 7.18. Class “local” has the highest value, which is due to the fact that these measurements were connected with low wind speed and high pressure situations. These circumstances are favorable for a high aerosol accumulation. Air masses from northerly directions represent lower aerosol extinction (they come over the Atlantic Ocean) than those from southerly directions (they come over the European continent). The variability of the values within one sector is reduced compared to the overall value, but in remains high with values between 28 % (E) and 64 % (local). Mean values from northerly directions are significantly lower than those from southerly directions or with short trajectories.

7.2.3 Lidar ratio

In 78 cases an aerosol backscatter profile based on the extinction evaluation has been calculated. Only measurements, where a reliable calibration of the backscatter profile could be made have been taken for the lidar ratio statistics.

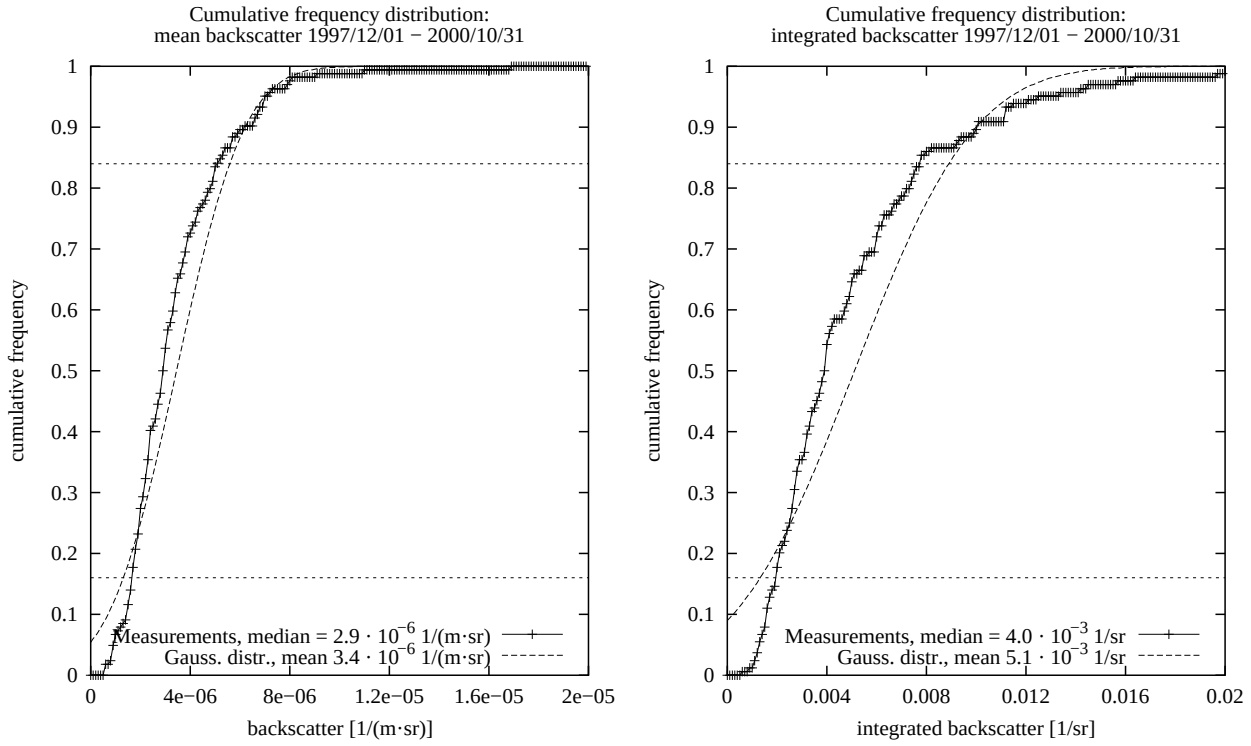

Figure 7.17: Cumulative frequency distribution of the mean aerosol backscatter (left side) and the integrated backscatter (right side) in the boundary layer in Hamburg including data from 1997/12/01 to 2000/10/31. For backscatter the medain is $2.9 \cdot 10^{-6} 1/(\mathrm{m} \cdot \mathrm{sr})$ with a 69%-interval width of $3.4 \cdot 10^{-6} 1/(m \cdot sr)$. The integrated backscatter has a medain of $4.0 \cdot 10^{-3} 1/\mathrm{sr}$ with a 69%-interval width of $5.8 \cdot 10^{-3} 1/\mathrm{sr}$. In both pictures also Gaussian distribution using the μ- and σ-values from table 7.5 are plotted.

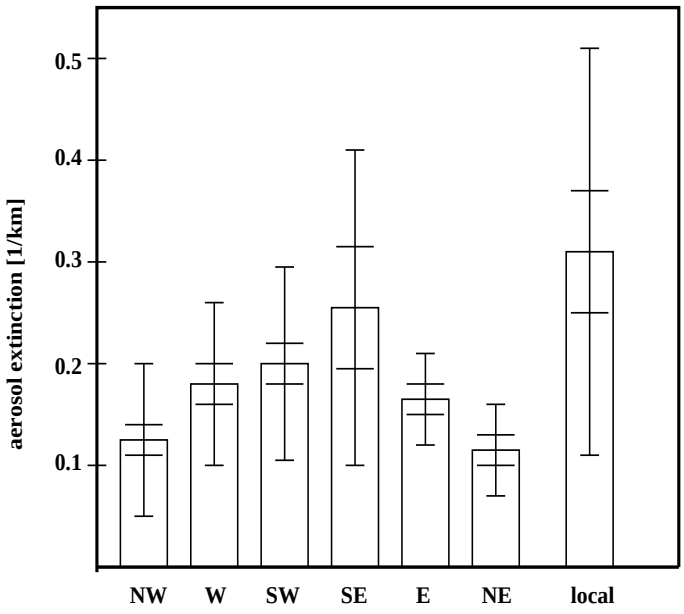

Figure 7.18: Mean aerosol extinction depending on the origin of the air mass. Inner errorbars represent the standard deviation of the average, outer errorbars of the individual value.

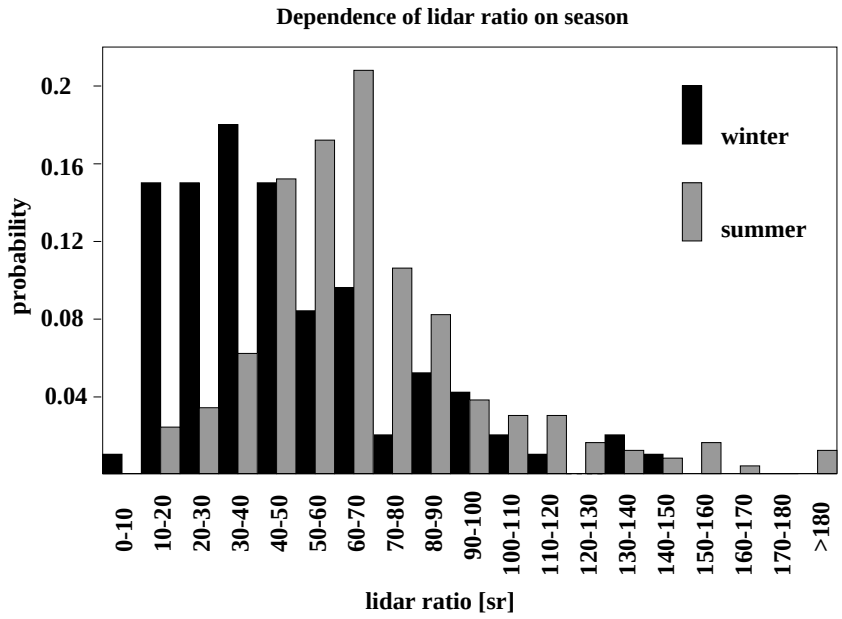

Figure 7.19: Probability histogram of the lidar ratio in steps of 10 sr, distinguished between summer (245 values) and winter (94 values).

All independent lidar ratio values (339) in the boundary layer have been statistically evaluated in a manner similar to the aerosol extinction. The histogram (Fig. 7.19) shows a higher probability for lower values in winter than in summer. The mean values are 63 sr for all values, 69 sr in summer and 48 sr in winter. Again, these values are high compared to the most probable values, in winter the median is 41 sr, in summer it is 64 sr. 69 % of the values are in summer between 45 and 91 sr, in winter between 21 and 81 sr.
Looking for a dependence of the measured lidar ratio on the origin of the air mass, no clear hints as for the aerosol extinction could be found. Lowest lidar ratios were observed in air masses coming from the northwest over the Atlantic Ocean. Model results (Ackermann, 1998) show values between 20 and 30 sr for maritime aerosols and between 60 and 70 sr for urban aerosols.

lidar ratio						
category	μ	σ	γ	μ/σ	median	n
1998-2000	63	34	2.16	0.54	59	339
summer	69	34	2.62	0.49	64	245
winter	48	30	1.19	0.62	41	94

Table 7.6: Lidar ratio statistics for all values and distinguished into seasons. Abbreviations mean μ: mean, σ: standard deviation γ: skewness, μ/σ: relative standard deviation of the individual value, n: number of used independent values.

7.3 Leipzig

by I. Mattis

7.3.1 Measurement statistics

The routine lidar observations at Leipzig are performed with the non-transportable aerosol Raman lidar, which is installed in a laboratory under the roof of the institute building. These measurements should be performed three times a week, at noon and at sunset on Monday and at noon on Thursday. The Raman signals, which are required for the evaluation of extinction and backscatter coefficients can be measured during nighttime only. Therefore in Leipzig further routine measurements were carried out at sunset on Thursday to derive a larger data set of extinction and backscatter profiles. Figure 7.20 gives an overview of the measurements, which were carried out in Leipzig from October 1997 until September 2000. Until March 1998 no measurements at 1064 nm could be performed because of problems with the beam expander. Because of the same reason, the power of the 355-nm light had to be reduced during some periods. In this time intervals it was not possible to determine the extinction coefficients at 355 nm and the water vapor mixing ratio.

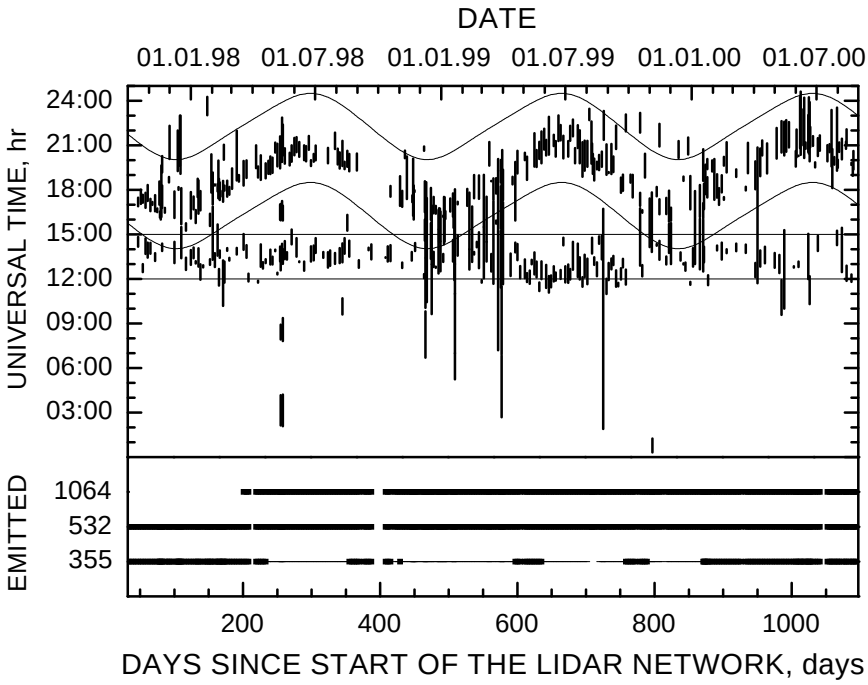

Figure 7.20: Schematic overview of the measurements performed in Leipzig between October 1997 and September 2000. Each of the vertical lines in the upper part belongs to one measurement. The length of the lines corresponds to the duration of the respective measurements. The thin lines indicate the boundaries of the time intervals of the routine measurements. The curves in the lower part show, which laser wavelengths were emitted. Periods, in which the maximum laser power was emitted, are marked by thick lines. The thin lines indicate time intervals, during which reduced laser power was used.

Figure 7.21 shows, that 64% of the possible AFS lidar network routine measurements were carried

out. 28% of the scheduled measurements could not be performed because of precipitation and 8% were missed because of technical problems. There were 90 additional measurements during intensive measurement periods such as high-pressure situations or cold front passages and to study local effects.

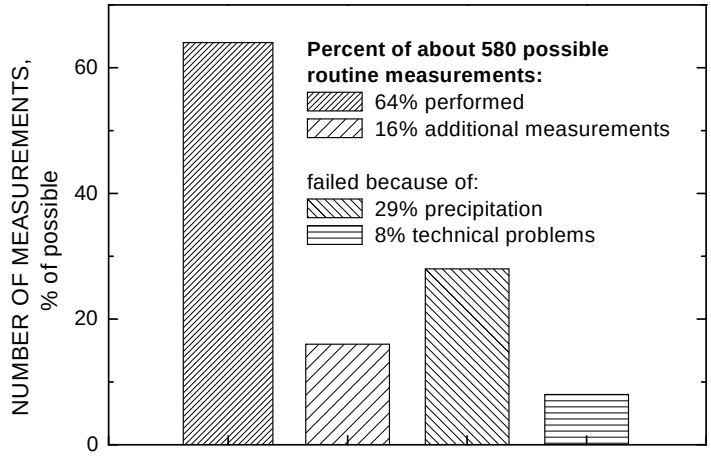

Figure 7.21: Number of lidar measurements performed with the aerosol Raman lidar at Leipzig between October 1997 and September 2000. The possible AFS measurements contains the routine observations 4 times a week.

As an example for the derived data set, Figure 7.22 shows all extinction profiles at 532 nm, which were derived in Winter 1997/98 and in summer 1998. The variability was slightly higher for the summer case but for both data sets the standard deviations are quite low. The differences between the mean winter and summer profiles of this example are also not significant. All following examinations will focus on the properties of extinction profiles separated into the 5 distinct trajectory clusters, which were introduced in Section 6.

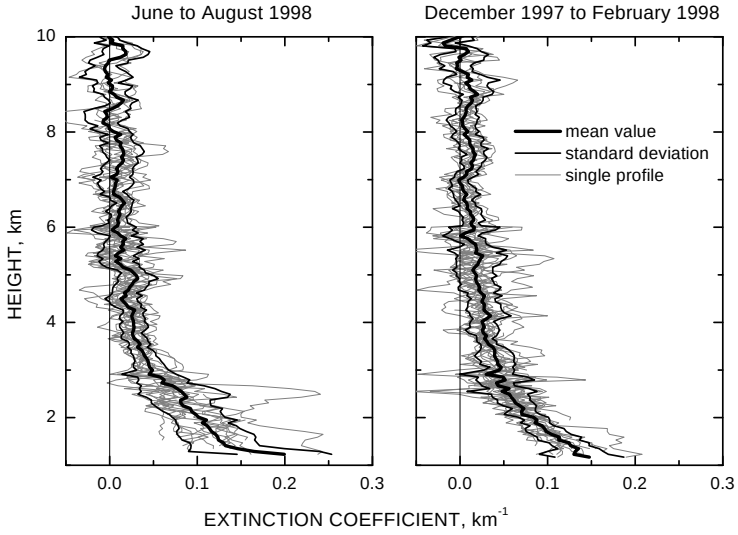

Figure 7.22: Profiles of the extinction coefficients at 532 nm. The averaged profiles were derived between June and August 1998 (left) and from December 1997 to February 1998 (right). The thin grey lines correspond to the single measurements. The thick black curves show the mean profiles and the thinner ones indicate the variability in terms of the standard deviation.

7.3.2 Classification of Extinction profiles by the use of cluster analysis of atmospheric trajectories.

The method of classification of optical aerosol properties in dependence on the large-scale weather regime described in Section 6 was applied to extinction profiles, which were derived from routine measurements in Leipzig between April and September in 1998 and 1999. The results of this procedure are presented in this section.

The extinction profiles used in this study have been screened for clouds. Cases completely free of clouds, extinction profiles measured in cloud-free cells within convective cloud fields, as well as profiles above or below clouds were considered. Since this study focuses on extinction properties of particles within the atmospheric dust layer, the profiles were cut off at the top of the atmospheric dust layer in cloud-free cases, or at the base height of convective clouds. Because of the incomplete overlap between laser beam and receiver field of view currently no trustworthy extinction profiles can be retrieved below a height of approximately 1.1 km. For most of the profiles measured during the winter months (October to March) the top height of the atmospheric dust layer was lower than 1.1 km. To evaluate the measurements, which were performed in 2000, below 2 km, a correction for the incomplete overlap would be necessary. The winter measurements as well as those of 2000 were thus not included in this study. Figure 7.23 shows the resulting 72 extinction profiles for the summers of 1998 and 1999. Each of them was assigned to the cluster of its corresponding trajectory.

All further investigations were carried out with the extinction profiles determined for ambient relative humidity (measured profiles) and with the same profiles normalized to 0% relative humidity (normalized profiles). An averaged humidity correction function for maritime and urban particles (Hänel, 1998) was used. This normalization was done to reduce the variability in the total data set of extinction profiles because of the influence of the humidity growth of particles on their optical properties. In the second step, mean extinction values were calculated for the layer extending from 1.1 km height to the top of the dust layer. These extinction values may best represent the conditions around the 850-hPa level. If extinction data were not available close to 1.1 km, the value of the lowest point of the respective profile was used for the height range between this lowest point and 1.1 km.

As can be seen from Figure 7.23, the largest extinction coefficients were found in cluster a). They were associated with continental aerosols since the trajectories in cluster a) show an aerosol transport from eastern Europe to Leipzig. The lowest extinction coefficients correspond to cluster e), which is associated with high-speed westerly winds (see Figure 6.5). Figure 7.24 shows, that the number of profiles in the different trajectory clusters is almost normally distributed. In contrast, the number of the associated extinction profiles is more variable. Although only 20% of the trajectories fall within cluster c), about 30% of the measurements belong to these trajectories, which correspond to southwesterly winds. Under the influence of this weather regime, the measurements were not that often disturbed by precipitation or low clouds. In contrast, only three extinction profiles are associated with cluster e) because the other routine measurements associated with this cluster could not be carried out because of precipitation.

In Figure 7.25, the cluster-mean extinction coefficients are presented. As already indicated in Figure 7.23, this figure clearly shows that the largest values in the measured as well as in the normalized extinction coefficients are found in cluster a). The lowest values belong to cluster e). The extinction coefficients of clusters b) and d) are most influenced by the humidity normalization since the corresponding weather regimes are characterized by high relative humidities. The 1999 dry extinction values are 56% lower in cluster d) (west) and 52% in cluster b) (northwest) than the measured ones. In contrast, the extinction coefficients of 1998 of cluster a) (east) are reduced only by 28%. The differences in the strength of the humidity correction between the distinct clusters can be amplified, if no averaged humidity correction function but different functions in dependence on the actual cluster

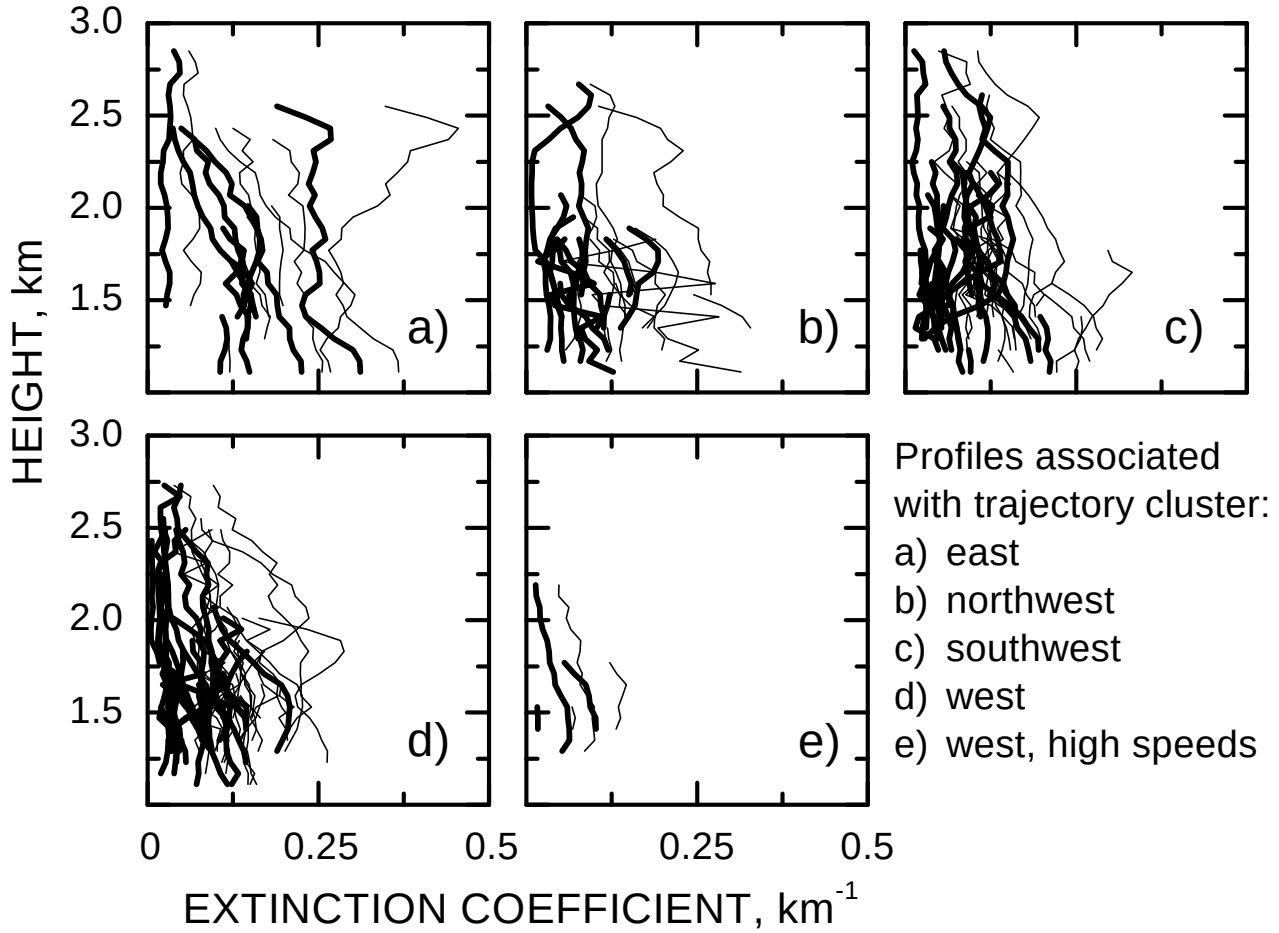

Figure 7.23: Extinction profiles measured in the summers of 1998 and 1999. Each profile was assigned to the cluster of its corresponding trajectory. The thin curves show the particle extinction coefficients at 532 nm. Thick lines belong to the same profiles but normalized to 0% relative humidity.

(Hänel, 1998) will be used.

The variability in the cluster-mean extinction coefficients between the two summers is quite low. In Table 7.7 the total mean extinction values and the reduction of the variability of the data set caused by the clustering are summarized. The total mean value averaged over all clusters is $0.15\,\mathrm{km}^{-1}$ for the measured and $0.08\,\mathrm{km}^{-1}$ for the normalized extinction coefficients. The total standard deviations of all profiles are about 45% for the measured profiles and 65% for the normalized profiles. The mean standard deviations within the clusters are 40% and 56%, respectively. The variability of the total data set increased after the humidity normalization. This increase may indicate differences in the optical properties of dry particles, which are smeared out by swelling effects.

Figure 7.26 shows the mean aerosol layer heights of the different clusters. Since in the presence of low clouds only the cloud base height could be determined, the boundary layer height derived in these cases is underestimated. Nevertheless, the mean aerosol layer height during nighttime is about 2000 m with a variability of 19% in 1998 and 21% in 1999. There are no significant differences between the clusters. But the value of cluster a) (east) seems to be slightly higher than those of the other clusters.

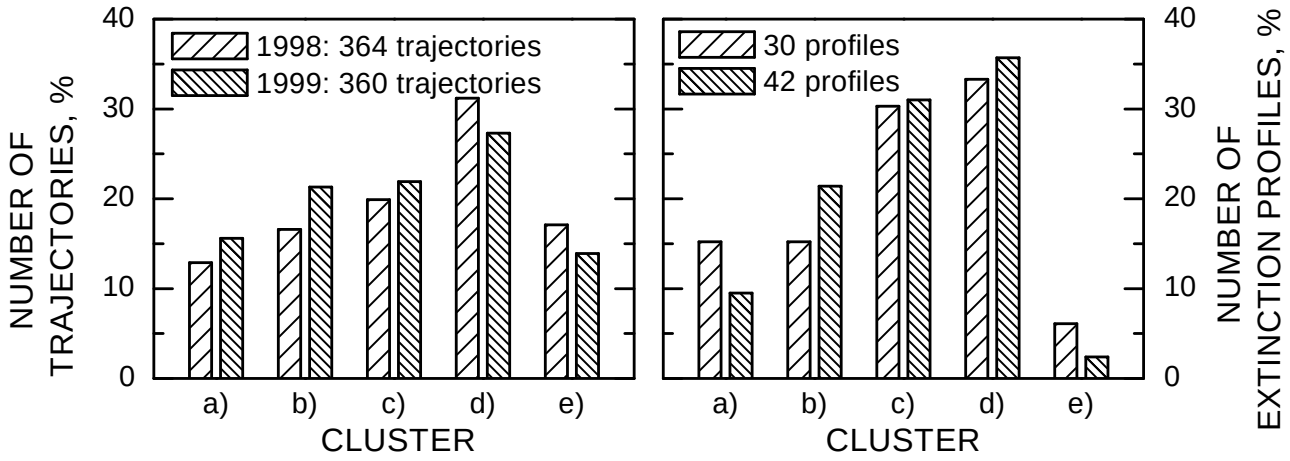

Figure 7.24: Number of trajectories (left) and of the associated extinction profiles (right) within the different clusters. The left columns belong to the trajectories and measurements of summer 1998, the right ones show the values for 1999.

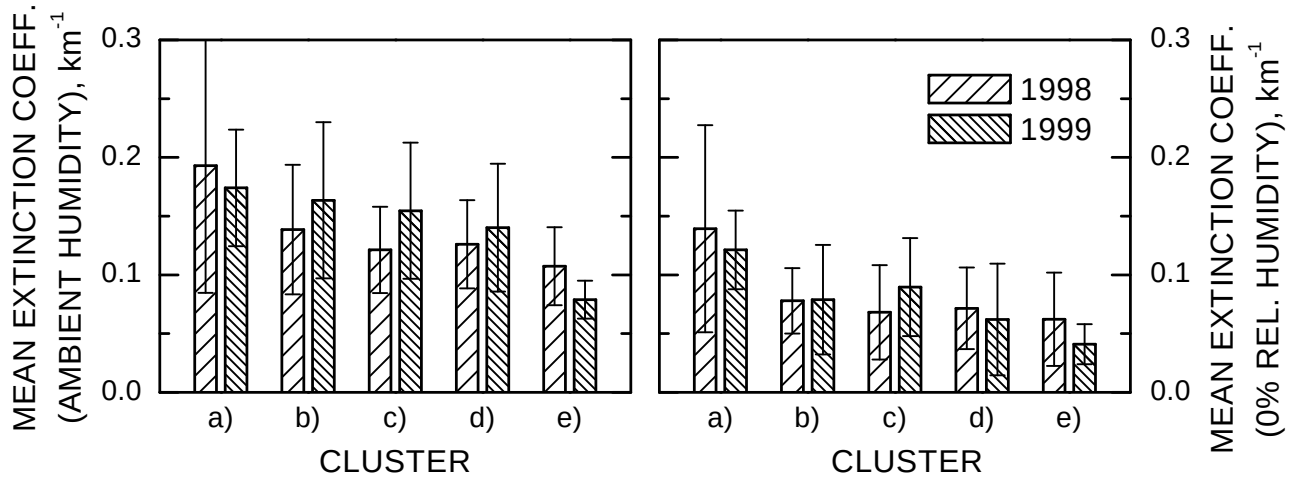

Figure 7.25: Mean extinction coefficients of the different clusters. The mean values were calculated from the measured profiles (left) and from the normalized profiles (right). The error bars indicate the standard deviation of the profiles within the different clusters. The left columns belong to the measurements of the summer 1998, the right ones show the values for 1999.

7.3.3 Conclusions

Extinction profiles which were derived from routine measurements in Leipzig between April and September in 1998 and 1999 were divided into distinct groups by the use of cluster analysis of the corresponding trajectories as described in Section 6. The variability of the measured as well as of the normalized extinction coefficients is decreased by the clustering. But the decrease of the variability was not as strong as expected. On the one hand, this may be explained by the general low variability of the entire data set. On the other hand this result may indicate that there is no strong dependence of the extinction coefficients in the atmospheric dust layer on the large-scale weather regime at Leipzig. To obtain more knowledge about seasonal dependencies and interannual variations, this study has to be continued with a larger data set, which also contains the profiles of the winter months and those

year	ambient humidity		
	mean extinction [km^{-1}]	total variability [%]	variability within clusters [%]
1998	0.14	50	39
1999	0.15	40	34
Both	0.15	45	40
0% relative humidity			
1998	0.08	70	55
1999	0.08	60	47
Both	0.08	65	56

Table 7.7: Total mean extinction values in the atmospheric dust layer averaged over all profiles. The total variability is calculated as standard deviation of all extinction profiles. The variability within the clusters was determined from the standard deviations of all profiles within the different clusters, averaged over all clusters.

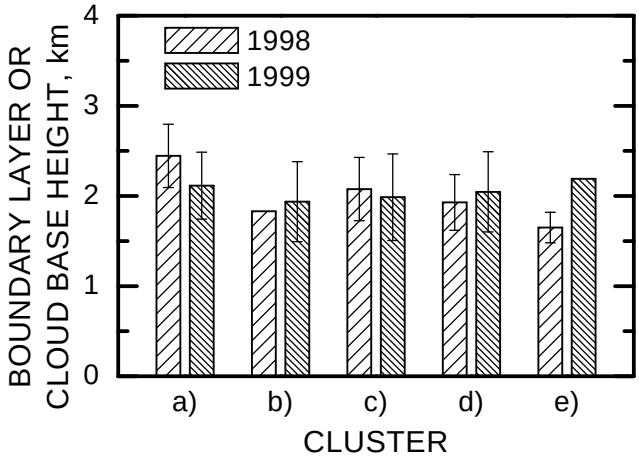

Figure 7.26: Mean aerosol layer heights of the different clusters. In the presence of low clouds, only the cloud base height could be determined. The left columns belong to the measurements of summer 1998, the right ones show the values for 1999.

of 2000. For that reason it is necessary to correct the extinction profiles for the incomplete overlap between the laser beam and the receiver field of view. A correction method is suggested in (Wandinger and Ansmann, 2000a) and (Wandinger and Ansmann, 2000b).

7.4 Munich

by M. Wiegner

7.4.1 Measurements

The final goal of the German Lidar Network was the establishment of local aerosol climatologies to provide typical aerosol distributions and their variability quantitatively. The extinction coefficient was selected as the quantity of interest, preferably at the three Nd:YAG wavelengths. If extinction coefficients are not retrievable, backscatter coefficients should be used instead. The temporal sampling was defined by one measurement near local noon on Mondays and Thursday and an additional measurement on Mondays around sunset.

The primary focus of the project was the establishment of a homogeneous data base. Correspondingly, measurements were performed between December 8., 1997, and August 28., 2000, in Munich on 2 days in 1997, 60 days in 1998, 77 days in 1999, and 48 days in 2000 according to the regular schedule. Unfortunately, low clouds prevented the determination of vertical aerosol profiles on more than half of the days (see Tab. 7.8 in Sect. 7.4.3). Thus, measurements were taken on another 33 days in 1998, 16 days in 1999, and 8 days in 2000 to increase the data base. During 21 days in July and August 1998, the MIM lidar was operated in Lindenberg in the framework of LACE'98 to support the local closure experiment and to participate in the quality assurance program for the lidar systems. During 8 days in May 1999, the lidar was used at Hohenpeissenberg in a special program to investigate aerosol distributions in remote areas – in contrast to a city like Munich – and strong orographic terrain.

Technical problems that prevented regular measurements for a significant time only happened in April 1998. However, during LACE'98, the controlling microprocessor unit for data acquisition and system control was damaged; further details are given in Section 3. As a consequence, a secondary focus of the project emerged and a lot of manpower had to be shifted to develop a temporary hardware solution to immediately continue the regular measurements and to build up a new concept in parallel to our measurement obligations. In spite of this inconvenient situation the measurement program could be fulfilled and the main scientific aspects could be addressed.

7.4.2 Data evaluation

The third focal point of the MIM activities was the development and testing of methods to retrieve extinction coefficients as a routine job. It is well known, that the lidar equation is underdetermined and, thus, the knowledge of the lidar ratio is required. Typical values for a limited number of aerosol types are available from the literature, however, uncertainties remain, if 'non-standard' aerosols are present or the aerosol type cannot be characterized precisely.

To overcome this problem, we make use of the scanning capability of our lidar system. On the one hand, the line of sight of the lidar can be changed quickly, on the other hand, horizontal measurements are possible. They allow to apply the slope method which directly gives the extinction coefficient.

Scanning allows the application of the so called two-angle approach. The evaluation of the signals from a pair of zenith angles is straight forward: The extinction coefficient is derived from an equation only depending on the signals of the two directions and the corresponding angles. In particular, neither a lidar ratio nor a boundary value must be known. Together with the achievable high temporal resolution and the possibility of day time operation it is a very attractive approach. The two-angle

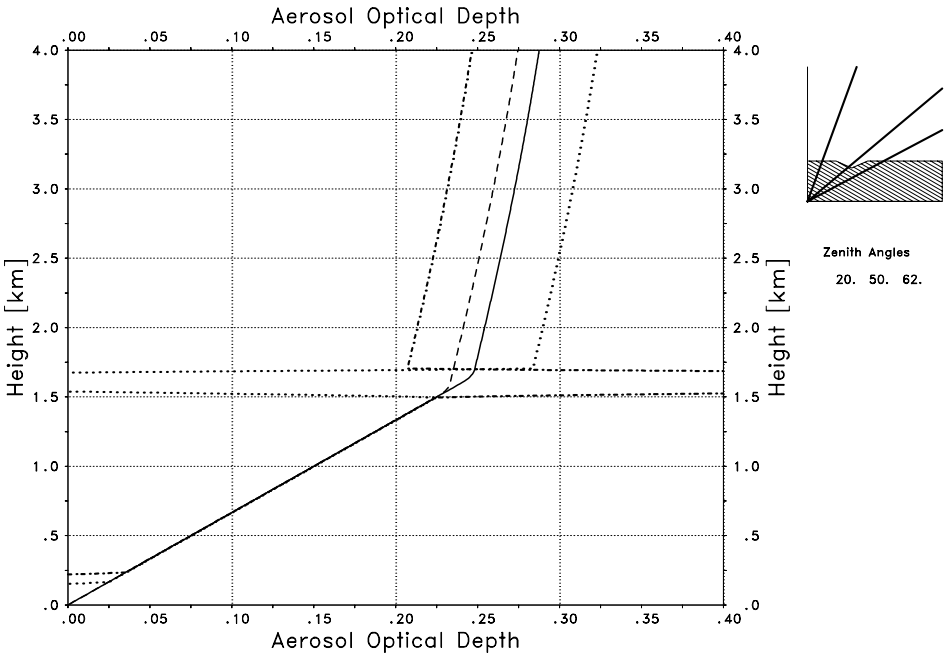

Figure 7.27: *Numerical simulation of the influence of a spatial inhomogeneity at the top of the PBL on the retrieved optical depth (details see text)*

approach has already been published in literature, however, experience from routine operation was missing. The potential in 'real life' was subject of our routine measurements.
Typically, we perform a number of scan cycles of three zenith angles (20°, 50° and 62°) each, which allows us to evaluate signals from two different pairs of angles. However, vertical extinction profiles can only be obtained if the atmosphere is horizontally homogeneous over the time of the measurements. It was found from our data base that this hard requirement is fulfilled only in rare situations. How far this condition can be relaxed, if we restrict ourselves to the determination of the optical depth, or the extinction coefficient of limited layers, was investigated first by numerical simulations.
One example of a frequently observed situation is shown in Fig. 7.27: A spatial inhomogeneity at the top of the boundary layer, which affects only one out of three lines of sight of the scanning lidar (small panel) is assumed. The full and the dashed lines shows the real increase of τ_p with height while the dotted and dashed-dotted lines shows the retrieved optical depth. It can be seen that it is not possible to retrieve the optical depth above the inhomogeneity, but, the mean extinction coefficient of the underlying layer can be derived from the slope. Above the PBL, the slope of the curve is so low that already small errors or inhomogeneities would prohibit any retrieval. At the inhomogeneity itself, unrealistic (e.g., negative) extinction coefficients show up. Similar results are found for inhomogeneities close to the surface, which might even be invisible for the lidar because they are below the complete overlap. They prevent any τ_p-retrieval, but the determination of mean extinction coefficients of homogeneous layers above is not influenced. As a consequence, the application of the two-angle approach requires a very careful look at each individual data set; this is quite time consuming and cannot be done automatically.
Whether the stability of the atmosphere was sufficient and the two-angle approach could be applied, we decided from comparing different pairs of angles and from the observation of the temporal evolution of the atmosphere by subsequent lidar measurements. Our experience from the lidar network showed that under stable conditions, in particular in the afternoon when convection has died, there is

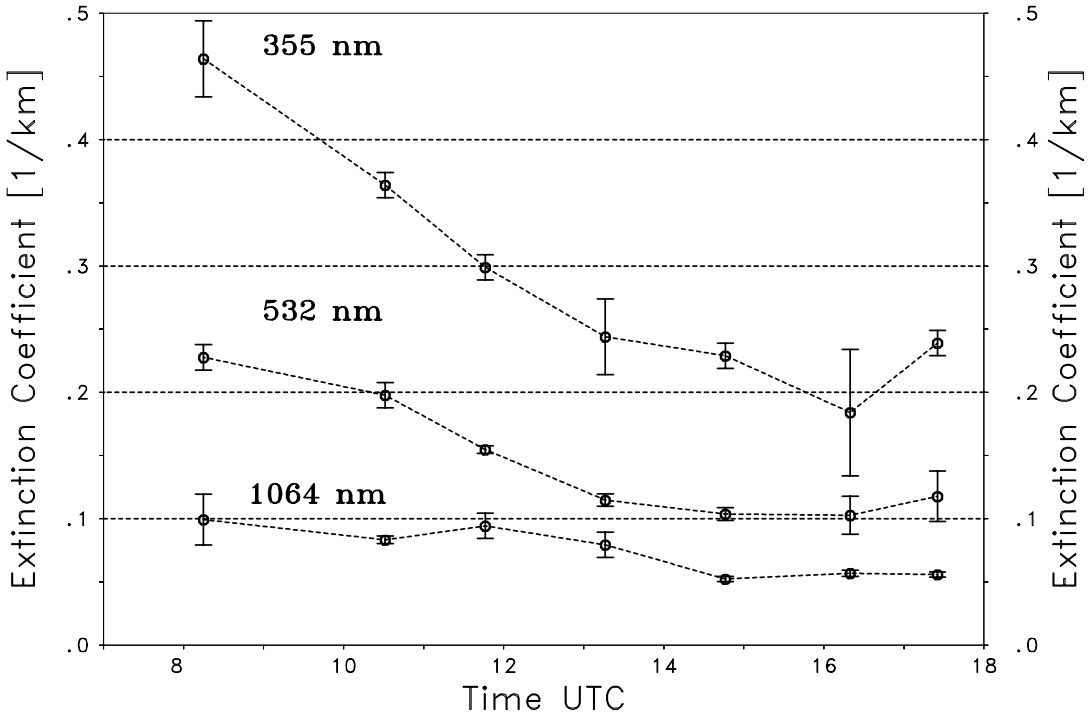

Figure 7.28: *Aerosol extinction coefficient at 50 m above lidar site for λ=1.064 μm (bottom), λ=0.532 μm (middle), and λ=0.355 μm (top) at seven selected times at Munich (April 1st, 1999)*

a good chance to apply this technique to atmospheric layers of some hundred meters in vertical extent. However, as anticipated from the model calculations, the algorithm is restricted to layers within the planetary boundary layer where the signals are high compared to the background. This limitation is, however, no significant drawback, because most of the aerosol load is concentrated in this layer.
In spite of that rather poor spatial resolution this information is very valuable for the quantitative determination of extinction profiles. The first step of the solution is obtained from the analytical backward integration of the lidar equation for a realistic 'first guess' lidar ratio. Variation of the lidar ratio gives a set of possible solutions of the extinction coefficient. In a second step the most probable solution is found by comparison with the mean extinction coefficients at those heights, where it is known from the two-angle approach. So, the numerical inversion of the lidar equation gives the desired high spatial resolution, and the two-angle approach helps to find a correct lidar ratio.
From the quasi-horizontal measurements – which has been performed on a regular basis since October 23, 1998, the extinction is derived very close to the surface, typically averaged over the altitude from 30 to 70 m above ground. An example of such a retrieval is shown for April, 1st, 1999 (Fig. 7.28). Extinction coefficients at three wavelengths with a time resolution of approximately one hour are plotted. A significant temporal change can be observed during the day. Note, that the accuracy of α_p is quite high as indicated by the error bars. These data serve as plausibility check for the Klett/two-angle profiles and for an reliable downward extrapolation of the aerosol extinction profile. As a result an extinction profile from the surface to the free troposphere is obtained under ideal conditions and multi-angle measurements.

7.4.3 Results

As stated before, measurements were performed on 273 days. A more detailed survey is given in Tab. 7.8 in a similar form as presented for the other stations. While the number of performed measure-

ments is quite high (65.5%) – note, that with the additional measurements on Tuesdays, Wednesdays and Fridays the number would be even higher – the number of measurements which are not disturbed by low clouds is less than 50%. For 1999 only preliminary numbers are available, because evaluation of data from broken cloud fields is still ongoing and might slightly increase the number of profiles. On the other hand, horizontal measurements could often be evaluated in the presence of low clouds and, in a few cases, also two-angle measurements. In so far, Tab. 7.8 is misleading to give the total number of aerosol extinction or backscatter profiles.

Measurements 1997/12/01 – 2000/08/31						
months	possible measurem.	performed measurem.	perf./poss. measurem. [%]	class 1	class 2	class 1/ perf. meas. [%]
12/97 - 03/98	52	27	51.9	11	16	40.7
04/98 - 09/98	51	28	54.9	13	15	46.4
10/98 - 03/99	75	54	72.0			
04/99 - 09/99	67	49	73.1			
10/99 - 03/00	78	52	66.7	14	12	53.8
04/00 - 08/00	66	45	68.2	18	27	40.0
all	389	255	65.5			44.4
class 1 : measurement without low clouds possible class 2 : measurement with clouds below 2000 m						

Table 7.8: Overview over regular measurements at Munich; for details see text

It is of course difficult to characterize an aerosol distribution by a small set of numbers. A suitable parameter is the height of the planetary boundary layer, which we have defined as that height h_{PBL}, where

$$\alpha_p(h_{PBL}) = \frac{1}{2\,h_{PBL}} \cdot \int_0^{h_{PBL}} \alpha_p(z)dz$$

is valid. Though in most cases in Munich a unique PBL-top can be found by this procedure, it also happens that several layers and no sharp boundary to the free troposphere exist. Another criterion of the aerosol distribution is the aerosol optical depth τ_p of the planetary boundary layer. We prefer this parameter instead of a mean aerosol extinction coefficient, because the first better suits to describe radiative properties.
The annual cycle – in particular measurements from the second half of the year are still missing – of h_{PBL} is shown in Fig. 7.29. Note, that heights refer to altitude above mean sea level, i.e., in most winter cases the top of the PBL was between 0.2 km and 0.7 km above the lidar site. Though there is a significant scatter of the data points, it is clearly visible that h_{PBL} increases from winter to summer. A similar trend is obvious in the $\tau_{p,PBL}$-values for wavelengths 532 nm and 355 nm; the variation is, however, even larger. The reasons are manifold: certainly, meteorological variables such as the relative humidity, or the source regions of the advected aerosol, influence the optical depth. However, the extrapolation from the first lidar data level to the surface also significantly influences $\tau_{p,PBL}$.
Consequently, the sounding of the lowest atmosphere was an important issue in our measurements. As already stated in Section 3 the overlap of our lidar is at about 250 m. Together with the scanning capability this allows a very good observation of the lowest atmosphere which is a big advantage over

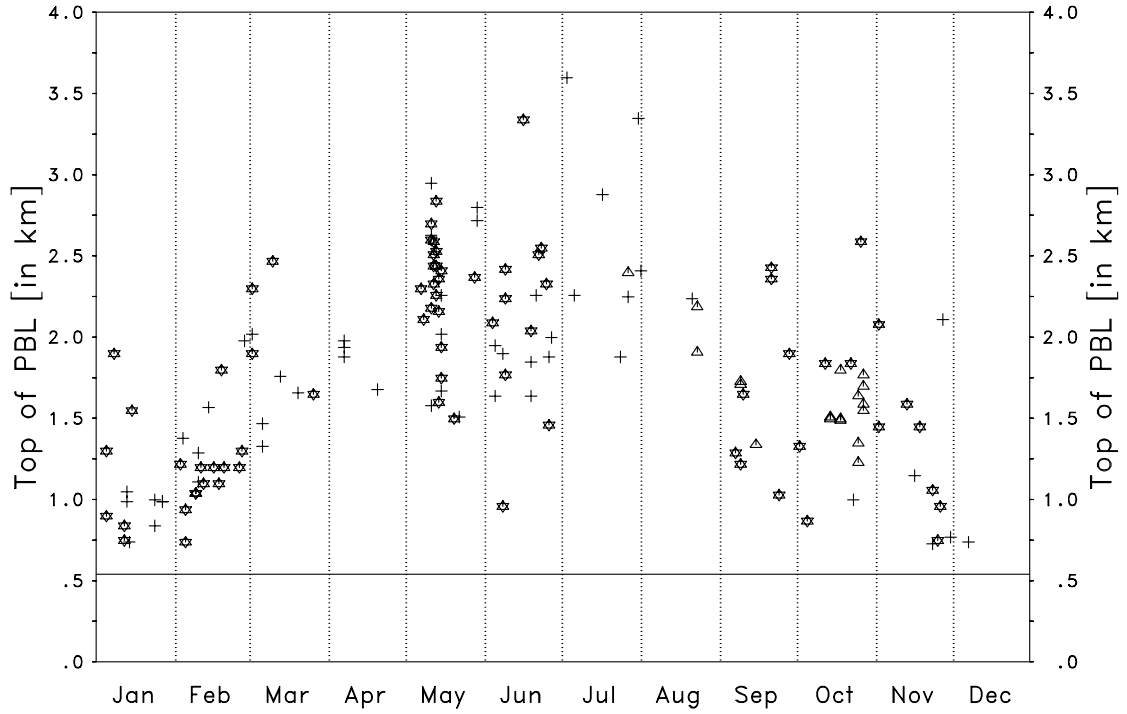

Figure 7.29: *Height (above mean sea level) of the planetary boundary layer; stars, triangles and crosses are for 1998, 1999 and 2000, respectively.*

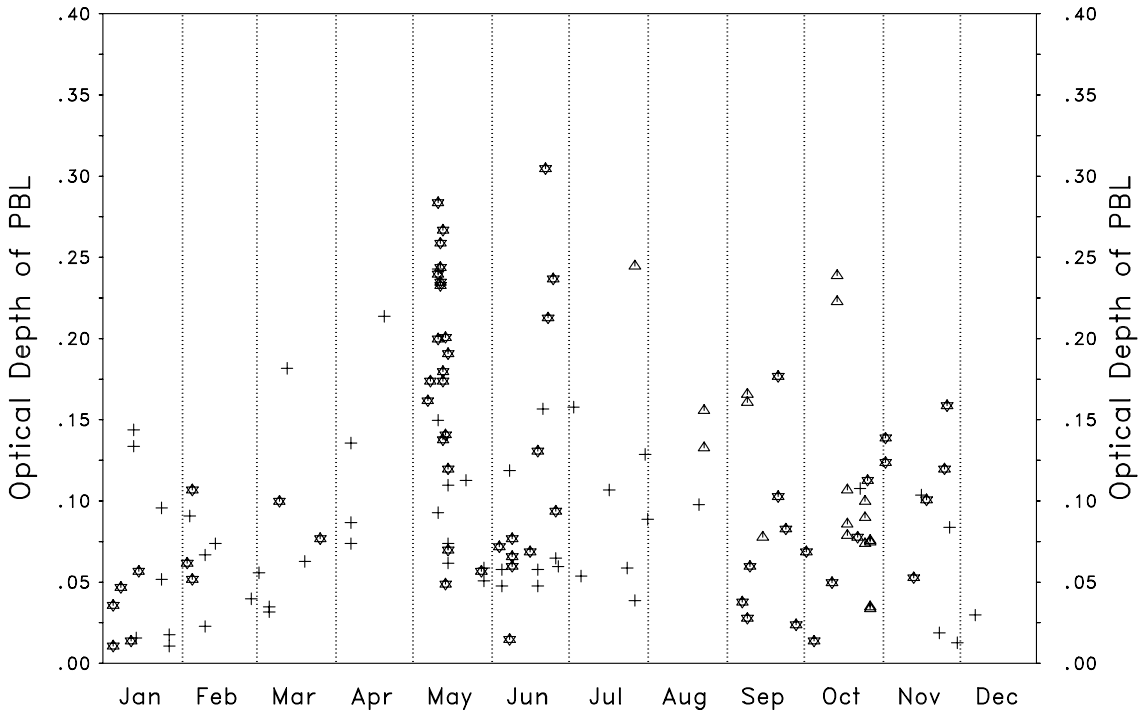

Figure 7.30: *Aerosol optical depth of the planetary boundary layer (λ=532 nm); stars, triangles and crosses are for 1998, 1999 and 2000, respectively.*

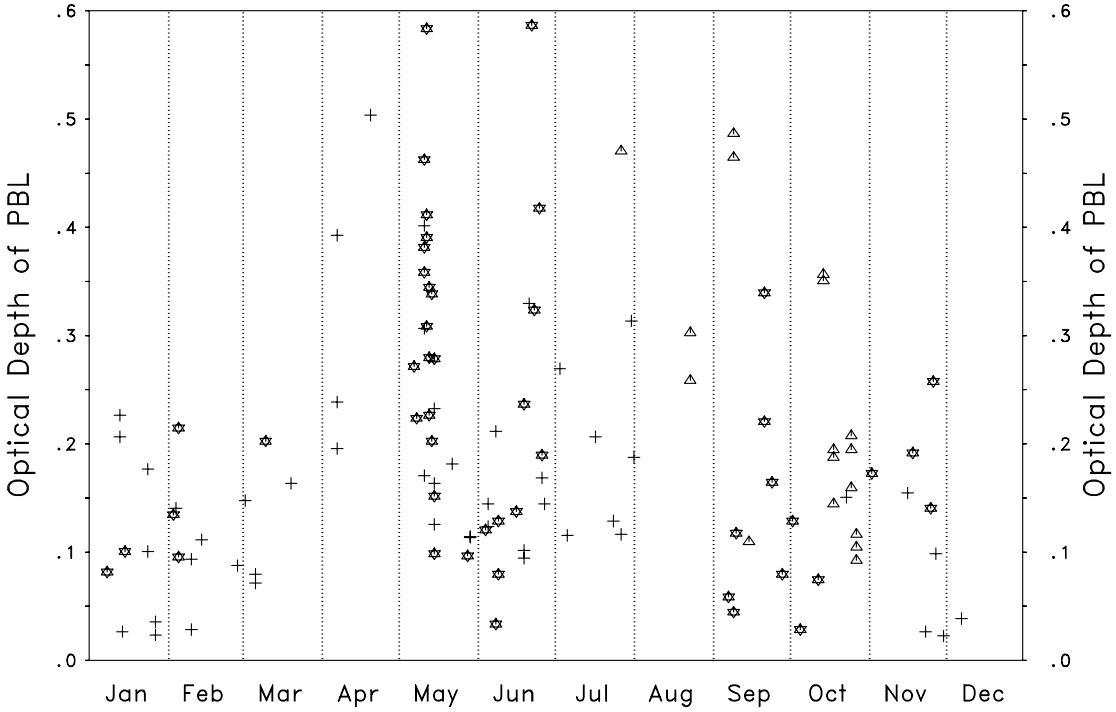

Figure 7.31: *Aerosol optical depth of the planetary boundary layer (λ=355 nm); stars, triangles and crosses are for 1998, 1999 and 2000, respectively.*

many other lidars. As a consequence, we investigated the temporal evolution of the aerosol distribution in the planetary boundary layer on several occasions in detail. Two examples are discussed here.

An example of changes of the backscatter coefficient β_p for 532 nm as a function of height most probably induced by orography is illustrated in the five panels of Fig. 7.32. Data are from August 10, 1998, between 08:15 UT and 12:49 UT, taken during LACE in Lindenberg, where our lidar was located on the top of a small hill. The relative errors of β_p in the PBL are between 7% (panel 2 and 3) and 14% (panel 5). The pronounced feature between 3 and 4 km in altitude was an aerosol layer originating from forest fires in Canada. Of particular interest is, however, the development of the planetary boundary: The top of the boundary layer is lifted over several hundred meters within 10 minutes and the structure also changed significantly. Such dramatic effects are not only caused by convective activities but also by the orographic disturbance of the advected flow. An influence of the relative humidity f, that might increase aerosol extinction dramatically, can be excluded in this case: close to the surface f was lower than 41%, at the top of the PBL it reached 54%. Under these conditions a significant growth of the particles is rather unlikely. The temporal changes are also visible in the corresponding horizontal measurements (not shown here), so that the determination of α_p at the surface shows also large uncertainties. In our case, $\alpha_p = 0.047 \pm 0.016\, km^{-1}$ was found as an average for the time period from 12:10 and 12:33 UT corresponding to a lidar ratio of about 43 sr.

Another example from Munich (June 23, 1998) is shown in Fig. 7.33. Three α_p profiles for 532 nm and 355 nm between 16:14 UT and 16:28 UT demonstrate rapid changes at the top of the PBL, both in height and in extinction, while the lower troposphere is constant in time.

These case studies show that not only in orographically structured terrain the determination of half-hour-averages of aerosol distributions smooths out a lot of small scale features. It was often found that in particular one and two hours before local noon the aerosol distribution undergo changes within minutes. As a consequence, one should remind that averages have uncertainties which are not caused

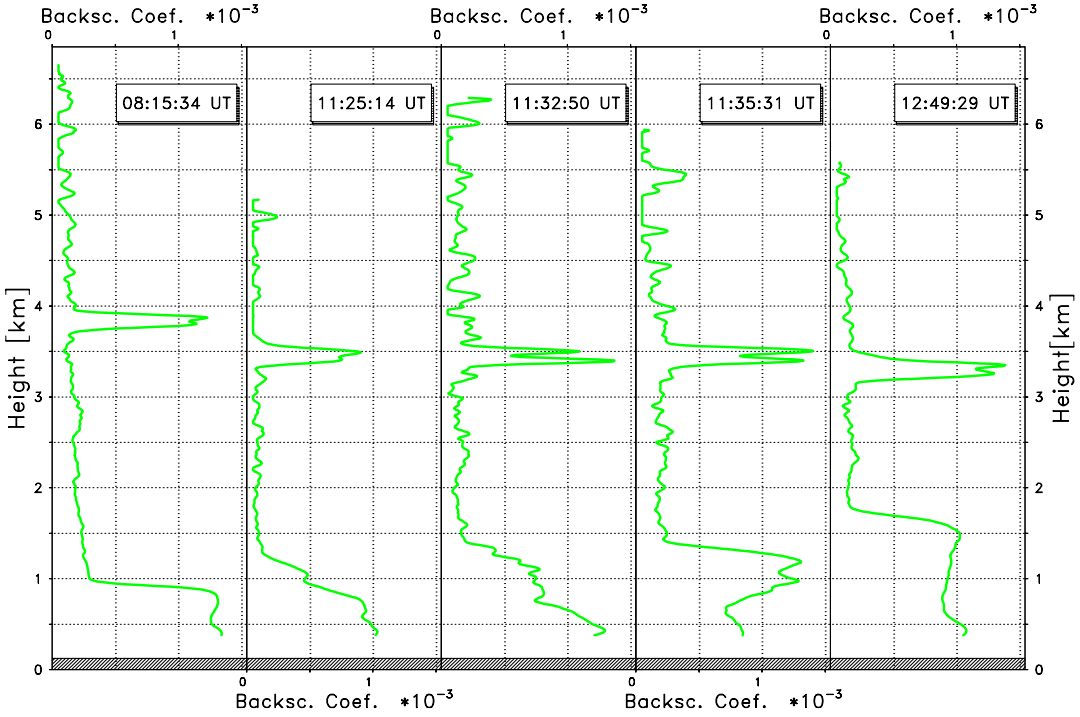

Figure 7.32: *Backscatter coefficients in* $km^{-1}\,sr^{-1}$ *for 532 nm as determined from the Munich lidar (Lindenberg, August 10., 1998, times as indicated)*

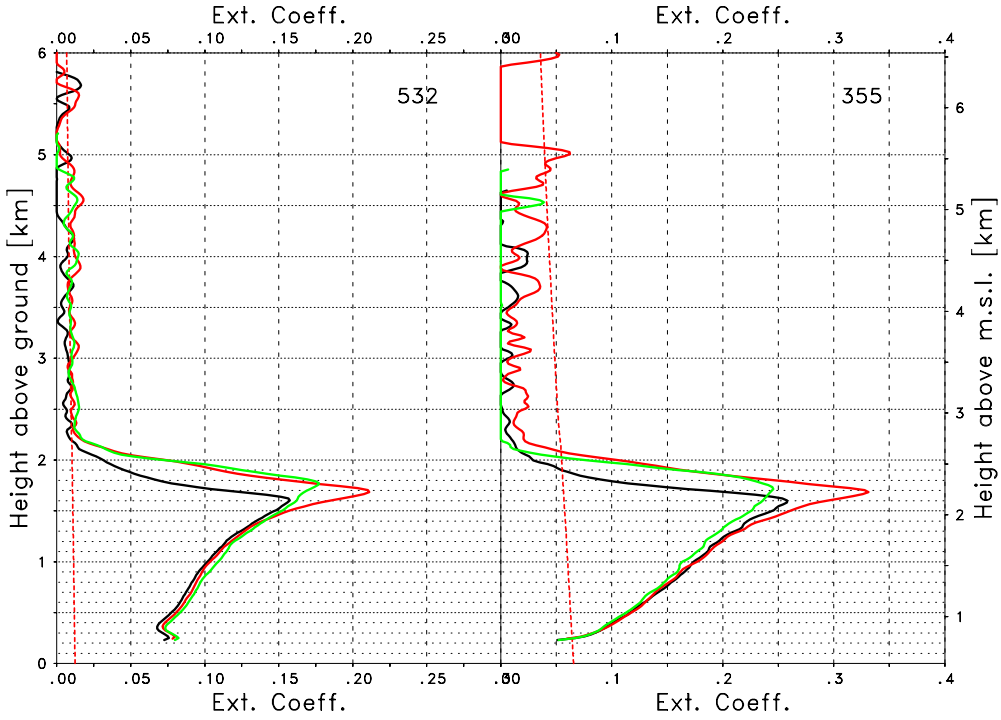

Figure 7.33: *Extinction coefficients in* $km^{-1}\,sr^{-1}$ *for 532 nm and 355 nm for June 23, 1998*

by measurement errors but rather on the meteorological conditions. Another consequence of these findings is that the determination of extinction coefficients by combining measurements from different zenith angles is hardly possible at such times of the day.
We also provided measurements of complete diurnal cycles for two reasons. First, we wanted to detect periods of typically stable and unstable layering, and second, to judge on the representativeness of the times of the day of the regular measurements. One example of unstable aerosol layers can be found in Section 7.3.

7.4.4 Summary and conclusions

The measurements were successfully performed for almost three years, and a data base covering the full time span could be established. However, due to the severe damage of the system during LACE, more manpower than expected had to be allocated to hardware work. As a consequence, the statistical evaluation of the data is delayed.
Nevertheless, several conclusions, which are of general interest, can be found from the Munich measurements.

- The lidar system has been substantially upgraded. Measurements from August 2000 show lidar signals for 355 nm with perfect Rayleigh-fits up to 15 km. Graphical interfaces have been developed to facilitate system control, on-line quality checks and – to a certain extent – automatically data evaluation.
- Methods to derive the aerosol distribution in the lowest troposphere, often even down to the surface, have been successfully implemented and tested. They are based on the scanning facility of the lidar and the combination of Klett-inversion, two-angle approach and slope method.
- Rapid fluctuations in the aerosol distribution of the boundary layer could be verified.
- Especially in winter, aerosols are often concentrated in the lowest 300 m of the atmosphere. To resolve this feature, scanning lidars and/or lidars with a very early overlap are required.

Regular measurements from the German Lidar Network are continued in the framework of EARLINET. The prolongation of the existing time series will allow to amend statistical conclusions significantly.

7.5 Garmisch-Partenkirchen

by S. Kreipl

Because of the pronounced diurnal cycle of the wind system in the Alpine valley a special measurement schedule was established at the Garmisch-Partenkirchen site. Instead of two measurements in the afternoon and at night soundings were performed in the morning and in the afternoon, before and after the formation of the valley wind. In order to compare to the Monday-night measurements it was decided to do regular soundings at Garmisch on Tuesday morning, too.
Table 7.9 shows the number of days with at least one measurement. In addition to the routine measurements there were also additional ones, especially under special meteorological conditions such as frontal passages, high pressure, or potential advection via long-range transport.

Year	Routine measurem./ climatology (days)	Cancellations (days)			Additional measurem. (days)
		Weather	Technical	Other	
1998	40	26	8	5	9
1999	57	59	29	6	6
2000	28	23	36	11	9

Table 7.9: Measurement days during 1998–2000.

Due to lack of personnel measurements did not begin before April 1998. They ended by the end of August 2000 when the project Aerosolforschungsschwerpunkt expired. The large number of days cancelled due to bad weather in 1999 is striking: It reflects the hard winter 1998/1999 which, except for two days, did not allow any measurement in January/February 1999, and an exceptionally rainy summer. Moreover, the trailer holding the lidar system was rebuilt: the old plastic cover was replaced by a stable aluminium cover in 1999, and in 2000 the detector system was completely exchanged.

Period	Measurem. scheduled (days)	Measurem. performed (days)	Perf./sched. measurem. (%)	Class 1 (days)	Class 2 (days)	Class 1/ perf. meas. (%)
4/98–9/98	75	36	48.0	31	5	86.1
10/98–3/99	73	11	15.1	11	0	100.0
4/99–9/99	67	37	55.2	34	3	81.1
10/99–3/00	76	28	36.8	23	5	82.1
4/00–8/00	60	13	21.7	12	1	92.3
4/98–8/00	351	125	35.6	111	14	88.8

Table 7.10: Six-monthly measurement statistics for the project; the measurement days are classified according to their quality in respect of data evaluation.

Table 7.10 shows a more detailed listing of the measurements performed. In addition, some measure of quality is introduced by distinguishing two cases named “class 1” and “class 2” [1]: Class 1 means that a measurement was possible without clouds (ceiling) below 2000 m a. g. l., whereas class 2 means that there were inevitable clouds below 2000 m. The latter makes a successful data evaluation rather implausible as calibration is nearly impossible.
The rather high percentage of class 1 measurements is ascribed to the orographic situation at Garmisch-Partenkirchen: Clouds are mostly seen above the ridges flanking the Loisach valley. Clouds also over the valley are associated with bad weather which implies that no measurement is possible at all.

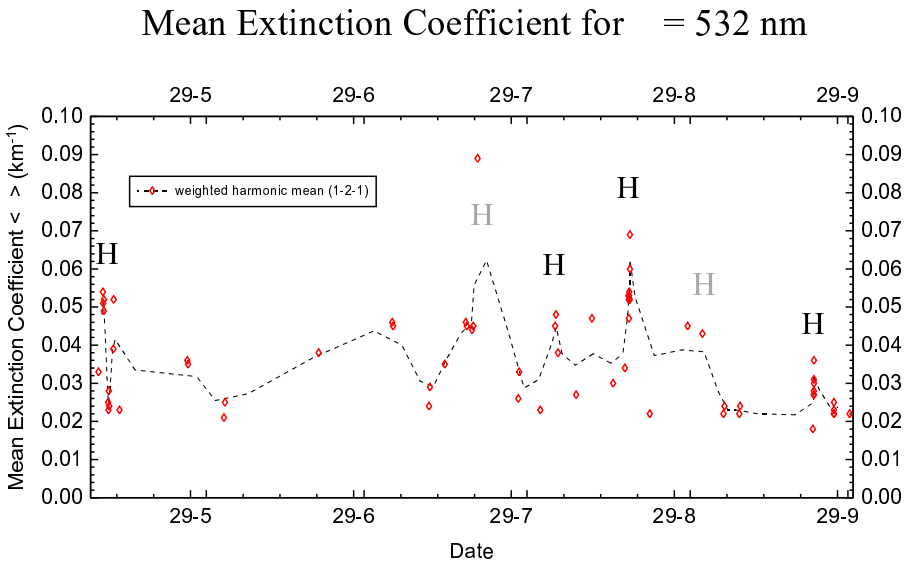

Figure 7.34: Mean extinction coefficients in the boundary layer or the summer 1998; the dashed line pictures a weighted 1-2-1 mean of the data, revealing stable high pressure conditions with constantly high extinction coefficients. Such periods are marked by “**H**”. A grey “H” stands for a less pronounced high pressure situation.

The mean extinction coefficient for the six months of summer 1998 is shown in Figure 7.34. The time scale covers the period from May 1 to September 29. For this period the mean extinction coefficient for the boundary layer was calculated using only lidar profiles with no cloud signals. The dashed line is the result of a weighted harmonic 1-2-1 mean. It clearly shows some peaks with high extinction values. Most of these peaks could be assigned to high pressure situations, marked by “**H**”. This is one of the reasons for the averaging over three points: A *stable* high pressure situation lasting some days causes an accumulation of aerosol resulting in higher opacity. The high pressure period in May 1998 (cf. Sec. 7.3) can be clearly seen. Some periods are marked by a grey “H” declaring that it was a less pronounced high pressure situation. The peak on July 21/22, for example, shows the rising pressure behind a waved cold front. The vertical extent of the flown in cold air was rather small so the air was not exchanged completely, again resulting in higher extinction coefficients.
Figure 7.35 shows the annual variation in 1999 of the mean extinction coefficient for a wavelength of 532 nm. 1999 is the only year that was (theoretically) completely covered by data collected in the AFS project. As for Fig. 7.34 only profiles showing no cloud signals at all were considered (“better than class 1”). Once again, the data were averaged by a weighted harmonic 1-2-1 mean. The curves are shown for elevations of 1, 2, and 3 km above ground level. The results show that autumn 1999 was

[1]This classification is based on a suggestion by V. Matthias from MPI, Hamburg

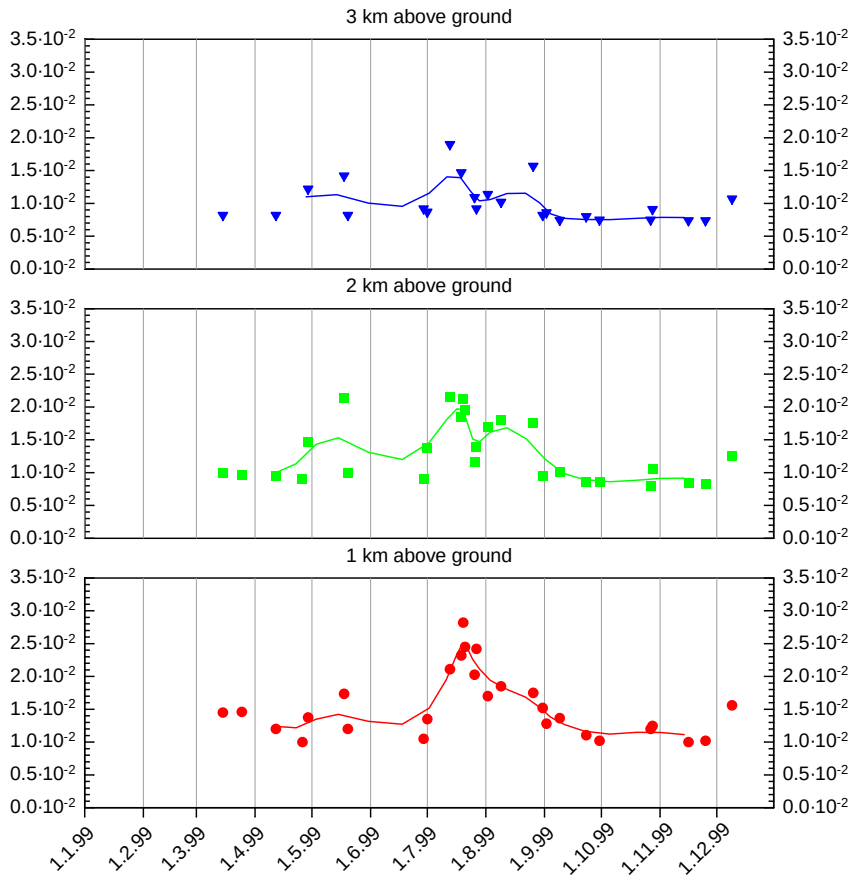

Figure 7.35: Mean annual variation of the 532 nm extinction coefficient; note the high values in the summer—this gives evidence that there is an effective vertical transport mechanism.

very low in aerosol. In fact, there were none of the typically autumnal high pressure episodes that are likely to produce elevated aerosol extinction coefficients due to a lack of air-mass exchange. From the beginning of July until the beginning of September the mean extinction coefficient is enhanced for all three heights. This is the result of the effective vertical transport mechanism in the Alps described in Sec. 8.6. The results in regard to orography are presented in the separate section “Vertical Transport of Aerosol in the Alpine Wind System”.

The data acquisition for this project ended in June 2000 due to the final assembly of the new detection system. As a consequence, no meaningful statistical evaluation for 2000 is possible. However, the results obtained in the previous years seem to be confirmed by the 2000 data. With three years of data the first step for a long-term climatology for Garmisch-Partenkirchen is done. But there is still some way to go in order to get a statistically relevant climatology. Hopefully, the data to be gained during the EARLINET project, which is a successor of the AFS lidar network, can be used to extend the information about climatology of the Loisach valley.

A more detailed summary of the Garmisch-Partenkirchen climatology including a trajectory cluster analysis will be found in the doctoral thesis of S. Kreipl which is to appear in Summer 2001.

Chapter 8

Special observations

8.1 Special observations under high pressure conditions

by M. Wiegner

In addition to the main task within the German Aerosol Lidar Network, the performance of regular measurements in order to establish an aerosol climatology, it was considered useful to observe aerosol distributions during dedicated episodes. Coordinated efforts to investigate the influence of the synoptic situation on diurnal cycles of the aerosol distribution are of special benefit. Intensive observation periods at a single station are also quite valuable to find typical diurnal cycles and time scales of changes in the aerosol distribution. This will help to interpret the regular measurements on the prescribed times in view of their representativeness for the whole day.
With the manpower and resources allocated to this project some first steps towards this challenging goal could be performed sucessfully.
The condition that "the same weather" would occur in whole Germany turned out to be a very restrictive one. The reasons are the variety of landscapes and the quite different climatological conditions at the stations. Consequently, only very few periods were met where the large scale flow was stable for several days over whole Germany. One example of such a period was a week in May, 1998. Measurements in excess to the regular schedule were made from May 11 till May 15 at all stations.
An overview of the synoptic situation and the history of the aerosol parcels met at the stations is given in Figs. 8.1 and 8.2. Shown are the backtrajectories for a period of four days for each of the German Lidar Network stations. Six levels between 975 hPa and 200 hPa are plotted as indicated.
It is clearly seen that the flow regime totally changed during the 5-day period. The transition from advection of polluted continental air masses from southerly directions (see Fig. 8.1) to clear polar air masses as indicated in Fig. 8.2 occured during the night from May 13 to May 14
Selected examples from Hamburg (Fig. 8.3), Leipzig (Fig. 8.4) and Munich (Fig. 8.5) are shown as a North-South cross section of aerosol distributions. To facilitate the comparison between the stations backscatter coefficient profiles β_p are shown, and the same axes were chosen: height up to 8 km and β_p up to 0.01 km^{-1} sr^{-1}.
The profiles from Hamburg (Fig. 8.3) reflect quite well the change of the flow regime: During the first days of the period β_p-profiles are in the order of $6{\cdot}10^{-3}$ km^{-1} sr^{-1} for λ=351 nm in the planetary boundary layer (PBL), whereas during the northern flow backscatter coefficients are less than a third of that values. This change is rather due to a removal of particles than to the influence of relative humidity f. During daytime f was below 40% in most cases, so that a significant growth of the particles is very unlikely. Furthermore, the vertical structure of the PBL changed from a sharp top at about

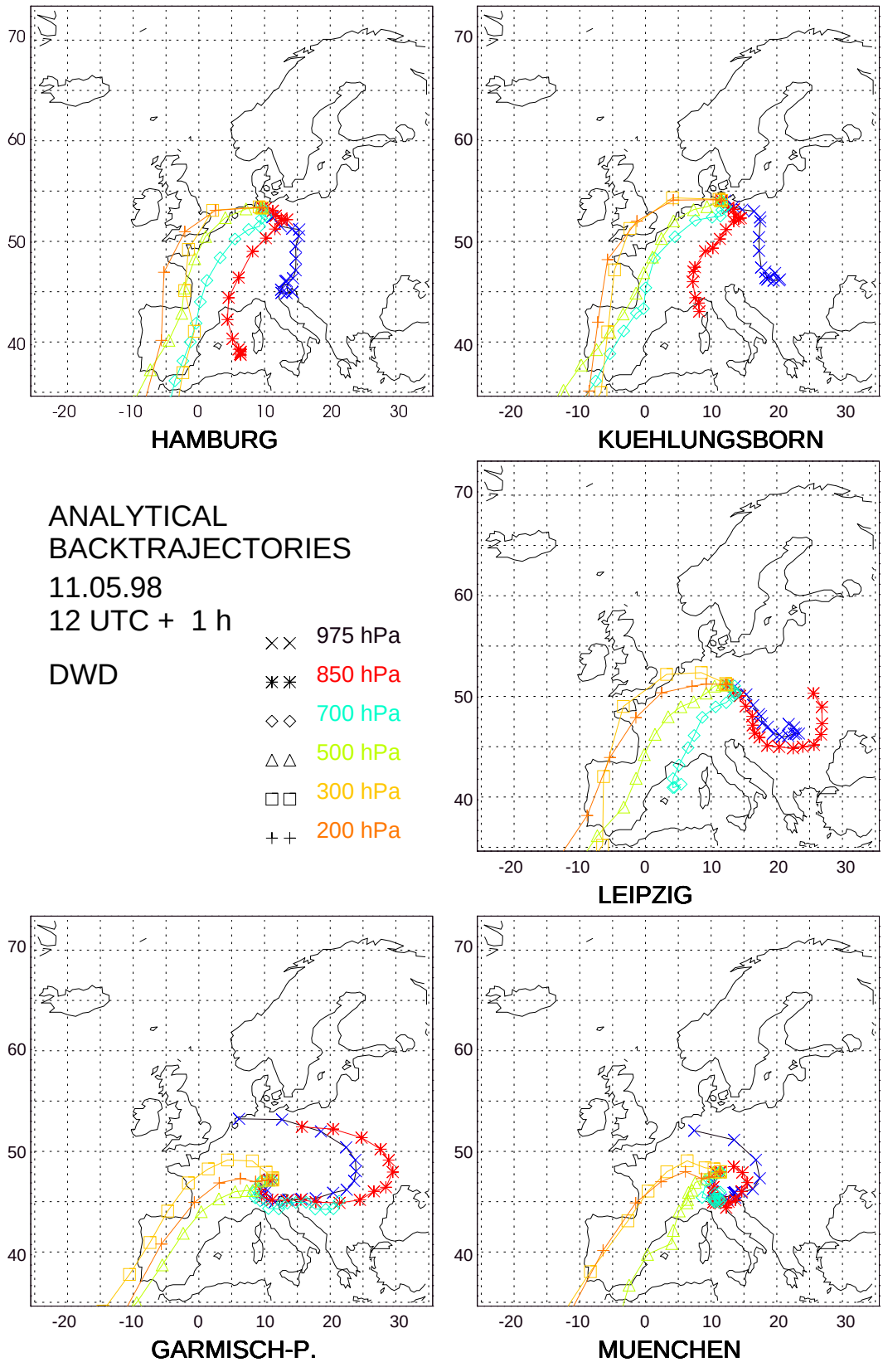

Figure 8.1: Backward Trajectories for the Lidar Network stations with respect to 1300 UT of May 11, 1998

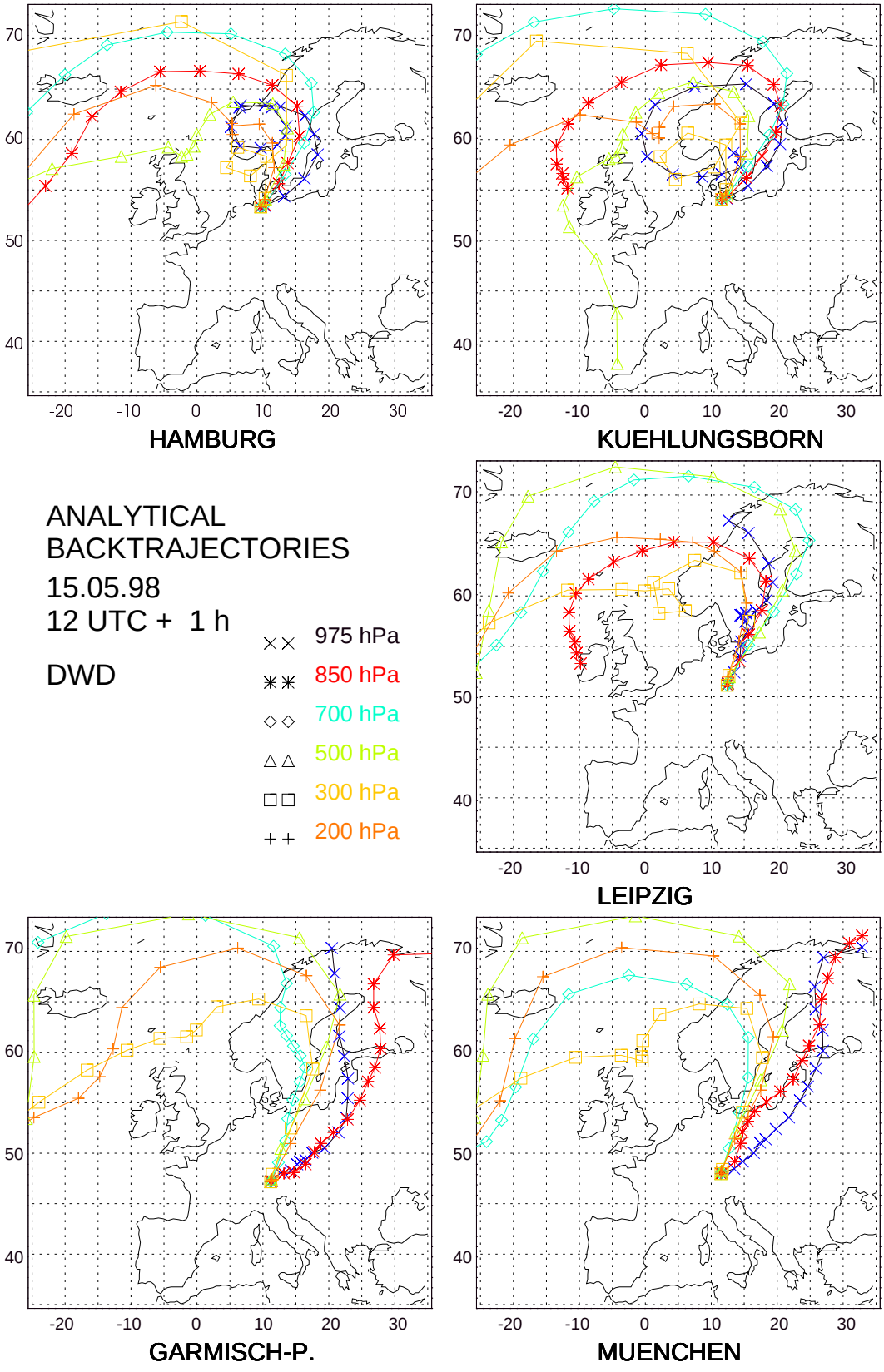

Figure 8.2: Backward Trajectories for the Lidar Network stations with respect to 1300 UT of May 15, 1998

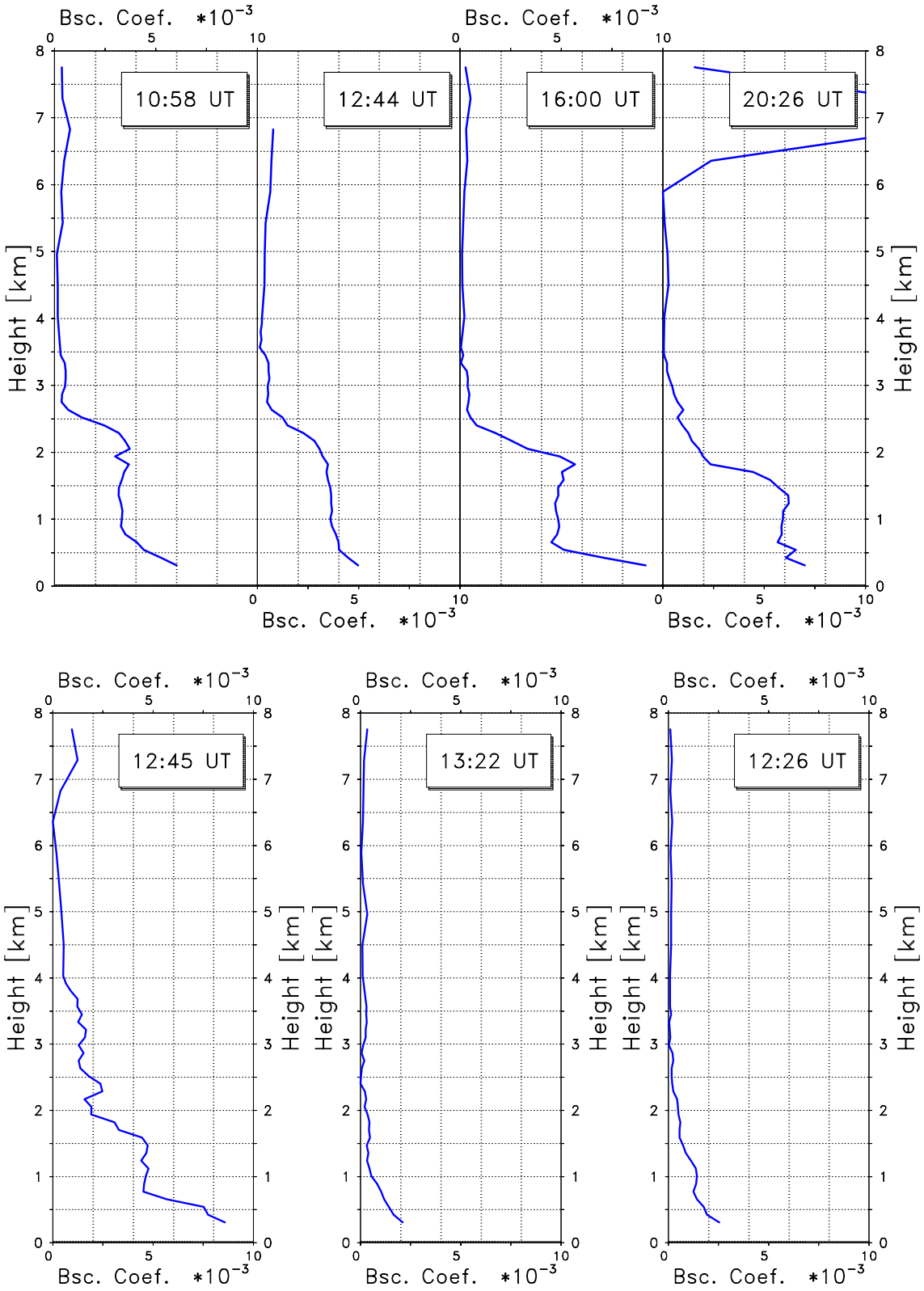

Figure 8.3: *Backscatter coefficients in* $km^{-1}\,sr^{-1}$ *for 351 nm in Hamburg: top: May 11; bottom from left to right: May 12, May 14, May 15; times of the day are indicated*

2 km to a more gradually slope in the clean air. These values agree quite well with measurements from Kühlungsborn (not shown here) which also show $\beta_p \approx 6{\cdot}10^{-3}\,\mathrm{km^{-1}\,sr^{-1}}$ in the UV and about 2-3$\cdot 10^{-3}\,\mathrm{km^{-1}\,sr^{-1}}$ for 532 nm. The relative humidity was in the 40%-range. The PBL was slightly higher. After the transition to the northern flow, aerosol backscatter was even lower than in Hamburg.
A change in the aerosol distribution of similar significance was observed in Leipzig (Fig. 8.4). While for the first three days the PBL-height was in the range of 2.0 to 2.5 km and typical β_p values of 6-8$\cdot 10^{-3}$ $\mathrm{km^{-1}\,sr^{-1}}$ for a wavelength of 532 nm were observed, the following two days show a decrease in PBL-height and aerosol load ($z_{PBL} \approx 1.5\,\mathrm{km}$, $\beta_p \approx 4{\cdot}10^{-3}\,\mathrm{km^{-1}\,sr^{-1}}$). Again, the air was relatively dry, f was in the range of 50% during daytime and 70% during nighttime for the whole period, so that a significant influence of particle growth is rather unlikely.
Further downstream, in Munich (Fig. 8.5), the effect was not that pronounced. The PBL-height – reaching up to 3.0 km – was almost constant for the whole period with the exception of only two profiles between the evening of May 14 and noon of May 15. The backscatter coefficients were comparable with the Hamburg and Kühlungsborn data but significantly lower than in Leipzig. Typically, β_p did not exceed $3{\cdot}10^{-3}\,\mathrm{km^{-1}\,sr^{-1}}$ for 532 nm. After the change of the large scale flow β_p dropped to $1{\cdot}10^{-3}$ $\mathrm{km^{-1}\,sr^{-1}}$ for a limited duration, but at 14 UT on May 15, β_p was at the same order as before. Subsequent measurements were disturbed by low level clouds. The relative humidity showed values in the 30% range close to the surface with an increase to the top of the PBL with $f \approx 65\%$. This finding shows that obviously the flow from North, carrying clear air from the coast to the central part of Germany was not very effective after another 500 km (compared to Leipzig) of transport range. This assumption is confirmed by the trajectories for the 975 hPa and 850 hPa levels which prove (Fig. 8.2) that the flow in the lower troposphere did not come directly from polar regions but experienced a long transport over the continent (Poland). Insofar a direct link to the Leipzig measurement was not existing.
Special conditions are present in Garmisch-Partenkirchen. Due to the strong orographic structure in this Alpine region, in particuar the aerosol distribution in the PBL is much stronger influenced by local orographic driven circulations. Often elevated layers could be observed. Nevertheless, an effect of the change in the large scale flow seems to be present: during the first four days of the period the backscatter gradually increased, whereas on May 15. β_p dropped by a factor of approximately two. The corresponding α_p for two wavelengths as indicated are plotted in Fig. 8.6. This observation corresponds to the Munich data with a time shift of a few hours and can, thus, be attributed to the change of the synoptic situation.
As a by-product of the comparison of the aerosol distributions at Munich and Garmisch a Saharan dust layer 4.5 km above msl. was observed in the late afternoon and night of May 14 and at 3 km the following day (cf. Fig. 8.6).
Summarizing the findings from all stations it can be stated that the absolute values of β_p are comparible with the largest values observed in Leipzig and the lowest in Garmisch-Partenkirchen and Kühlungsborn (last two days only). To categorize the general structure of the aerosol profiles is of course difficult due to their large temporal variability. There are hints that at the continental stations (Leipzig and Munich) the top of the PBL is more pronounced than near the sea (Kühlungsborn, Hamburg). In Garmisch often elevated aerosol layers are observed in the afternoon as a consequence of local circulation pattern characterised by a partial night-time removal of aerosol and daytime aerosol advection (see Sec. 8.4).
It can be seen that at all stations a more or less significant change in the aerosol load happened when the clear airmasses from polar regions arrived at the station, though the precise time cannot be determined from the aerosol data due to observational gaps (e.g., restrictions during night). It is not yet possible to separate the influences of long range transport and local sources on the aerosol distribution. However, the similar behaviour at all stations suggest that the aerosol distribution is not

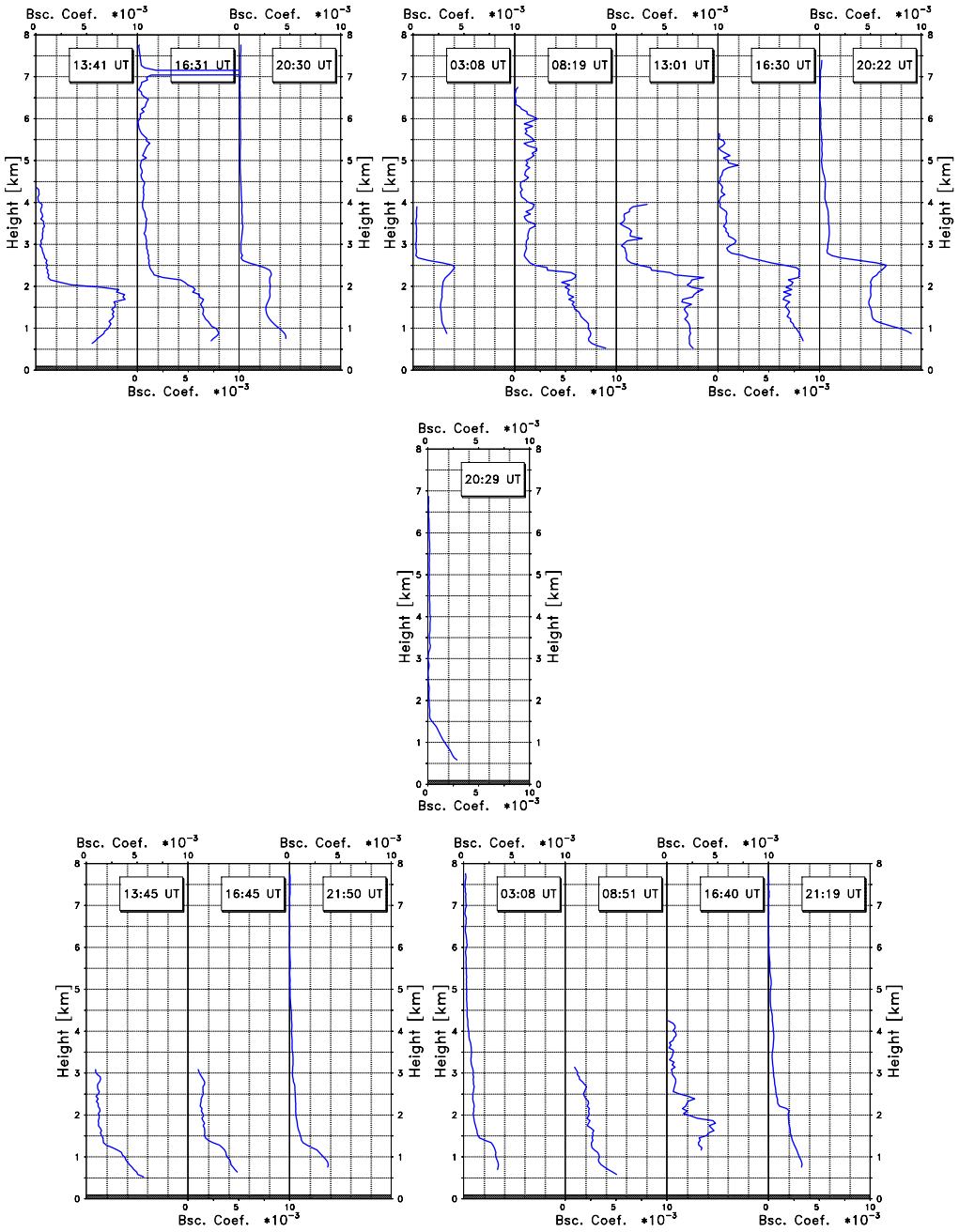

Figure 8.4: *Backscatter coefficients in* $km^{-1}\,sr^{-1}$ *for 532 nm in Leipzig: top: May 11 (left), May 12 (right); center: May 13; bottom: May 14 (left), May 15 (right); times of the day are indicated*

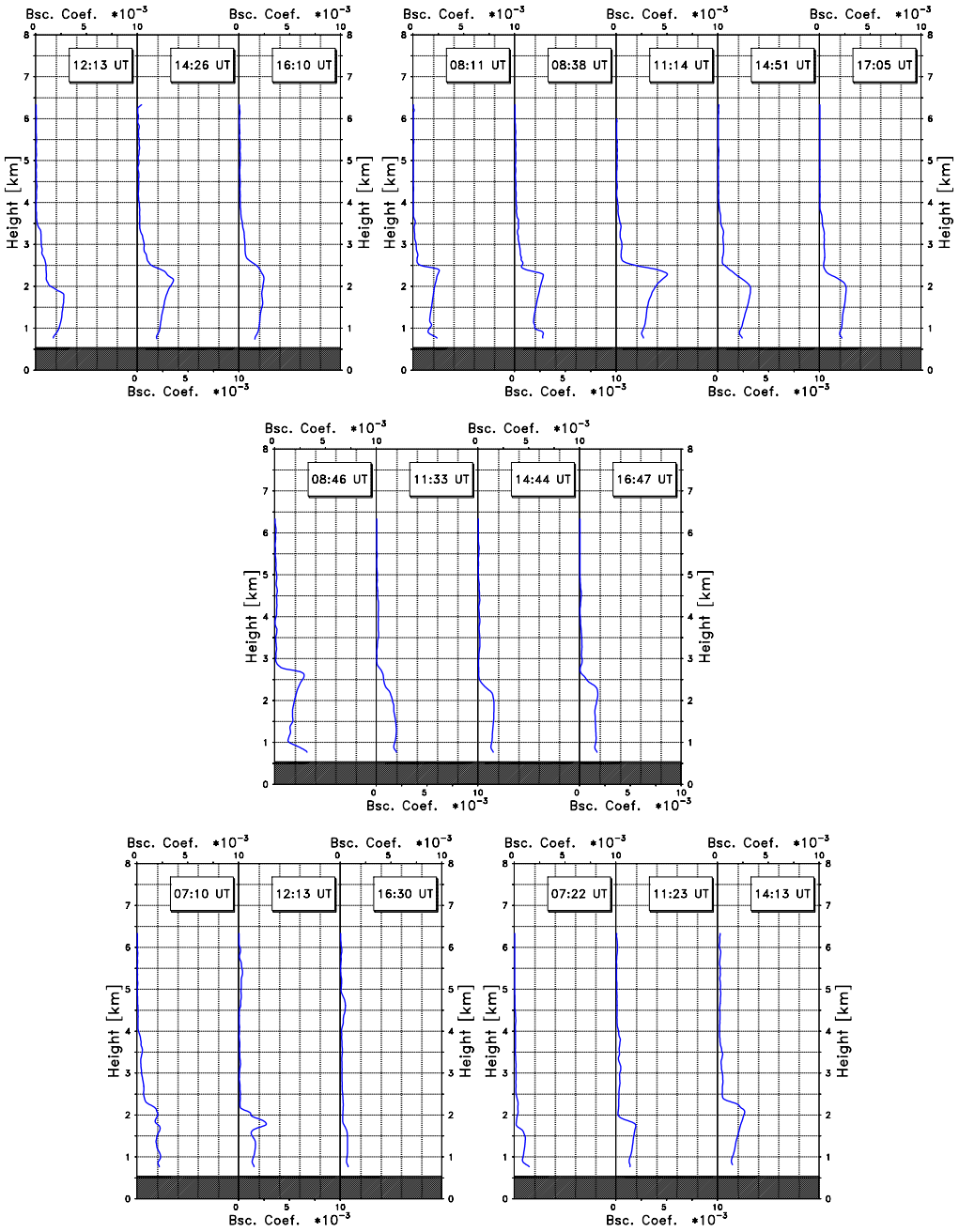

Figure 8.5: *Backscatter coefficients in* $km^{-1}\,sr^{-1}$ *for 532 nm in Munich: top: May 11. (left), May 12. (right); center: May 13.; bottom: May 14. (left), May 15. (right); times of the day are indicated*

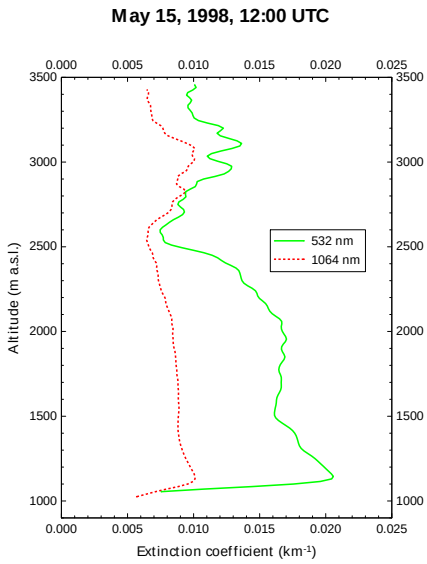

Figure 8.6: *Extinction coefficients for 532 nm and 1064 nm in Garmisch-Partenkirchen: May 15, 1998, 12 GMT*

dominantly determined by local effects.

Another subject addressed by the lidar network is the investigation of the temporal development of aerosol distributions and the influence of orography. The latter is discussed in detail in Section 8.4, but the role of topography was also encountered during the studies of the temporal development. An example is discussed in detail in Section 7.4. The main conclusion is that not only the aerosol backscatter and extinction can change rapidly, but also the height of the PBL by more than 200 m.

Investigations of the temporal behaviour of the aerosol distribution were made over different duration and resolution at all stations of the network. Only two examples are shown here.

The first example concerns measurements on the development of the PBL with 10s resolution (Fig. 8.7). The measurements were taken between 09:07 UT and 10:23 UT of July 29, 1999, in Munich. To ensure comparable atmospheric conditions the line of sight was not changed. As a consequence, it was not possible to derive extinction coefficients α_p, so range corrected signals, or attenuated backscatter, (1064 nm) were plotted instead. It can be seen that the surface layer gradually raised from 0.8 km above ground at 9:07 UT to 1.3 km at 10:10 UT when it merged with the residual layer, which has been present as an individual layer throughout the morning at about 1.5 km. At the top of this layer pre-condensation occured after 10:12 indicating the top of the PBL. It is interesting to see that another persistent layer of only about 100 m in vertical extent has existed, and a rather faint layer at 2.3 km which dissolved at about 09:42 UT. All of these layers showed a wave-like structure in a time domain of a few minutes.

This example shows a frequent feature, that small scale structures are superimposed on the main aerosol layer (the PBL) in the lower troposhere. Though the consequences for the radiation field or the establishment of aerosol climatologies are certainly almost negligible, they are relevant for the evaluation of lidar data. In height ranges, where the aerosol abundance is variable in time and space, the applicability of the two angle approach is seriously limited. To a certain extent these problems can be reduced by temporal averaging but a high temporal resolution is not possible anyway. Furthermore, it its demonstrated that the uncertainty inherent in half-hour-averages of aerosol parameters are not only caused by measurement errors but also on the changing meteorological conditions.

It was found on several occasions that such situations occured in particular one and two hours before

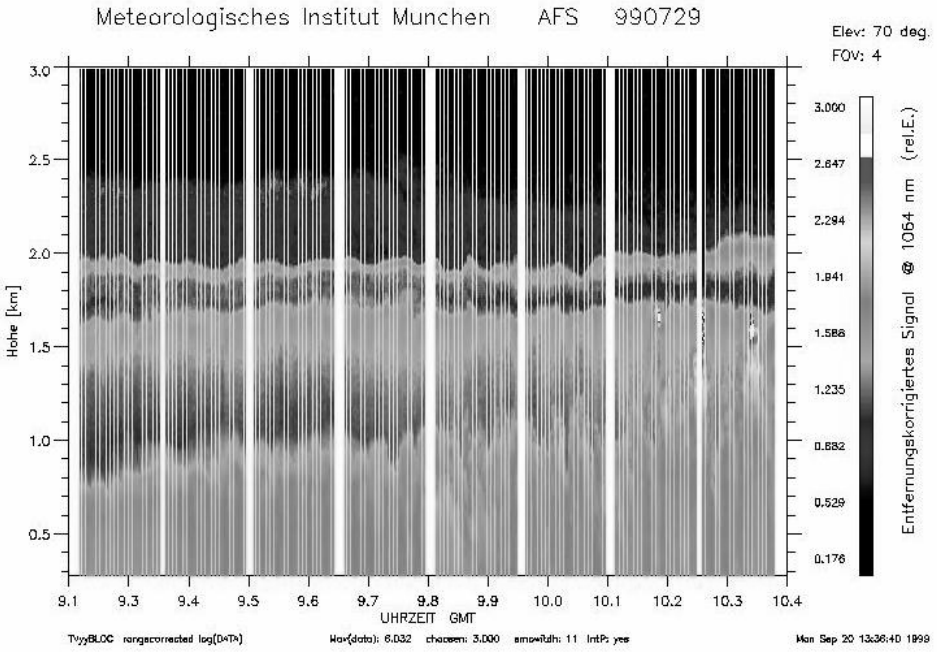

Figure 8.7: *Development of the PBL: range corrected signal for 1064 nm over height above ground (Munich, July 29., 1999)*

local noon.
The variablility of troposheric aerosol layers was also investigated on longer time scales. An example of three consecutive diurnal cycles is shown in Fig. 8.8.
It can be seen that distinct aerosol layers can persist for 12 to 24 hours at different levels. During their lifetime most of them change their vertical extent, altitude and intensity. This example clearly illustrates the problems in linking aerosol profiles of the Lidar Network stations. Though the general distributions and optical depths can be expected to be similar under similar meteorological conditions – this was demonstrated during the May 1998-period – the direct comparison of individual profiles will be limited to very rare situtations. Interpretations of aerosol profiles in view of meteorological conditions should rather be made on the basis of local averages.

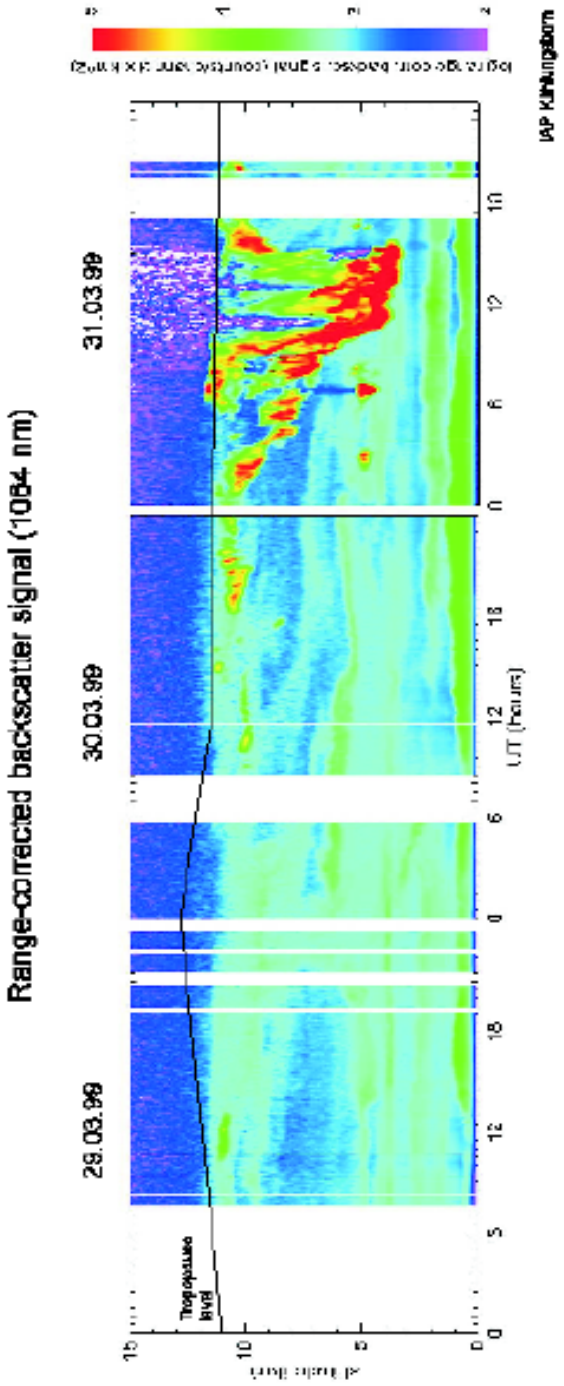

Figure 8.8: *Time series of the tropospheric aerosol distribution: range corrected signal for 1064 nm over height above ground (Kühlungsborn, March 29 till 31, 1999)*

8.2 Special observations for cold front passages

by R. Eixmann

In this work cold front passages are defined as boundaries between air masses which are characterized by different meteorological parameters, as for example temperature, humidity and aerosol content. The air mass boundary itself is recognized by significant weather changes. The usual distinction in front passages of polar and subpolar type is not considered to be relevant here, since the air mass boundary is present in both cases.
One objective of the German Lidar Network was to perform measurements shortly after cold front passages. From the meteorological point of view it was very unlikely to find favorable weather conditions short after the front passed. Frequently, strong convection prevented lidar measurements short after the front passage. This phenomenon was not restricted to daytime, since the lidar station Kühlungsborn is located close to the Baltic Sea, which frequently had a higher temperature than the air. This led to strong convective activity near the coastline also during nighttime.
Measurements after cold front passages are of high interest, because an exchange of air masses occurs in very short time (hours). The new air mass is characterized by different origin and optical properties of the aerosol particles. Additionally, it turned out that frequently after a cold front has passed, a stable high pressure period built up. Thus, the measurements taken after cold front passages were also the first in a series of measurement during the high pressure period.
Another important task was the comparison of aerosol properties of air masses crossing more than one lidar station of the network. In January 2000, a frontal passage crossed Germany from North to South, traveling over the lidar stations Hamburg, Kühlungsborn, Leipzig, Munich and Garmisch-Partenkirchen within 36 hours. In total, 16 cold front passages have been observed at Kühlungsborn in the time frame of the German Lidar Network. From 14 of those measurements aerosol backscatter profiles could be calculated, in the other 2 cases the cloud base height was too low for evaluation. For the trajectory analysis, however, all 16 days were used.

8.2.1 Trajectory analysis

In order to investigate whether air masses with different geographical origin show different aerosol backscatter coefficients, a trajectory cluster analysis was performed. The algorithm is similar to that used in chapter 6 of this report and will be described in detail in (Eixmann, 2001) Basis for the analysis were the backward trajectories for the days of the frontal passages with arrival times above Kühlungsborn at 13:00 and 19:00 UT. This has been done for the pressure levels 975, 850, 700, and 500 hPa. From the analysis emerged, that vertical wind shearings were dominant after front passages. At the 500-hPa level, westerly winds prevailed, independently of the wind direction at the 975- and 850-hPa levels. These levels show a significantly higher variability. At the 850-hPa level, the air mass origin after the cold front passage was north-west in 80% of all cases, while at 20%, the origin was above the continent, from south-east. Figure 8.9 gives the result of the cluster analysis for the 850-hPa and 700-hPa level, representative for the other altitude levels. The air masses after the frontal passage originated mainly from the North Atlantic. This means that the front passed from north-west towards south-east. The second most frequent direction after the frontal passage is south-east. This requires that the front passed from south-east to north-west, containing air masses with continental origin. Regarding the vertical development of the backward trajectories it could be stated that the air masses were mixed vertically only to a very small extend. Figure 8.10 gives the vertical evolution of the backward trajectories for Kühlungsborn at 850 hPa and 700 hPa. The trajectories show as well

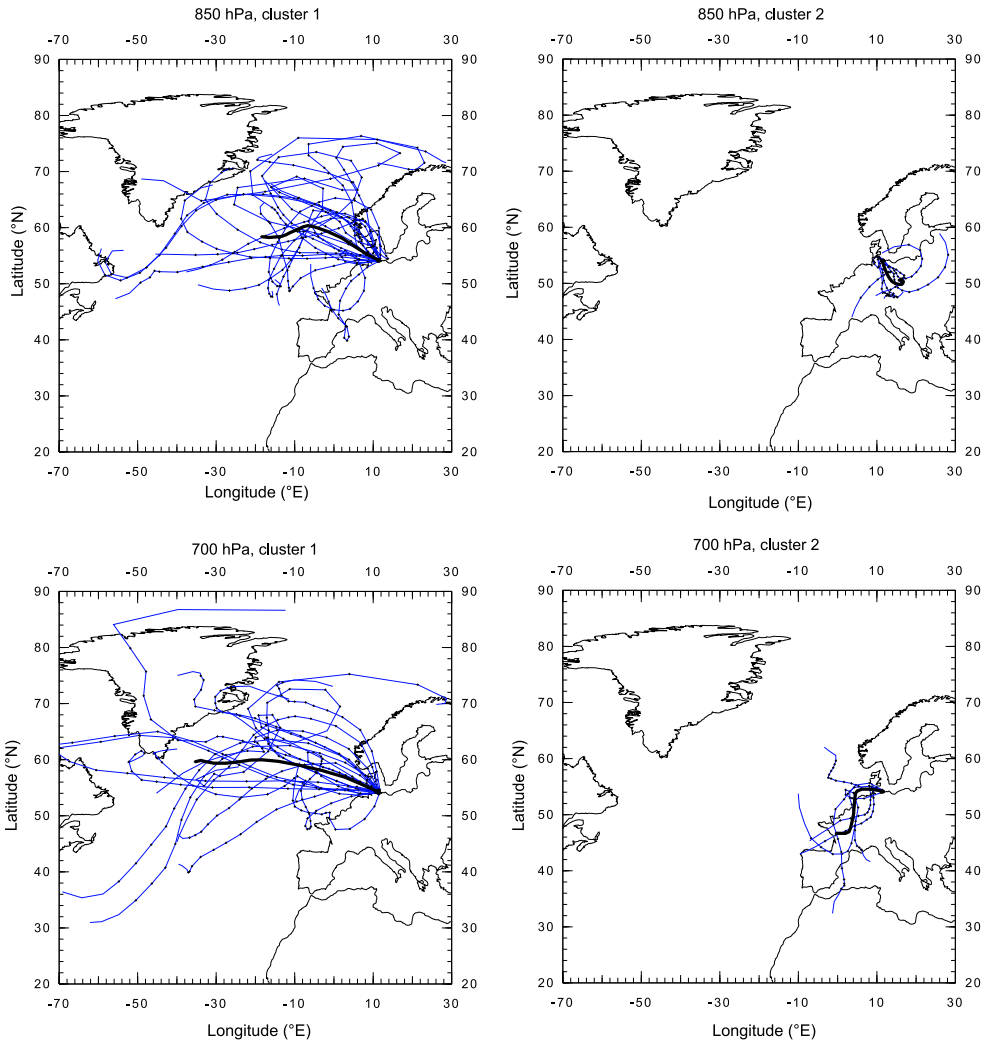

Figure 8.9: Cluster analysis of the backward trajectories for all observed cold front passages. The 2 dominating clusters are given for 850 hPa (upper row) and 700 hPa (lower row).

upward and downward motion but do not show a general vertical movement.
Regarding the performed cluster analysis, the following picture emerges (Figure 8.11): All backscatter profiles are plotted with respect to their trajectory cluster. The straight lines represent the profiles after the frontal passage, the dotted lines represent measurements short before the front passage. The comparison between the cluster does not reveal a significant difference of the backscatter profiles with respect to the different clusters. This implies, that the aerosol backscatter coefficients are independent from the air mass origin.

8.2.2 Wavelength dependency of the measured profiles

In order to be able to quantify the air masses better, the backscatter coefficients were analyzed by their wavelength dependency. For this reason, the data points were normalized to the value measured at 532 nm. Two selection criterioa were used: 1. selection by air mass origin (cluster analysis) 2. selection by season.The results are plotted in Figure 8.12. It turns out that there were no significant differences in the wavelength dependency, neither with respect to the trajectory clusters nor to the seasonal changes.

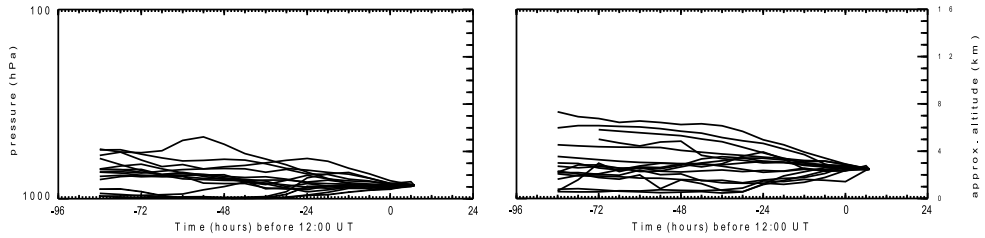

Figure 8.10: Vertical evolution of the backward trajectories of all observed cold front passages, for 850 hPa (left) and 700 hPa (right).

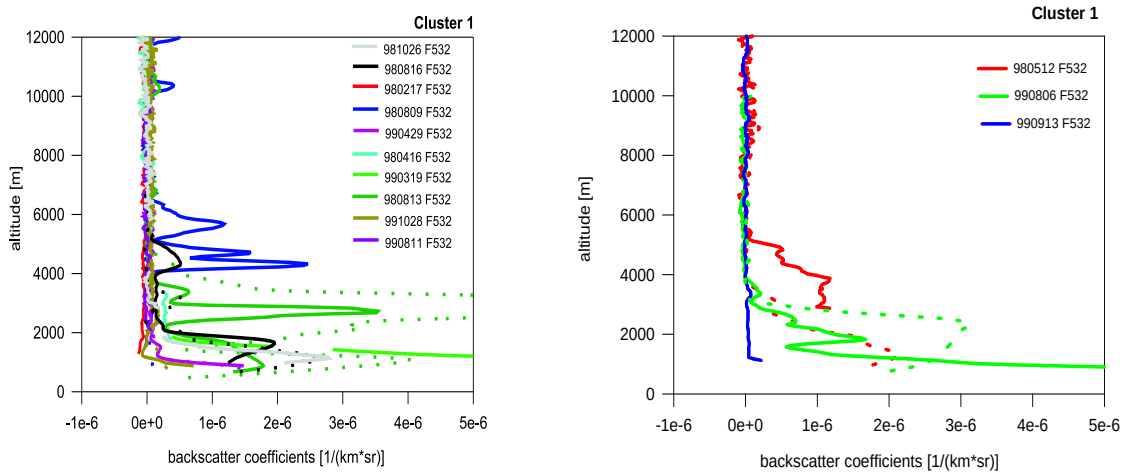

Figure 8.11: Backscatter coefficients measured before and after cold front passages, sorted by trajectory clusters as given in Figure 8.9.

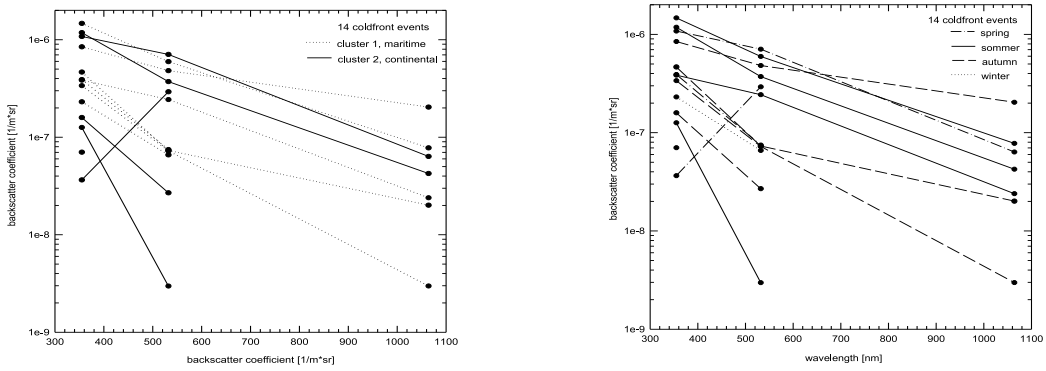

Figure 8.12: Comparison of the wavelength dependency of the normalized aerosol backscatter coefficients measured after the frontal passage between the boundary layer top and 5 km. Left: grouped by trajectory clusters, right: grouped by season.

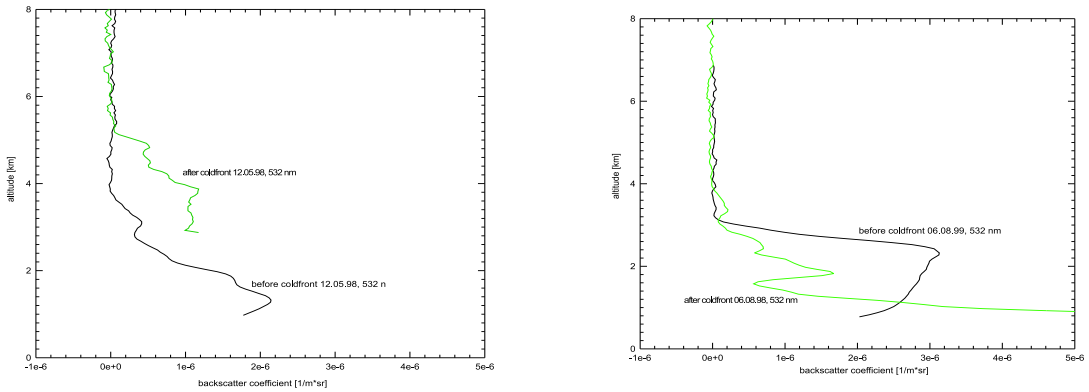

Figure 8.13: Examples of backscatter profiles measured at Kühlungsborn before and after a cold front passage. Left: stronger boundary layer after the passage, right: weaker boundary layer after the passage.

8.2.3 Comparison of the backscatter coefficient before and after a cold front passage

Backscatter profiles measured before and after a frontal passage were compared. Additionally to the total of 14 measurements taken after the frontal passage, 8 measurements have been taken before the passage (up to 48 hours). The variability of the investigated air masses was so high, that no significant differences in the backscatter coefficients could be found before and after the frontal passage. As an example, two profiles of backscatter coefficients are shown in Figure 8.13, one showing a stronger, the other showing a weaker boundary layer after the passage.

8.2.4 Cold front passage January 17-19, 2000, over several stations of the Lidar Network

One objective for lidar measurements after frontal passages was to try to investigate the same air mass at different lidar stations. Between January 17^{th} and 19^{th}, 2000, such an occasion occurred, when an air mass change moved from northern to southern Germany, with the corresponding cold front crossing the lidar stations Hamburg and Kühlungsborn on the 17^{th} around noon time, Leipzig during the 18^{th}, and reaching Munich and Garmisch-Partenkirchen on the 19^{th} of January. The trajectories calculated for Leipzig and Garmisch-Partenkirchen (Figure 8.14) passed over northern Germany for all altitude levels, thereby allowing the comparison of backscatter profiles of the same air masses. Additionally, after the air mass change, an aerosol layer was observed by 4 stations. At Munich, no measurements were possible due to bad weather conditions. In order to characterize changes of the aerosol properties on their way from northern to southern Germany, backscatter profiles measured at Hamburg and Kühlungsborn were compared with profiles obtained at Leipzig and at Garmisch-Partenkirchen.
Following the backward trajectories ending at Garmisch-Partenkirchen on January 19 in different altitude levels, it turns out that they crossed the lidar station at Hamburg only a short time before. For the ending point Leipzig, January 18, it can be seen that these air masses moved over Kühlungsborn a few hours before. (Figure 8.14)
A comparison of the backscatter profiles was now possible under the condition that the time interval between the measurements corresponds to the time the air mass needed for traveling from Hamburg

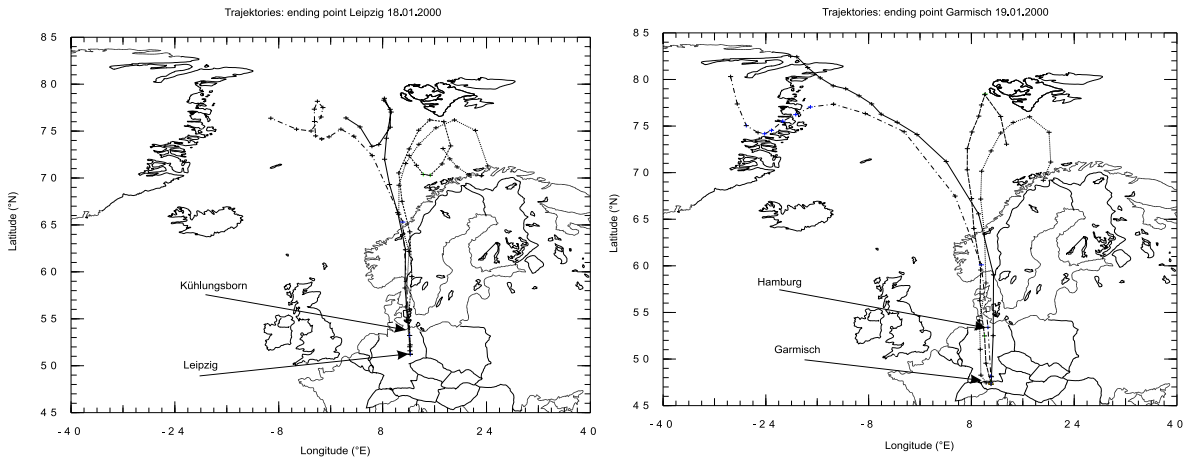

Figure 8.14: Backward trajectories ending at Leipzig on January 18, 2000 (left), and at Garmisch-Partenkirchen on January 19, 2000. Dotted line: 850 hPa, short dashed line: 700 hPa, solid line 500 hPa, dash-dotted line: 300 hPa.

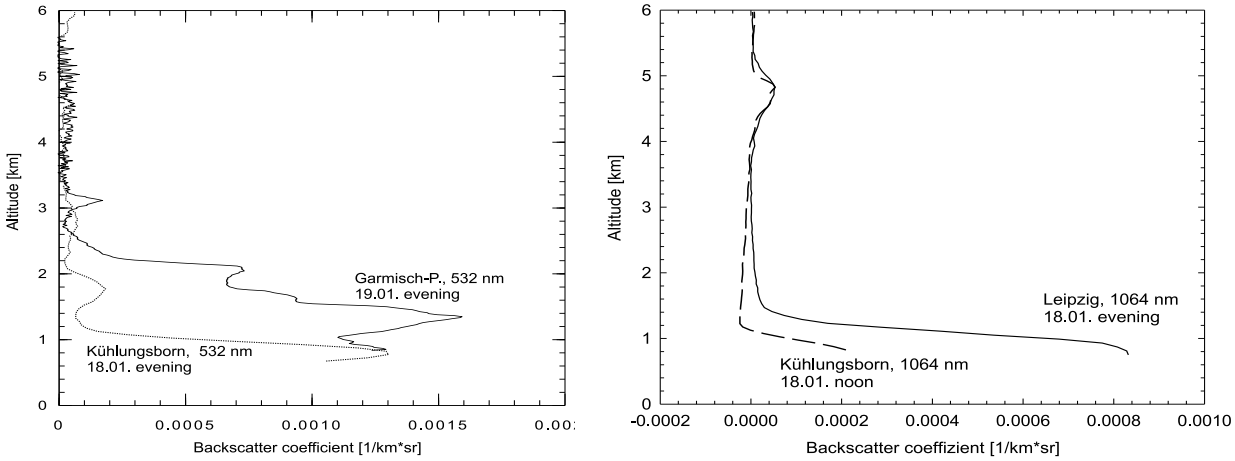

Figure 8.15: Comparison of backscatter coefficients measured in the same air mass during its movement from northern to southern Germany. Left: Kühlungsborn, January 18, and Garmisch-Partenkirchen, January 19. Right: Kühlungsborn, noon of January 18, and Leipzig, evening of January 18.

to Garmisch-Partenkirchen and from Kühlungsborn to Leipzig, respectively. The comparison (Figure 8.15) reveals, that over the long distance between Hamburg and Garmisch-Partenkirchen the shape and height of the planetary boundary layer (PBL) has changed, but the aerosol layer is still present and has slightly increased in height. Between Kühlungsborn and Leipzig the PBL height differs only to a very little extent, and the aerosol layer is observed at almost the same altitude.

While the comparisons above investigated the same air masses at different times, a comparison of the lidar stations was possible simultaneously, but in a different measurement volume (Figure 8.16). Although the horizontal distance is only about 200 km, both stations observe different air masses, as the trajectories reveal. the PBL height is significantly higher at Hamburg. The The aerosol layer can be seen at both stations, but it is about 1 km lower above Hamburg than it is above Kühlungsborn.

The aerosol layer observed at all station can be characterized by the following properties: It shows a slope from east to west, since it was observed at Hamburg and Garmisch at 3.8 and 3.2 km, respectively, and at K'born and Leipzig at about 4.8 km. Also, it shows a slight slope from north to south.

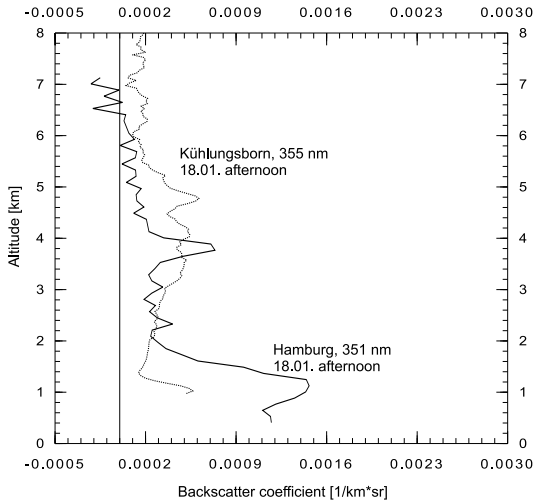

Figure 8.16: Comparison of backscatter coefficients measured on January 18, afternoon, above Kühlungsborn and above Hamburg.

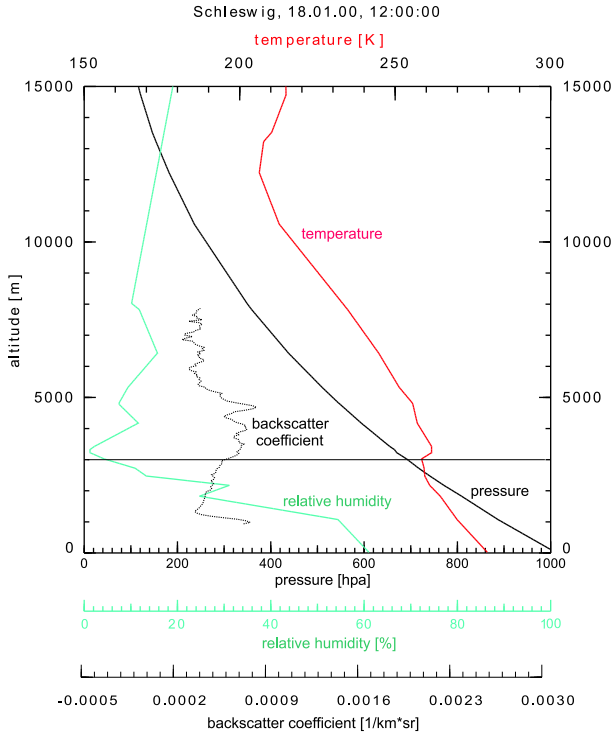

Figure 8.17: Temperature, pressure and relative humidity obtained from a radiosonde launch at Schleswig (approx. 150 km north-west), along with the backscatter profile measured at Kühlungsborn on January 18. Between 3 and 5 km, the relative humidity is below 15%. The temperature profile shows an inversion at 3 km, limiting vertical exchange with the altitudes below.

Data from a radiosonde launch at Schleswig (Figure 8.17) reveal that this aerosol layer was in an altitude region with a very low relative humidity. The vertical development of the backward trajectories shows, that 72 hours prior to the measurement, the air mass has been lifted from the boundary layer into the free troposphere by a low pressure system north of the scandinavian coast.
Using a night time measurement at Kühlungsborn which yields 3 backscatter and 2 extinction coefficients of the aerosol layer, a comparison with the data from the OPAC software package (Optical Properties of Aerosols and Clouds, (Hess et al., 1998)) indicated that the aerosol layer over Kühlungsborn consisted of small particles.
Since the uplifting of the air mass occurred several days prior to our measurements, the aerosol particles have had a lifetime long enough to be detected over Germany. After the uplifting due to a strong baroclinic state of the atmosphere no vertical displacement has taken place until the air masses reached Germany. This agrees with the observation of a temperature inversion (Figure 8.17) which suppresses the vertical mixing of the atmosphere in this altitude range and is a condition for the long lifetime of such aerosol layers. The frequently assumed short lifetime of aerosol particles in the free atmosphere is not valid for cases like this.

8.3 The stratospheric aerosol layer observed by lidar at Garmisch-Partenkirchen

by H. Jäger

8.3.1 Introduction

Stratospheric aerosol particles influence the radiation budget directly by scattering and absorption of radiation and indirectly by heterochemical processes affecting the stratospheric ozone layer. During the past decades lidar remote sensing has proved to be invaluable in detecting and monitoring the occurrence, magnitude, spread and decay of numerous volcanic eruption clouds perturbing the stratospheric aerosol layer. Lidar measurements at Garmisch-Partenkirchen (47.5°N, 11.1°E) have contributed to the understanding of the stratosphere since 1976. The interest in the stratospheric aerosol layer consisting of sulfuric acid droplets grew considerably in the past decade when heterogeneous ozone destruction mechanisms were proposed to take place on these aerosol particles even under moderate stratospheric conditions in addition to the highly effective reactions on polar stratospheric clouds.

This report is a contribution to the German research program Aerosolforschungsschwerpunkt (AFS) and summarizes observations of the stratospheric sulphate aerosol layer during the AFS period 1997 to 2000. The observations also contribute to the international Network for the Detection of Stratospheric Change (NDSC) as part of the program of the Alpine Station, one of five primary NDSC sites.

The presently very low aerosol level in the stratosphere is suitable to study processes which sustain a minimum stratospheric aerosol content. However, observations of the stratospheric aerosol layer during the period of the AFS program can only be understood and interpreted when referring to the preceding years, which were governed by a volcanic event of global impact, namely the violent eruption of Mount Pinatubo in the Philippines (15.1°N, 120.4°E) on June 15, 1991. This eruption caused one of the major perturbations of the stratosphere in the past century and produced the largest volcanic cloud ever observed in the stratosphere by lidar and other advanced techniques. The Pinatubo eruption injected initially 12–15 Mt of sulfur dioxide into the stratosphere, as estimated by (McPeters, 1993), or 20 Mt after (Bluth et al., 1992), resulting in a global stratospheric aerosol mass load of sulfuric acid amounting to 20–30 Mt, as deduced from SAGE II satellite data by (McCormick and Veiga, 1992). Spread and decay observations of the Pinatubo eruption cloud at Garmisch-Partenkirchen were summarized by (Jäger, 1992), (Jäger, 1996), and (Jäger et al., 1997).

8.3.2 Observations

The backscatter lidar at Garmisch-Partenkirchen utilizes a Nd:YAG laser as the radiation source transmitting 532-nm pulses into the atmosphere. Elastic backscatter by molecules and particles is recorded with a 52-cm-diameter telescope, a photomultiplier tube, and a photon counter. The system provides information on the height distribution of the particle backscatter coefficient. These profiles are calibrated with calculated backscatter profiles of a purely molecular atmosphere derived from actual data of the Munich radiosonde (100 km north of Garmisch-Partenkirchen). All profiles are corrected for extinction losses by particles and molecules including ozone.

Parameters important in the understanding of the impact of stratospheric aerosols on climate and heterogeneous chemical processes are the optical depth, the mass and the surface area concentration

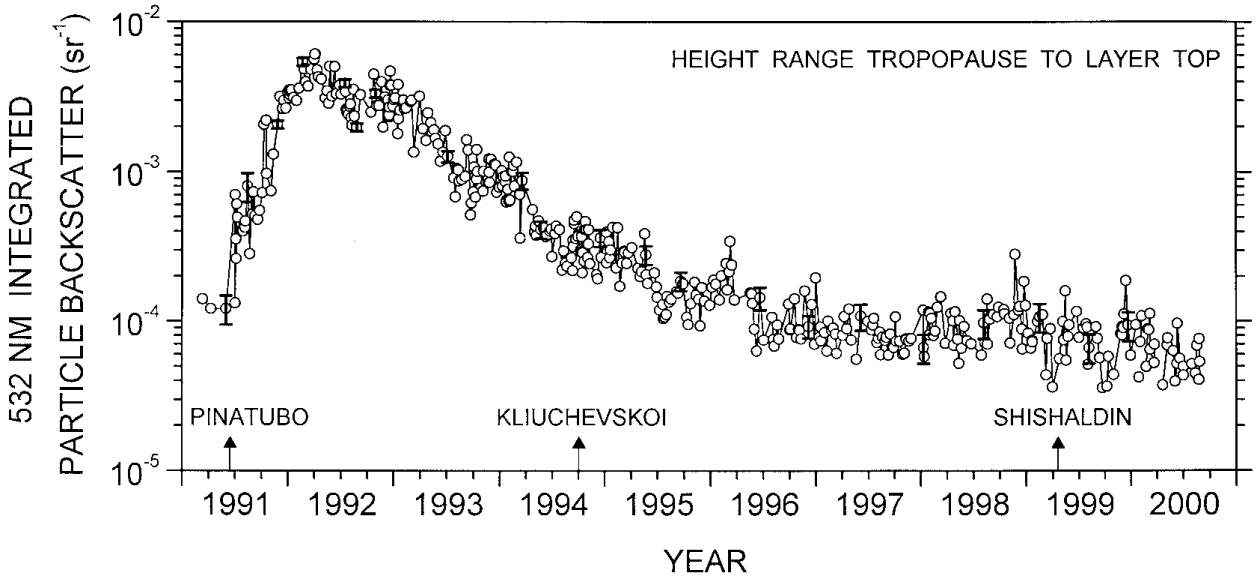

Figure 8.18: Integrated particle backscatter coefficient in the height range tropopause to the top of the aerosol layer.

of stratospheric particles. These parameters are calculated using conversion factors derived from a time and height resolving aerosol model based on monomodal and bimodal size distributions of the stratospheric sulfuric acid aerosol derived from balloonborne particle counter data from Laramie (41°N), Wyoming (Jäger and Hofmann, 1991; Jäger et al., 1995; Jäger et al., 1997).

8.3.3 Results

8.3.3.1 Pinatubo episode

The observations of the build-up, the maximum, and the decay of the Pinatubo perturbation at the northern midlatitude site of Garmisch-Partenkirchen is documented in the time series of the column backscatter coefficient, integrated over the height range tropopause to layer top (Figure 8.18). The integral backscatter is modulated by column height fluctuations caused by the seasonal tropopause height variation. The tropopause fluctuates between 8 and 15 km according to the Munich radiosonde, with typical summer values in the 12–13 km range and winter values at 10–11 km.
The height distribution of aerosols is indicated in Figure 8.19 by profiles of the scattering ratio which is the ratio of measured total to calculated molecular backscatter. Maxima of the scattering ratio are mostly observed in the height range 15 to 20 km with exceptions after volcanic eruptions.

8.3.3.2 Background aerosol

It has become obvious from the results obtained during this project that the observed exponential decay of the Pinatubo aerosol load terminated in 1996. Some characteristic values of the aerosol layer are summarized in Table 8.1.
The ongoing low level of aerosol concentration in the stratosphere allows also small volcanic input to be observed which under highly perturbed volcanic conditions would remain undetected. A recent natural input was caused by the eruption of Mt. Shishaldin (Aleutian Islands, Alaska) on April 19,

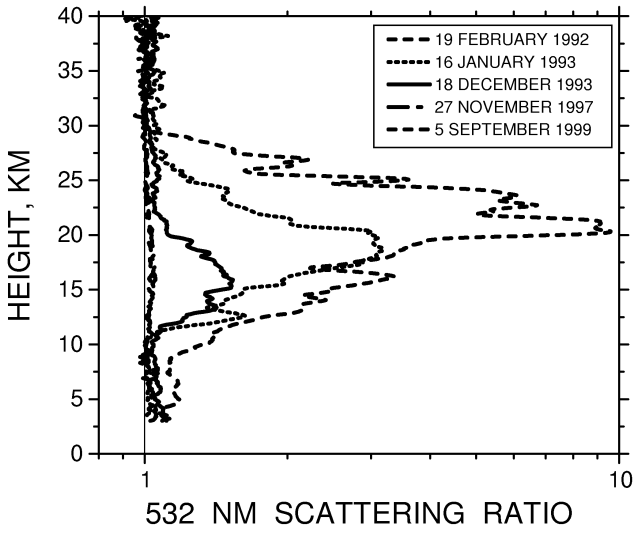

Figure 8.19: Profiles of the 532 nm scattering ratio showing maximum and decay of the Pinatubo eruption cloud over Garmisch-Partenkirchen.

Table 8.1: Characteristics of 1997–1999 background and Pinatubo maximum.

Integral Tropopause to layer top	1997–1999 Average	Range Min	Range Max	Pinatubo Maximum April 1992
532 nm part. backscatter, sr^{-1}	$8.8 \cdot 10^{-5}$	$3.6 \cdot 10^{-5}$ – $2.8 \cdot 10^{-4}$		$4.8 \cdot 10^{-3}$
532 nm part. optical depth	$4.4 \cdot 10^{-3}$	$1.8 \cdot 10^{-3}$ – $1.4 \cdot 10^{-2}$		0.16
Particle mass, g m^{-2}	$1.6 \cdot 10^{-3}$	$6.7 \cdot 10^{-4}$ – $5.3 \cdot 10^{-3}$		0.062
Particle surface m^2 m^{-2}	0.023	0.01 – 0.075		0.32

1999 (GVN, 1999). Observations of small but distinct peaks in the lidar scattering ratio in the height range 14 to 18 km were made on May 6, 16 and 29, June 23, and July 1 (Figure 8.20). Isentropic backward trajectories calculated at CMDL/NOAA for May 6 and 16 confirm that the lidar peaks were caused by the Shishaldin eruption cloud. Figure 8.21 shows trajectories starting at 15 km at Garmisch-Partenkirchen on May 6, 12 UT, and May 7, 00 UT. Since the trajectory calculation is limited to 10 days, the calculation was restarted on May 2, 00 and 12 UT, half-way in time and location between the first trajectory pair (Jäger et al., 2000). Both secondary trajectories arrived at about 14 km over the American west coast between April 23 and 25, in an area where the Shishaldin aerosol layer was detected by POAM III (Polar Ozone and Aerosol Measurement) satellite observations between 12 to 16 km (GVN, 1999).

In comparison with earlier episodes detected at Garmisch-Partenkirchen the Shishaldin eruption was of minor strength and did not cause a major perturbation at northern midlatitudes.

An increase in fuel consumption of 4% per year (Schmitt and Brunner, 1997) draws attention to long-distance air traffic as a possible anthropogenic in-situ source for stratospheric aerosols. Garmisch-Partenkirchen is very close to major air traffic corridors and in the lee of the West European and North

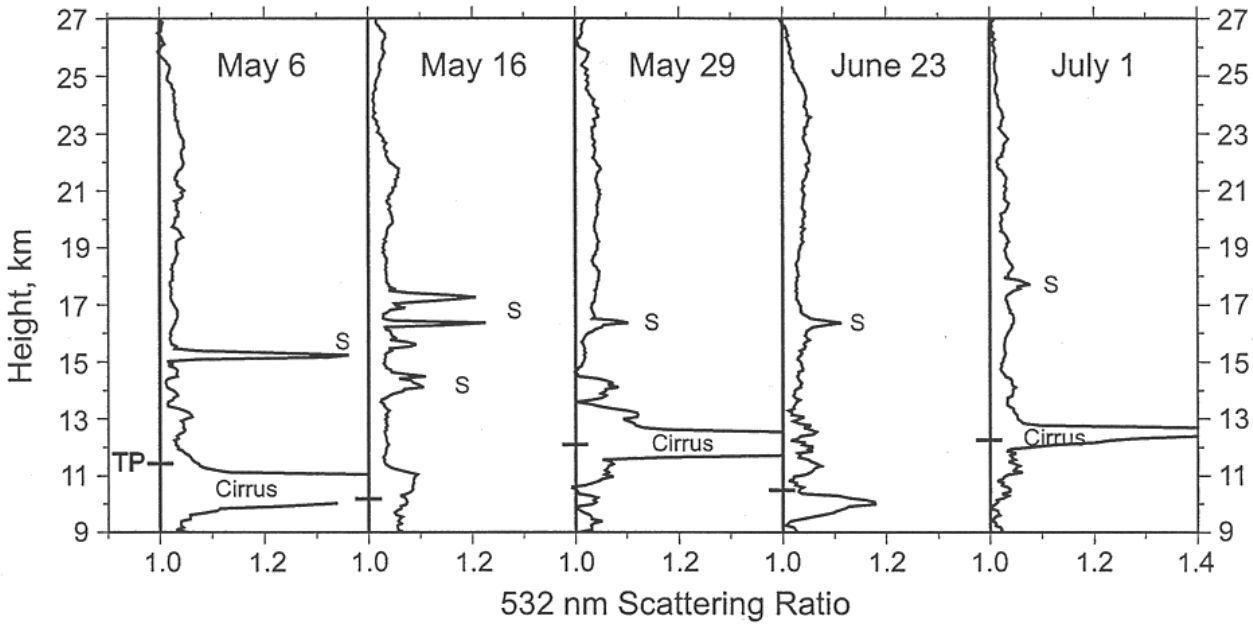

Figure 8.20: Lidar profiles of the scattering ratio of the stratospheric background aerosol with peaks of Shishaldin aerosols (S). TP marks the tropopause (Munich radiosonde).

Atlantic air traffic. Many lidar measurements seem to be affected by air traffic aerosols generated in the European and North Atlantic aviation corridors. Figure 8.22 shows optical depth values in the height range of air traffic (8–13 km) derived from lidar measurements. About 40% of those profiles not affected by cirrus clouds show increased extinction with respect to what is regarded as the natural background. This enhancement is not connected with the stratospheric aerosol layer. First results of a closer inspection of the backscatter signals show low depolarization values of few per cent. This is characteristic for very small or near-spherical particles (Jäger et al., 1998), most probably formed from the exhaust components soot, sulfuric acid, nitric acid, and water (Kärcher and Fahey, 1997). On the other hand, high depolarization ratios of about 50% prevail in contrails and cirrus clouds due to the presence of ice crystals.

8.3.4 Conclusions

The program in remote sensing of the stratospheric sulfate aerosol layer by ground-based lidar began at Garmisch-Partenkirchen in 1976. Figure 8.23 shows the entire time series since 1976, which is characterized by the major volcanic perturbations caused by El Chichon in 1982 and Pinatubo in 1991, and by a number of minor eruptions in the northern hemisphere. Lidar data of recent years indicate that the new background following the decay of the Pinatubo load varies around the 1979 average. The winter maxima associated with low tropopause heights stay rather constant above this value, whereas the summer minima (high tropopauses) exhibit a slow decay below the 1979 value. The lower integration limit for summer columns is 13 to 15 km, for winter columns 10 to 12 km. Summer columns thus exclude the height range of air traffic, winter columns include part of it. It may be concluded that in the stratosphere above 13 km some decay of the aerosol load is still going on which is compensated by a natural or anthropogenic aerosol increase in the lowermost stratosphere below 13 km.

The question regarding the existence of an air traffic signal in the aerosol content of the lower strato-

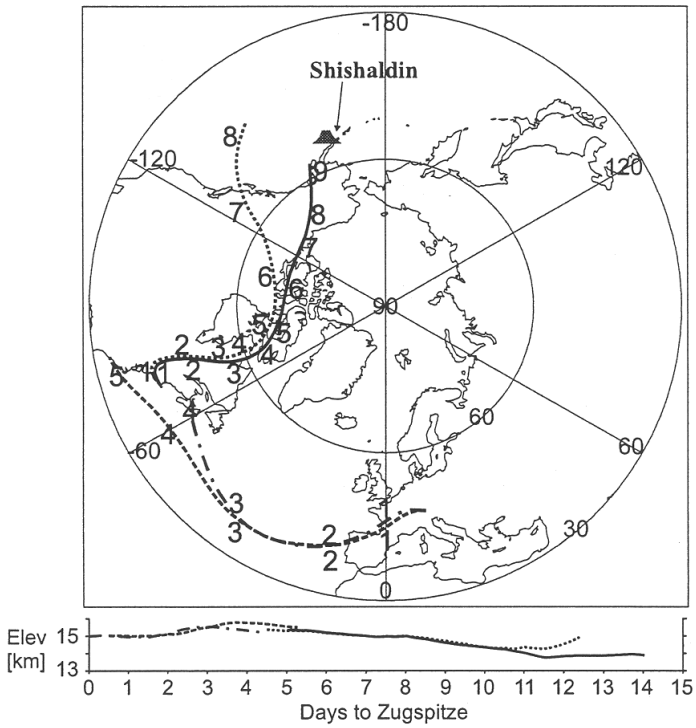

Figure 8.21: Isentropic backward trajectories starting at Garmisch-Partenkirchen at a height of 15 km on May 6, 12 UT and May 7, 00 UT, and restarting on May 2, 00 UT and 12 UT. The calculations are based on NCEP meteorological data.

sphere can only be answered conclusively by analysing existing data and by further observations of the variability of the stratospheric background aerosol undisturbed by major volcanic eruptions.

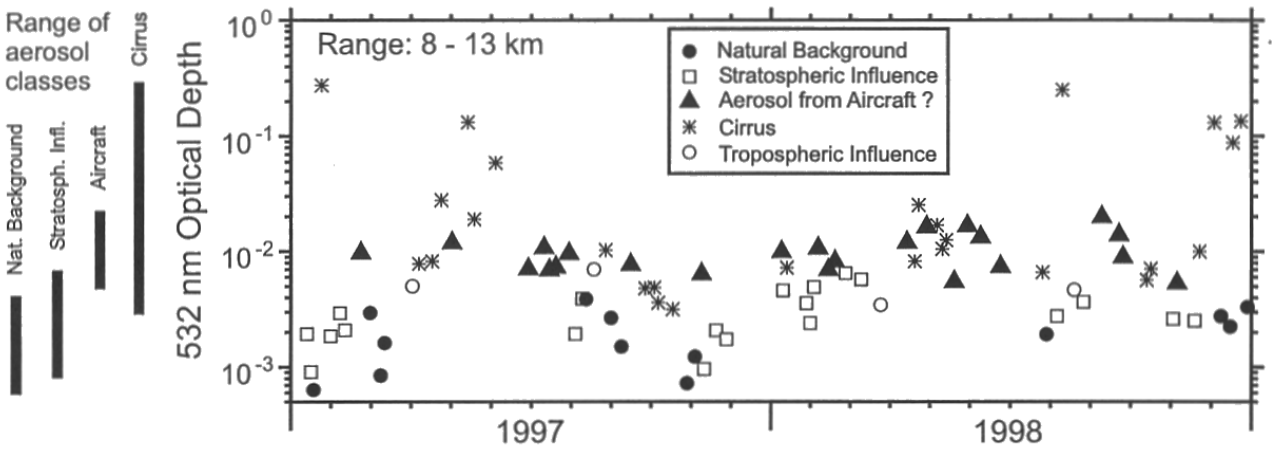

Figure 8.22: Classification of optical depth values in the height range 8 to 13 km derived from 532 nm lidar backscatter measurements.

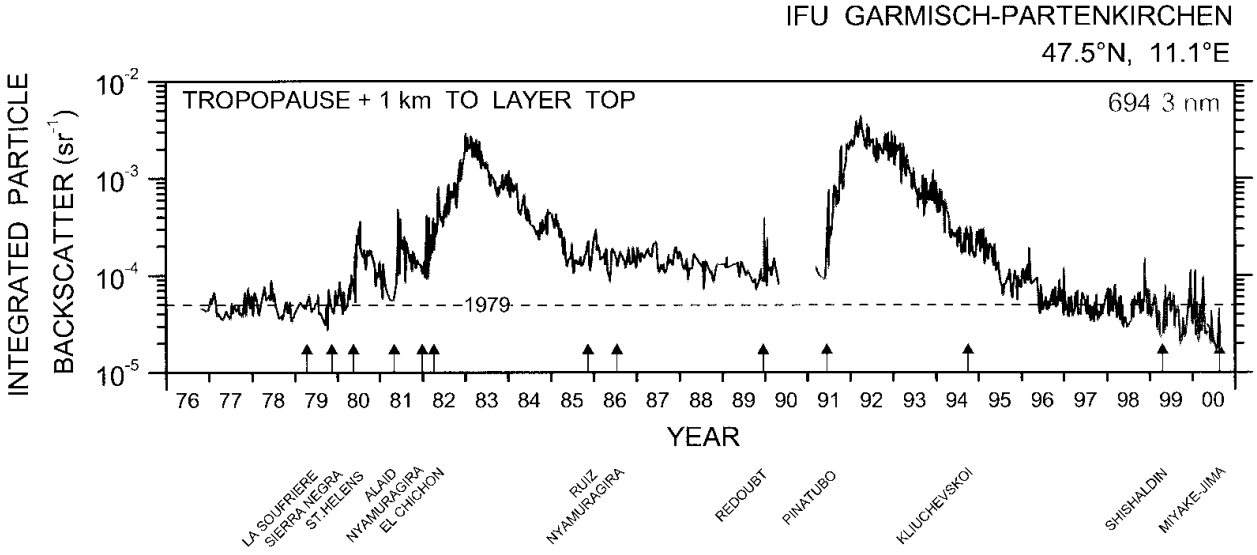

Figure 8.23: Integrated particle backscatter of the stratospheric aerosol layer, seen by lidar over Garmisch-Partenkirchen. The dashed line is the 1979 mean. Volcanic eruptions are marked. Seasonal cycles are caused by the annual tropopause variation. Data after 1990 are converted to the wavelength of 694 nm of a ruby laser system used in earlier measurements.

8.4 Vertical transport of aerosol in the Alpine wind system

by T. Trickl

The level of air pollution has grown throughout the troposphere. The vertical transport mechanisms responsible for the pollution export from the boundary layer have been recently reviewed by Beck et al. (Beck et al., 1997). Detailed estimates for the vertical transport in that paper are limited to the atmosphere above flat terrain and have yielded moderate vertical exchange. One important mechanism, for which higher efficiencies may be expected, is orographically induced transport. For example, Jacob et al. (Jacob et al., 1993) emphasized on the role of the Rocky Mountains in the large-scale export of pollution O_3 out of the North-American boundary layer.

The Alpine wind system has been studied by numerous authors and in many field campaigns (e. g., (Brehm and Freytag, 1982; Vergeiner and Dreiseitl, 1987; Hennemuth, 1987; Müller and Whiteman, 1988; Neininger and Dommen, 1996; Puxbaum and Wagenbach, 1998; Seibert et al., 1998; Ambrosetti et al., 1998). The most important details of orographically induced transport are summarized in the review articles by (Vergeiner and Dreiseitl, 1987) and (Whiteman, 1990). IFU researchers have been involved in several of these field studies, focussing on the investigation of the day- and nighttime circulation in and above different Alpine valleys (e. g., (Reiter et al., 1983; Reiter et al., 1984a; Müller and Reiter, 1986; Müller and Whiteman, 1988)). During daytime there is a formation of an up-valley flow in the bottom section of the valley (named valley wind), caused by horizontal temperature and pressure differences along the valley (e. g., (Vergeiner and Dreiseitl, 1987)). Slope winds also contribute to the mass budget. In contrast to the larger-scale mechanisms driving the valley wind their build-up is ascribed to local thermal effects. The up-valley and up-slope winds may eventually lead to a reverse anti-valley wind above the range of the valley wind. In this wind system pollution from the boundary layer inside the valley may be lifted to heights above 1500 to 2000 m and subsequently transported outside the mountains where it may become mixed into the free troposphere.

Aerosol is a very suitable tracer for vertical-exchange studies. Within the 1996 VOTALP (Vertical Ozone Transport in the Alps) Mesolcina Valley Experiment (Furger et al., 2000) the IFU three-wavelength aerosol lidar was used (Carnuth and Trickl, 2000) in addition to number of ground-based and air-borne instruments of the partner institutes. During this campaign the lidar was tilted parallel and perpendicular to the valley axis which resulted in three-dimensonal mapping of the aerosol distribution in the lower part of the valley. The final data analysis took place in the early phase of the lidar network. It was found that, in contrast to the longitudinal distribution, the transverse distribution was rather asysmmetric. The aerosol layer was separated into two distinct vertical zones (see Fig. 8.24). The boundary layer, which was gradually filled with aerosol from outside the valley (Lago Maggiore area) during the morning hours, expanded from 1.5 km to 2.3 km a. s. l. in the course of the day. It was topped by a second layer starting at around noon which extended to approximately 4.3 km a. s. l., i. e., 1.3 km above the highest summits in the upper part of the Mesolcina valley. Wind measurements onboard two research aeroplanes showed that the wind direction in the upper layer was exactly down-valley. This confirmed our idea of the onset of an anti-valley wind returning from the upper part of the valley where the pollution was lifted to higher altitudes. The pattern built up for different directions of the synoptic wind which suggests little interaction. The lack of interference by the synoptic wind was ascribed to a partial channeling in the very deep valley. The high aerosol concentrations aloft demonstrate the high efficiency of the vertical transport. From measurements for which wind data existed an export efficiency of about 80% was estimated. Based on complementary measurements Swiss colleagues found similar values. They concluded that the valley is vented to higher elevations about five times per day (Furger et al., 2000).

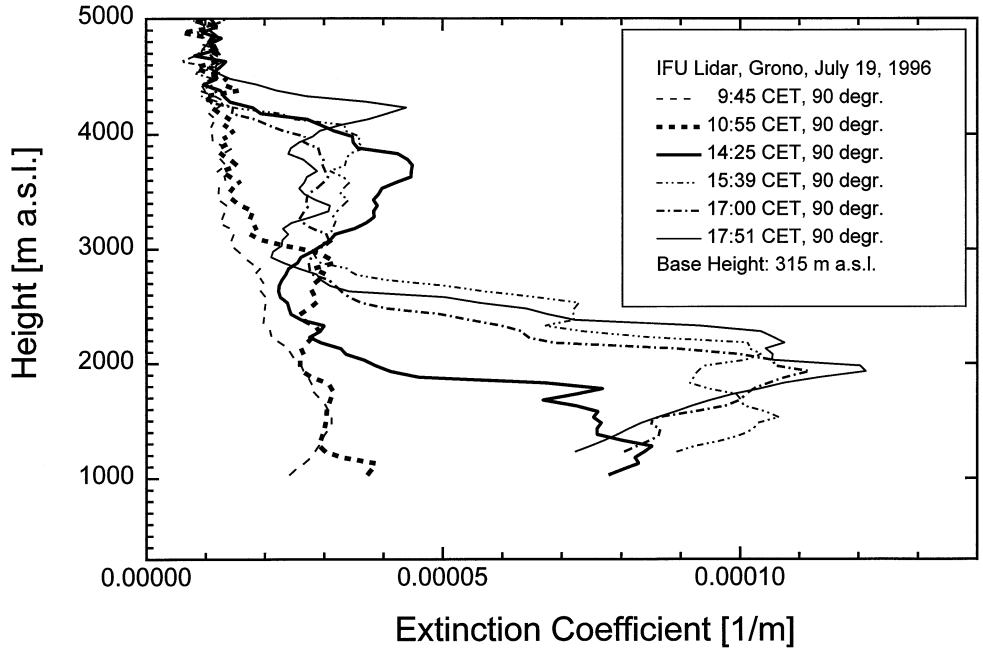

Figure 8.24: 1064-nm extinction profiles selected from the vertical measurements in the Mesolcina on July 19, 1996; the gradual build-up of a reverse flow is reflected by the upper step forming in the aerosol profile.

The Loisach valley at Garmisch-Partenkirchen, the place of the investigations within this project, is flanked by mountains which reach just 2000 m. At the upper end the incoming flow is blocked by the much higher Wetterstein mountain range (2400 m to 3000 m). In this way a much more open valley structure than in the Mesolcina exists. The interference by the synoptic wind should, therefore, be much more significant and, indeed, there is no reproducible formation of a two-step aerosol. Carnuth et al. (Carnuth et al., 2000) reported the first example two-step layer formation with aerosol transport up to heights for measurements with the ozone lidar at IFU in 1991.
Figure 8.25 shows a single-day series from July 26, 1999, again showing the formation of such a two-layer distribution. During the project a total of five such series were measured. From an analysis of Munich radiosonde data it was found that in all these cases the synoptic wind speed was 5 m/s and less. The wind direction was between east and south. It is obvious that these conditions should be favourable for the build-up of a valley-wind-anti-valley-wind circulation. In the future we plan to use the new ultra-light aircraft of our institute for a complete anaysis of the wind field and the determination of aerosol-size distributions. This work will be part of EARLINET and the AFO-2000 project VERTIKATOR.

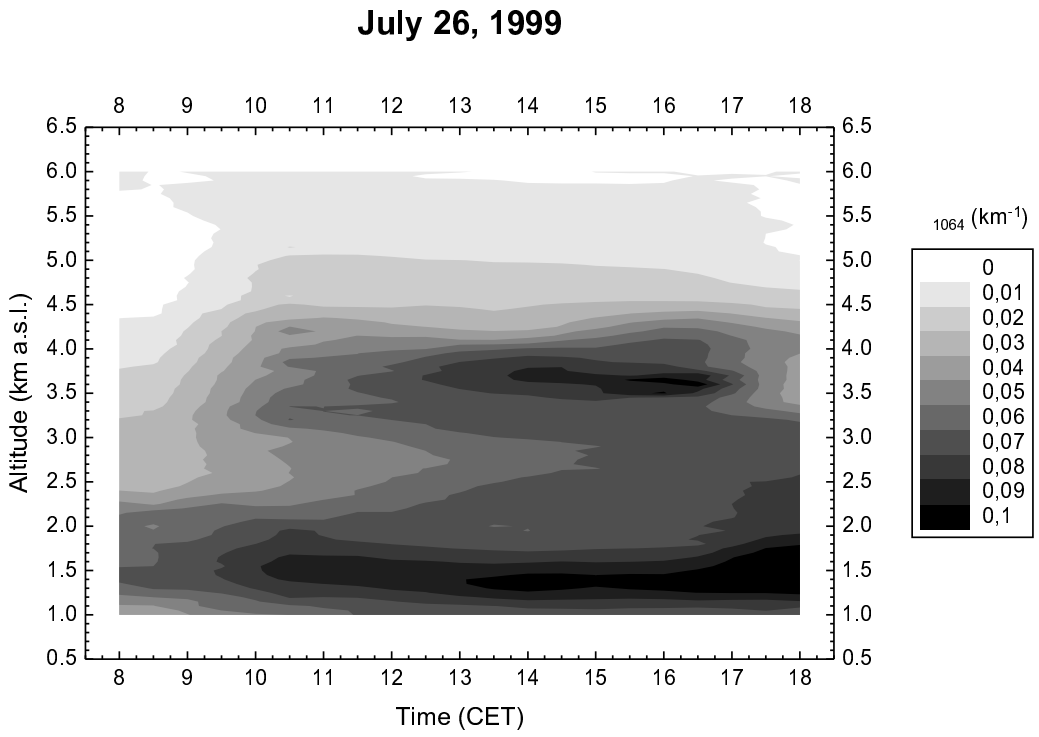

Figure 8.25: Diurnal variation of the 1064-nm extinction coefficient on July 26, 1999; note the distinct aerosol layer above 3.5 km which is ascribed to the reverse flow formation above the valley wind.

8.5 Long-range transport of aerosol

by T. Trickl and U. Wandinger

Aerosol may be a suitable indicator of long-range air-pollution transport in the free troposphere. In contrast to other indicators such as CO it may readily be detected in the entire free troposphere by lidar remote sensing. It has been known for some time that dust particles even of North American origin may reach Central Europe in considerable quantities (e. g., (Reiter et al., 1984b)). However, the best-known extra-European source area is the Sahara desert. Saharan dust episodes are quite frequently observed over the Alps and in South Germany during Föhn episodes (Jäger et al., 1988). In recent years the potential importance of boreal wild fires for the air pollution in the northern hemisphere has been emphasized on (Wotawa and Trainer, 2000, Wotawa, private communication, 2000). The large areas of forest burning year by year in North America, in particular in Canada, and in Siberia are expected to correlate significantly with free-tropospheric CO measured at high-altitude stations such as the Zugspitze summit.
First lidar observation of high amounts of ozone imported from the boundary layer of the United States were recently made at one of the network stations (Stohl and Trickl, 1999; Stohl and Trickl, 2000). This kind of intercontinental transport is associated with high-pressure zones entering Central Europe from the west and an advection pattern resembling an S rotated by 90 degrees. The central part of this S is covered by a front which may lift the air from the North-American boundary-layer to heights even beyond 10 km a. s. l. (warm conveyor belt (Browning, 1990)). There, rapid transport to Europe takes place in the jet stream followed by anti-cyclonic subsidence in the final phase.

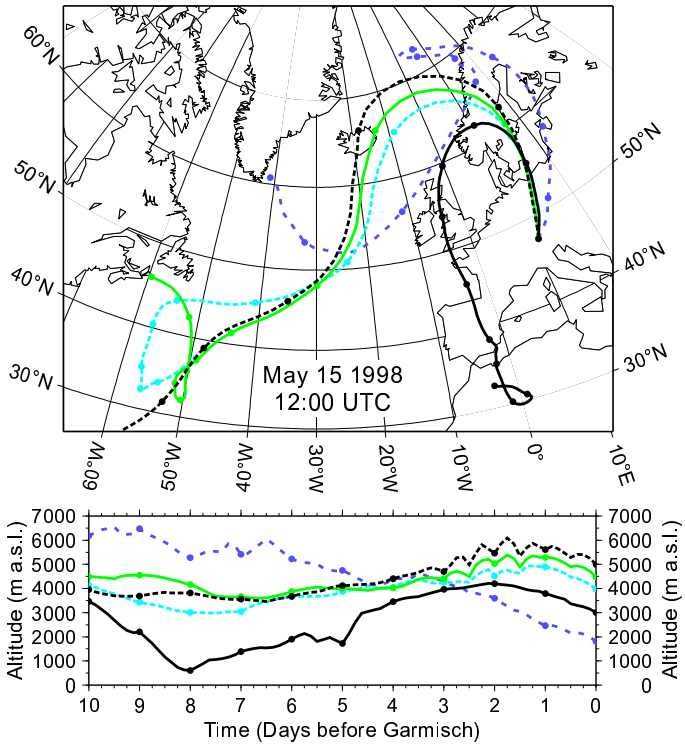

Figure 8.26: 10-day isentropic backward trajectories provided by NOAA CMDL for May 15, 1998, 12:00 UTC

Within the warm conveyor belt the boundary-layer aerosol may be subject to washout. Indeed, in the

early phase of the soundings at IFU during periods of intercontinental transport the measurements were limited to the ultraviolet wavelenghts of the ozone lidar and did not show discernible aerosol signatures. This indicates very small amounts of aerosol hidden in the dominating signal contribution from Rayleigh backscattering. During the lidar-network project, in addition, measurements with wavelengths in the visible and near infrared were made under conditions favourable for the observation of intercontinental transport. Even with the higher sensitivity of an aerosol lidar particle-related structures were not seen in all cases.

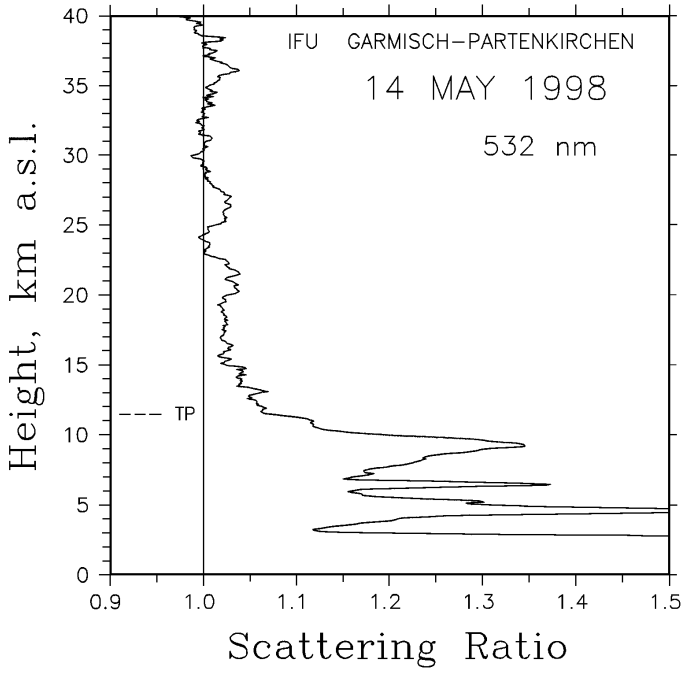

Figure 8.27: Scattering ratio obtained from the measurement of the stratospheric lidar at IFU on May 14, 1998; three distinct aerosol peaks are seen in the free troposphere. “TP” denotes the tropopause level obtained from the Munich radiosonde.

A good example is the period May 11 to 15, 1998 (see Sec. 8.1.1). Figure 8.26 shows backward trajectories for May 15, 12:00 UTC, taken from the routine calculations made by NOAA CMDL for the Zugspitze station twice a day. In the height range near 5 km the S-shaped advection pattern mentioned above is seen. Related aerosol structures have been reported by all network stations, at least for May 14, some also for May 15. In Fig. 8.27 the results of the night-time soundings with the stratospheric aerosol lidar of IFU shortly before the end of May 14 is depicted. Pronounced aerosol peaks are seen at about 4.5, 6.7, and 9 km which, due to the trajectory results, might be ascribed to input from North America.
This episode is interesting because it shows in addition to the typical advection pathways with source regions in the stratosphere, over different regions in North America and over the Central Atlantic (Eisele et al., 1999; Stohl and Trickl, 2000), import from North Africa. The air from North Africa is represented by the trajectory at 3 km a. s. l. which makes a rather long detour over Wales and Southern Norway before it reaches Central Europe and the network area, which is a rather rare situation. Fig. 8.6 shows measurements at IFU on May 15 with 532 nm and 1064 nm. The wavelength dependence in the aerosol peak around 3 km is low which suggests the presence of large particles as usually found in air from the Sahara desert (Jäger et al., 1988).

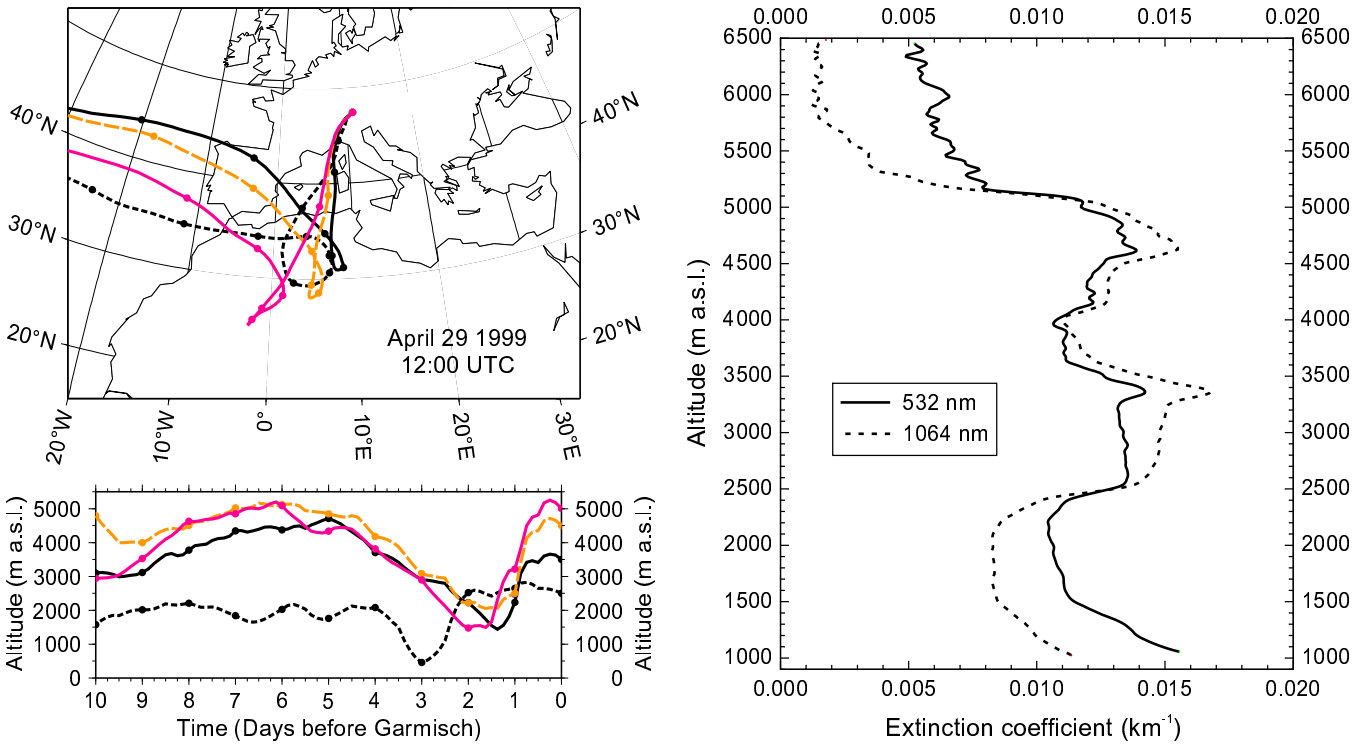

Figure 8.28: Isentropic backward trajectories and lidar results for prefrontal advection of Saharan dust to Garmisch-Partenkirchen on April 29, 1999

The commonly observed advection pathway of Saharan dust is that directly across the Alps rather than the exceptional case described above. Such events were observed at IFU on 9 occasions since May 1998 (unambiguous cases only). Figure 8.28 shows NOAA backward trajectories and lidar measurements on April 29, 1999. Prefrontal upward transport up to 5 km is seen which is completed before the air mass reaches the Alps. This behaviour was found to be typical of this advection pathway. Again, a low wavelength dependence is seen for the corresponding layers identified by the lidar measurements.

The S-shaped advection pathway from North America to Europe seems to be the most important one for the import of North American boundary-layer air. However, also straight advection along the great circle was observed. During the four-day episode from May 26 to 30, 1999, very high ozone values, sometimes exceeding 130 ppb, were detected in a confined layer above 5 km. Sounding with the highly sensitive stratospheric aerosol lidar revealed the simultaneous presence of small amounts of aerosol in exactly the same layer during the full observation period. One example is given in Fig. 8.29. The variability of both the ozone and aerosol concentration was high. The FLEXTRA backward trajectories provided by A. Stohl show a direct inflow from the area around the Great Lakes for all heights on the first two days and a gradual transition to less straight advection in the following. A pronounced rise from the boundary layer to more than 5 km near that area within less than 10 h was calculated. For May 27, increasingly contributions from air masses not exhibiting the sharp rise are present in the height range of interest. Since aerosol was observed during the entire observation period in the high-O_3 layer it is difficult to explain the peak concentrations by stratospheric air, although a stratospheric admixture should be considered. Indeed, frequently layers with extremely low humidity were detected in radiosonde data from nearby ascents by a team from the Paul-Scherrer-Institut.

In the following we briefly evaluate the frequency of aerosol layers in the free troposphere indicat-

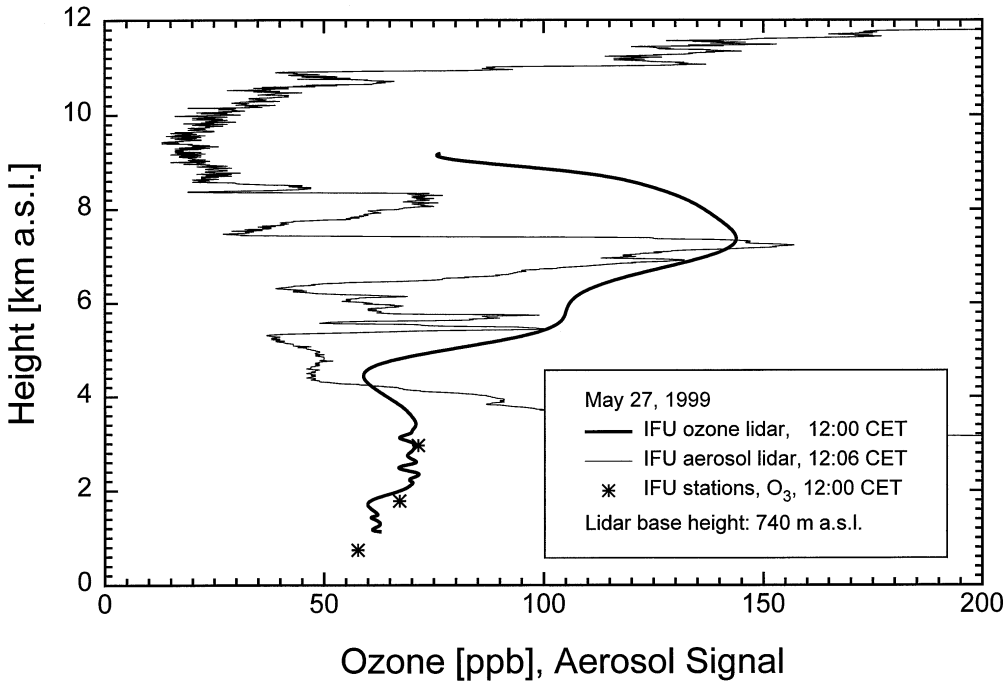

Figure 8.29: Ozone and aerosol profiles (range corrected signal) obtained at IFU on May 27, 1999

ing long-range transport. Two stations have contributed to this topic, Kühlungsborn and IFU. For Kühlungsborn 33 cases with free tropospheric layers have been reported out of 190 measurement days. In order to make the results comparable with those of IFU, where the rather high Alpine boundary layer prohibits to detect advected aerosol layers below about 3 km above the ground, we further reduce the height range to altitudes of 3 km and above. This reduces the number of cases to 21 (11%). The IFU data are taken from the results of the stratospheric lidar (532 nm) because of its excellent signal-to-noise ratio in the free troposphere which allows small amounts of aerosol to be resolved. The structures were counted only if they exceeded 5% of the Rayleigh backscatter coefficient. We select only those measurements for which the aerosol layers may be clearly distinguished from boundary-layer aerosol or from residual cirrus clouds. For the three years of the project the measurements may be distributed as follows:

	days with aerosol	all days
Winter (Dec. 21–March 20)	12 (36.4%)	33
Spring (March 21–June 20)	17 (65.4%)	26
Summer (June 21–Sept. 20)	12 (44.4%)	27
Autumn (Sept. 21–Dec. 20)	6 (18.2%)	33

A clear spring aerosol peak is seen. The overall fraction of cases with free-tropospheric aerosol layers is 39.5% which is quite substantial and indicates a rather strong contribution of long-range transport

to the composition of the free troposphere over Central Europe. The fractions should be seen as a lower limit since the influence of washout may not be quantified. The discrepancy with respect to the Kühlungsborn results stimulates some detailed intercomparison.

A topic of growing importance is the investigation of of intercontinental transport of forest-fire plumes. Two important fires in North America were identified by their aerosol plume in the network area which took place in August 1998 (Canadian fires) and August 2000 (Montana fires). In the following we describe in some detail the results for the 1998 case for which data are available from all instruments of the lidar network and accompanied by extensive trajectory calculations.

The August-1998 fire plume was detected in the free troposphere during the LACE 98 field experiment. Forest fires in northwestern Canada were identified as the source of this event. While the mobile systems of MPI, MIM, and IfT took measurements at the Lindenberg field site, the stationary systems at Kühlungsborn, Leipzig, and Garmisch-Partenkirchen continued the routine lidar network observations. At Lindenberg, a distinct aerosol layer between 3 and 6 km height was continuously observed from the morning of 9 August to the evening of 10 August 1998. The measurements are described in detail in (Wandinger et al., 2000) (see also Sec. 4.2 and Sec. 5). At the other stations, measurements were taken during distinct time intervals on 9 and 10 August 1998.

The origin of the free-troposphere aerosol layer was studied with two transport models, the Lagrangian trajectory model FLEXTRA (version 3.2d) (Stohl et al., 1995) and the Langrangian particle dispersion model FLEXPART (version 3.2) (Stohl et al., 1998; Stohl and Trickl, 1999). Both models are driven with hemispheric model-level wind fields provided by the European Centre for Medium-Range Weather Forecasts (T213 L31 model, (ECMWF, 1995)), with a horizontal resolution of 1^{o} and a time resolution of 3 h (analyses at 0, 6, 12, 18 UTC; 3-h forecasts at 3, 9, 15, 21 UTC).

In Fig. 8.30, eight-day backward trajectories for arrival at Lindenberg at 2300 UTC on 9 August 1998 are presented. At this time, the strongest aerosol load was observed. The long-term three-dimensional backward trajectories were calculated with the FLEXTRA model and indicate the advection of air masses throughout the troposphere from the North Atlantic across the North Sea directly to the measurement site. On this way, the air did not cross highly industrialized regions. The backward trajectories for the height region from 3–5 km (pressure levels 700 to 550 hPa) originate from northwestern Canada. There, strong forest fires occured in late July and early August 1998. The gray-shaded areas in Fig. 8.30 indicate the locations of the strongest fires, that burned about 6–10 days prior to the measurement. The trajectory analysis shows that the air mass traveled below 2000 m height in the forest-fire region and was then lifted above southern Greenland. An additional mixing of polluted and clean air masses might have occurred there around 450 hPa. Almost all air parcels with arrival heights of 2–6 km crossed southern Greenland in this height level 40 to 80 h prior to the measurement. The remarkable event of the transport of forest-fire aerosols from northwestern Canada to Europe was also observed with satellites (Hsu et al., 1999).

Figure 8.31 shows profiles of the particle backscatter coefficient obtained with lidar at Kühlungsborn, Lindenberg, Leipzig, and Garmisch-Partenkirchen in comparison to profiles of an aerosol tracer as derived from the FLEXPART model for 10 August 1998 around noon. The four lidar stations represent roughly a north-to-south cross section along Germany. Free-troposphere aerosols were observed at all stations. The FLEXPART simulations are in very good agreement with the lidar observations. In the FLEXPART simulation, particles were released within boxes for which forest fires were reported (see gray-shaded areas in Fig. 8.30) beginning on 1 August 1998. CO emmissions were estimated from the weekly burnt forest area and a corresponding number of particles was started randomly distributed between the surface and 2500 m height above ground. Transport simulations were performed for both a CO and an aerosol tracer. In contrast to the CO tracer, the aerosol tracer is removed by dry and wet deposition. A detailed analysis of the transport of the fire emissions from Canada to Europe in August 1998 is presented in (Forster et al., 2000).

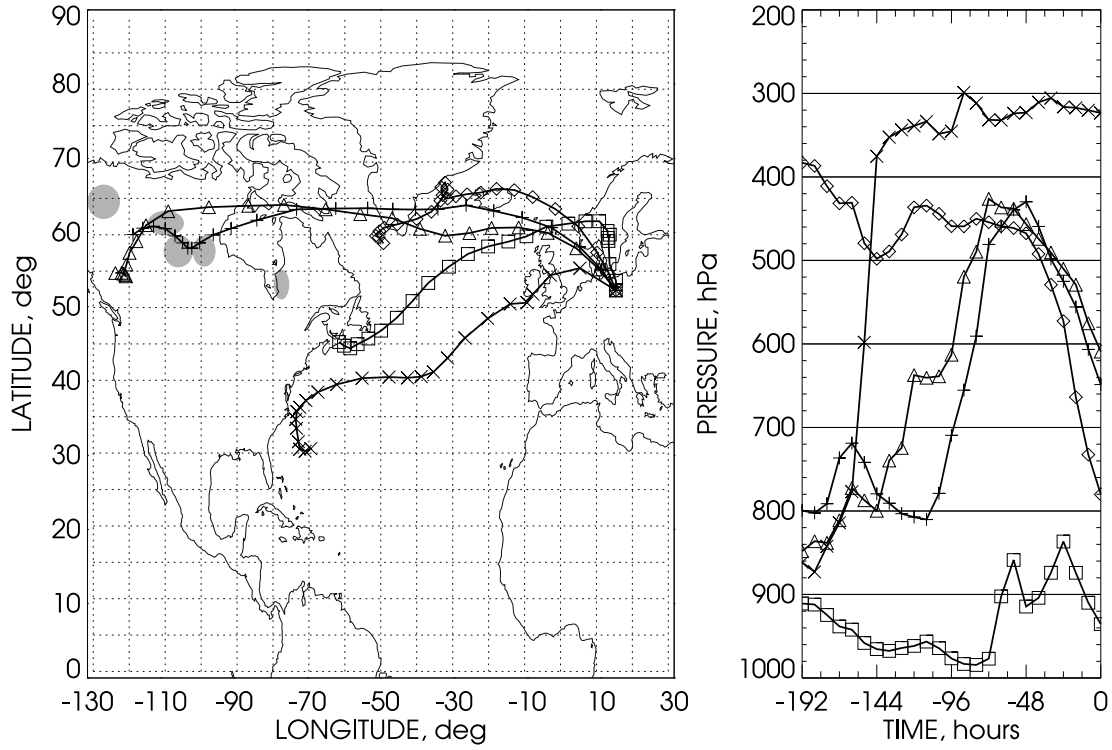

Figure 8.30: Eight-day backward trajectories for arrival at Lindenberg on 9 August 1998, 2300 UTC. The arrival heights are 750, 2250, 3750, 4250, and 9000 m (right panel, time 0, from bottom to top). The left panel presents a horizontal projection of the trajectories with their positions marked every 8 hours. Gray-shaded areas indicate the locations of forest fires in Canada around August 1–4, 1998.

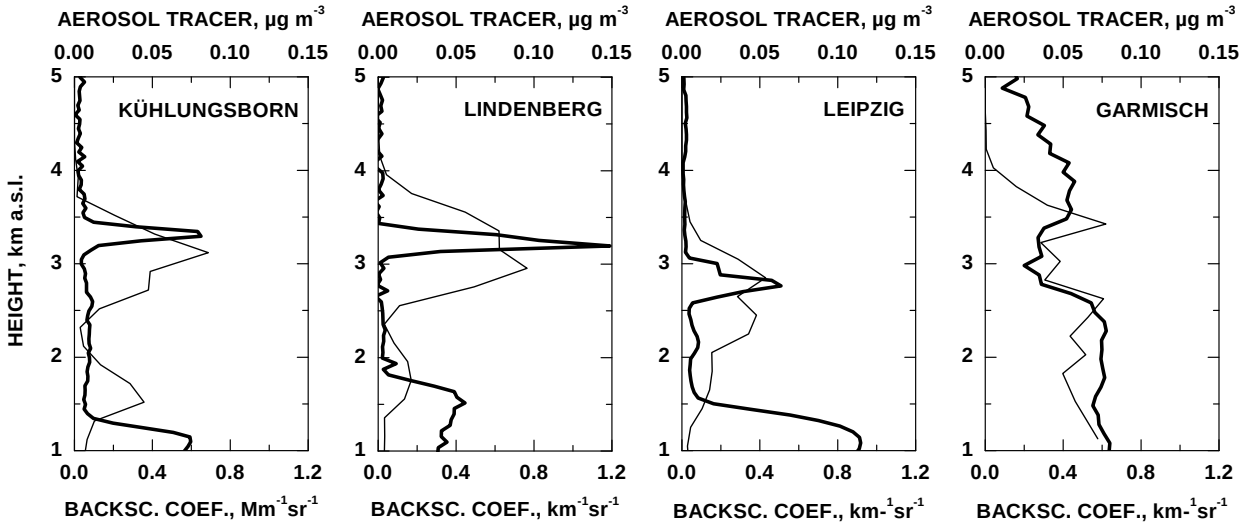

Figure 8.31: Measured backscatter coefficients (thick lines) and corresponding modeled aerosol-tracer concentrations (thin lines) around noon on 10 August 1998. Lidar measurements were taken at Kühlungsborn (1113–1323 UTC, 532 nm, 50-m resolution), Lindenberg (IfT lidar, 1300–1400 UTC, 532 nm, 60-m resolution), Leipzig (1305–1423 UTC, 1064 nm, 60-m resolution), and Garmisch-Partenkirchen (1202–1205 UTC, 1064 nm, 100-m resolution). The model calculations hold for the time period 1200–1400 UTC.

8.6 Aerosol and relative humidity

by V. Matthias

One of the most important modifications of aerosols in the boundary layer is their hygroscopical growth. With increasing relative humidity, water is accumulated around the aerosol particles, changing their size and refractive index significantly. Figure 8.32 shows this change in size and real part of the refractive index for the aerosol component “water soluble” beginning with relative humidities of 70 % (d’Almeida et al., 1991). “Water soluble” is the most important aerosol component in industrial areas as middle Europe, it consists mainly of sulfate and nitrate particles. These changes have high influence on the scattering characteristics of the aerosols and therefore also on measured lidar signals.

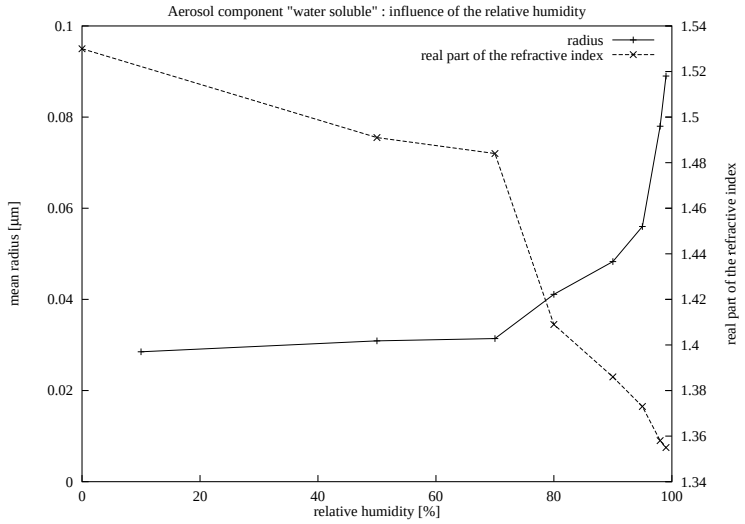

Figure 8.32: Influence of the relative humidity on radius and refractive index on aerosols. Displayed is the aerosol component “water soluble” as defined by d’Almeida et al. (1991).

With lidars, the aerosol backscatter and extinction is always measured under ambient conditions including the effects of hygrocopical growth of the aerosols. This can result in quite large discrepancies of the scattering coefficients measured by lidar and by *in situ* instruments on board of research aircrafts or at ground. *In situ* instruments typically measure aerosol characteristics as size distribution and scattering coefficient in dried state at humidities around 20 %. Correcting for that effect using hygroscopical growth factors (Tang and Munkelwitz, 1993) can on the other hand lead to quite good agreement, as is shown in figure 8.33 and discussed in chapter 4 and in (Wandinger et al., 2000). However for most cases, an adequate corection of the dry measured aerosol properties to ambient conditions will be difficult, since extensive information on the chemical composition of the aerosol is necessary. In the shown case, this information was available from the aircraft measurements.

Lidar signals are directly influenced by the scattering properties of aerosol particles. But changes in the detected signal cannnot directly be assigned to hygroscopic growth since they can result from changes in the aerosol distribution as well as from changes in the optical charcteristics of the scattering particles. Horizontal and vertical transport of the atmospheric aerosols result in additional fluctuations of the lidar signals.

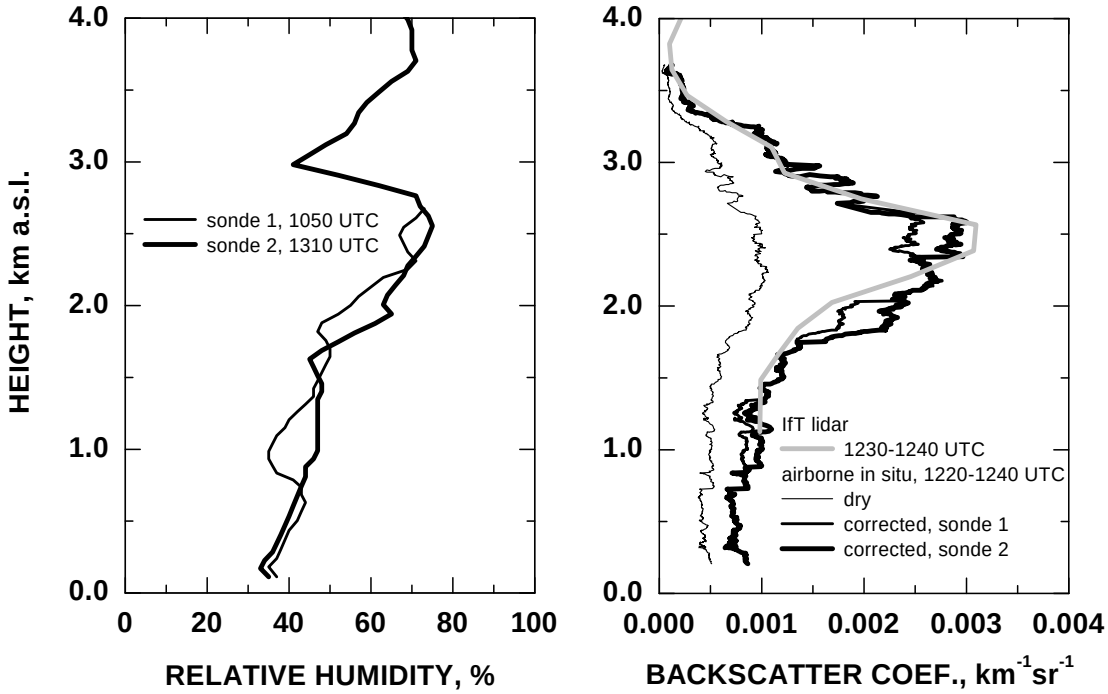

Figure 8.33: Intercomparison of aerosol backscatter profiles measured with lidar at 532 nm and with *in situ* instruments on board a research aircraft. After humdity correction the profiles show good agreement.

These circumstances and the fact that relative humidities significantly higher than 70 % are needed to observe a remarkable effect make it rather difficult to measure the influence of the relative humdity on atmospheric aerosols directly by lidar. Anyhow, such effort has been made during the Lindenberg aerosol charcterization experiment (LACE 98) using the MPI water vapour DIAL (Wulfmeyer and Bösenberg, 1998; Bösenberg, 1998). Favourable conditions for these measurements were present in the afternoon of August 8^{th} 1998. Between 14:34 UT and 15:26 UT a well mixed boundary layer up to altitudes of ca. 2100 m could be observed. The water vapour density could be measured with high accuracy with the lidar between ca. 400 m and 1800 m using the near range receiving telescope. The profiles showed almost constant water vapour denstity in the order of 10 g/m^3 within the PBL, resulting in increasing relative humidity with height. Two radiosondes launched at 13:13 UT and at 16:49 UT gave an almost constant temperature gradient of -9.2 K/km within the boundary layer. Assuming this temperature gradient to be constant during the considered episode and using measured ground values of the temperature, the water vapour profiles measured with the DIAL system could be assigned to profiles of the relative humidity, showing values up to ca. 85 % at the top of the boundary layer (see figure 8.34, left side). This can be regarded as sufficiently high to see hygroscopic effects on the aerosol optical properties. The distribution of the aerosol particles themselves was regarded to be homogeneous since convection was still active at ground temperatures of 29°C and no additional layers could be observed in the aerosol backscatter by the lidar. So all changes of the aerosol backscatter within the boundray layer can be assigned to hygroscopical effects on the aerosols.

For the evaluation of the 50 minutes episode, profiles of the water vapour density and the aerosol backscatter at 729 nm have been calculated with a resolution of 2 minutes and 120 m. This for investigations in the boundary layer rather coarse resolution has been selected because the lidar signals

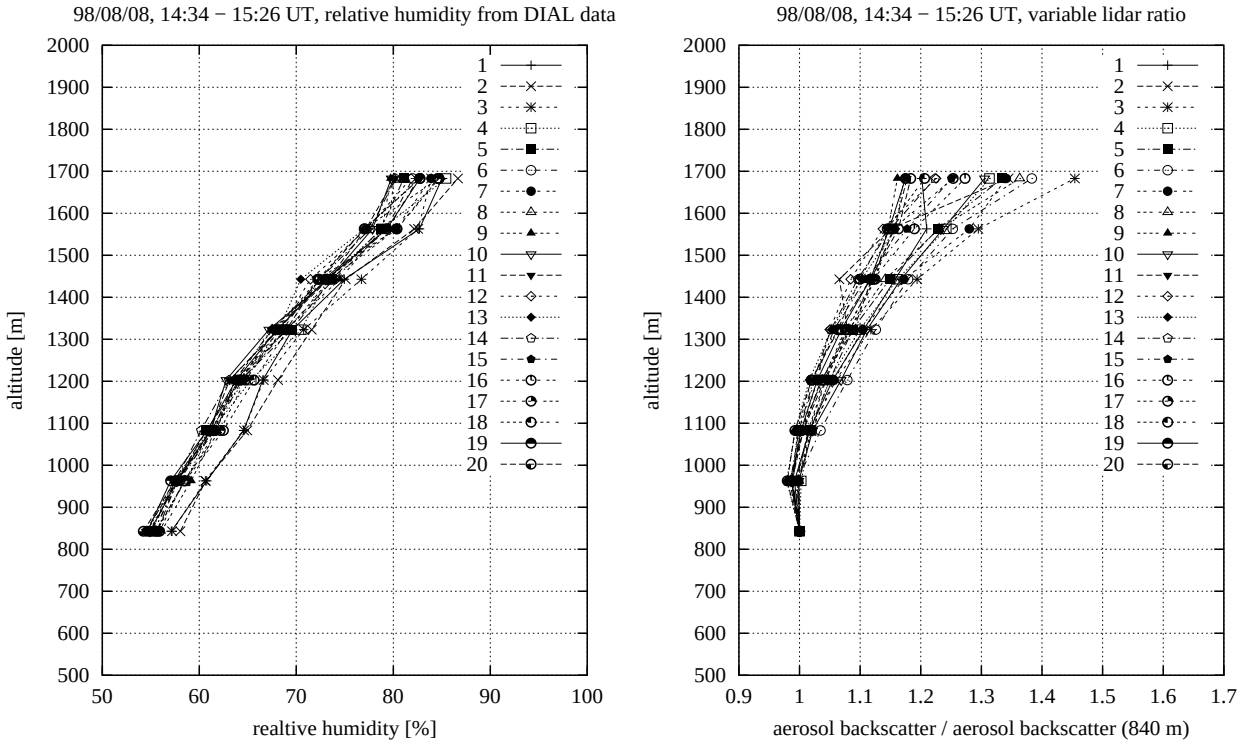

Figure 8.34: Calibrated aerosol backscatter profiles at 730 nm and the corresponding relative humidity. The backscatter profiles have been evaluated with a lidar ratio variable in height. The relative humidity is out of DIAL data with a temperature profile from radiosondes.

measured on the water vapour absorption line at 730 nm was already very weak at the top of the boundary layer.
The profiles have been selected for those being fully representative for the boundary layer up to an altitude of 1680 m. In some cases, the fluctuations in the boundary layer height went down to 1500 m, which means that the assumptions about temperature gradient and homogreneous distribution of the aerosol particles no longer hold in those cases. So five profiles have been skipped and 20 remained for the observation of hygroscopical growth effects.

The aerosol backscatter profiles have been evaluated with the inversion algorithm described in chapter 4.1, relying on Fernald's publication (1984). A lidar ratio of 50 sr up to 960 m, slowly increasing to 80 sr at 2100 and again 50 sr above has been chosen and the reference height was between 2500 m and 3000 m assuming an aerosol backscatter almost zero. This lidar ratio follows model calculations performed with the OPAC data set (Hess et al., 1998) for increasing humidity at 750 nm and for urban aerosol. All aerosol profiles have been calibrated to their values in 800 m to reduce temporal fluctuations of the whole profile when looking at the increase of the aerosol backscatter with height and therefore with humidity.
All 20 calibrated aerosol profiles between 800 m and 1700 m and the corresponding relative humidity profiles are shown in figure 8.34. All aerosol profiles show an increase of the aerosol backscatter with height, but with a large scatter of the values at upper altitudes. This can result from horizontal transport effects and from aerosol inhomogeneities, always present in the atmosphere. Vertical transport is also important, because the actual size of an aerosol particle at a given relative humidity depends on the humidity in the area the particle comes from. Particle diameter is not a unique function in dependence on relative humidity (Tang and Munkelwitz, 1993). Additionally, temperature fluctuations have

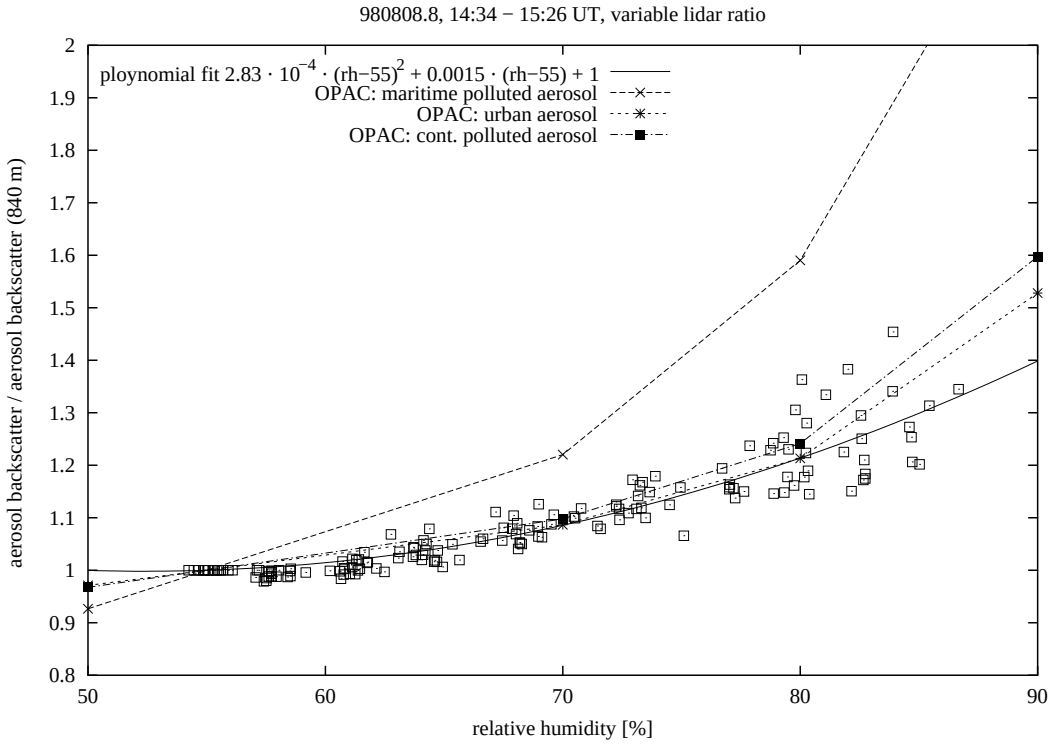

Figure 8.35: Dependence of aerosol backscatter on relative humidity assuming constant number density within the PBL. Comparisons have been made with model calculations using the OPAC data set (Hess et al., 1998).

been neglected when calculating the relative humidity profiles and a larger spread of these values at 1680 m due to this effect are very likely. On the other hand the error caused by 1 K temperature fluctuations is in the order of only 5 % in the relative humidity. Entrainment from aerosol-free air from the free troposphere does not play a major role since the considered highest altitude is well below the top of the boundary layer and additionally “suspicious” profiles have been sorted out.
An increase of the aerosol backscatter with relative humidity can be observed for this episode (fig. 8.35) and a second order polynom can be fitted to the observed data. One gets remarkably good agreement with the aerosol compositions “urban” and “continental polluted” derived from OPAC. Those compositions contain different mixtures of the aerosol types “water soluble”, “insoluble” and “soot” representing industrial aerosols. Looking at back trajectories calculated by the German Weather Service for Leipzig, one recognizes low speed westerly flow, therefore air masses originating from western Germany, Belgium and France. The mismatch of the measured data with maritime polluted aerosol containing mainly sea salt is not surprising. A high amount of sea salt leads to much higher growth of the aerosols with humidity.
Summarizing it has been found that the increase of the aerosol backscatter with increasing relative humidity could be measured using only water vapour DIAL data. The results fit very good with model results from the OPAC aerosol model. The assumptions made for this case study seem to be reasonable and introduce not too large errors. On the other hand, meteorological conditions under which such effect can be observed are rare. Additional measurements as vertical wind, highly resolved temperature profiles and aerosol number density measurements would be very useful to get better insight in the growth of aerosol particles under ambient conditions.

Chapter 9

Summary

by J. Bösenberg

The German Aerosol Lidar Network has attempted, for the first time worldwide, to establish a climatological data set for the aerosol vertical distribution over several stations in a quantitative and coordinated approach.

Quantitative results have been obtained by employing advanced lidar methods like Raman or scanning lidar to retrieve profiles of the extinction coefficient directly. The standard backscatter lidar retrieval with its well known deficiencies has been used only to amend the extinction data, in particular for daytime measurements, for stratospheric measurements, and for the two stations which were not equipped with Raman lidar capabilities. To provide for a sufficiently homogeneous data set substantial effort was put into data quality assurance. An intercomparison at system level was performed for 6 of the total of 8 systems that have been used in this project, and the agreement was found very satisfactory. For results obtained with the same method the deviations were less than about 10%, and for different methods the differences were still less than about 25%. In view of the uncertainties of standard lidar retrievals this is an excellent result.

The intercomparison of the backscatter retrieval algorithms resulted in some revisions of previously used programs. After that only neglible differences were found, but only if the same input parameters were used. The intercomparison demonstrated very clearly the strong dependence of its results on the choice of input parameters which are known for synthetic data only, but not for real measurements.

At the start of the project it had been decided to perform regularly scheduled measurements to establish a climatological data set for which the bias due to the restriction of observations by weather conditions was minimised or at least could be estimated from the number of occurrance of unfavorable conditions. In addition to these measurements the systems were used to perform some coordinated measurements to study the large scale behaviour during specific synoptic situations. Persistent high pressure systems and cold front passages were addressed specifically during this project. It turned out that coordinated observations of such features were rather difficult because of the relatively long distances between the stations. Therefore only isolated case studies were possible.

Other special observations addressed the vertical exchange processes in an Alpine valley. It was clearly demonstrated that aerosols can be used effectively as a tracer for the flow pattern in a complex terrain, and that lidar masurements are very suitable to investigate the associated aerosol patterns.

It was also demonstrated that the information on the vertical distribution of aerosol in connection with trajectory analysis can be used very succesfully to identify the sources of specific aerosol layers that have been transported to the measurement site over very long distances. Long range transport of forest fire aerosol from Canada, and of desert dust from the Sahara have been identified successfully.

Special attention was given by two groups to study the possibilities of retrieving aerosol microphysical properties from lidar measurements. This is a delicate task because this inversion is severely ill-posed in a mathematical sense. The result of these studies, however, is quite positive. It has been established that through sophisticated regularisation algorithms the basic microphysical parameters like number concentration, mode radius, and refractive index can in fact be retrieved from lidar measurements. The necessary set of measured input quantities of course depends on both the detailed properties of the aerosol under study and the accuracy of the measured optical parameters. It turned out that a minimum useful set of measurements for this kind of retrievals is the backscatter at the fundamental plus the second and third harmonics of the Nd:YAG-laser plus, most importantly, true extinction measurements at 532 and 355 nm. For future applications, where true microphysical retrievals are to be used for aerosol characterisation rather than phenomenological values like the ”lidar ratio” or the wavelength dependence of backscatter, this seems to be a feasible set of measurements that can be performed on a routine basis.
The combination of lidar retrievals of water vapor profiles and aerosol backscatter has been used to investigate the growth of aerosol with increasing relative humidity under true atmospheric conditions. This task turned out to be more complicated than expected because horizontal and vertical transport processes have a rather large effect on the observed backscatter coefficient, so that it is difficult to extract the change that is due to hygroscopic growth only. Nevertheless, under specific conditions the attempt to estimate the increase in backscatter coefficient with increasing relative humidity had quite promising results. The observed growth rates are in fairly good agreement with model calculations if realistic assumptions are made on the aerosol composition. The low aerosol load of the stratosphere opened the possibility to study anthropogenic sources in this region. There is evidence now that the aerosol content of the lowest portion of the stratosphere is noticeably influenced by aircraft exhausts.
The German Aerosol Lidar Network also served to continue the long time series of stratospheric aerosol profiling at Garmisch-Partenkirchen. The period covered by the measurements was characterised by a very low level of volcanic aerosol in the stratosphere. Obviously the material that had been injected by previous eruptions, mainly that of Mount Pinatubo in 1991, has been removed in the meantime, and smaller eruptions in the meantime did not inject substantial masses of aerosol into the stratosphere.
However, the main goal of the network operations was the establishment of a climatological data set. This task was accomplished very succesfully. For four of the stations the percentage of succesful measurements was about 60 to 65 %, leading to 1120 aerosol profiles for the climatological data set. Only for the Alpine station the hit rate was much lower, here 125 profiles could be collected for this purpose. Using this data set, which is worldwide by far the largest and most systematically collected data set on the aerosol vertical distribution, different approaches were made to analyse the temporal and vertical distribution. The derived products include:

- the seasonal dependence of boundary layer heights
- the mean extinction and backscatter profiles
- the mean optical depth, separately for PBL and free troposphere
- the seasonal dependence of aerosol extinction
- the statistical distribution of aerosol extinction
- the dependence of aerosol optical properties on the airmass history
- the statistical distribution of extinction-to-backscatter ratio values.

The latter are very important for future satellite lidar retrievals. Explanations of the observed variability were attempted using either sector analysis or cluster analysis, both based on the large data set of coinciding backtrajectories provided by the German Weather Service. It is certainly not too surprising that these analysis attempts are not really explaining the variability to a satisfactory extent. The number of factors influencing the aerosol properties is so large that a simple geographical history of the aerosol trajectory is not sufficient to determine its properties. More succes can only be expected when models are used that include at least the major factors for aerosol generation and modification. It was clear from the beginning that the rather limited number of stations and the rather limited time frame would not suffice to establish a data set that would permit to study all details of the aerosol vertical distribution. Even rather simple statistical analyses including several factors controlling the variability of aerosol properties very soon come to a point where the increase of factors leads to a decrease in number of cases for specific combinations of control factors so that statistical significance can no longer be maintained. But the concept and the performance of the German Aerosol Lidar Network has convinced many colleagues in Europe that it is worth contributing to this task. With the help of this strong community it was possible to obtain support from the European Commission for a much larger European network, the ”European Aerosol Research Lidar Network”, EARLINET, which now continues the work that has been started in Germany in a much larger frame. Now 20 stations distributed over whole Europe, including the German stations, by and large follow the methodology that has been developed within the frame of the German Aerosol Lidar Network. This serves to provide a much broader basis for statistical analyses, and also provides for much broader spatial coverage to exploit cross correlations between different stations and to assess the aerosol distribution on a continental scale.

Acknowledgement

Daily calculations of prognostic and analytic backward trajectories were performed by Deutscher Wetterdienst, Offenbach. We thank Barbara Fay for scientific advice.
We are very grateful to the scientific and technical staff of the Meteorological Observatory Lindenberg and especially to Ulrich Leiterer for the round-the-clock support during LACE 98 (lidar-net intercomparison campaign) and for providing radiosonde and photometer data.
Trajectory and transport calculations with the FLEXTRA and FLEXPART models concerning the long-range transport of aerosols were performed by Andreas Stohl and his co-workers (Technische Universität München, Lehrstuhl für Bioklimatologie und Immissionsforschung, Freising).
Markus Fiebig (Deutsches Zentrum für Luft- und Raumfahrt, Oberpfaffenhofen) and Manfred Wendisch (Institut für Troposphärenforschung Leipzig) kindly provided airborne *in situ* data.
We thank all participants of LACE 98 for a very fruitful cooperation.
The financial support of this work by the Federal Minister for Research and Education within the funding focus “Atmospheric Aerosol Research (AFS)” is gratefully acknowledged.

Bibliography

Ackermann, J. (1998). The extinction-to-backscatter ratio of tropospheric aerosols: A numerical study. *Journal of Atmospheric and Oceanic Technology*, 15:1043 – 1050.

Allen, R., Boland, W., Faber, V., and Wing, G. (1985). Singular values and condition numbers of galerkin matrices arising from linear integral equations of the first kind. *J. Math. Anal. Appl.*, 109:564–590.

Alpers, M., Eixmann, R., Höffner, J., Köpnick, T., Schneider, J., and von Zahn, U. (1999). The Rayleigh/Mie/Raman Lidar at IAP Kühlungsborn. *J. Aerosol Sci.*, Suppl. 1:637–638.

Althausen, D., Müller, D., Ansmann, A., Wandinger, U., Hube, H., Clauder, E., and Zörner, S. (2000). Scanning six-wavelength eleven-channel aerosol lidar. *Journal of Atmospheric and Oceanic Technology*, 17:1469–1482.

Ambrosetti, P., Anfossi, D., Cieslik, S., Graziani, G., Lamprecht, R., Marzorati, A., Nodop, K., Sandroni, S., Stingele, A., and Zimmermann, H. (1998). Mesoscale transport of atmospheric trace constituents across the Central Alps: TRANSALP tracer experiments. *Atmospheric Environment*, 32:1257–1272.

Ansmann, A., Riebesell, M., Wandinger, U., Weitkamp, C., Voss, E., Lahmann, W., and Michaelis, W. (1992a). Combined Raman Elastic-Backscatter LIDAR for Vertical Profiling of Moisture, Aerosol Extinction, Backscatter, and LIDAR Ratio. *Appl. Phys.*, B 55:18–28.

Ansmann, A., Riebesell, M., and Weitkamp, C. (1990). Measurement of atmospheric aerosol extinction profiles with a Raman lidar. Technical Report 90/E/27, GKSS.

Ansmann, A., Wandinger, U., Riebesell, M., Weitkamp, C., and Michaelis, W. (1992b). Independent measurement of extinction and backscatter profiles in cirrus clouds by using a combined Raman elastic-backscatter lidar. *Appl. Opt.*, 31:7113–7131.

Arshinov, Yuri, F. and Bobrovnikov, S. M. (1999). Use of a fabry-perot interferometer to isolate pure rotational raman spectra of diatomic molecules. *Appl. Opt.*, 38:4635–4638.

Arshinov, Yuri, F., Bobrovnikov, S. M., Zuev, V. E., and Mitev, V. M. (1983). Atmospheric temperature measurements using pure rotational raman lidar. *Appl. Opt.*, 22:2984–2990.

Arshinov, Y. F., Bobrovnikov, S. M., Serikov, I., Althausen, D., Mattis, I., Wandinger, U., and Ansmann, A. (2001). Spectrally absolute instrumental approach to isolate pure rotational raman lidar returns from nitrogen molecules of the atmosphere. In Dabas, A. and Pelon, J., editors, *Laser remote sensing of the atmosphere. Selected papers of the 20th International Laser Radar Conference*. Ecole Polytechnique.

Beck, J. P., Asimakopoulos, N., Bazhanov, V., Bock, H. J., Chronopoulos, G., DeMuer, D., Ebel, A., Flatøy, F., Hass, H., Van Haver, P., Hov, Ø., Jakobs, H. J., Van Pul, W. A. J., Speth, P., Trickl, T., and Varotsos, C. (1997). Exchange of Ozone Between the Atmospheric Boundary Layer and the Free Troposphere. In Hov, Ø., editor, *Transport and Chemical Transformation of Pollutants in the Troposphere, Vol. 6, Tropospheric Ozone Research*, pages 111–130. Springer, Berlin, Heidelberg.

Bissonnette, L. R. and Hutt, D. L. (1994). Multiple scattering lidar and cloud properties. In *17^{th} International Laser Radar Conference, Paper 29B1*, page 541.

Bluth, G. J. S., Doiron, S. D., Schnetzler, C. C., Krueger, A. J., and Walter, L. S. (1992). Global tracking of the SO_2 clouds from the June 1991 Mount Pinatubo eruptions. *Geophys. Res. Lett.*, 19:151–154.

Böckmann, C. (2001). Hybrid regularization method for the ill-posed inversion of multiwavelength lidar data to retrieve. *Appl. Opt.*, 40:1–14.

Böckmann, C. and Sarközi, J. (1999). The ill-posed inversion of multiwavelength lidar data by a hybrid method of variable projection. *Proc. SPIE Intern. Soc. Opt. Eng.*, 3186:282–293.

Böckmann, C. and Wauer, J. (2000). The influence of spheroids on the inversion in the retrieval of microphysical particle parameters from lidar data. *Proc. SPIE Intern. Soc. Opt. Eng.*, 4015:1–8.

Böckmann, C. and Wauer, J. (2001). Algorithms for the inversion of light scattering data from uniform and non-uniform particles. *J. Aerosol Sci.*, 32:49–61.

Bodhaine, B., Wood, N., Dutton, E., and Slusser, J. (1999). On rayleigh optical depth calculations. *J. Atmospheric and Oceanic Technol.*, 16:1854–1861.

Bohren, C. F. and Huffman, D. R. (1983). *Absorption and scattering of light by small particles*. John Wiley & Sons, New York.

Bösenberg, J. (1998). Ground-based differential absorption lidar for water vapor and temperature profiling: methodology. *Appl. Opt.*, 37:3845–3860.

Bösenberg, J., Timm, R., and Wulfmeyer, V. (1997). Study on retrieval algorithms for a backscatter lidar. Final report. MPI-Report 226, Max-Planck-Institut für Meteorologie, Hamburg, Germany.

Brehm, M. and Freytag, C. (1982). Erosion of the Night-Time Thermal Circulation in an Alpine Valley. *Archives for Meteorology, Geophysics, and Bioclimatology B*, 31:331–352.

Browning, K. A. (1990). Organization of clouds and precepitation in extra-tropical cyclones. In Newton, C. and Holopainen, E., editors, *Extratropical Cyclones: The Erik H. Palmen Memorial Volume*, pages 129–153. American Meteorological Society, Boston.

Carnuth, W., Kempfer, U., and Trickl, T. (2000). High-lights of the Tropospheric Lidar Studies at IFU during the TOR Project. *submitted*.

Carnuth, W. and Trickl, T. (1994). A powerful eyesafe infrared aerosol lidar: Application of stimulated Raman backscattering of 1.06 μm radiation. *Rev. Sci. Instrum.*, 65:3324–3331.

Carnuth, W. and Trickl, T. (2000). Transport studies with the IFU three-wavelength lidar during the VOTALP Mesolcina experiment. *Atmospheric Environment*, 34:1425–1434.

Chang, S.-H. (1952). A generalization of a theorem of hille and tamarkin with applications. In *Proc. London Math. Soc.*, pages 22–29.

d'Almeida, G., Koepke, P., and Shettle, E. P. (1991). *Atmospheric aerosols: global climatology and radiative characteristics*. Deepak Publ., Hampton, Virginia, USA.

de Hoog, F. (1980). Review of fredholm equations of the first kind. In R.S. Anderssen, F. d. H. and Lukas, M., editors, *The application and numerical solution of integral equations*, pages 119–134. Sijthoff & Noordhoff, Leyden.

Dorling, S., Davies, T., and Pierce, C. (1992). Cluster analysis: A technique for estimating the synoptic meteorological controls on air and precipitation chemistry-method and applications. *Atmos. Environ.*, 26A:2575–2581.

ECMWF (1995). User guide to ECMWF products 2.1 . Meteorological Bulletin M3.2, ECMWF, Reading, UK.

Edlen, B. (1953). The dispersion of standard air. *Journal of the Optical Society of America*, 43:339.

Eisele, H., Scheel, H. E., Sladkovic, R., and Trickl, T. (1999). High-Resolution Lidar Measurements of Stratosphere-Troposphere Exchange. *Journal of the Atmospheric Sciences*, 56:319–330.

Eisele, H. and Trickl, T. (1997). Second Generation of the IFU Stationary Tropospheric Ozone Lidar. In Ansmann, A., Neuber, R., Rairoux, P., and Wandinger, U., editors, *Advances in Atmospheric Remote Sensing with Lidar*, pages 379–382. Springer, Berlin Heidelberg.

Eixmann, R. (2001). Ph.D. Thesis, Rostock University. *in preparation*.

Elterman, L. (1968). UV, Visible, and IR Attenuation for Altitudes to 50 km, 1968. Environmental Research Papers 285, AFCRL-68-0153, Environmental Research.

Fernald, F. G. (1984). Analysis of Atmospheric Lidar Observations: Some Comments. *Appl. Opt.*, 23:652–653.

Ferrare, R. A., Melfi, S. H., Whiteman, D. N., Evans, K. D., and Leifer, R. (1998). Raman lidar measurements of aerosol extinction and backscattering 1. methods and comparisons. *J. Geophys. Res.*, 103:19663–19672.

Fiebig, M., Petzold, A., Wandinger, U., Wendisch, M., Kiemle, C., Stifter, A., Ebert, M., Rother, T., and Leiterer, U. (2000). Optical closure for an aerosol column: method, accuraxy, and inferable properties, applied to a biomass burning aerosol and its radiative forcing. *Journal of Geophysical Research*, submitted.

Forster et al. (2000). Transport of boreal forest fire emissions from canada to europe. *Journal of Geophysical Research*, submitted.

Freudenthaler, V., Homburg, F., and Jäger, H. (1994). Ground-based mobile scanning LIDAR for remote sensing of contrails. *Annales Geophysicae*, 12:956–961.

Furger, M., Dommen, J., Graber, W. K., L., P., Prévôt, A., Emeis, S., Grell, G., Trickl, T., Gomiscek, B., Neininger, B., and Wotawa, G. (2000). The VOTALP Mesolcina Valley Campaign 1996 - concept, background and some highlights. *Atmospheric Environment*, 34:1395–1412.

Golub, G., Heath, M., and Waba, G. (1979). Generalized cross-validation as a method for choosing a good ridger paramete. *Technometrics*, 21:215–223.

Gonzales, C. R., Veefkind, J. P., and de Leeuw, G. (2000). Aerosol optical depth over Europe in August 1997 derived from ATSR-2 data. *Geophys. Res. Lett.*, 27:955–958.

Groetsch, C. W. (1993). *Inverse Problems in the Mathematical Sciences*. Vieweg und Sohn, Braunschweig, Wiesbaden.

Grund, C. J. and Eloranta, E. W. (1991). University of Wisconsin high spectral resolution lidar. *Opt. Eng.*, 30:6–12.

Gutkowicz-Krusin, D. (1993). Multiangle lidar performance in the presence of horizontal inhomogeneities in atmospheric extinction and scattering. *Applied Optics*, 32:3266–3272.

GVN (1999). Bulletin of the Global Volcanic Network. Technical Report 4, Smithsonian National Museum of Natural History, Washington, DC 20560.

Hänel, G. (1998). Vertical profiles of the scattering coefficient of dry atmospheric particles over europe normalized to air at standard temperature and pressure. *Atmos. Environ.*, 32:1743–1755.

Hansen, P. (1988). Computation of the singular value expansion. *Computing*, 40:185–199.

Hansen, P. (1992). Numerical tools for analysis and solution of fredholm integral equations of the first kind. *Inverse Problems*, 8:849–875.

Hansen, P. (1998). *Rank-Deficient and Discrete Ill-Posed Problems*. SIAM, Philadelphia.

Hartley, W. S., Hobbs, P. V., Ross, J. L., Russell, P. B., and Livingston, J. M. (2000). Properties of aerosols aloft relevant to direct radiative forcing off the mid-atlantic coast of the united states. *J. Geophys. Res.*, 105:9859–9885.

Hennemuth, B. (1987). Heating of a Small Alpine Valley. *Meteorology and Atmospheric Physics*, 36:287–296.

Hess, M., Koepke, P., and Schult, I. (1998). Optical properties of aerosols and clouds: The software package OPAC. *Bull. Amer. Meteor. Soc.*, 79:831–844.

Hofmann, B. (1994). On the degree of ill-posed problems for nonlinear problems. *J. Inv. Ill-Posed Problems*, 2:61–76.

Hofmann, B. (1999). *Mathematik inverser Probleme*. Teubner (Stuttgart - Leipzig, 1999).

Hsu, N., Herman, J., Gleason, J., Torres, O., and Seftor, C. (1999). Satellite detection of smoke aerosols over a snow/ice surface by toms. *Geophysical Research Letters*, 23:1165–1168.

Jacob, D. J., Logan, J. A., Gardner, G. M., Yevich, E. M., Spivakovski, C. M., Wofsy, S, C., Sillman, S., and Prather, M. J. (1993). Factors Regulating Ozone Over the United States and Its Export to the Global Atmosphere. *Journal of Geophysical Research*, 98:14817–14826.

Jäger, H. (1992). The Pinatubo eruption cloud observed by lidar at Garmisch-Partenkirchen. *Geophys. Res. Lett.*, 19:191–194.

Jäger, H. (1996). *Three years of remote sensing of Pinatubo aerosol extinction, mass, and surface area*, volume I 42 of *NATO ASI Series*, pages 61–70. Springer, Berlin Heidelberg.

Jäger, H., Carnuth, W., and Georgi, B. (1988). Observations of Saharan Dust at a North Alpine Mountain Station. *Journal of Aerosol Science*, 19:1235–1238.

Jäger, H., Deshler, T., and Hofmann, D. J. (1995). Midlatitude lidar backscatter conversions based on balloonborne aerosol measurements. *Geophys. Res. Lett.*, 22:1729–1732.

Jäger, H., Deshler, T., Homburg, F., and Freudenthaler, V. (1997). Advances in Atmospheric Remote Sensing with Lidar. In Ansmann, A., Neuber, R., Rairoux, P., and Wandinger, U., editors, *Advances in Atmospheric Remote Sensing with Lidar*, pages 485–488. Springer, Berlin Heidelberg.

Jäger, H., Freudenthaler, V., and Homburg, F. (1998). Remote sensing of optical depth of aerosols and clouds related to air traffic. *Atmos. Environment*, 32:3123–3127.

Jäger, H. and Hofmann, D. J. (1991). Midlatitude lidar backscatter to mass, area and extinctions conversion model based on insitu aerosol measurements from 1980 to 1987. *Appl. Opt.*, 30:127–138.

Jäger, H., Mücke, R., and Harris, J. (2000). The stratospheric aerosol layer after the decay of the Pinatubo perturbation. In Harris, Guirlet, and Amanatidis, editors, *Air pollution research report 73, Stratospheric ozone 1999*, pages 87–90. European Comission.

Kärcher, B. and Fahey, D. W. (1997). The role of sulfur emission in volatile particle formation in jet aircraft exhaust plumes. *Geophys. Res. Lett.*, 24:389–392.

Klett, J. D. (1981). Stable analytical inversion solution for processing lidar returns. *Appl. Opt.*, 20:211–220.

Klett, J. D. (1985). Lidar inversion with variable backscatter/extinction ratios. *Appl. Opt.*, 24:1638–1643.

Kottmeier, C. and Fay, B. (1998). Trajectories in the antarctic lower troposphere. *JGR*, 103(D9):10947–10959.

Kunz, G. J. and Trickl, T. (1996). Lidar measurements of atmospheric extinction during the MAPTIP trial. *Proceedings of S.P.I.E.*, 2828:31–38.

Louis, A. (1989). *Inverse und schlecht gestellte Probleme*. B.G. Teubner, Stuttgart.

Matthias, V. (2000). *Vertikalmessungen der Aerosolextinktion und des Ozons mit einem UV-Raman-Lidar*. PhD thesis, Universität Hamburg.

Mattis, I., Jaenisch, V., Müller, D., Franke, K., , and Ansmann, A. (2001). Classification of particle extinction profiles derived within the framework of the german lidar network by the use of cluster analysis of backtrajectories. In Dabas, A. and Pelon, J., editors, *Laser remote sensing of the atmosphere. Selected papers of the 20th International Laser Radar Conference.* Ecole Polytechnique.

McCormick, M. P. and Veiga, R. E. (1992). SAGE II measurements of early Pinatubo aerosols. *Geophys. Res. Lett.*, 19:155–158.

McPeters, R. D. (1993). The atmospheric SO_2 Budget for Pinatubo derived from NOAA-11 SBUV/2 spectral data. *Geophys. Res. Lett.*, 20:1971–1974.

Mie, G. (1908). Beiträge zur Optik trüber Medien, speziell kolloidaler Metallösungen. *Ann. Physik*, 25:377–455.

Müller, D., Wagner, F., Wandinger, U., and Ansmann, A. (2000). Microphysical particle parameters from extinction and backscatter lidar data by inversion with regularization: Experiment. *Appl. Opt.*, 39:1879–1892.

Müller, D., Wandinger, U., Althausen, D., Mattis, I., and Ansmann, A. (1998). Retrieval of physical particle properties from lidar observations of extinction and backscatter at multiple wavelengths. *Appl. Opt.*, 37:2260–2263.

Müller, D., Wandinger, U., and Ansmann, A. (1999a). Microphysical particle parameters from extinction and backscatter lidar data by inversion with regularization: Simulation. *Appl. Opt.*, 38:2358–2368.

Müller, D., Wandinger, U., and Ansmann, A. (1999b). Microphysical particle parameters from extinction and backscatter lidar data by inversion with regularization: Theory. *Appl. Opt*, 38:2346–2357.

Müller, H. and Reiter, R. (1986). Untersuchung der Grenzschicht über einem großen Alpental bei Berg-Talwindzirkulation. *Meteorologische Rundschau*, 39:247–256.

Müller, H. and Whiteman, C. D. (1988). Breakup of a Nocturnal Temperature Inversion in the Dischma Valley during DISKUS. *Journal of Applied Meteorology*, 27:188–194.

Neininger, B. and Dommen, J. (1996). Luftverschmutzung und Meteorologie in der Schweiz, Umweltmaterialien Nr. 63. Technical report, Bundesamt für Umwelt, Wald und Landwirtschaft (BUWAL), Bern, Switzerland.

Puxbaum, H. and Wagenbach, D. (1998). Editorial. *Atmospheric Environment*, 32:3923.

Reiter, R., Müller, H., Sladkovic, R., and Munzert, K. (1983). Aerologische Untersuchungen der tagesperiodischen Gebirgswinde unter besonderer Berücksichtigung des Windfeldes im Talquerschnitt. *Meteorologische Rundschau*, 36:225–242.

Reiter, R., Müller, H., Sladkovic, R., and Munzert, K. (1984a). Aerologische Untersuchungen des tagesperiodischen Windsystems im Inntal während MERKUR. *Meteorologische Rundschau*, 37:176–190.

Reiter, R., Pötzl, and Sladkovic, R. (1984b). Determination of the Concentration of Chemical Main and Trace Elements (Chemical Matrix) in the Aerosol from 1972 to 1982 at a North-Alpine Pure Air Station at 1780 m a. s. l., Part II: Parametric Correlation Analysis of the Chemical Matrix with Consideration of Meteorological Quantities. *Archives for Meteorology, Geophysics and Bioclimatology*, 35:1–30.

Sarközi, J. (2000). Untersuchung des Einflusses verschiedener Aerosoltypen (Form und substantielle Zusammensetzung) auf das Inversionsergebnis des schlecht gestellten Lidaroperators. Master's thesis, Universität Potsdam.

Sasano, Y., Browell, E. V., and Ismail, S. (1985). Error caused by using a constant extinction/backscattering ratio in the lidar solution. *Appl. Opt.*, 24:3929–3932.

Sasano, Y. and Nakane, H. (1984). Significance of the extinction / backscatter ratio and the boundary value term in the solution for the two-component lidar equation. *Appl. Opt.*, 23:11–13.

Schmitt, A. and Brunner, B. (1997). Emissions from aviation and their development over time. DLR-Mitteilung 97-04.

Seibert, P., Kromp-Kolb, H., Kasper, A., Kalina, M., Puxbaum, H., Jost, D. T., Schwikowski, M., and Baltensberger, U. (1998). Transport of polluted boundary layer air from the Po valley to high-Alpine sites. *Atmospheric Environment*, 32:3953–3965.

Stohl, A. (1998). Computation, accuracy and applications of trajectories —a review and bibliography. *Atmos. Environ.*, 32(6):947–966.

Stohl, A., Hittenberger, M., and Wotawa, G. (1998). Validation of the lagrangian particle dispersion model flexpart against constant volume balloon flights during etex. *Atmospheric Environment*, 24:4245–4264.

Stohl, A. and Trickl, T. (1999). A textbook case of long-range transport: Simultaneous observation of ozone maxima of stratospheric and North American origin in the free troposphere over Europe. *Journal of Geophysical Research*, 104:30445–30462.

Stohl, A. and Trickl, T. (2000). Observation of High Ozone Concentrations over Europe during Episodes of Intercontinental Transport. In *Atmospheric Ozone, Proceedings of the Quadrennial Ozone Symposium 2000*, pages 653–654.

Stohl, A., Wotawa, G., Seibert, P., and Kromp-Kolb, H. (1995). Interpolation errors in wind fields as a function of spatial and temporal resolution and their impact on different types of kinematic trajectories. *Journal of Applied Meteorology*, 34:2149–2165.

Tang, I. and Munkelwitz, H. (1993). Composition and temperature dependence of the deliquescence properties of hygroscopic aerosols. *Atmospheric Environment*, 27A:467–473.

United States Committee on Extension to the Standard Atmosphere (1976). *U. S. Standard Atmosphere, 1976*. National Oceanic and Amospheric Administration, Washington.

Vergeiner, I. and Dreiseitl, E. (1987). Valley Winds and Slope Winds – Observations and Elementary Thoughts. *Meteorology and Atmospheric Physics*, 36:264–286.

Völger, P., Bösenberg, J., and Schult, I. (1996). Scattering Properties of Selected Model Aerosols Calculated at UV-Wavelengths : Implications for DIAL Measurements of Tropospheric Ozone. *Contr. Atm. Physics*, 69(1):177–187.

Wandinger, U. and Ansmann, A. (2000a). Experimental determination of the laser-beam-receiver-field-of-view overlap function. In *20^{th} International Laser Radar Conference, Vichy, France*.

Wandinger, U. and Ansmann, A. (2000b). Experimental determination of the lidar overlap profile with raman lidar. *Appl. Opt.*, submitted September 2000.

Wandinger, U., Müller, D., Böckmann, C., Althausen, D., Matthias, V., Bösenberg, J., Weiß, V., Fiebig, M., Wendisch, M., Stohl, A., and Ansmann, A. (2000). Optical and microphysical characterization of biomass-burning and industrial-pollution aerosols from multiwavelength lidar and aircraft measurements. *Journal of Geophysical Research*, submitted.

Wendisch, M. et al. (2000). Aerosol-radiation interaction in the cloudless atmosphere during lace 98. part 1: measured and calculated solar and spectral surface insolations. *Journal of Geophysical Research*, submitted.

Whiteman, C. D. (1990). Observations of Thermally Developed Wind Systems in Mountainous Terrain. In *Atmospheric Processes over Complex Terrain*, pages 5–323. American Meteorological Society, Boston.

Wiegner, M., Quenzel, H., Rabus, D., Völker, W., Völger, P., Ackermann, J., Khler, C., Fergg, F., and Wildgruber, G. (1995). The mobile three-wavelength backscatter lidar of the meteorological institute of the university munich. In *Lidar and Atmospheric Sensing, SPIE Vol. 2505*, pages 2–10.

Wing, G. (1985). Condition numbers of matrices arising from the numerical solution of linear integral equations of the first kind. *J. Integral Equations*, 9:191–204.

Wotawa, G. and Trainer, M. (2000). The Influence of Canadian Forest Fires on Pollutant Concentrations in the United States. *Science*, 288:324–328.

Wulfmeyer, V. and Bösenberg, J. (1998). Ground–based differential absorption lidar for water vapor profiling: Assessment of accuracy, resolution, and meteorological applications. *Appl. Opt.*, 37:3825–3844.